

## THE GAS-SENSITIVE PROPERTIES OF TIN DIOXIDE FILMS

 Nuritdin Y. Yunusaliyev

Andijan State University named after Z.M. Babur, Andijan, Uzbekistan

\*Corresponding Author e-mail: [aboboevscp@gmail.com](mailto:aboboevscp@gmail.com)

Received September 3, 2024; revised November 15, 2024; accepted November 25, 2024

This study investigates the fabrication and performance of SnO<sub>2</sub> thin films for gas sensing applications, utilizing a deposition method at 2 bar pressure and 8 ml/min flow rate. A multilayer structure was developed, comprising 14 layers, each with a thickness of 250 nm, optimized for sensitivity and stability. The gas sensor, featuring a film heater and sensitive elements doped with a 1% silicon additive, demonstrated a wide operational temperature range (20-370 °C). Characterization of resistance changes revealed significant hysteresis before isothermal annealing, with resistance values stabilizing after prolonged exposure to 370 °C. Post-annealing, the sensor exhibited three orders of magnitude higher resistance, indicating improved stability and electronic transport properties. Doping with a 1N AgNO<sub>3</sub> solution significantly enhanced sensitivity to ammonia, with a detection threshold of 500 ppm, while sensitivity to alcohol vapors decreased, indicating selectivity. Experimental results confirm that local doping and thermal treatment effectively enhance the metrological characteristics of SnO<sub>2</sub>-based sensors, making them suitable for detecting toxic gases.

**Keywords:** Gas sensor; Tin dioxide; Silver; Ammonia; Alcohol; Temperature; Tin dioxide

**PACS:** 78.30.Am

### INTRODUCTION

Gas sensors of the resistive type based on metal oxide semiconductors (tin dioxide, zinc oxide) offer a number of advantages compared to other gas sensors: they allow for the detection of many inorganic and organic gases in the air, have a fast response time, and high sensitivity [1-3]. However, the problem of integrating such sensors into mass production remains unresolved, as it is quite difficult to simultaneously achieve stability, selectivity, and high sensitivity [4, 5].

Typically, tin dioxide (SnO<sub>2</sub>) is deposited on a cold substrate, resulting in an amorphous film structure, and prior to working with a long-stored sensor, an extended high-temperature annealing process (above the sensor's operating temperatures) is necessary for the crystallization of the film, desorption of residual gases, and stabilization of its electrical parameters [6-8].

The aim of this study is to investigate the influence of isothermal annealing modes and Ag doping on the stability of gas sensing properties of tin dioxide films and to improve the metrological characteristics of gas sensors.

### MATERIALS AND METHODS

The experimental method involved the deposition of SnO<sub>2</sub> films at an air pressure of 2 bar with a speed of 8 ml/min. The distance from the spraying head to the preheated silicon substrate was 85 cm [9]. The SnO<sub>2</sub> film was applied in a single layer for 18 minutes. Multilayer deposition of the SnO<sub>2</sub> film occurred every 1 minute with a subsequent 30-second break to restore the substrate temperature. In this way, 14 layers were obtained. The sample for investigation is a gas sensor crystal with dimensions of 1×1 mm<sup>2</sup>, manufactured using microelectronic technology [10]. Its structure includes a film heater, two sensitive elements based on tin dioxide with a 1% atomic silicon additive (film thickness 250 nm, sensitive element area size 200×320 μm<sup>2</sup>), and contacts for the sensitive layer in the form of a platinum pin structure with a distance of 10 μm between contacts [11-13].

Studies were conducted on the dependence of resistances of sensitive elements on the voltage at the heater  $U = 0$  V, Ohm: alpha-temperature power supply) during heating and cooling. The temperature of different crystals at the same applied voltage may vary, so calibration of the sensor heater was carried out before starting the work. The following formula is used to convert the value of the heater voltage to temperature [14]:

$$R_H = R_{H0}(1 + \alpha(T - T_{20})) \quad (1)$$

where  $R_H$  - resistance of the heater when voltage is applied to it.  $R_{H0}$  - resistance of the heater when  $U = 0$  V,  $\alpha$  - temperature coefficient of resistance, C<sup>-1</sup>;  $T$  — temperature of heating, °C;  $T_{20} = 20$ °C, room temperature.

The Table 1 shows the operating temperature of the sensor under corresponding voltages applied to the heater. The operating temperature range of this sample is within 20-370°C.

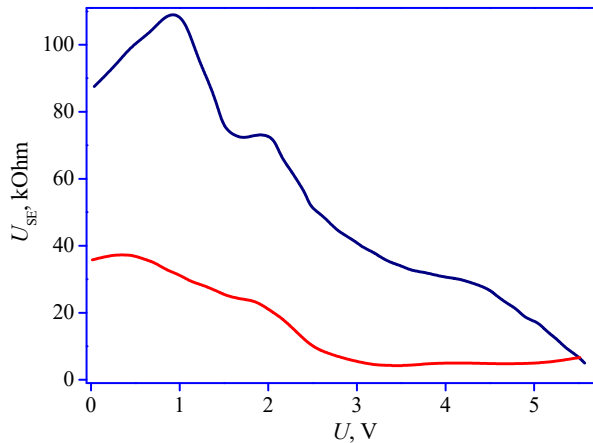
**Table 1.** Relationship between temperature and voltage on the heater (power supply).

U, V	0.5	1	1.5	2	2.5	3	3.5	4	4.5	5	5.5
T, °C	19	50	60	95	127	146	204	245	282	326	367

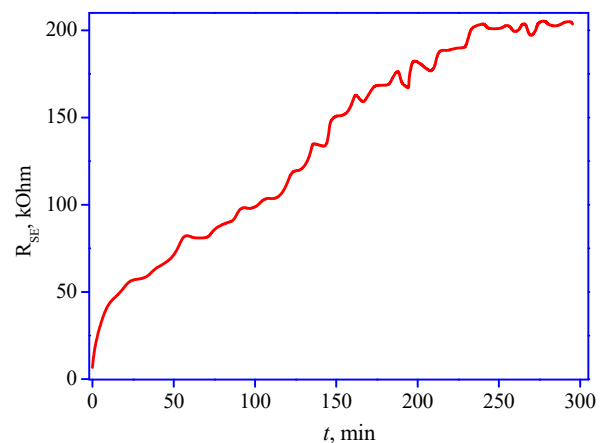
### RESULTS AND DISCUSSION

Figure 1 shows the dependencies of  $R(U)$  obtained before annealing. It should be noted that the resistances during both heating and cooling do not return to their initial values. The difference in resistance values of the SE amounts to 115% (52 kOhm). Isothermal annealing allows achieving less dispersion in resistance values.

Investigation of the change in resistances of the SE sensor over time during isothermal annealing (Fig. 2) has been conducted. Annealing was carried out at  $T_{\text{const}} = 370^\circ\text{C}$ . It is evident that the resistance of the SE increases, and after 4 hours of annealing, stabilization occurs. The annealing time of the sensor after storage may vary from half an hour to several hours of continuous exposure to high temperature.



**Figure 1.** Relationship between  $R_{SE}$  and the heating voltage  $U$  during the heating and cooling processes conducted prior to annealing the sensor (Red-heating, blue-cooling)



**Figure 2.** Relationship between the resistance of the sensor  $R_{SE}$  and time during isothermal annealing

Furthermore, the dependence of the  $R_{SE}$  values on  $U$  after isothermal annealing was investigated (Fig. 3). It was found that as a result of annealing, the resistance of the sensitive element returns to its original state after heating and cooling. However, compared to the values obtained before annealing, the resistances are three orders of magnitude higher. In order to determine the range of controlled gas concentrations, it is necessary to study the dependence of sensitivity on gas concentration [15-17]. Experiments have previously been conducted to investigate the influence of doping with various concentrations of silver, and a 1N solution of Ag was chosen as optimal. Figure 4 shows the dependencies of gas sensitivity on ammonia concentration within the range of 500 to 5000 ppm. At room temperature, a sample with doping of the sensor layer with a 1N solution of Ag ( $R_{SE,1}$ ) and a control layer without doping ( $R_{SE,2}$ ) was investigated.

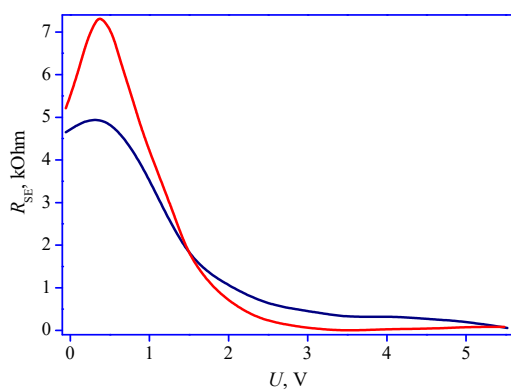


**Figure 3.** Relationship between  $R_{SE}$  and the voltage on the heater  $U_{BP}$  during heating and cooling processes conducted after the annealing of the sensor. (Red-heating, blue-cooling)

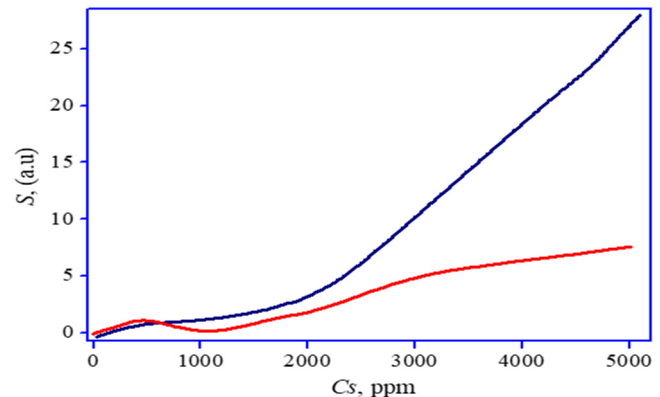


**Figure 4.** Dependence of the gas sensitivity of the doped sample 1N solution on the introduced concentration of ammonia vapors at  $T=210^\circ\text{C}$ :  $R_{SE,1}$  - sensitive sensor element with an undoped surface (control sample - red curve);  $R_{SE,2}$  - sensitive sensor element with a doped surface (blue curve)

It has been established that the change in resistance of the doped sample ( $R_{SE,2}$ ) is 20% at an ammonia concentration in the air of 500 ppm, while  $R_{SE,1}$  (control) shows no reaction within this range. Additionally, the graph demonstrates a significant difference, approximately threefold, when comparing the sensitivity of the two elements at higher ammonia concentrations.

During the measurements, it was noted that after silver doping, the sensor's sensitivity to alcohol vapors decreases. An experiment was conducted to establish this relationship, as depicted in Fig. 5, to determine the influence of  $C_s = 3000$  ppm when applying voltage to the gas sensor.

As shown in Fig. 4, after doping the surface of SnO<sub>2</sub>, its sensitivity decreased by a factor of 3, while the temperature of maximum sensitivity remained practically unchanged, making it possible to create a selective microelectronic sensor for ammonia and alcohol.

A series of experiments was conducted to study the effect of doping on the selectivity of the sensor to different gases. The first part of the experiments involved determining the saturation time of the film with toxic ammonia vapors and, consequently, the maximum sensitivity. For this purpose, the sample was placed under a sealed dome, into which toxic gas vapors with concentrations of  $C_s=2000$  ppm were introduced. The processes of interaction between ammonia and the semiconductor surface represent a prolonged process with a time delay of approximately 10-12 minutes.

The second part of the research involves establishing the dependence of  $S_g$  on the applied heating voltage and the operating modes of the sensor element, where the highest sensitivity to alcohol vapor ( $C_s=2000$  ppm) is observed. The gas sensor's built-in heater was supplied with voltages ranging from 0.5 V to 5 V in steps of 0.5 V, using the DC Power Supply HY3005 for heating the sensor's active surface. Resistance values were measured from the sensitive elements using Mastech MY64 multimeters [18]. It was found that the same sensor exhibits sensitive properties to different gases in different modes. Therefore, the next step was to conduct an experiment to determine the sensitivity of the doped sensor to two toxic gases simultaneously.

The gas sensor with the application of a doping substance at a concentration of 1N was investigated. Subsequently, samples were placed under the sealed dome of the measuring setup, and vapors of gases such as alcohol and ammonia were introduced at concentrations of 2000 ppm. The results of the effect of AgNO<sub>3</sub> impurities and operating modes on the sensitivity of the tested sample are shown in Figure 5.

Figure 6 can be divided into 3 parts: I - far left, II - central/middle, III - far right. In the first part, the steady state of the gas sensor is demonstrated without any external influences. In the second part of the graph, two toxic gases were introduced. The behavior of the curve in this segment indicates that the sensor film exhibits a sensitivity peak at room temperature (response to ammonia). Then, in segment 3, voltages ranging from 0.5 V to 5 V were applied in steps of 0.5 V. Subsequently, from the behavior of the curve, it is evident that the sensitive element's surface undergoes annealing and thermal stabilization. At a voltage value of  $U=5$  V, a second peak appears, corresponding to the reaction of the semiconductor film SnO<sub>2</sub> to alcohol vapors.

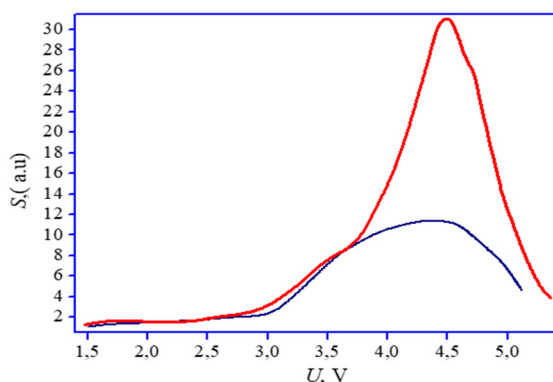


**Figure 5.** Effect of doping (1N solution) on the sensitivity to alcohol vapor  $C_s=3000$  ppm when applying voltage to the gas sensor. (before – red curve, after – blue curve)

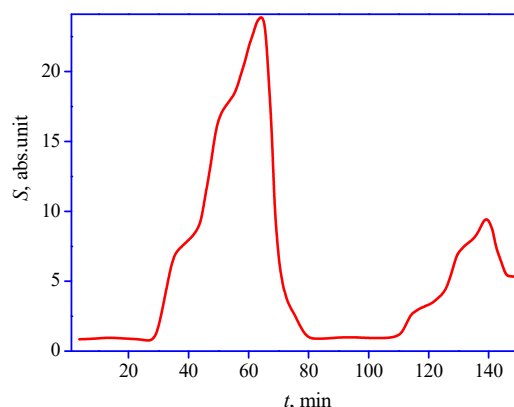


**Figure 6.** Sensitivity of the gas sensor doped with silver to a mixture of two gases - alcohol (2000 ppm) and ammonia (2000 ppm)

As a result of the research, a technique for local doping of SnO<sub>2</sub> sensing layers in microelectronic sensors has been developed. It has been demonstrated that SnO<sub>2</sub> sensing layers doped with AgNO<sub>3</sub> are sensitive to ammonia vapors at room temperature. The type of dependence of gas sensitivity on the concentration of ammonia in the range of 50 ppm to 5000 ppm has been determined. Sensitivity thresholds of SnO<sub>2</sub> films doped with 1N solution have been identified, which amounted to 500 ppm of ammonia in the air. Through experimentation, the selective response of the microelectronic sensor to vapors of two toxic gases simultaneously has been proven.

## CONCLUSION

Therefore, these studies confirm that isothermal annealing improves the stability of gas sensor operation, increasing  $R_{SE}$  and releasing oxygen chemical bonds on the surface of the sensitive SnO<sub>2</sub> layer, thereby enhancing the electronic transport properties of the film. Doping Ag into the sensor layers of SnO<sub>2</sub> in gas sensors allows to improve the metrological characteristics (sensitivity, selectivity, power consumption) of the samples and makes them a good material for creating a selective indicator of toxic and explosive gases.

## Funding

The present research work was financed under the project FZ-292154210 granted by the Ministry of Innovative Development of the Republic of Uzbekistan.

## ORCID

Nuritdin Y. Yunusaliyev, <https://orcid.org/0000-0003-3766-5420>

## REFERENCES

- [1] H.C. Wang, and M.J. Yang, "Fast response thin film SnO<sub>2</sub> gas sensors operating at room temperature," *Sensors and Actuators B: Chemical*, **119**(2), 380–383 (2006). <https://doi.org/10.1016/j.snb.2005.12.037>
- [2] A. Mirzaei, *et al.*, "Resistive gas sensors based on metal-oxide nanowires," *J. Appl. Phys.* **126**, 241102 (2019). <https://doi.org/10.1063/1.5118805>
- [3] G. Velmathi, S. Mohan, and Rabinder Henry, "Analysis and Review of Tin Oxide-Based Chemoresistive Gas Sensor," *IETE Technical Review*, (2015). <https://doi.org/10.1080/02564602.2015.1080603>
- [4] S.Z. Zainabidinov, A.Y. Boboev, N.Y. Yunusaliyev, and J.N. Usmonov, "An optimized ultrasonic spray pyrolysis device for the production of metal oxide films and their morphology," *East Eur. J. Phys.* **3**, 293 (2024), <https://doi.org/10.26565/2312-4334-2024-3-30>
- [5] A.S. Saidov, S.Z. Zainabidinov, M.U. Kalanov, A.Y. Boboev, and B.R. Kutlimurotov, "Peculiarities of photosensitivity of n-(GaAs)-p-(GaAs)<sub>1-x-y</sub>(ZnSe)<sub>x</sub>(Ge)<sub>y</sub> structures with quantum dots," *Applied Solar Energy*, **51**(3), 206–208 (2015). <https://doi.org/10.3103/S0003701X15030111>
- [6] S. Zainabidinov, A.Y. Boboev, and N.Y. Yunusaliyev, "Effect of  $\gamma$ -irradiation on structure and electrophysical properties of S-doped ZnO films," *East European Journal of Physics*, (2), 321–326 (2024). <https://doi.org/10.26565/2312-4334-2024-2-37>
- [7] P. Patil, R. Kawar, S. Tanay, D. Amalnerkar, and P.S. Chigare, "Effect of substrate temperature on structural, electrical and optical properties of sprayed tin oxide (SnO<sub>2</sub>) thin films," *Ceramics International*, **29**, 725–734 (2003). [https://doi.org/10.1016/S0272-8842\(02\)00224-9](https://doi.org/10.1016/S0272-8842(02)00224-9)
- [8] T. Kobayashi, *et al.*, "Process of crystallization in thin amorphous tin oxide film," *Journal of Crystal Growth*, **243**(1), 143–150 (2002). [https://doi.org/10.1016/S0022-0248\(02\)01445-8](https://doi.org/10.1016/S0022-0248(02)01445-8)
- [9] F.A. Akgul, *et al.*, "Structural and electronic properties of SnO<sub>2</sub>," *Journal of Alloys and Compounds*, **579**, 50–56 (2013). <http://dx.doi.org/10.1016/j.jallcom.2013.05.057>
- [10] S.Z. Zainabidinov, Sh.U. Yuldashev, A.Y. Boboev, and N.Y. Yunusaliyev, "X-ray diffraction and electron microscopic studies of the ZnO<S> metal oxide films obtained by the ultrasonic spray pyrolysis method," *Herald of the Bauman Moscow State Technical University, Series Natural Sciences*, **112**(1), 78–92. (2024). <https://doi.org/10.18698/1812-3368-2024-1-78-92>
- [11] A. Aqilah, N.M. Sin, M. Mamat, M. Hussin, M. Abdullah, and N. Asli, "Effect of Annealing Temperature on the Structural Properties and Performance of ZnO/SnO<sub>2</sub> Nanostructure of AZO-Based Humidity Sensor," *Nano Hybrids and Composites*, **45**, 53 (2024). <https://doi.org/10.4028/p-QIV6Q7>
- [12] U.O. Kutliev, M.K. Karimov, F.O. Kuryozov, and K.U. Otabaeva, "Analysis of InGaP(001) surface by the low energy ion scattering spectroscopy," *Journal of Physics: Conference Series*, **1889**(2), 022063 (2021). <https://doi.org/10.1088/1742-6596/1889/2/022063>
- [13] M.K. Karimov, U.O. Kutliev, S.B. Bobojonova, and K.U. Otabaeva, "Investigation of Angular Spectrum of Scattered Inert Gas Ions from the InGaP (001) Surface," *Physics and Chemistry of Solid State*, **22**(4), 742–745 (2021). <https://doi.org/10.15330/pcss.22.4.742-745>
- [14] A. Ibtisam, L. Doowon, Ch. Myoungsu, and H.D. Kim, "Advanced recovery and enhanced humidity tolerance of CNTs gas sensor using a filament heater," *Chemical Engineering Journal*, **496**, 154014 (2024). <https://doi.org/10.1016/j.cej.2024.154014>
- [15] V.E. Bochenlov, and G.B. Sergeev, "Sensitivity, Selectivity, and Stability of Gas-Sensitive Metal-Oxide Nanostructures," in: *Metal oxide nanostructures and their applications*, vol. 3. (American Scientific, Publishers, USA, 2010), pp. 31–52.
- [16] U.O. Kutliev, M.U. Otabaev, and M.K. Karimov, "Investigation Ne ions scattering from the stepped InP(001)<math>\leq 10^{\circ}</math> surface," *Journal of Physics: Conference Series*, **2388**(1), 012092 (2022). <https://doi.org/10.1088/1742-6596/2388/1/012092>
- [17] Sh.B. Utamuradova, Sh.Kh. Daliev, J.J. Khamdamov, Kh.J. Matchonov, and Kh.Y. Utemuratova, "Research of the Impact of Silicon Doping with Holmium on its Structure and Properties Using Raman Scattering Spectroscopy Methods," *East Eur. J. Phys.* (2), 274 (2024). <https://doi.org/10.26565/2312-4334-2024-2-28>
- [18] S. Zainabidinov, Sh.Kh. Yulchiev, A.Y. Boboev, B.D. Gulomov, and N.Y. Yunusaliyev, "Structural properties of Al-doped ZnO films," *East Eur. J. Phys.* (3), 282 (2024). <https://doi.org/10.26565/2312-4334-2024-3-28>

## ГАЗОЧУТЛИВІ ВЛАСТИВОСТІ ПЛІВОК ДІОКСИДУ ОЛОВА

Нурітдін Ю. Юнусалієв

*Андижанський державний університет імені З.М. Бабур, Андижан, Узбекистан*

У цій роботі досліджується виготовлення та ефективність тонких плівок SnO<sub>2</sub> для датчиків газу з використанням методу осадження при тиску 2 бар і швидкості потоку 8 мл/хв. Було розроблено багат шарову структуру, що складається з 14 шарів, кожен з яких має товщину 250 нм, оптимізованих для чутливості та стабільності. Газовий датчик, який має плівковий нагрівач і чутливі елементи, легувані 1% добавкою кременію, продемонстрував широкий діапазон робочих температур (20-370°C). Характеристика змін опору виявила значний гістерезис перед ізотермічним відпадом, а значення опору стабілізувалися після тривалого впливу 370°C. Після відпаду датчик продемонстрував на три порядки більший опір, що вказує на покращену стабільність і електронні транспортні властивості. Допування 1N розчином AgNO<sub>3</sub> значно підвищило чутливість до аміаку з порогом виявлення 500 ppm, тоді як чутливість до парів спирту знизилася, що свідчить про селективність. Експериментальні результати підтверджують, що локальне легування та термічна обробка ефективно покращують метрологічні характеристики датчиків на основі SnO<sub>2</sub>, роблячи їх придатними для виявлення токсичних газів.

**Ключові слова:** газовий датчик; діоксид олова; срібло; аміак; спирт; температура; діоксид олова

## INVESTIGATION OF VOLT-AMPERE CHARACTERISTICS OF A GAS-SENSITIVE SENSOR BASED ON TIN DIOXIDE

✉ Sirajidin Z. Zainabidinov<sup>a</sup>, ✉ Akramjon Y. Boboev<sup>a,b</sup>, ✉ Nuritdin Y. Yunusaliyev<sup>a</sup>,  
✉ Bakhtiyor D. Gulomov<sup>c</sup>, ✉ Jakhongir A. Urinboev<sup>a</sup>

<sup>a</sup>Andijan State University named after Z.M. Babur, Andijan, Uzbekistan

<sup>b</sup>Institute of Semiconductor Physics and Microelectronics, National University of Uzbekistan, Tashkent, Uzbekistan

<sup>c</sup>Andijan state pedagogical institute, Andijan, Uzbekistan

\*Corresponding Author e-mail: [aboboevscp@gmail.com](mailto:aboboevscp@gmail.com)

Received September 30, 2024; revised November 20, 2024; accepted November 25, 2024

The volt-ampere characteristics of the sensitive elements of gas sensors are investigated and plotted in coordinates corresponding to various mechanisms of the transfer current. It has been established that the prevailing mechanism of current transfer in the section from 0 to 6 V is Ohm's law, in the interval (3 - 6) V the Mott's law is fulfilled, and at higher voltages deviations from these laws are observed. It is determined that the laws of Ohm and Mott confirm the mechanism of the flow of currents limited by the space charge.

**Key words:** Tin dioxide; Sensor; Heterojunction; Gas sensing; Sensitive element

**PACS:** 78.30.Am

### INTRODUCTION

Currently, microelectronic gas sensors are widely used for environmental monitoring, ventilation and air conditioning systems, household devices, and the automotive industry [1,2]. They are also employed to determine the maximum permissible concentrations of hazardous gases in mining, chemical, and metallurgical industries [3,4]. Among a wide range of metal oxide semiconductors, tin dioxide is considered the most promising sensing material [5]. Gas-sensitive resistive-type sensors are manufactured using tin dioxide, which detect the presence of gases in the air by measuring changes in resistance between contacts.

The miniaturization of gas sensors, while maintaining operational voltages, increases the electric field in the gap between contacts. This stimulates the migration of ion-adsorbed gas particles across the active layer surface, influencing the overall characteristics of gas-sensitive devices and enabling gas analysis and recognition [6,7].

Research into the electrophysical characteristics of metal-oxide-semiconductor structures typically involves measuring their volt-farad characteristics (often at high frequencies) for dielectric oxide layers and their volt-ampere characteristics (IVC) under direct current for oxide layers with relatively high conductivity. This study presents experimental results on the current transport mechanism in heterojunctions based on SnO<sub>2</sub>/Si.

### EXPERIMENTAL METHOD

The results of the study of current flow mechanisms in SnO<sub>2</sub> films based on the investigation of the current-voltage characteristics of test structures are presented. The object of the study is the sensitive element of a gas sensor. The crystal of the gas sensor, measuring 1×1 mm<sup>2</sup>, contains the following elements: on an oxidized silicon substrate, a heater and contacts for the sensitive layer in the form of an intersecting pin structure, made based on Ti-Pt, and two gas-sensitive elements based on tin dioxide, doped with 1 at. % silicon [8]. The resistance of the heater is -29.8 Ohms. The sensitive elements have resistances of 4.2 and 4.6 MOhms, respectively.

For the research, the following equipment was used: two power sources (DC Power Supply HY 3005), three multimeters (MASTECHMY64), and a measuring stand [9-10]. The current through the gas-sensitive element is controlled by the voltage drop across the standard load resistance connected in series with the gas-sensitive element. The voltage applied to the sensitive element ranged from 0 to 30 V with a step of 1 V. As the voltage on the sensitive element increased, the current through the sensitive element also increased. The current values on the sensitive element ranged from 0 to 4.5 mA.

### RESULTS AND DISCUSSION

Figure 1 shows the volt-ampere characteristic of the gas sensor's sensitive element, measured at room temperature in the voltage range from 0 to 31 V. It was found that with a change in voltage from 1 to 31 V, the current changes from 0 to 4.19 mA. From Figure 1, it can be seen that the volt-ampere characteristic of the sensitive element can be conditionally divided into 3 sections, each with a different slope: section 1 from 0 to 6 V, section 2 from 6 to 17 V, section 3 from 17 to 31 V.

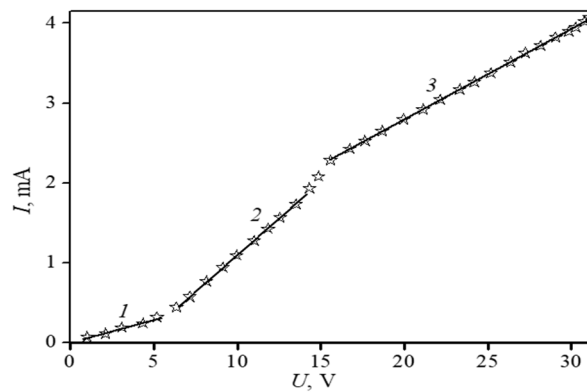


**Figure 1.** Volt-ampere characteristic of the gas sensor's sensitive element, measured at room temperature in the voltage range (0 - 31) V.

To evaluate the current conduction mechanisms, the volt-ampere characteristics were transformed into the following coordinates:  $I/U = F(U)$  - Ohm's law [11,12],  $I/U^{1/2} = F(U^{1/2})$  - Poole-Frenkel mechanism [13-15],  $I/U^2 = F(U^2)$  - Mott's law[16] (Fig. 2-4).

In the voltage range of (0 - 6) V (Fig. 2), rectification of the volt-ampere characteristic in the coordinates  $I/U = F(U)$  occurs, which means that Ohm's law is satisfied.

The construction of the  $I/U^{1/2} = F(U^{1/2})$  coordinate corresponds to the Poole-Frenkel mechanism (Fig. 3). The current-voltage characteristic constructed in these coordinates linearly increases over the entire voltage range, and therefore the Poole-Frenkel mechanism does not work in this case.

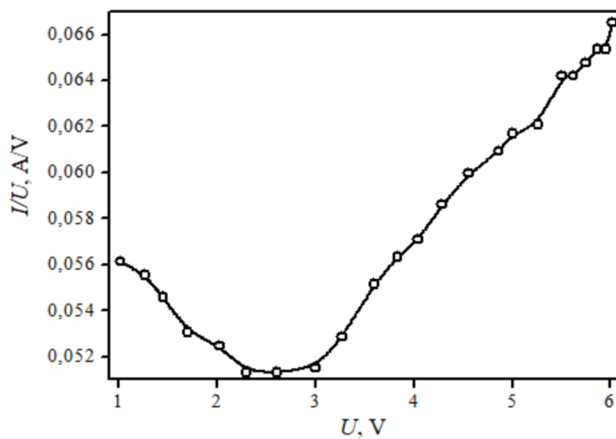


**Figure 2.** Volt-ampere characteristic of the sensitive element (SE1) of the gas sensor in the  $I/U = F(U)$  coordinates within the voltage range of (0 - 6) V

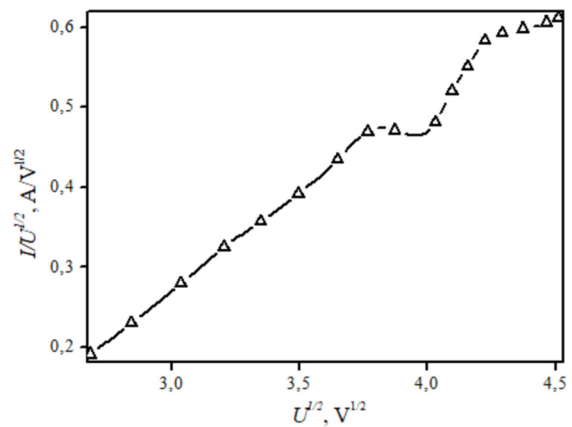


**Figure 3.** Volt-ampere characteristic of the sensitive element (SE1) of a gas sensor, plotted in the coordinates  $I/U^{1/2} = F(U^{1/2})$  within the voltage range of (6 - 20) V

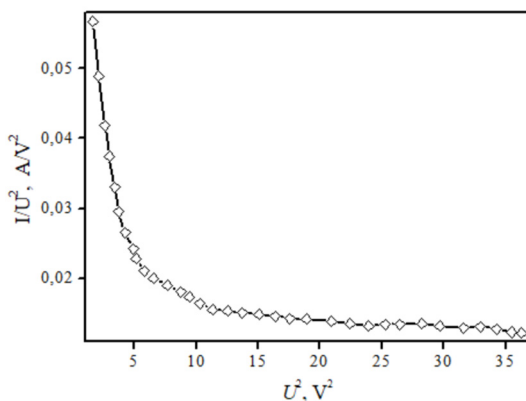


**Figure 4.** Volt-ampere characteristic of the sensitive element (SE1) of the gas sensor, measured at room temperature, in the coordinates  $I/U^2 = F(U^2)$  in the voltage range (0-6)

In the voltage range of (3-6) V or (9-30) V (Fig. 4), rectification of the volt-ampere characteristic in the coordinates  $I/U^2 = F(U^2)$  occurs, which means that Ohm's law is satisfied. With further increase in voltage in the coordinates  $I/U^2 = F(U^2)$ , the function shows an increasing trend and no leveling off is observed.

It is known that the main physical mechanisms of charge carrier transport in semiconductors are: currents obeying Ohm's law; currents limited by space charge; currents determined by barrier (Schottky) emission; the volume mechanism of Poole-Frenkel - enhanced by the electric field ionization of impurity centers; electron tunneling through thin layers of insulators and semiconductors; hopping conductivity through impurities in semiconductors [17-19]. The traditional analysis of current transport mechanisms in solids is based on the measurement of static volt-ampere characteristics [20]. In the low voltage mode, while the average concentration of free charge carriers is approximately equal to the equilibrium concentration, Ohm's law will be observed. Its characteristic feature is the linearity of the VAC structure, the dependence of  $j = \sigma E$  or  $I = U/R$  and its rectification in the coordinates  $I/U = f(U)$ . At higher voltages, the volt-ampere characteristic begins to obey the quadratic law of Mott and the VAC structure rectifies in the coordinates  $I/U^2 = F(U^2)$ . The linearity of the VAC in the coordinates  $I/U^{1/2} = F(U^{1/2})$  is characteristic of the Poole-Frenkel effect. Obviously, there may be conditions when both two or more charge transport mechanisms can act simultaneously.

### CONCLUSIONS

The voltammetric characteristics of gas sensor sensitive elements were investigated and plotted in coordinates corresponding to different mechanisms of charge transfer. It was established that the predominant charge transfer mechanism in the range of 0 to 6 V follows Ohm's law, while in the range of 3 to 6 V, Mott's law applies. Therefore, in the voltage range from 0 to 6 V, the simultaneous manifestation of Ohm's and Mott's laws confirms a current flow mechanism limited by space charge. At higher voltages, deviations from these laws were observed.

The results obtained can be applied in gas sensing technology to determine the operating temperature of sensors, facilitating the recognition of gas types.

### Conflict of Interests

The authors declare that they have no conflict of interests

### Funding

The present research work was financed under the project FZ-292154210 granted by the Ministry of Innovative Development of the Republic of Uzbekistan

### ORCID

©Sirajidin Z. Zainabidinov, <https://orcid.org/0000-0003-2943-5844>; ©Akramjon Y. Boboev, <https://orcid.org/0000-0002-3963-708X>  
 ©Nuritdin Y. Yunusaliyev, <https://orcid.org/0000-0003-3766-5420>; ©Bakhtiyor D. Gulomov, <https://orcid.org/0009-0005-8614-6311>  
 ©Jakhondir A. Urinboev, <https://orcid.org/0009-0003-4903-4164>

### REFERENCES

- [1] S. Hooshmand, P. Kassanos, M. Keshavarz, P. Duru, C.I. Kayalan, I. Kale, and M.K. Bayazit, "Wearable Nano-Based Gas Sensors for Environmental Monitoring and Encountered Challenges in Optimization," *Sensors*, **23**, 8648 (2023). <https://doi.org/10.3390/s23208648>
- [2] S. Nath, A. Dey, P. Pachal, J.K. Sing, and S.K. Sarkar, "Performance Analysis of Gas Sensing Device and Corresponding IoT Framework in Mine Microsyst," *Technol*, **27**, 3977–3985 (2021). <https://doi.org/10.1007/s00542-019-04621-x>
- [3] A.V. Martirosyan, and Y.V. Ilyushin, "The Development of the Toxic and Flammable Gases Concentration Monitoring System for Coalmines," *Energies*, **15**, 8917-8919, (2022). <https://doi.org/10.3390/en15238917>
- [4] A.V. Shaposhnik, P.V. Moskalev, K.L. Chegereva, A.A. Zviagin, and A.A. Vasiliev, "Selective gas detection of H<sub>2</sub> and CO by a single MOX-sensor," *Sensors and Actuators B: Chemical*, **334**, 129376, (2021). <https://doi.org/10.1016/j.snb.2020.129376>
- [5] H.C. Wang, Y. Li, and M.J. Yang, "Fast response thin film SnO<sub>2</sub> gas sensors operating at room temperature. *Sensors and Actuators B: Chemical*, **119**, 380-383 (2006). <http://dx.doi.org/10.1016%2Fj.snb.2005.12.037>
- [6] M.A. Carpenter, S. Mathur, and A. Kolmakov, *Metal Oxide Nanomaterials for Chemical Sensors*, (Springer Science & Business Media, New York, 2012).
- [7] B. Saruhan, L.R. Fomekong, and S. Nahiriak, "Review: Influences of Semiconductor Metal Oxide Properties on Gas Sensing Characteristics". *Front. Sens.* **2**, 657931 (2021). <https://doi.org/10.3389/fsens.2021.657931>
- [8] S. Zainabidinov, A.Y. Boboev, and N.Y. Yunusaliyev, "Effect of  $\gamma$ -irradiation on structure and electrophysical properties of S-doped ZnO films," *East European Journal of Physics*, (2), 321–326 (2024). <https://doi.org/10.26565/2312-4334-2024-2-37>
- [9] S. Zainabidinov, A. Y. Boboev, Kh. A. Makhmudov, et al., "Photoelectric Properties of n-ZnO/p-Si Heterostructures," *Applied Solar Energy*, **57**(6), 475–479 (2021). <http://doi:10.3103/S0003701X21060177>
- [10] Sh.B. Utamuradova, Sh.Kh. Daliyev, J.J. Khamdamov, Kh.J. Matchonov, and Kh.Y. Utemuratova, "Research of the Impact of Silicon Doping with Holmium on its Structure and Properties Using Raman Scattering Spectroscopy Methods," *East Eur. J. Phys.* **2**, 274 (2024), <https://doi.org/10.26565/2312-4334-2024-2-28>
- [11] M. Klas, Š. Matejčik, B. Radjenović, and M. Radmilović-Radjenović, "Measurements of the Volt-Ampere Characteristics and the Breakdown Voltages of Direct-Current Helium and Hydrogen Discharges in Microgaps," *Physics of Plasmas*, **21**(10), 103503 (2014). <https://doi.org/10.1063/1.4897303>
- [12] U.O. Kutliev, M.U. Otabaev, and M.K. Karimov, "Investigation Ne ions scattering from the stepped InP(001)<math>\langle 110 \rangle</math> surface," *Journal of Physics: Conference Series*, **2388**(1), 012092 (2022). <https://doi.org/10.1088/1742-6596/2388/1/012092>
- [13] D.S. Jeong, and Ch.S. Hwang, "Tunneling-assisted Poole-Frenkel conduction mechanism in HfO<sub>2</sub> thin films," *J. Appl. Phys.* **98**, 113701 (2005). <https://doi.org/10.1063/1.2135895>
- [14] S.Z. Zainabidinov, A.S. Saidov, M.U. Kalanov, and A.Y. Boboev, "Synthesis, Structure and Electro-Physical Properties n-GaAs-p-(GaAs)<sub>1-x-y</sub>(Ge<sub>2</sub>)<sub>x</sub>(ZnSe)<sub>y</sub> Heterostructures," *Applied Solar Energy*. **55**(5), 291–308 (2019). <https://doi.org/10.3103/S0003701X1905013X>

- [15] S.Z. Zainabidinov, A.S. Saidov, A.Y. Boboev, and D.P. Abdurahimov, "Structure, morphology and photoelectric properties of n-GaAs-p-(GaAs)<sub>1-x</sub>(Ge<sub>2</sub>)<sub>x</sub> heterostructure, Herald of the Bauman Moscow State Technical University, Series Natural Sciences, **1**(100), 72–87 (2022). <http://dx.doi.org/10.18698/1812-3368-2022-1-72-87>
- [16] D. Mizginov, O. Telminov, S. Yanovich, D. Zhevnenko, F. Meshchaninov, and E. Gornev, "Investigation of the Temperature Dependence of Volt-Ampere Characteristics of a Thin-Film Si<sub>3</sub>N<sub>4</sub> Memristor," Crystals, **13**, 323 (2023). <https://doi.org/10.3390/cryst13020323>
- [17] M.K. Karimov, U.O. Kutliev, S.B. Bobojonova, and K.U. Otabaeva, "Investigation of Angular Spectrum of Scattered Inert Gas Ions from the InGaP (001) Surface," Physics and Chemistry of Solid State, **22**(4), 742–745 (2021)
- [18] Sh.B. Utamuradova, Sh.Kh. Daliyev, J.J. Khamdamov, Kh.J. Matchonov, and Kh.Y. Utemuratova, "Research of the Impact of Silicon Doping with Holmium on its Structure and Properties Using Raman Scattering Spectroscopy Methods," East Eur. J. Phys. **2**, 274 (2024), <https://doi.org/10.26565/2312-4334-2024-2-28>
- [19] U.O. Kutliev, M.K. Karimov, F.O. Kuryozov, and K.U. Otabaeva, "Analysis of InGaP(001) surface by the low energy ion scattering spectroscopy," Journal of Physics: Conference Series, **1889**(2), 022063 (2021). <https://doi.org/10.1088/1742-6596/1889/2/022063>
- [20] M. S. Dresselhaus, Solid State Physics Part (I): Transport Properties of Solids Fall, (2001).

**ДОСЛІДЖЕННЯ ВОЛЬТ-АМПЕРНИХ ХАРАКТЕРИСТИК ГАЗОЧУТЛИВОГО СЕНСОРА  
НА ОСНОВІ ДІОКСИДУ ОЛОВА**

**Сіражідін З. Зайнабідінов<sup>a</sup>, Акрамжон Ю. Бобоєв<sup>a,b</sup>, Нурітдін Ю. Юнусалієв<sup>a</sup>, Бахтіор Д. Гуломов<sup>c</sup>  
Джахонгір А. Урінбоєв<sup>a</sup>**

<sup>a</sup>Андижанський державний університет імені З.М. Бабур, Андижан, Узбекистан

<sup>b</sup>Інститут фізики напівпровідників та мікроелектроніки Національного університету Узбекистану, Ташкент, Узбекистан

<sup>c</sup>Андижанський державний педагогічний інститут, Андижан, Узбекистан

Досліджено та побудовано вольт-амперні характеристики чутливих елементів газових сенсорів у координатах, що відповідають різним механізмам перенесення струму. Встановлено, що переважаючим механізмом передачі струму на ділянці від 0 до 6 В є закон Ома, в інтервалі (3–6) В виконується закон Мотта, а при більш високих напругах спостерігаються відхилення від цих законів. Визначено, що закони Ом і Мотт підтверджують механізм протікання струмів, обмежених просторовим зарядом.

**Ключові слова:** діоксид олова; датчик; гетероперехід; датчик газу; чутливий елемент

## COMPUTATIONAL STUDY OF DRUG DELIVERY SYSTEMS WITH RADIONUCLIDE AND FLUORESCENCE IMAGING MODALITIES. I. ALBUMIN-BASED SYSTEMS FOR DOXORUBICIN DELIVERY

 V. Trusova<sup>a\*</sup>,  U. Tarabara<sup>a</sup>, I. Karnaukhov<sup>b</sup>,  A. Zelinsky<sup>b</sup>,  B. Borts<sup>b</sup>, I. Ushakov<sup>b</sup>, L. Sidenko<sup>b</sup>,  G. Gorbenko<sup>a</sup>

<sup>a</sup>Department of Medical Physics and Biomedical Nanotechnologies, V.N. Karazin Kharkiv National University  
4 Svobody Sq., Kharkiv, 61022, Ukraine

<sup>b</sup>National Science Center "Kharkov Institute of Physics and Technology", Kharkiv, Ukraine

\*Corresponding Author: [valerija.trusova@karazin.ua](mailto:valerija.trusova@karazin.ua)

Received August 15, 2024, revised September 22, 2024; accepted November 3, 2024

Molecular docking and molecular dynamics methodologies were employed to design and evaluate delivery systems for the antineoplastic agent doxorubicin (DOX) utilizing human serum albumin (HSA) as the carrier. To engineer a drug delivery system (DDS) with dual imaging modalities, complexes of the radionuclide technetium-99m (TCC) and near-infrared (NIR) fluorescent dyes, including indocyanine green (IG), methylene blue (MB), heptamethine cyanine dye AK7-5, and squaraine dye SQ1, were integrated into the protein nanocarriers. The highest binding affinities to the proteins were identified for TCC [<sup>99m</sup>Tc]Tc-diisopropyl iminodiacetic acid (TcDIS), [<sup>99m</sup>Tc]Tc-hydrazinonicotinic acid-H6F (TcHYN), [<sup>99m</sup>Tc]Tc-Mebrofenin (TcMEB), as well as the fluorescent dyes IG and SQ1. Molecular docking analyses revealed that most technetium complexes (TCCs) bind to HSA domain I, with some exceptions showing affinity for domains I and III or domain III alone. Ternary and quaternary protein-ligand systems were explored using multiple ligand docking approaches. In ternary systems, DOX binding sites were identified either in domain I or in a region spanning multiple domains, depending on potential overlap with TCC binding sites. For quaternary systems incorporating NIR fluorophores, binding affinities decreased in the order: IG > SQ1 > AK7-5 > MB. Molecular dynamics simulations of HSA-DOX-MB and HSA-DOX-IG complexes demonstrated stable associations between the components, with consistent center-of-mass distances and minimal perturbation of HSA structure. These findings support the potential of HSA as a suitable carrier for developing dual-modality imaging nanocarriers incorporating both radionuclide and fluorescence imaging capabilities.

**Keywords:** Drug delivery systems; Human serum albumin; Doxorubicin; Technetium complexes; Fluorescent dyes; Molecular docking; Molecular dynamics

**PACS:** 87.14.C++c, 87.16.Dg

The development of targeted drug nanocarriers has emerged as a critical strategy in enhancing the therapeutic efficacy of anticancer agents while mitigating their systemic toxicity [1,2]. Among these, protein-based drug delivery systems (PDDS) have garnered significant attention due to their exceptional biocompatibility, biodegradability, and ability to accumulate in tumor tissues via the enhanced permeability and retention (EPR) effect [3,4]. Proteins offer unique advantages as drug delivery vehicles, including their natural abundance, renewable sources, and the presence of multiple functional groups for drug loading and targeting modifications. Albumin, a naturally occurring protein, has emerged as a promising carrier for drug delivery due to its biocompatibility, non-immunogenicity, and ability to bind and transport a wide range of therapeutic agents [5,6]. The use of albumin-based delivery systems offers several advantages, including prolonged circulation time, enhanced permeability and retention effect, and the potential for passive and active targeting of tumor tissues. In recent years, the integration of multimodal imaging modalities into drug delivery systems has gained significant attention [7,8]. Such systems not only facilitate the monitoring of drug distribution and accumulation in real-time but also provide valuable insights into the pharmacokinetics and pharmacodynamics of the therapeutic agents. In this study, we employed computational tools, specifically molecular docking and molecular dynamics simulations, to design albumin-based multimodal delivery systems for doxorubicin. Our approach involved the incorporation of radiopharmaceuticals, specifically technetium-99m (<sup>99m</sup>Tc) coordination complexes, and near-infrared (NIR) fluorescent dyes, including indocyanine green, methylene blue, heptamethine cyanine dye AK7-5, and squaraine dye SQ1. The integration of these imaging modalities aims to enhance the precision of drug delivery and enable the simultaneous tracking of therapeutic and diagnostic agents.

### METHODS

Human serum albumin (HSA) in its dimeric form (PDB ID: 1A06) was used as a main component of the designed PDDS. A therapeutic component of the examined drug delivery systems was represented by one of the most widespread antitumor drug doxorubicin (DOX), anthracycline antibiotic whose antineoplastic properties arise mainly from its abilities to intercalate into DNA, inhibit topoisomerase II, disrupt gene expression, generate reactive oxygen species and produce damage of cell membranes [9]. To design the PDDS, in the present study we used 12 <sup>99m</sup>Tc-based radiopharmaceuticals

(Fig. 1): [ $^{99m}\text{Tc}$ ]Tc-Sestamibi (TcSES), [ $^{99m}\text{Tc}$ ]Tc-Tetrofosmin (TcTET), [ $^{99m}\text{Tc}$ ]Tc-Medronate (TcMED), [ $^{99m}\text{Tc}$ ]Tc-dimercaptosuccinic acid (TcDMSA), [ $^{99m}\text{Tc}$ ]Tc-diethylenetriaminepentaacetate (Tc-DTPA), [ $^{99m}\text{Tc}$ ]Tc-mercaptoacetyltriglycine (TcMAG), Pertechnetate [ $^{99m}\text{Tc}$ ]TcO $_4^-$  (TcPER), [ $^{99m}\text{Tc}$ ]Tc-Exametazime (TcEXA), [ $^{99m}\text{Tc}$ ]Tc-diisopropyl iminodiacetic acid (TcDIS), [ $^{99m}\text{Tc}$ ]Tc-ethylene cysteine dimer (TcECD), [ $^{99m}\text{Tc}$ ]Tc- hydrazinonicotinic acid-H6F (TcHYN), [ $^{99m}\text{Tc}$ ]Tc-Mebrofenin (TcMEB). To create the dual-labelled PDDS with both nuclear and optical imaging modalities, the examined protein systems were loaded by the binary combinations of the above  $^{99m}\text{Tc}$  complexes and four NIR fluorescent dyes (FD), Methylene Blue (MB), Indocyanine Green (IG), cyanine AK7-5 and squaraine SQ1 (Fig. 2). To identify the most energetically favorable binding sites for TCC, DOX, FD in the HSA, HSA-Lz, HSA-TRF, HSA-Hb protein systems the molecular docking studies were performed using the HDock server.60 Prior to the docking procedure, the structures of HSA dimers and its complexes with Lz, TRF and Hb were relaxed through 1 ns MD simulations. The structures of ligands were built in MarvinSketch (version 18.10.0) and the geometries were further optimized in Avogadro (version 1.1.0). The selected docking poses were visualized with the UCSF Chimera software (version 1.14) and analyzed with Protein-Ligand Interaction Profiler [10]. The molecular dynamics simulations were performed to evaluate the stability of some of the examined protein-ligand assemblies, viz. the ternary complexes HSA – DOX – IG and HSA – DOX – MB. The input files for MD calculations were prepared using the CHARMM-GUI input generator [11]. The .itp files of DOX, IG and MB were obtained from the corresponding .mol2 files, using the CHARMM General Force Field, followed by the correction of the dye/drug partial charges according to those assigned by RESP ESP charge Derive Server [12]. The drug-dye-protein complexes were solvated in a rectangular box with a minimum distance of 10 Å from the protein to the box edges and 0.15 M NaCl (neutralizing ions) were added to the systems. The TIP3P water model was used. The molecular dynamics simulations and analysis of the trajectories were performed using the GROMACS software (version 2023.3) with the CHARMM36m force field in the NPT ensemble with the time step for MD simulations 2 fs. The calculations were performed at a temperature of 310 K using the V-rescale thermostat. The minimization and equilibration of the systems were carried out during 50000 and 125000 steps, respectively. The time interval for MD calculations was 1 ns HSA – DOX – MB complex and 10 ns for HSA – DOX – IG complex. The correction of MD trajectories after the MD run, was performed using the `gmx trjconv` GROMACS command. The visualization of the snapshots of MD runs and calculations of the protein backbone root-mean-square deviation (RMSD), the protein solvent-accessible surface area (SASA), and the distances between the centers of mass of protein and ligand were performed in VMD.

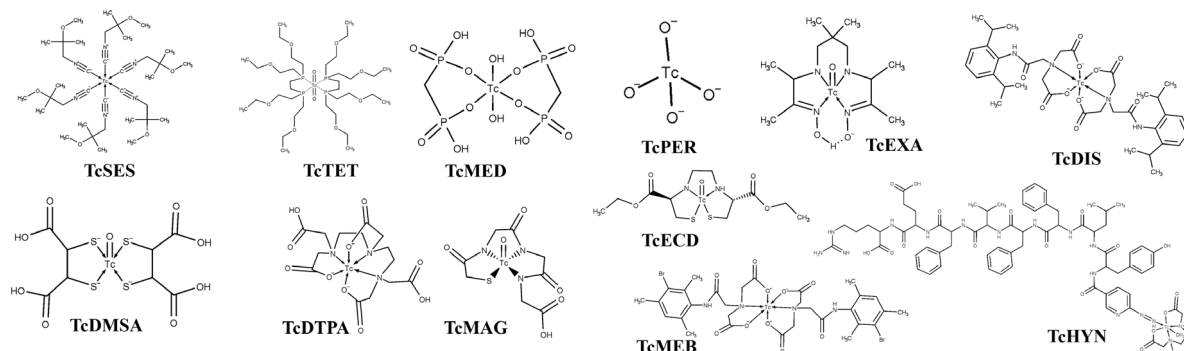


Figure 1. Chemical structures of Technetium-99m complexes

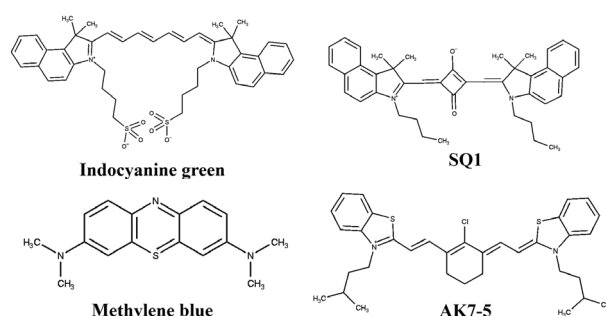


Figure 2. Chemical structures of fluorescent dyes

## RESULTS AND DISCUSSION

At the first step of the study, we compared the binding affinities of different  $^{99m}\text{Tc}$  pharmaceuticals for HSA. Shown in Fig. 3 are the best score complexes of TCC with the albumin dimer. A polypeptide chain of HSA monomer contains 585 amino acid residues with three homologous domains: I (amino acid residues 1-195), II (amino acid residues 196-383), and III (amino acid residues 384-585). Each of these three domains consists of two subdomains (A and B), stabilized by 17 disulfide bonds. It is generally recognized that the majority of drugs bind to HSA through the two sites known as

Sudlow sites I and II, which are located in hydrophobic cavities of subdomains IIA and IIIA, respectively [13]. It appeared that the binding sites for the five TCC (TcMED, TcEXA, TcECD, TcDMSA, TcDTPA) are situated on the domain I, within the region extending from LEU115 to LYS190 and all contain 7 identical amino acid residues LEU115, ARG117, TYR138, ILE142, TYR161, LEU182 and ARG186 (Fig. 3., Table 1). The consistency in binding location suggests a common structural recognition mechanism for these TCCs by HSA, which may be attributed to the physicochemical properties shared among these compounds. This finding is particularly relevant as it indicates a potential competitive binding scenario among these TCCs, which could influence their pharmacokinetics when administered concurrently or in close succession.

A high degree of similarity is observed also for TcTET and TcDIS, which both form contacts with the residues of the domains I and III (ASN109, ARG114, LEU115, ARG145, LYS190, GLU425, GLU520, ILE523). Likewise, the complexes of TcSES and TcMEB with HSA share similar amino acid residues GLU188, LYS195, ARG218, ARG222, GLU292, VAL293, HSD440 and TYR452. This divergent binding pattern implies a potentially different mode of interaction for these TCCs with HSA. The distinct binding site for TcSES and TcMEB suggests that these compounds may not directly compete with the majority of TCCs for HSA binding, potentially allowing for their use in combination with other  $^{99m}\text{Tc}$  pharmaceuticals without significant pharmacokinetic interference. The binding site for TcPER is located in the domain I, while the interface residues of the complex HSA-TcMAG encompass all protein domains.

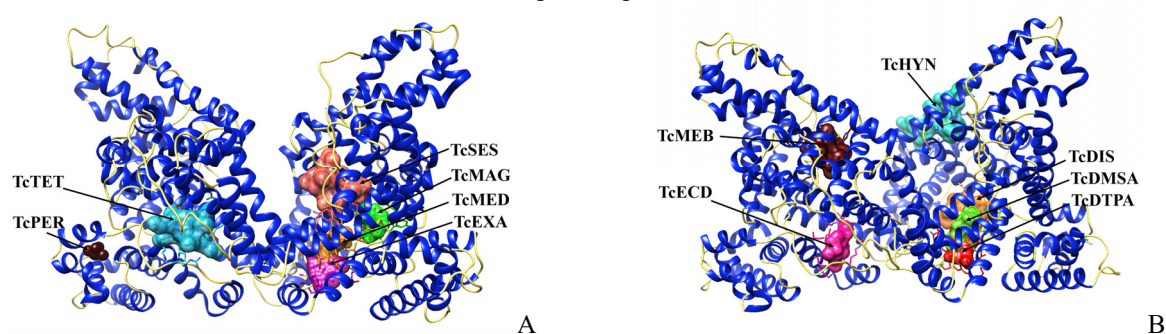


**Figure 3.** The most energetically favorable complexes of TCC with HSA

**Table 1.** The interface amino acid residues and the types of interactions involved in the binding of technetium 99m complexes (TCC) to human serum albumin (HSA)

TCC	HSA-TCC interface residues	Types of interactions
TcSES	TYR <sub>150A</sub> *, GLU <sub>153A</sub> , PHE <sub>156A</sub> , PHE <sub>157A</sub> , ARG <sub>160A</sub> , GLU <sub>188A</sub> , ALA <sub>191A</sub> , SER <sub>192A</sub> , LYS <sub>195A</sub> , GLN <sub>196A</sub> , LYS <sub>199A</sub> , ARG <sub>218A</sub> , ARG <sub>222A</sub> , HSD <sub>288A</sub> , GLU <sub>292A</sub> , VAL <sub>293A</sub> , LYS <sub>436A</sub> , HSD <sub>440A</sub> , TYR <sub>452A</sub>	Hydrophobic interactions, hydrogen bonds
TcTET	ASN <sub>109B</sub> , ARG <sub>114B</sub> , LEU <sub>115B</sub> , ARG <sub>145B</sub> , LYS <sub>190B</sub> , GLU <sub>425B</sub> , ARG <sub>428B</sub> , GLU <sub>520B</sub> , ILE <sub>523B</sub>	Hydrophobic interactions, hydrogen bonds
TcMED	LEU <sub>115A</sub> , ARG <sub>117A</sub> , TYR <sub>138A</sub> , ILE <sub>142A</sub> , HSD <sub>146A</sub> , PHE <sub>149A</sub> , LEU <sub>154A</sub> , PHE <sub>157A</sub> , TYR <sub>161A</sub> , LEU <sub>182A</sub> , ASP <sub>183A</sub> , LEU <sub>185A</sub> , ARG <sub>186A</sub> , ASP <sub>187A</sub> , GLY <sub>189A</sub> , LYS <sub>190A</sub>	Hydrogen bonds
TcMAG	ASP <sub>107A</sub> , ASP <sub>108A</sub> , ASN <sub>109A</sub> , ARG <sub>145A</sub> , HSD <sub>146A</sub> , PRO <sub>147A</sub> , TYR <sub>148A</sub> , LYS <sub>190A</sub> , ALA <sub>191A</sub> , SER <sub>193A</sub> , ALA <sub>194A</sub> , ARG <sub>197A</sub> , GLU <sub>425A</sub> , ASN <sub>458A</sub> , GLN <sub>459A</sub>	Hydrogen bonds, salt bridges
TcEXA	LEU <sub>115A</sub> , VAL <sub>116A</sub> , ARG <sub>117A</sub> , PRO <sub>118A</sub> , MET <sub>123A</sub> , PHE <sub>134A</sub> , LYS <sub>137A</sub> , TYR <sub>138A</sub> , LEU <sub>139A</sub> , GLU <sub>141A</sub> , ILE <sub>142A</sub> , ARG <sub>145A</sub> , TYR <sub>161A</sub> , PHE <sub>165A</sub> , LEU <sub>182A</sub> , ARG <sub>186A</sub>	Hydrophobic interactions, hydrogen bonds
TcECD	LEU <sub>115B</sub> , ARG <sub>117B</sub> , PRO <sub>118B</sub> , MET <sub>123B</sub> , PHE <sub>134B</sub> , LYS <sub>137B</sub> , TYR <sub>138B</sub> , GLU <sub>141B</sub> , ILE <sub>142B</sub> , TYR <sub>161B</sub> , LEU <sub>182B</sub> , ASP <sub>183B</sub> , LEU <sub>185B</sub> , ARG <sub>186B</sub>	Hydrophobic interactions, hydrogen bonds, salt bridges
TcDMSA	LEU <sub>115A</sub> , VAL <sub>116A</sub> , ARG <sub>117A</sub> , PRO <sub>118A</sub> , MET <sub>123A</sub> , TYR <sub>138A</sub> , ILE <sub>142A</sub> , HSD <sub>146A</sub> , PHE <sub>149A</sub> , LEU <sub>154A</sub> , PHE <sub>157A</sub> , TYR <sub>161A</sub> , LEU <sub>182A</sub> , LEU <sub>185A</sub> , ARG <sub>186A</sub> , ASP <sub>187A</sub> , GLU <sub>188A</sub> , GLY <sub>189A</sub> , LYS <sub>190A</sub>	Hydrogen bonds, salt bridges
TcDIS	ASN <sub>109A</sub> , PRO <sub>110A</sub> , LEU <sub>112A</sub> , ARG <sub>114A</sub> , LEU <sub>115A</sub> , ARG <sub>145A</sub> , HSD <sub>146A</sub> , ARG <sub>186A</sub> , LYS <sub>190A</sub> , PRO <sub>421A</sub> , GLU <sub>425A</sub> , GLU <sub>520A</sub> , ILE <sub>523A</sub>	Hydrophobic interactions, hydrogen bonds
TcPER	TYR <sub>30B</sub> , HSD <sub>67B</sub> , THR <sub>68B</sub> , PHE <sub>70B</sub> , GLY <sub>71B</sub> , LEU <sub>74B</sub> , GLU <sub>95B</sub> , ARG <sub>98B</sub> , ASN <sub>99B</sub> , PHE <sub>102B</sub>	Hydrogen bonds
TcDTPA	LEU <sub>115A</sub> , VAL <sub>116A</sub> , ARG <sub>117A</sub> , PRO <sub>118A</sub> , MET <sub>123A</sub> , PHE <sub>134A</sub> , LEU <sub>135A</sub> , LYS <sub>137A</sub> , TYR <sub>138A</sub> , GLU <sub>141A</sub> , ILE <sub>142A</sub> , TYR <sub>161A</sub> , LEU <sub>182A</sub> , ARG <sub>186A</sub>	Hydrogen bonds, salt bridges
TcHYN	GLU <sub>383A</sub> , LEU <sub>387A</sub> , ASN <sub>391A</sub> , LEU <sub>394A</sub> , LEU <sub>407A</sub> , VAL <sub>409A</sub> , ARG <sub>410A</sub> , TYR <sub>411A</sub> , LEU <sub>430A</sub> , LEU <sub>453A</sub> , GLU <sub>492A</sub> , SER <sub>489A</sub> , LYS <sub>541A</sub> , GLU <sub>542A</sub> , LYS <sub>545A</sub>	Hydrogen bonds, $\pi$ -stacking, salt bridges
TcMEB	GLU <sub>188B</sub> , LYS <sub>195B</sub> , TRP <sub>214B</sub> , ARG <sub>218B</sub> , GLN <sub>221B</sub> , ARG <sub>222B</sub> , GLU <sub>292B</sub> , VAL <sub>293B</sub> , GLU <sub>294B</sub> , ASN <sub>295B</sub> , LYS <sub>436B</sub> , HSD <sub>440B</sub> , LYS <sub>444B</sub> , PRO <sub>447B</sub> , CYS <sub>448B</sub> , ALA <sub>449B</sub> , ASP <sub>451B</sub> , TYR <sub>452B</sub>	Hydrophobic interactions, hydrogen bonds, salt bridges

Meanwhile, TcHYN, which in contrast to the other TCC, possesses a specific peptide (YLFFVFER) in its structure (Fig. 1), binds to HSA on the domain III, with some of the interface residues (ARG410, TYR411, SER489) belonging to

the Sudlow site II. Furthermore, as judged from the comparison of the best docking scores (BDS) for the HSA-TCC complexes (Fig. 4), TcHYN has the highest affinity for HSA, with BDS values following the order TcHYN > TcDTPA > TcDIS > TcMEB > TcDMSA > TcSES > TcTET > TcMED > TcMAG > TcECD > TcEXA > TcPER. The highest affinity of TcHYN for HSA suggests that peptide conjugation could be a promising strategy for enhancing the albumin-binding properties of radiopharmaceuticals, potentially leading to improved in vivo stability and target tissue accumulation.

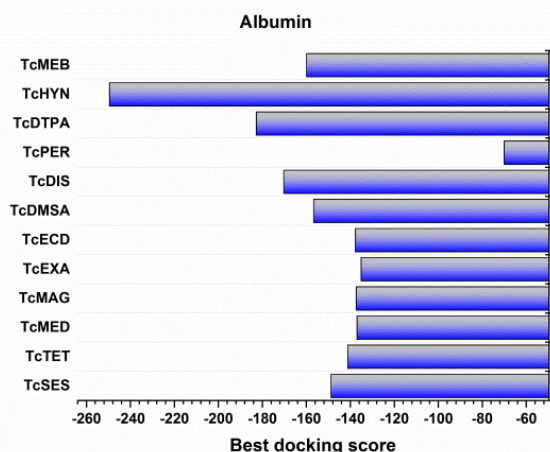


**Figure 4.** The best docking score values obtained for the TCC complexes with HSA

At the next steps of the investigation, we employed the multiple ligand docking approach [14] to explore the ternary (HSA-TCC-DOX) and quaternary (HSA-TCC-DOX-FD) protein-ligand systems. The ternary systems were obtained by the docking of doxorubicin to the best score complexes of TCC with HSA (Fig. 5). The following features of the ternary systems are worthy of mention: i) when the HSA binding sites for TCC and DOX do not overlap, the DOX binding site is located in the domain I of HSA molecule, encompassing 16 residues from the region flanked with PRO<sub>113</sub> and ARG<sub>186</sub> (site HSA<sub>113-186</sub>) (Fig. 5, A); ii) when the HSA binding sites for TCC and DOX overlap with each other (as in the cases of TcMED, TcEXA, TcDMSA and TcDTPA), DOX binds to another HSA site containing 23 amino acid residues from the region flanked with ASP<sub>107</sub> and GLN<sub>459</sub> (Fig. 5, B).

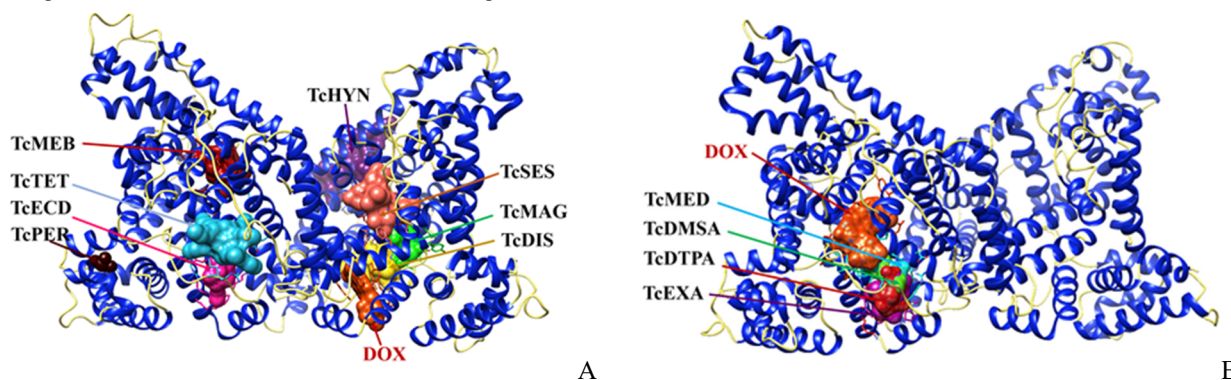


**Figure 5.** The highest affinity binding sites for DOX in the HSA-TCC systems

Next, to obtain the systems with dual imaging modality, the best score complexes HSA-TCC-DOX were docked with one of four NIR fluorophores, two traditionally used dyes, methylene blue and indocyanine green, and two emerging fluorophores, heptamethine cyanine dye AK7-5, and squaraine dye SQ1. A comparative analysis of the docking results obtained for the quaternary systems (HSA + TCC + DOX + FD) indicates that the affinities of the examined dyes for HSA/HSA-DOX decrease in the row: IG (BDS = -207.2/-190.3) > SQ1 (BDS = -186.1/-185.9) > AK7-5 (BDS = -162.4/-162.9) > MB (BDS = -127.1/-117.3). This hierarchy of binding affinities provides crucial information for the selection of optimal fluorophores in the context of technetium-based dual-modality imaging systems. While the amino acid composition of the fluorophore binding sites varied across different technetium complexes and protein components, a consistent pattern emerged, allowing for the identification of predominant interaction sites for each system. Notably, a specific albumin site, designated as HSA<sub>115-186</sub>, was identified as the preferential binding region for MB in both HSA-DOX and HSA-TCC-DOX complexes (Fig. 6). This finding suggests a potential interaction between the technetium complexes and the fluorophores, which could have implications for the overall stability and efficacy of the dual-modality imaging system.

At the last step of the study, we performed the molecular dynamics simulation of two of the examined complexes, to assess their stability in aqueous solution. Because of the problems associated with the parametrization of <sup>99m</sup>Tc complexes the MD simulations were carried out for the systems HSA-DOX-MB and HSA-DOX-IG. As illustrated in Fig. 7, DOX and FD remain bound to HSA during the simulation time (1 ns for MB and 10 ns for IG).

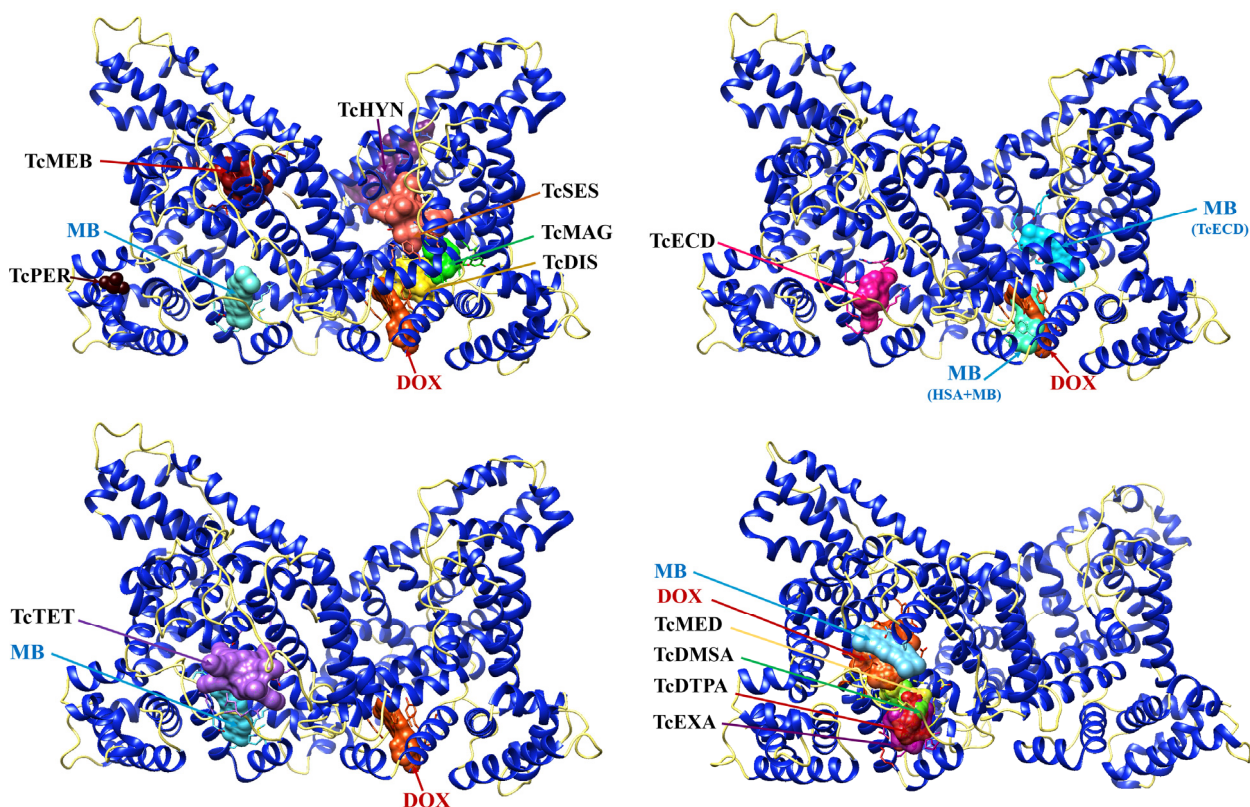


**Figure 6.** The most energetically favorable docking poses in the complexes with HSA-TCC-DOX-MB

The persistence of DOX and fluorescent dye (FD) binding to HSA throughout the simulation periods (1 ns for MB and 10 ns for IG) suggests a stable association between these components. This stability is further corroborated by the relatively consistent center-of-mass distances observed between the protein and ligands. The IG system exhibited distances ranging from 2.4 to 2.8 nm, while the MB system showed distances between 2.3 and 2.7 nm. DOX maintained the closest proximity to HSA, with distances varying from 2.2 to 2.5 nm. These findings indicate that all ligands remain in close association with HSA, with DOX potentially exhibiting the strongest interaction (Fig. 8, A, B).

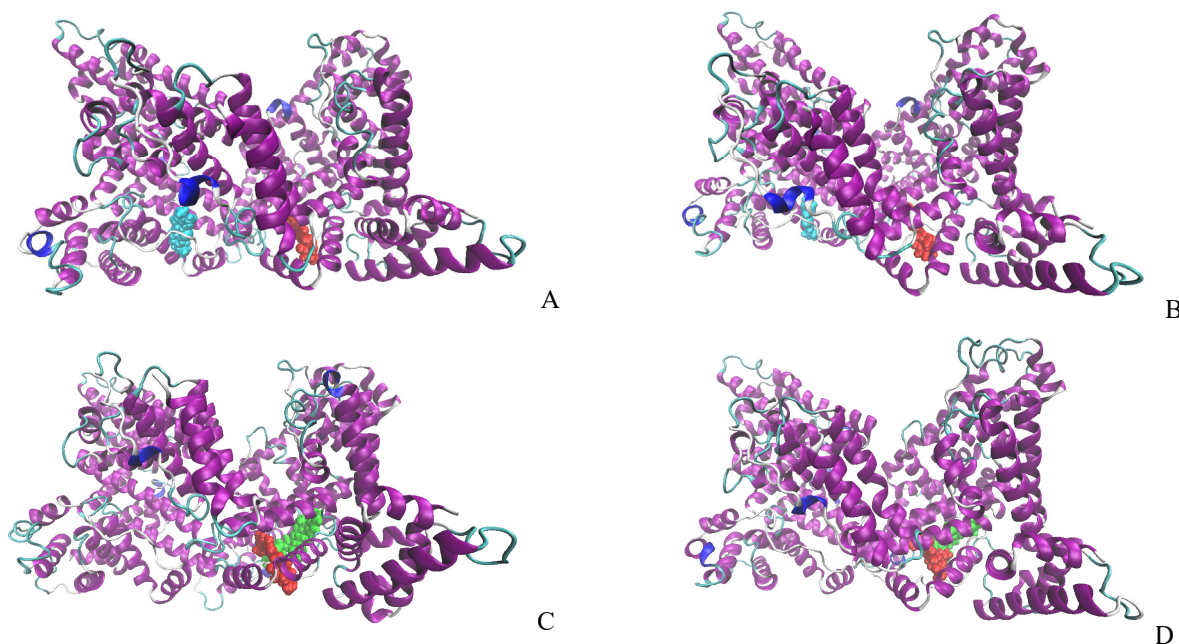


**Figure 7.** The snapshots of HSA-DOX-MB (A, B) and HSA-DOX-IG (C, D) complexes corresponding to the timepoints of 0 ns (A, C); 1 ns (B) and 10 ns (D).

The structural integrity of the HSA molecule in the presence of DOX, MB, and IG was assessed through Root Mean Square Deviation (RMSD) and Solvent Accessible Surface Area (SASA) analyses. The results suggest that the albumin

structure remains largely unperturbed upon ligand binding, as evidenced by the absence of significant fluctuations in these parameters (Fig. 8, C-F). This structural stability is crucial for maintaining the functional properties of HSA as a drug carrier.

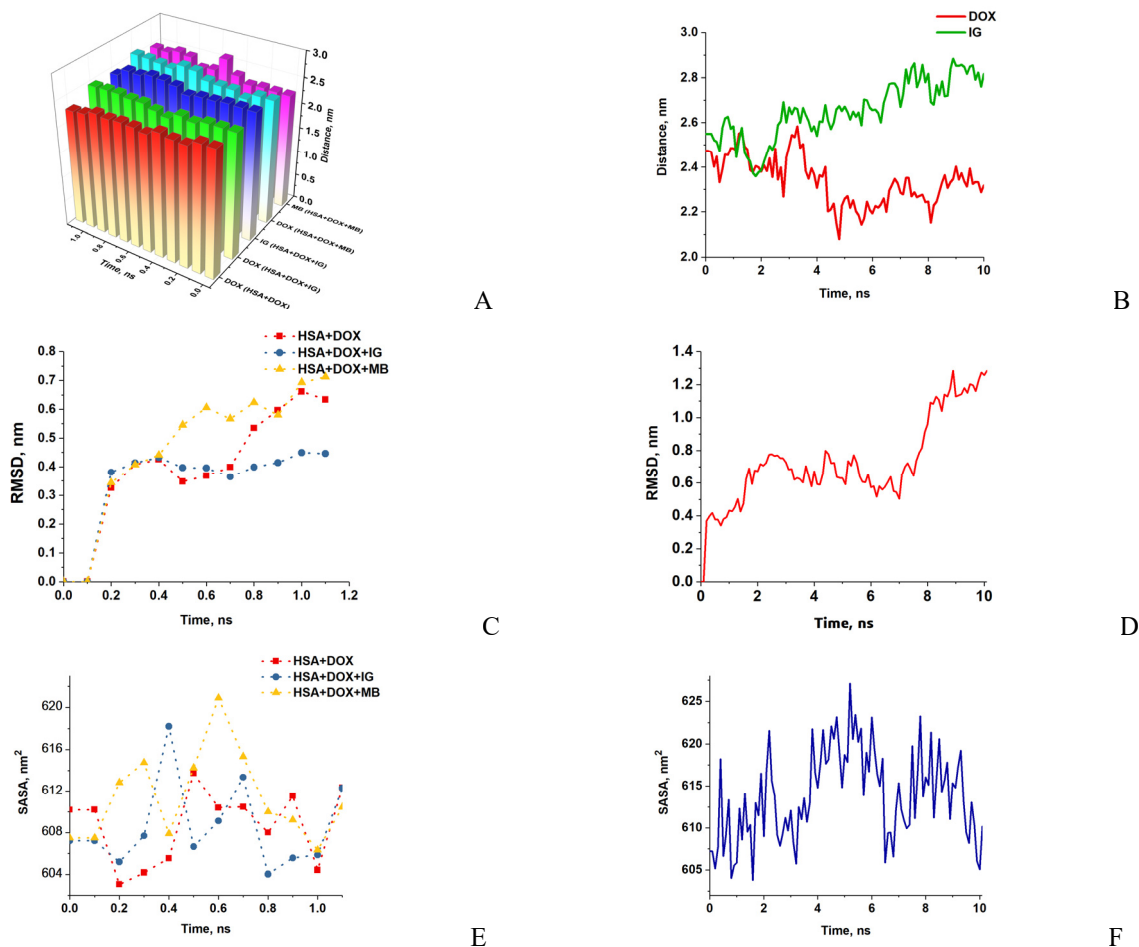


**Figure 8.** The distances between the centers of mass (A, B), RMSD (root mean square deviation) of the protein backbone atoms (C, D) and SASA (solvent accessible surface area) (E, F) calculated for the systems HSA-DOX, HSA-DOX-MB and HSA-DOX-IG.

Taken together, our findings indicate that HSA is suitable for the development of the DOX nanocarriers with both radionuclide and fluorescence imaging modalities.

## CONCLUSIONS

The collective findings from this study provide strong evidence supporting the suitability of HSA as potential platform for developing DOX nanocarriers with dual imaging modalities. The demonstrated stability of these complexes, coupled with their ability to incorporate both radionuclide and fluorescence imaging agents, presents a promising avenue for advancing targeted drug delivery systems with enhanced diagnostic capabilities. It is important to note, however, that while these results are encouraging, further studies are warranted to fully elucidate the long-term stability, pharmacokinetics, and in vivo efficacy of these systems. Additionally, the impact of technetium complexes on the overall stability and functionality of these nanocarriers remains to be explored, necessitating the development of more accurate parametrization methods for  $^{99m}\text{Tc}$  in future MD simulations.

## Acknowledgements

This project has received funding through the EURIZON project, which is funded by the European Union under grant agreement No.871072.

## ORCID

Valeriya Trusova, <https://orcid.org/0000-0002-7087-071X>; Uliana Tarabara, <https://orcid.org/0000-0002-7677-0779>  
Galyna Gorbenko, <https://orcid.org/0000-0002-0954-5053>; Andrey Zelinsky, <https://orcid.org/0000-0002-4110-8523>  
Borys Borts, <https://orcid.org/0000-0002-1492-4066>

## REFERENCES

- [1] S. Adepu, S. Ramakrishna, *Molecules*. **26**, 5905 (2021). <https://doi.org/10.3390/molecules26195905>
- [2] Y. Sung, S. Kim, *Biomater. Res.* **24**, 12 (2020). <https://doi.org/10.1186/s40824-020-00190-7>

- [3] D. Jao, Y. Xue, J. Medina, X. Hu, *Materials (Basel)*. **10**, 517 (2017). <https://doi.org/10.3390/ma10050517>
- [4] S. Hong, D. Choi, H. Kim, C. Park, W. Lee, H. Park, *Pharmaceutics*. **12**, 604 (2020). <https://doi.org/10.3390/pharmaceutics12070604>
- [5] M. Larsen, M. Kuhlmann, M. Hvam, K. Howard, *Mol. Cell Ther.* **4**, 3 (2016). <https://doi.org/10.1186/s40591-016-0048-8>
- [6] A. Spada, J. Emami, J. Tuszynski, A. Lavasanifar, *Mol. Pharmaceutics*. **18**, 1862-1894 (2021). <https://doi.org/10.1021/acs.molpharmaceut.1c00046>
- [7] S. Hari, A. Gauba, N. Shrivastava, R. Tripathi, S. Jain, A. Pandey, *Drug Deliv. Transl. Res.* **13**, 135-163 (2023). <https://doi.org/10.1007/s13346-022-01197-4>
- [8] Q. Shubhra, K. Guo, Y. Liu, M. Razzak, M. Serajum, A. Moshui, *Acta Biomater.* **131**, 493-507 (2021). <https://doi.org/10.1016/j.actbio.2021.06.016>
- [9] M. Kciuk, A. Gielecinska, S. Mujwar, D. Kołat, Z. Kałuzinska-Kołat, I. Celik, R. Kontek, *Cells*. **12**, 659 (2023). <https://doi.org/10.3390/cells12040659>
- [10] M. F. Adasme, K. L. Linnemann, S. N. Bolz, F. Kaiser, S. Salentin, V. J. Haupt, M. Schroeder, *Nucl. Acids Res.* **49**, W530-W534 (2021). <https://doi.org/10.1093/nar/gkab294>
- [11] J. Lee, X. Cheng, J. M. Swails, M. S. Yeom, P. K. Eastman, J. A. Lemkul, S. Wei, J. Buckner, J. C. Jeong, Y. Qi, S. Jo, V. S. Pande, D. A. Case, C. L. Brooks, III, A. D. MacKerell, Jr., J. B. Klauda, W. Im, *Chem. Theory Comput.* **12**, 405-413 (2016). <https://doi.org/10.1021/acs.jctc.5b00935>
- [12] E. Vanquelef, S. Simon, G. Marquant, E. Garcia, G. Klimerak, J.C. Delepine, P. Cieplak, F.Y. Dupradeau, *Nucleic Acids Res.* **39**, W511-W517 (2011). <https://doi.org/10.1093/nar/gkr288>
- [13] S. Patel, K. K. Sharma and A. Datta, *Spectrochim. Acta A Mol. Biomol. Spectrosc.* **138**, 925-931 (2015). <https://doi.org/10.1016/j.saa.2014.10.015>
- [14] H. Li, C. Li, *Comput. Chem.* **31**, 2014-2022 (2010). <https://doi.org/10.1002/jcc.21486>

**КОМП'ЮТЕРНЕ ДОСЛІДЖЕННЯ СИСТЕМ ДОСТАВКИ ЛІКІВ З РАДІОНУКЛІДНИМИ  
ТА ФЛУОРЕСЦЕНТНИМИ МОДАЛЬНОСТЯМИ ВІЗУАЛІЗАЦІЇ. І. СИСТЕМИ НА ОСНОВІ АЛЬБУМІНУ  
ДЛЯ ДОСТАВКИ ДОКСОРУБІЦИНУ**

**В. Трусова<sup>a</sup>, У. Тарабара<sup>a</sup>, І. Карнаухов<sup>b</sup>, А. Зелінський<sup>b</sup>, Б. Борц<sup>b</sup>, І. Ушаков<sup>b</sup>, Л. Сіденко<sup>b</sup>, Г. Горбенко<sup>a</sup>**

<sup>a</sup>*Кафедра медичної фізики та біомедичних нанотехнологій, Харківський національний університет імені В.Н. Каразіна  
м. Свободи 4, Харків, 61022, Україна*

<sup>b</sup>*Національний науковий центр «Харківський фізико - технічний інститут», Харків, вул. Академічна, 1, 61108, Україна*

Методи молекулярного докінгу та молекулярної динаміки були використані для дизайну та оцінки стабільності систем доставки антинеопластичного агента доксорубіцину (ДОКС) з використанням людського сироваткового альбуміну (ЛСА) як наноносія. Для створення системи доставки ліків (СДЛ) з компонентами дуальної візуалізації, комплекси радіонукліду технецію-99m (ТСС) та ближньоінфрачервоних (БЧ) флуоресцентних барвників, включаючи індоціаніновий зелений (ІЗ), метиленовий синій (МС), гептаметиновий ціаніновий барвник АК7-5 та сквараїновий барвник SQ1, були інтегровані в білкові наноносії. Найвищі спорідненості до білків були виявлені для ТСС [<sup>99m</sup>Tc]Tc-діізопропіл імінооцтової кислоти (TcDIS), [<sup>99m</sup>Tc]Tc-гідразинонікотинової кислоти-Н6F (TcHYN), [<sup>99m</sup>Tc]Tc-Мebroфеніну (TcMEB), а також для флуоресцентних барвників ІЗ та SQ1. Результати молекулярного докінгу показали, що більшість комплексів технецію зв'язуються з доменом І ЛСА, за деякими винятками, що показують спорідненість до доменів І та ІІІ або лише до домену ІІІ. Три- та чотирикомпонентні системи білок-ліганд були досліджені за допомогою методології множинного докінгу лігандів. У трикомпонентних системах місця зв'язування ДОКС були ідентифіковані або в домені І, або в області, що охоплює кілька доменів, залежно від потенційного перекриття з місцями зв'язування ТСС. Для чотирикомпонентних систем, що включають БЧ флуорофори, спорідненість зв'язування зменшувалася в порядку: ІЗ > SQ1 > АК7-5 > МС. Аналіз профілів молекулярної динаміки комплексів БСА-ДОКС-МС та БСА-ДОКС-ІЗ продемонстрував стабільність досліджуваних комплексів з незмінними відстанями до центру мас та незначними порушеннями структури БСА. Отримані результати свідчать про потенціал БСА як наноносія лікарських засобів з модальністю дуальної візуалізації на основі радіонукліду та флуоресцентного барвника.

**Ключові слова:** системи доставки ліків; людський сироватковий альбумін; доксорубіцин; комплекси технецію; флуоресцентні барвники; молекулярний докінг; молекулярна динаміка

## POLYPHENOL-MEDIATED MODULATION OF AMYLOID-LIPID INTERACTIONS

 U. Tarabara<sup>a</sup>,  V. Trusova<sup>a\*</sup>,  M.H. Thomsen<sup>b</sup>,  G. Gorbenko<sup>a</sup>

<sup>a</sup>*Department of Medical Physics and Biomedical Nanotechnologies, V.N. Karazin Kharkiv National University  
4 Svobody Sq., Kharkiv, 61022, Ukraine*

<sup>b</sup>*AAU Energy, Aalborg University, Niels Bohrs Vej 8, 6700 Esbjerg, Denmark*

*\*Corresponding Author e-mail: [valerija.trusova@karazin.ua](mailto:valerija.trusova@karazin.ua)*

Received September 11, 2024, revised October 30, 2024; accepted November 15, 2024

Förster resonance energy transfer (FRET) between the membrane fluorescent probes pyrene and TDV was employed to investigate the modulation of amyloid-lipid interactions by polyphenols. The effects of various polyphenols, including quercetin, curcumin, gallic and salicylic acids, on the complexation between the amyloid fibrils derived from N-terminal fragment of apolipoprotein A-I (ApoA-IF) and insulin (InsF), and liposomes composed of phosphatidylcholine (PC) and its mixtures with cardiolipin (CL), cholesterol (Chol), or phosphatidylglycerol (PG) were investigated. The incorporation of polyphenols resulted in decreased energy transfer efficiency, indicating a significant alteration in the spatial relationship between amyloid fibrils and lipid membranes. The magnitude of this effect was found to be dependent on lipid bilayer composition, the chemical nature of the polyphenols, and the type of amyloidogenic protein. Notably, curcumin exhibited the most pronounced impact across all systems, with a particularly strong effect on ApoA-IF compared to InsF. This differential response suggests protein-specific mechanisms of interaction and highlights the potential for targeted therapeutic approaches. Our findings provide novel insights into the intricate interplay between polyphenols, amyloid fibrils, and lipid membranes, contributing to the fundamental understanding of amyloid-related pathologies and opening new avenues for the development of polyphenol-based therapeutic strategies in amyloid-associated disorders.

**Key words:** *Amyloid fibrils; Lipid bilayer; Polyphenols; Förster resonance energy transfer*

**PACS:** 87.14.C++c, 87.16.Dg

Amyloid-membrane interactions are pivotal in the pathogenesis of numerous neurodegenerative diseases, including Alzheimer's and Parkinson's diseases [1,2]. These interactions can lead to membrane disruption, altered cellular homeostasis, and ultimately, cell death. The amyloid fibrils, which are the aggregates of misfolded proteins, can insert into lipid bilayers, causing structural perturbations that compromise membrane integrity. This disruption is often accompanied by the formation of ion-permeable pores, which can lead to dysregulated ion homeostasis and trigger apoptotic pathways [3]. Understanding the mechanisms underlying amyloid-membrane interactions is crucial for developing therapeutic strategies aimed at mitigating the amyloid toxicity. Various factors and substances can influence the complexation of lipids with fibrillar species, including lipid composition, membrane fluidity, and the presence of small molecules such as polyphenols. Lipid composition, for instance, can significantly affect the binding affinity and insertion depth of amyloid fibrils into the membrane. Cholesterol, a major component of cell membranes, has been shown to either stabilize or destabilize amyloid fibrils depending on its concentration and distribution within the bilayer [4,5]. Polyphenols (PF), which are abundant in various fruits and vegetables, have garnered attention for their potential to modulate these interactions [6,7]. These compounds can interact with both amyloid fibrils and lipid bilayers, altering their structural and functional properties. The consequences of these interactions may be profound, as they can affect membrane integrity, ion channel function, and cellular signaling pathways, thereby contributing to the progression of amyloid-related diseases. A wide arsenal of experimental techniques is employed to analyze biomolecular interactions, each offering unique insights into the dynamics and mechanisms at play. Among these techniques, fluorescence spectroscopy stands out due to its high sensitivity, specificity, and ability to provide real-time data on molecular interactions [8,9]. Fluorescence spectroscopy allows for the detection of subtle changes in the environment of fluorescent probes, making it an invaluable tool for studying complex biological systems. In the present study, we utilized one of the fluorescence spectroscopy modalities, Förster resonance energy transfer (FRET), to investigate the impact of different polyphenols on amyloid-lipid interactions. FRET is a powerful technique that enables the measurement of distances between two fluorophores in the range of 1-10 nm, making it ideal for studying interactions at the molecular level. The aim of the present study was to ascertain whether the efficiency of the Förster resonance energy transfer between the membrane fluorescent probes pyrene and TDV can serve as an indicator of polyphenol effects on fibril-lipid interactions. The lipid bilayers employed in our experiments were composed of distinct combinations of phosphatidylcholine (PC), cholesterol (Chol), cardiolipin (CL), and phosphatidylglycerol (PG). Amyloid fibrils were prepared from apolipoprotein A-I (Apo-IF) and insulin (InsF). This methodological approach enabled elucidation of the modulatory role of polyphenols on amyloid-membrane interactions, thereby providing significant insights into their potential therapeutic applications.

## METHODS

The bovine insulin, Tris, thioflavin T (ThT), cholesterol (Chol), quercetin (QR), curcumin (CR), salicylic (SA) and gallic acids (GA) were purchased from Sigma-Aldrich (St. Louis, MO, USA). The phosphonium dye TDV was kindly provided by Professor Todor Deligeorgiev (University of Sofia, Bulgaria). The N-terminal (1-83) fragment of apolipoprotein A-I with amyloidogenic mutation G26R was kindly provided by Professor Hiroyuki Saito (Kyoto Pharmaceutical University, Japan). All other reagents were of analytical grade and used without further purification.

The insulin amyloid fibrils were prepared by incubation of the protein solution (10 mg/ml) in 10 mM glycine buffer (pH 2.0) 24 hours at 37 °C under continuous orbital shaking. The fibrillization of N-terminal fragment of apolipoprotein A-I was conducted at 37 °C with constant agitation on an orbital shaker after the protein dialysis from 6M guanidine hydrochloride solution into 10mM Tris-HCl buffer, 150 mM NaCl, 0.01% NaN<sub>3</sub>, pH 7.4. The fibril growth was monitored through measuring the intensity of ThT fluorescence at excitation and emission wavelengths of 440 and 484 nm, respectively. Hereafter, the fibrillar forms of insulin and N-terminal fragment of apolipoprotein A-I are referred to as InsF and ApoA-IF, respectively. The large unilamellar vesicles were prepared from egg yolk phosphatidylcholine (PC) and its mixtures with beef heart cardiolipin (CL), cholesterol and phosphatidylglycerol (PG) in different molar proportions: neat PC, 11 mol% CL (CL11), 30 mol% cholesterol (Chol30), 11 mol% CL, 30 mol% Chol (CL11Chol30) and 20 mol% PG (PG20). The thin lipid films were obtained by evaporation of appropriate lipid solutions in ethanol, then hydrated with 1.2 ml of 10 mM Tris-HCl buffer (pH 7.4) and extruded through a 100 nm pore size polycarbonate filter. The concentration of lipids in the stock liposomal suspensions was 10 mM. The fluorescence measurements were carried out in 10 mM Tris-HCl buffer (pH 7.4) with a Shimadzu RF-6000 spectrofluorimeter (Shimadzu, Japan) using the 10 mm path-length quartz cuvettes. In the FRET measurements the fibril-liposome mixtures containing pyrene in concentration 5.1 μM were sequentially titrated with TDV solution in buffer. The fluorescence spectra were recorded from 360 to 640 nm with the excitation wavelength 340 nm. The excitation and emission band passes were set at 5 nm. The ratio of vibronic bands in the pyrene fluorescence spectra ( $I_1/I_3$ ) was calculated from the intensities at 374 nm (peak 1) and 383 nm (peak 3). The excimer-to-monomer fluorescence intensity ratio (E/M) was determined by measuring fluorescence intensity at the monomer (391 nm) and excimer (474 nm) peaks.

The stock solutions of polyphenols, *viz.* quercetin, curcumin, salicylic and gallic acids (Fig. 1), were prepared in dimethylsulfoxide in concentration 620 μM.

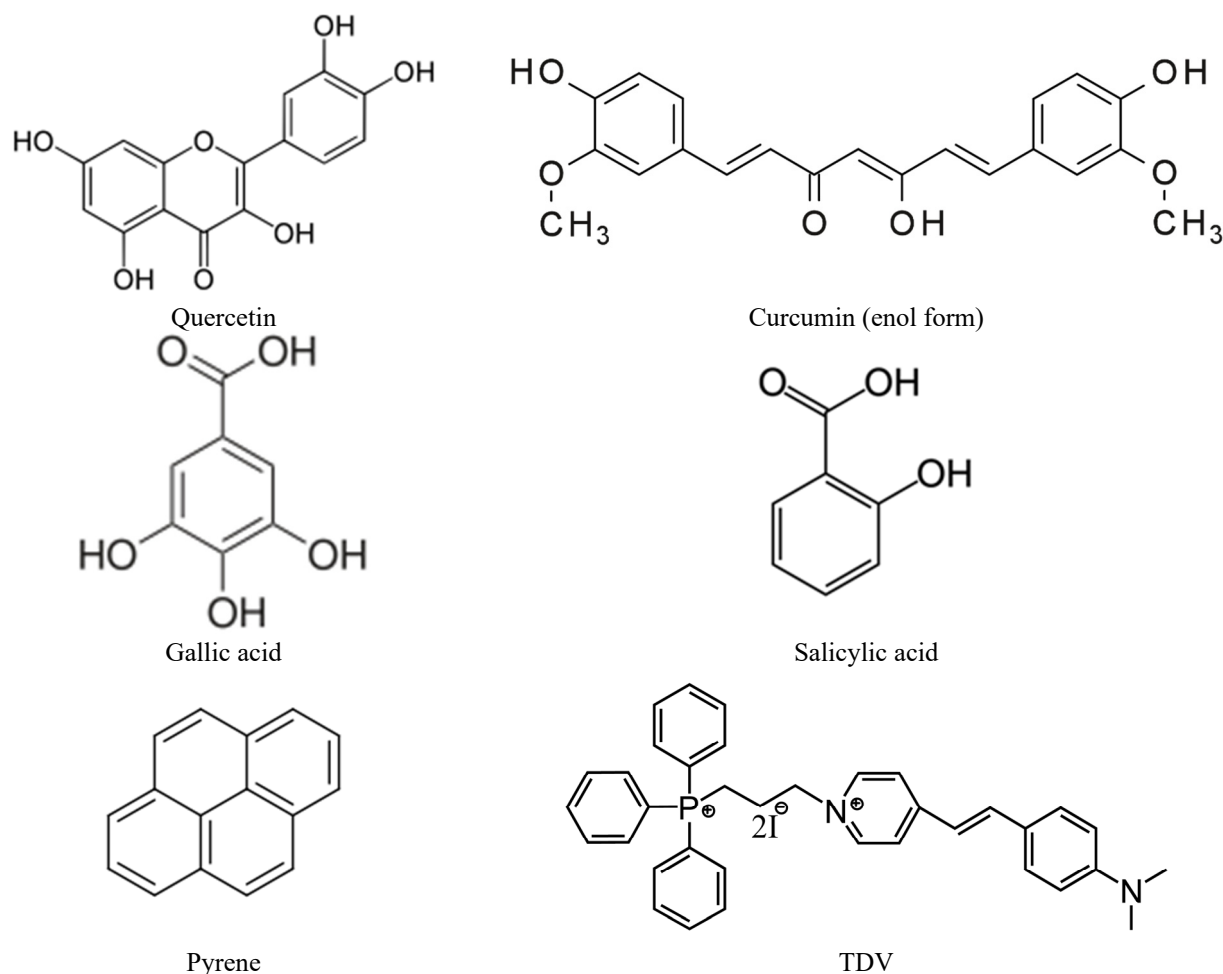


**Figure 1.** Chemical structure of the examined polyphenols and fluorescent probes

### RESULTS AND DISCUSSION

Figs. 2 and 3 illustrate the pyrene emission spectra in amyloid-lipid systems in the presence and absence of polyphenols at increasing concentrations of TDV. The data clearly demonstrate that as the concentration of TDV increases, there is a corresponding decrease in the fluorescence intensity of pyrene. This inverse relationship is indicative of the Förster resonance energy transfer occurring between the two membrane fluorescent probes, since TDV absorption spectrum strongly overlaps with the emission spectrum of pyrene excimers (Fig. 2, F).

The introduction of various polyphenols into the system significantly influenced the energy transfer process. The extent of this influence varied depending on several factors, including the chemical nature of the polyphenols, the specific composition of the liposomes, and the type of protein involved in the amyloid formation.

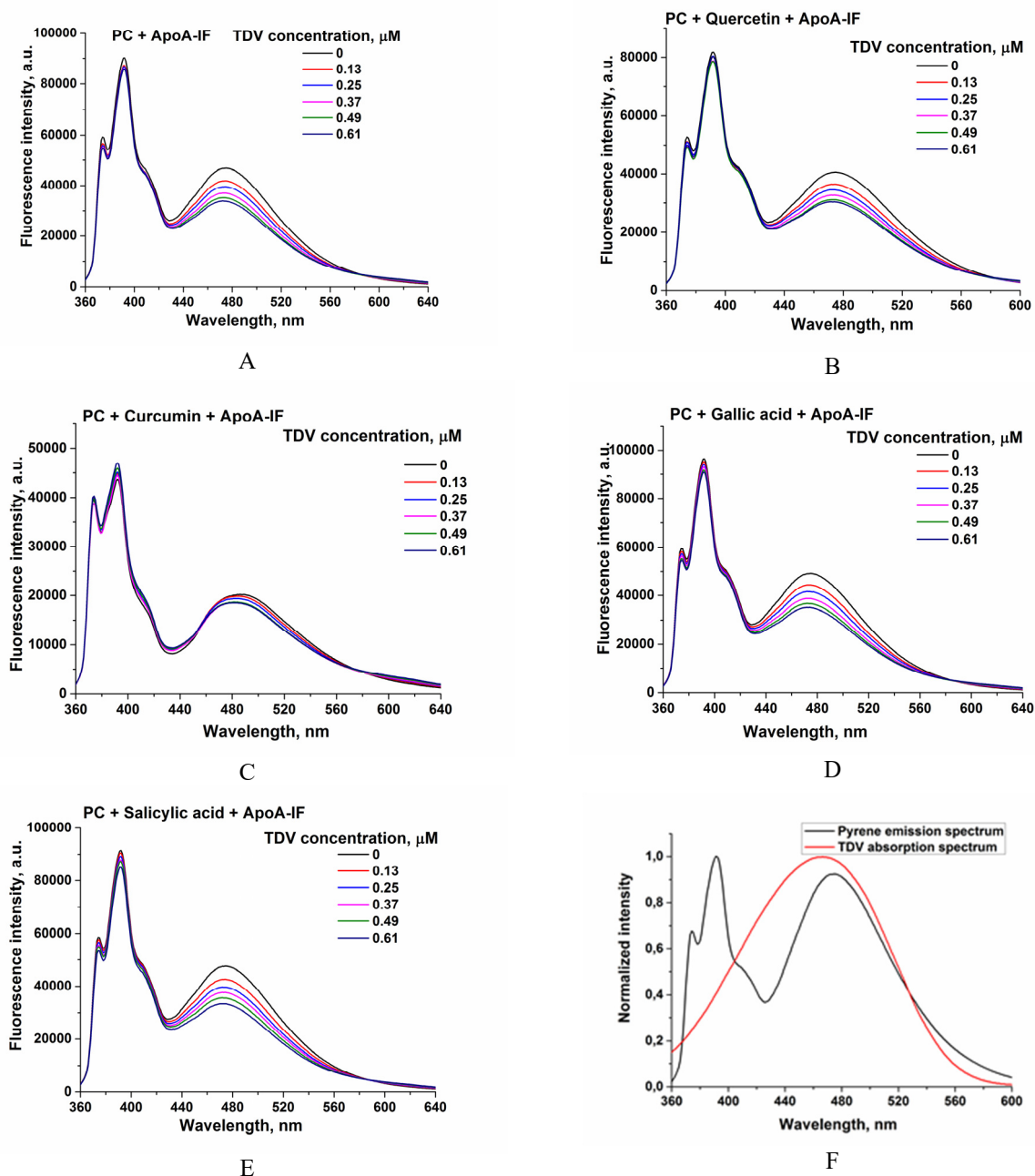


**Figure 2.** Pyrene fluorescence spectra in the systems PC+ApoA-IF+TDV (A) and PC+ApoA-IF+PF+TDV (B-E) measured at different concentrations of TDV. The overlap between pyrene emission and TDV absorption spectra (F). Lipid concentration was 67 μM, Pyrene concentration was 5.1 μM. ApoA-IF concentration was 1.1 μM. PF concentrations were – quercetin/curcumin – 2 μM, gallic acid/ salicylic acid – 20 μM

To assess the impact of polyphenols quantitatively, the energy transfer efficiency was calculated in all systems under study (Figs. 4, 5). The results reveal a notable influence of liposome composition on FRET efficiency between pyrene and TDV in amyloid-liposome systems.

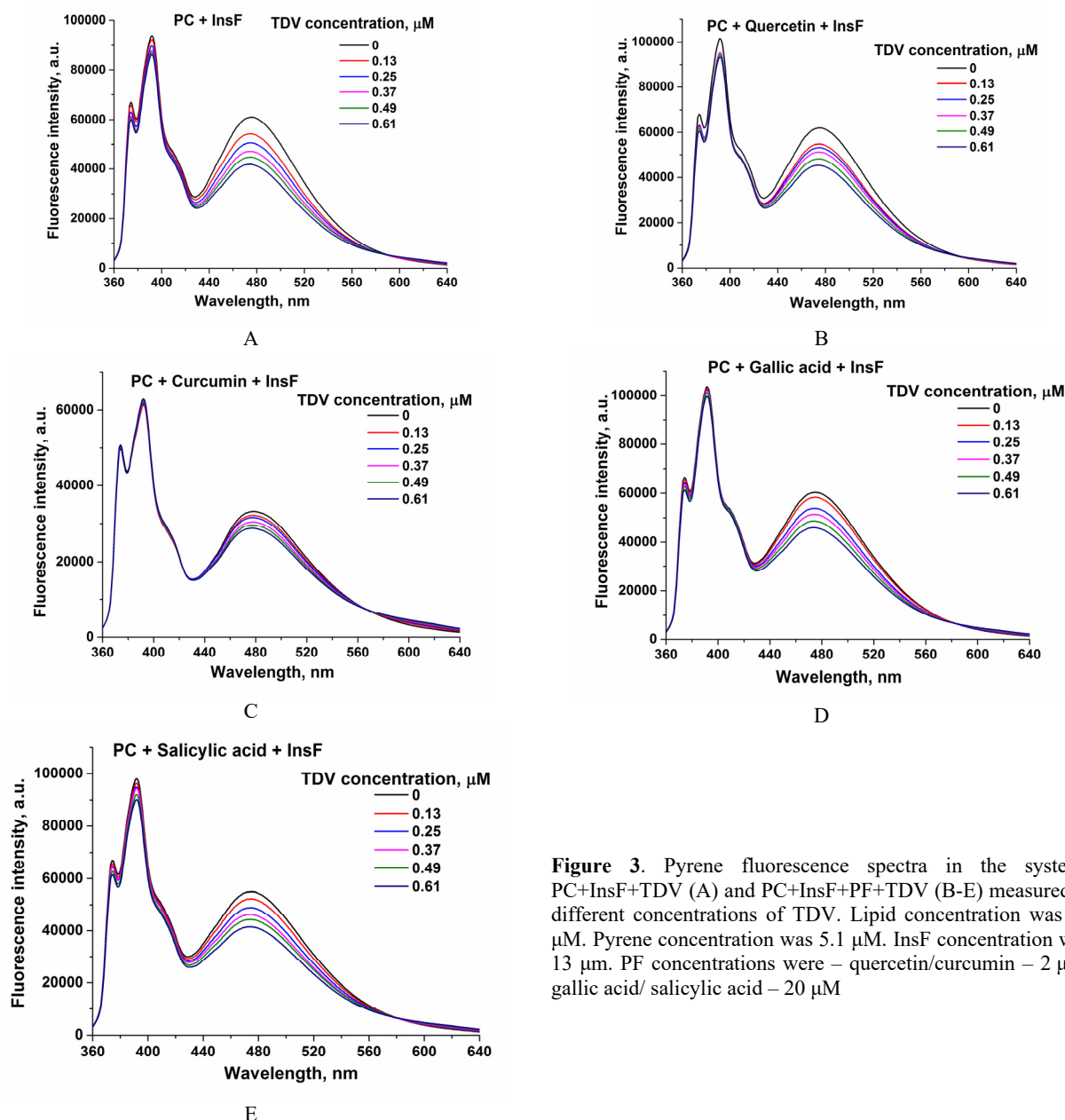


**Figure 3.** Pyrene fluorescence spectra in the systems PC+InsF+TDV (A) and PC+InsF+PF+TDV (B-E) measured at different concentrations of TDV. Lipid concentration was 67  $\mu\text{M}$ . Pyrene concentration was 5.1  $\mu\text{M}$ . InsF concentration was 13  $\mu\text{M}$ . PF concentrations were – quercetin/curcumin – 2  $\mu\text{M}$ , gallic acid/ salicylic acid – 20  $\mu\text{M}$

Interestingly, the FRET efficiency remained virtually consistent regardless of the amyloid fibril type, whether derived from apolipoprotein A-I or insulin, suggesting that the specific protein composition of the fibrils does not significantly affect energy transfer in these systems.

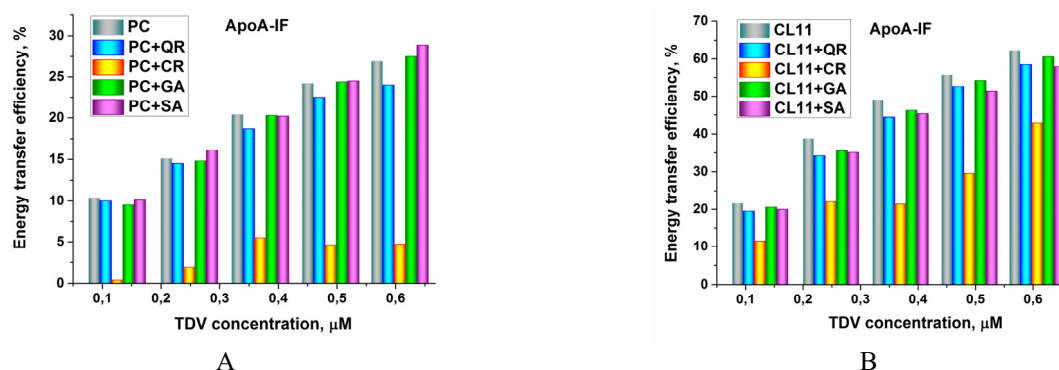


**Figure 4.** The efficiencies of the Förster resonance energy transfer between pyrene excimers and TDV observed in the systems PC+ApoA-IF+PF+TDV (A), CL11+ApoA-IF+PF+TDV (B), Chol30+ApoA-IF+PF+TDV (C), CL11Chol30+ApoA-IF+PF+TDV (D), PG20+ApoA-IF+PF+TDV (E)  
(continued on next page)

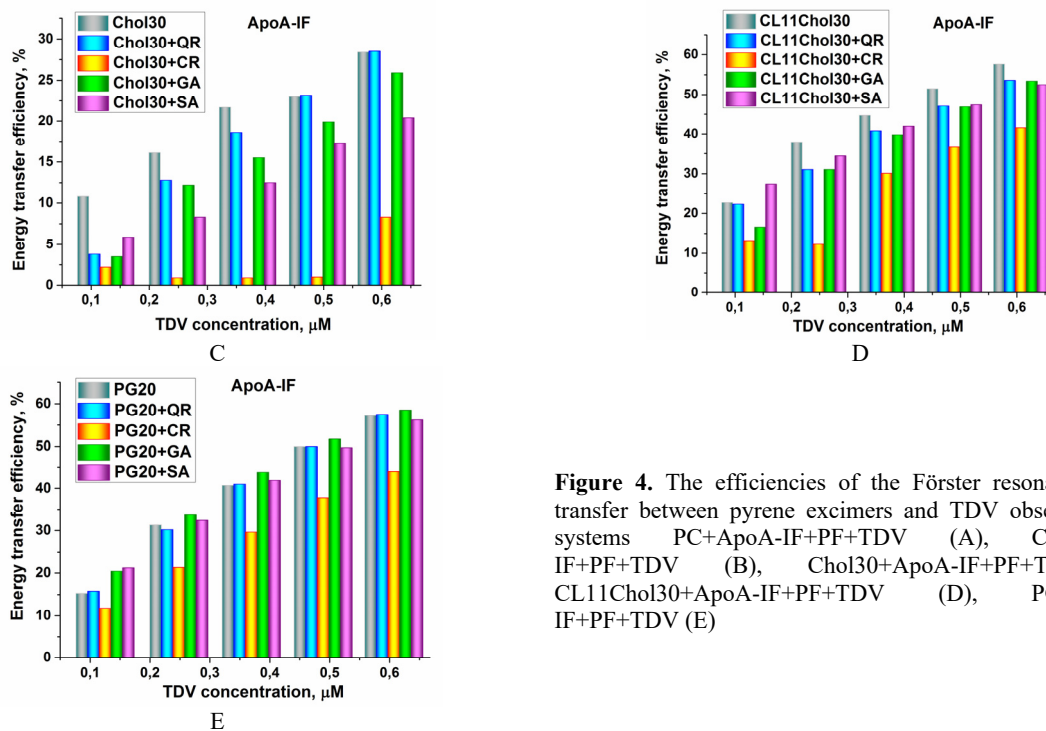


**Figure 4.** The efficiencies of the Förster resonance energy transfer between pyrene excimers and TDV observed in the systems PC+ApoA-IF+PF+TDV (A), CL11+ApoA-IF+PF+TDV (B), Chol30+ApoA-IF+PF+TDV (C), CL11Chol30+ApoA-IF+PF+TDV (D), PG20+ApoA-IF+PF+TDV (E)

The most striking observation was the marked variation in FRET efficiency across different lipid compositions. Neat PC bilayers exhibited a baseline FRET efficiency of ~30%, which served as a reference point for comparison with more complex lipid mixtures. The incorporation of cardiolipin (CL) into PC bilayers resulted in a dramatic increase in FRET efficiency to 60%, representing a two-fold enhancement compared to pure PC systems. This substantial increase may be attributed to CL unique molecular structure and its ability to alter membrane curvature and fluidity [10], potentially facilitating closer proximity or more favorable orientation between the donor and acceptor fluorophores.

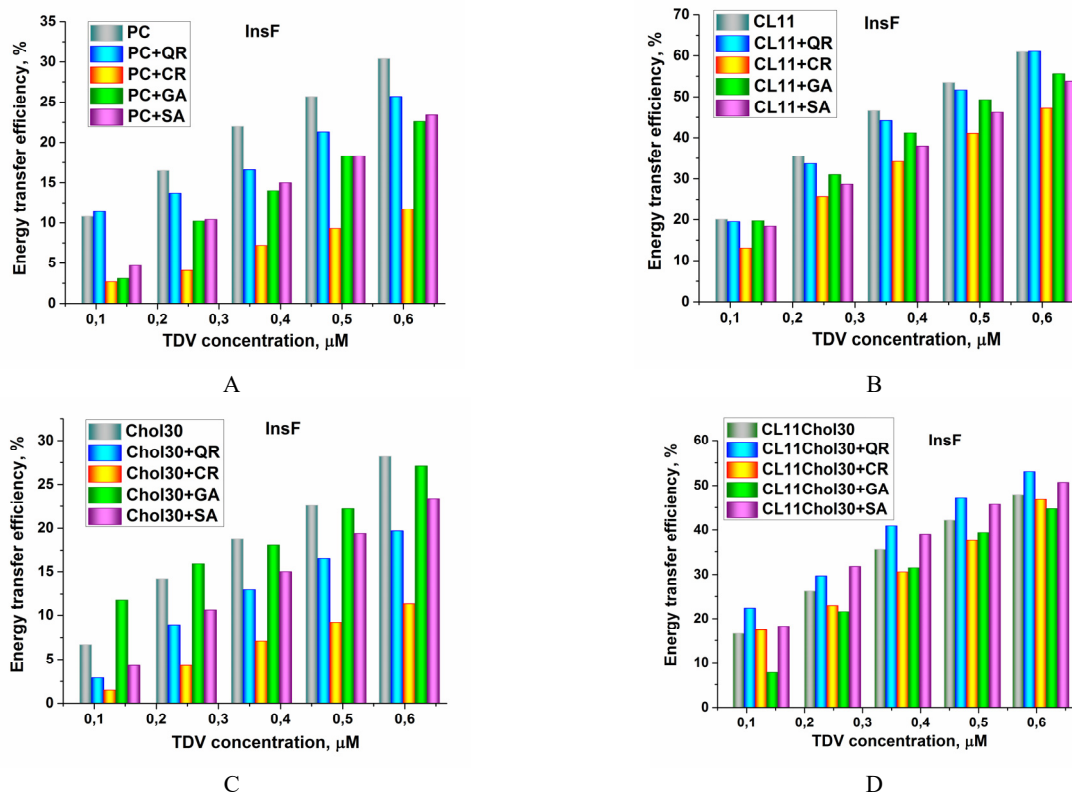


**Figure 5.** The efficiencies of the Förster resonance energy transfer between pyrene excimers and TDV observed in the systems PC+InsF+PF+TDV (A), CL11+InsF+PF+TDV (B), Chol30+InsF+PF+TDV (C), CL11Chol30+InsF+PF+TDV (D), PG20+InsF+PF+TDV (E).

(continued on next page)

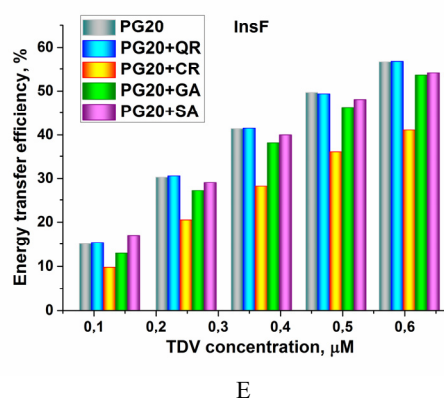


**Figure 5.** The efficiencies of the Förster resonance energy transfer between pyrene excimers and TDV observed in the systems PC+InsF+PF+TDV (A), CL11+InsF+PF+TDV (B), Chol30+InsF+PF+TDV (C), CL11Chol30+InsF+PF+TDV (D), PG20+InsF+PF+TDV (E).

Conversely, the addition of Chol to PC bilayers did not affect FRET efficiency. This observation suggests that well-known membrane-ordering effect of the sterol does not significantly influence the spatial relationship or energy transfer dynamics between pyrene and TDV in this context. However, the combination of PC, Chol, and CL yielded an intermediate FRET efficiency of ~50%, indicating a complex interplay between these lipid components. This result implies that while cholesterol alone does not enhance FRET efficiency, it does not completely negate the positive effect of cardiolipin when both are present in the membrane. The inclusion of PG into PC bilayers also led to a substantial increase in FRET efficiency, reaching ~55%. This enhancement, albeit slightly less pronounced than that observed with CL, suggests that negatively charged lipids generally promote more efficient energy transfer in these amyloid-liposome systems. The observed findings can be interpreted through several mechanistic lenses. First, the increased FRET efficiency in CL- and PG-containing bilayers may be due to electrostatic interactions between the negatively charged lipids and the amyloid fibrils, potentially altering the fibril orientation or proximity to the membrane surface. Second, changes in membrane fluidity and curvature induced by these lipids could modify the distribution or mobility of the fluorophores within the bilayer, thereby affecting their average separation distance and, consequently, FRET efficiency. Furthermore, the differential effects of various lipid compositions on FRET efficiency may reflect alterations in the membrane physical properties, such as thickness, lateral pressure profile, or phase behavior. These changes could indirectly influence the interaction between amyloid fibrils and the liposome surface, thus modulating the spatial relationship between the donor and acceptor molecules.

Next, we evaluated the impact of different polyphenols on amyloid-lipid complexation. To this end, the changes in the systems liposomes+amyloid+PF were calculated relative to the systems without PF (Figs. 6, 7).

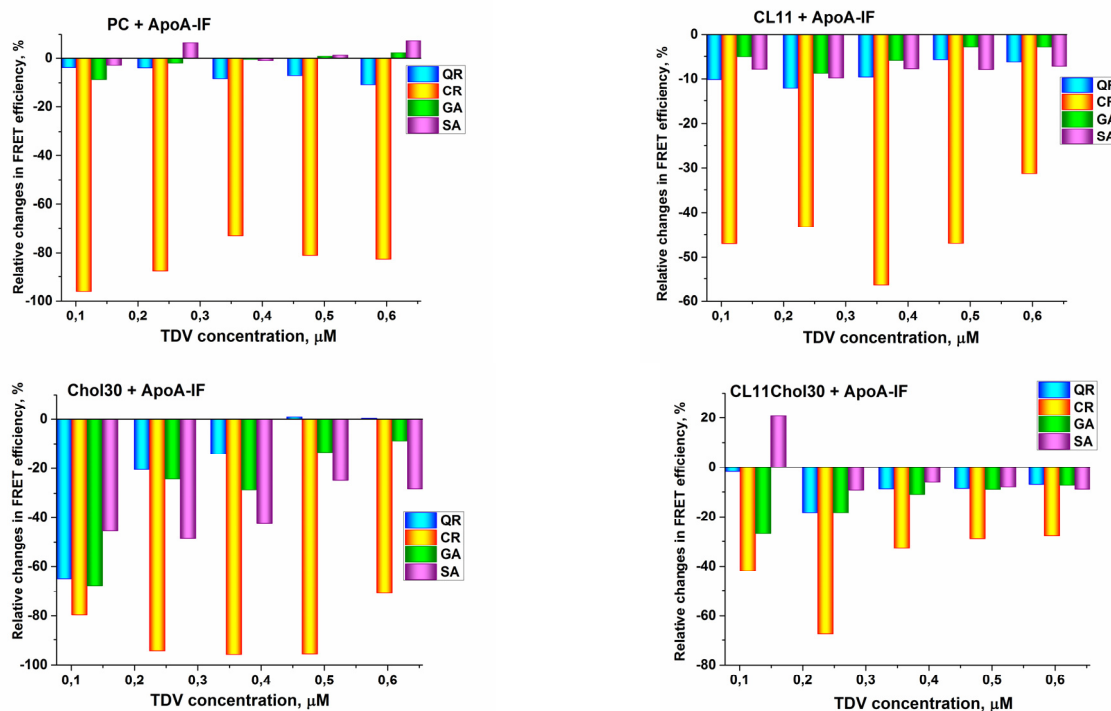


**Figure 6.** The changes in FRET efficiency relative to control without PF in the systems PC+ApoA-IF+PF+TDV (A), CL11+ApoA-IF+PF+TDV (B), Chol30+ApoA-IF+PF+TDV (C), CL11Chol30+ApoA-IF+PF+TDV (D), PG20+ApoA-IF+PF+TDV (E)

(continued on next page)

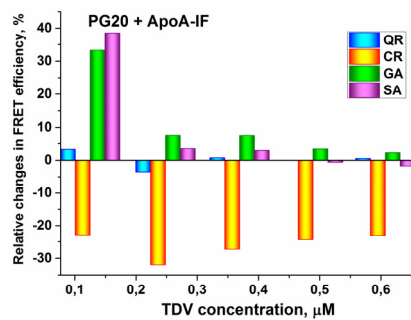


**Figure 6.** The changes in FRET efficiency relative to control without PF in the systems PC+ApoA-IF+PF+TDV (A), CL11+ApoA-IF+PF+TDV (B), Chol30+ApoA-IF+PF+TDV (C), CL11Chol30+ApoA-IF+PF+TDV (D), PG20+ApoA-IF+PF+TDV (E)

Analyzing these results, the following tendencies emerged: i) the incorporation of polyphenols into amyloid-lipid systems resulted in decrease of energy transfer efficiency, ii) the effect of polyphenols on amyloid-lipid interactions depends on lipid bilayer composition, chemical nature of polyphenols and the type of the protein, iii) for all systems there is no correlation between the increase in TDV concentration and the magnitude of polyphenols impact, iv) curcumin induced the changes in energy transfer efficiency in all systems under consideration. Furthermore, in the case of ApoA-IF in all types of lipid membranes except Chol30, the influence of quercetin, salicylic and gallic acids were within the experimental error, and only in Chol30 the changes in the efficiency of energy transfer were noticeable not only for curcumin but also for gallic and salicylic acids. In turn, in the presence of InsF, the statistically significant effect of polyphenols was observed for all polyphenols. Finally, the impact of curcumin on amyloid-lipid interactions is more pronounced in the case of ApoA-IF.

The most salient finding is the observed decrease in energy transfer efficiency upon incorporation of PF into the amyloid-lipid systems. This reduction in FRET efficiency suggests that polyphenols may modulate the spatial relationship between the amyloid fibrils and the lipid membranes, potentially altering the proximity or orientation of the fluorophores within the system. Several mechanisms may account for this phenomenon. First, PF are known to interact directly with amyloid fibrils, potentially inducing conformational changes or disrupting fibril structure [11]. Such interactions could lead to a reorganization of the amyloid-lipid interface, thereby increasing the average distance between the FRET donor (pyrene) and acceptor (TDV) molecules. This increased separation would result in reduced energy transfer efficiency, as FRET is highly sensitive to the distance on the nanometer scale. Furthermore, PF may exert their effects by modulating the properties of the lipid membranes themselves. Many polyphenolic compounds have been shown to interact with lipid bilayers, altering membrane fluidity, curvature, or lateral organization [12,13]. These changes in membrane properties could indirectly affect the binding or orientation of amyloid fibrils at the lipid interface, again leading to altered FRET efficiency.

The magnitude of the polyphenol-induced effect was found to be dependent on a complex interplay of factors, including the lipid bilayer composition, the chemical nature of the polyphenols, and the type of amyloidogenic protein. This multifactorial dependence underscores the intricate nature of these interactions and suggests that the modulation of amyloid-lipid complexation by polyphenols is not a simple, uniform process but rather a nuanced phenomenon influenced by the specific molecular characteristics of all components involved.

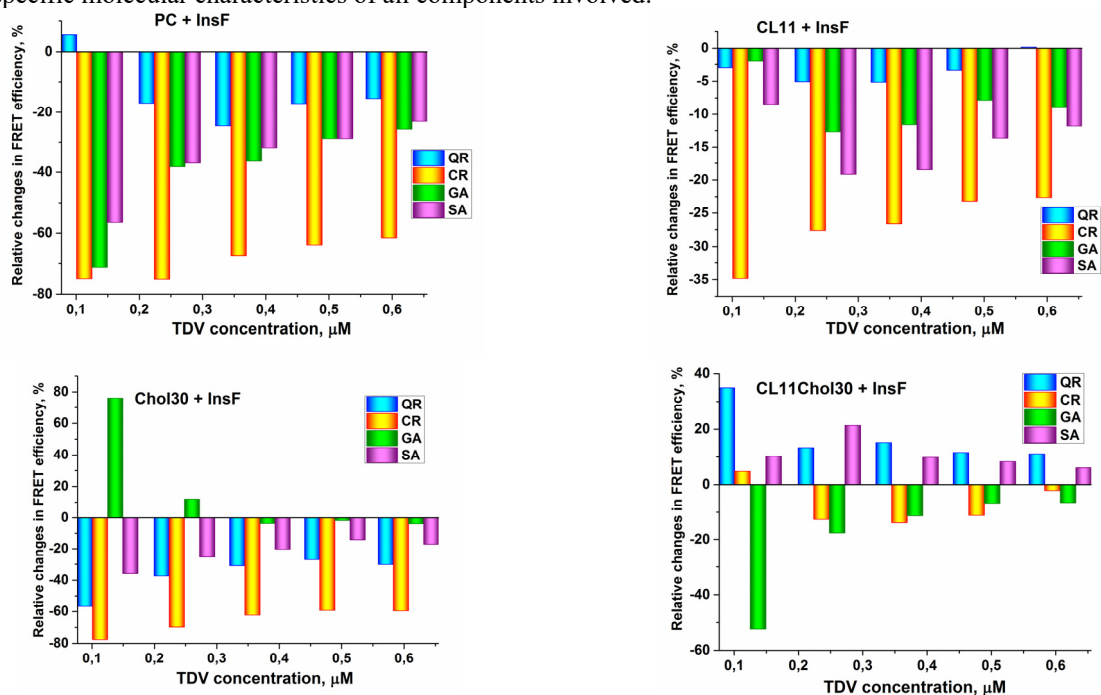


**Figure 7.** The changes in FRET efficiency relative to control without PF in the systems PC+InsF+PF+TDV (A), CL11+InsF+PF+TDV (B), Chol30+InsF+PF+TDV (C), CL11Chol30+InsF+PF+TDV (D), PG20+InsF+PF+TDV (E) (continued on next page)

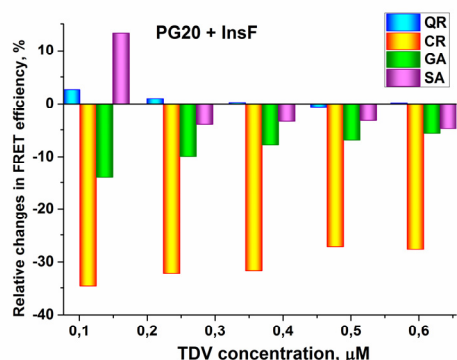


**Figure 7.** The changes in FRET efficiency relative to control without PF in the systems PC+InsF+PF+TDV (A), CL11+InsF+PF+TDV (B), Chol30+InsF+PF+TDV (C), CL11Chol30+InsF+PF+TDV (D), PG20+InsF+PF+TDV (E)

Among the polyphenols studied, CR demonstrated the most pronounced and consistent effect across all systems under consideration, exhibiting a remarkable ability to reduce FRET efficiency. This observation not only aligns with previous studies highlighting curcumin's potent ability to interact with amyloid fibrils and modulate their behavior but also extends our understanding of its effects in complex, membrane-associated systems [14]. The superior efficacy of curcumin in reducing FRET efficiency may be attributed to its unique molecular structure, which includes two aromatic rings connected by a flexible linker region, conferring both hydrophobic and hydrophilic properties. This amphipathic nature could allow CR to interact more effectively with both the amyloid fibrils and the lipid membranes, potentially disrupting their association or altering their relative orientations through multiple mechanisms. Furthermore, CR's ability to modulate oxidative stress and inflammation, processes often associated with amyloid pathology, may contribute to its pronounced effects in these systems [15].

The dependence of polyphenol effects on lipid bilayer composition suggests that the membrane environment plays a crucial and multifaceted role in mediating amyloid-lipid interactions. Different lipid compositions may alter a myriad of physical properties of the membrane, such as fluidity, curvature, surface charge, and lateral organization, which in turn could affect the binding of amyloid fibrils and the distribution of polyphenols within the system in complex and potentially synergistic ways. For instance, the presence of negatively charged lipids like CL or PG might enhance electrostatic interactions between the membrane and positively charged regions of the amyloid fibrils, potentially influencing the ability of polyphenols to disrupt these associations. Additionally, the incorporation of cholesterol could modulate membrane fluidity and the formation of lipid rafts, potentially creating specialized microenvironments that influence the interaction of both amyloid fibrils and polyphenols with the membrane.

Of particular interest is the observation that CR exerts a more pronounced impact on amyloid-lipid interactions in the case of ApoA-IF compared to InsF. This differential effect can be attributed to several factors related to the structural and physicochemical properties of these amyloidogenic proteins. ApoA-I, being an amphipathic protein with a high  $\alpha$ -helical content, possesses a unique structural plasticity that allows it to interact with lipids and undergo conformational changes. This inherent flexibility might render ApoA-IF more susceptible to CR-induced perturbations. Curcumin, with its amphipathic nature and ability to intercalate into lipid bilayers, may disrupt the delicate balance of hydrophobic and hydrophilic interactions that stabilize ApoA-IF, leading to more pronounced effects on fibril structure and stability. The pronounced effect of curcumin on ApoA-IF may also be attributed to its ability to modulate lipid-protein interactions. Curcumin has been shown to alter membrane fluidity and organization, which could indirectly affect the binding of ApoA-IF to lipid surfaces. Given that ApoA-I plays a crucial role in lipid metabolism and transport, its interaction with lipid membranes is likely more sensitive to curcumin-induced changes in membrane properties compared to insulin. The observed differences in CR impact on ApoA-IF and InsF interactions with lipid membranes may also have implications for understanding the role of these amyloidogenic proteins in their respective pathological contexts. ApoA-I is associated with atherosclerosis and cardiovascular diseases, while insulin is linked to type 2 diabetes. The enhanced susceptibility of ApoA-IF to CR-mediated modulation suggests that curcumin or its derivatives might be particularly effective in targeting ApoA-I-related amyloidoses.

## CONCLUSIONS

In summary, our findings indicate that the efficiency of FRET between pyrene as a donor and TDV as an acceptor is sensitive to the variables such as i) lipid composition of the model membranes; ii) the structural peculiarities of amyloid fibrils; and iii) the chemical nature of polyphenolic compounds. The observed reduction in FRET efficiency upon polyphenol incorporation suggests a significant and nuanced modulation of amyloid-lipid interactions, which could have important implications for understanding and potentially mitigating the membrane-mediated toxicity of amyloid species in various pathological conditions. These findings not only expand our fundamental understanding of the biophysical principles governing amyloid-membrane interactions but also open new avenues for the development of targeted therapeutic strategies in amyloid-related disorders.

## Acknowledgements

This project has received funding through the EURIZON project, which is funded by the European Union under grant agreement No. 871072.

#### ORCID

- Valeriya Trusova, <https://orcid.org/0000-0002-7087-071X>; Uliana Tarabara, <https://orcid.org/0000-0002-7677-0779>  
Mette Hedegaard Thomsen, <https://orcid.org/0000-0001-6805-7247>; Galyna Gorbenko, <https://orcid.org/0000-0002-0954-5053>

#### REFERENCES

- [1] R. Budvytyte, and G. Valincius, *Biochem. Soc. Trans.* **51**, 147 (2023). <https://doi.org/10.1042/BST20220434>
- [2] J. Viles, *Angew. Chem.* **62**, e202215785 (2023). <https://doi.org/10.1002/anie.202215785>
- [3] A. Camilleri, C. Zarb, M. Caruana, U. Ostermeier, S. Ghio, T. Högen, F. Schmidt, A. Giese, and N. Vassallo, *Biochim. Biophys. Acta.* **1828**, 2532 (2013). <https://doi.org/10.1016/j.bbamem.2013.06.026>
- [4] A. Ali, K. Zhaliaska, T. Dou, A. Holman, and D. Kourouski. *J. Phys. Chem. Lett.* **14**, 10886 (2023). <https://doi.org/10.1021/acs.jpcelett.3c02613>
- [5] I. Cook, and T. Leyh, *J. Biol. Chem.* **299**, 105445 (2023). <https://doi.org/10.1016/j.jbc.2023.105445>
- [6] H. Sanders, B. Jovcevski, M. Marty, and T. Pukala, *FEBS J.* **289**, 215 (2022). <https://doi.org/10.1111/febs.16122>
- [7] J. Khalifa, S. Bourgault, and R. Gaudreault, **20**, 603 (2023). <https://doi.org/10.2174/0115672050277001231213073043>
- [8] C. Riyer, and S. Scarlata, **450**, 79 (2008). [https://doi.org/10.1016/S0076-6879\(08\)03405-8](https://doi.org/10.1016/S0076-6879(08)03405-8)
- [9] F. Dos Santos Rodrigues, G. Delgado, T. Santana da Costa, L. Tasic. *BBA Adv.* **3**, 100091 (2023). <https://doi.org/10.1016/j.bbadv.2023.100091>
- [10] M. Phan, and K. Shin, *Biophys. J.* **108**, 1977 (2015). <https://doi.org/10.1016/j.bpj.2015.03.026>
- [11] Y. Nian, Y. Zhang, C. Ruan, B. Hu, *Curr. Opin. Food Sci.* **43**, 99 (2022). <https://doi.org/10.1016/j.cofs.2021.11.005>
- [12] A. Cassano, G. De Luca, C. Conidi, and E. Drioli, *Coord. Chem. Rev.* **351**, 45 (2017). <https://doi.org/10.1016/j.ccr.2017.06.013>
- [13] M. Karonen, *Plants.* **11**, 1809 (2022). <https://doi.org/10.3390/plants11141809>
- [14] J. Jakubowski, A. Orr, D. Le, P. Tamamis, *J. Chem. Inf. Model.* **60**, 289 (2020). <https://doi.org/10.1021/acs.jcim.9b00561>
- [15] C.-F. Lin, K.-H. Yu, C.-P. Jheng, R. Chung, C. Lee, *Pathogens*, **2**, 506 (2019). <https://doi.org/10.3390/pathogens2030506>

#### ВПЛИВ ПОЛІФЕНОЛІВ НА ВЗАЄМОДІЮ АМІЛОЇДНИХ ФІБРИЛ З ЛІПІДНИМИ МЕМБРАНАМИ

У. Тарабара<sup>a</sup>, В. Трусова<sup>a</sup>, М.Х. Томсен<sup>b</sup>, Г. Горбенко<sup>a</sup>

<sup>a</sup>Кафедра медичної фізики та біомедичних нанотехнологій, Харківський національний університет імені В.Н. Каразіна  
м. Свободи 4, Харків, 61022, Україна

<sup>b</sup>Університет Аальдборгу, вул. Н. Бора 8, 6700 Есб'єрг, Данія

Метод Фьорстерівського резонансного переносу енергії (ФРПЕ) між мембранними флуоресцентними зондами піреном та TDV був застосований у якості аналітичного інструменту для дослідження модулюючого впливу поліфенолів на взаємодію амілоїдних фібрил з ліпідними мембранами. Було вивчено ефекти різних поліфенолів, включаючи кверцетин, куркумін, галову та саліцилову кислоти, на комплексування між амілоїдними фібрилами, отриманими з N-термінального фрагменту аполіпопротеїну А-I (АроА-IF) та інсуліну (InsF), і ліпосомами, що склалися з фосфатидилхоліну (ФХ) та його сумішей з кардіоліпіном (КЛ), холестерином (Хол) або фосфатидилгліцеролом (ФГ). Включення поліфенолів призвело до зниження ефективності переносу енергії, що вказує на зміну просторового розташування амілоїдних фібрил та ліпідних мембран. Величина цього ефекту залежала від складу ліпідного бішару, хімічної природи поліфенолів та типу амілоїдогенного білка. Особливо виражений вплив мав куркумін, який демонстрував найсильніший ефект у всіх системах, зокрема у присутності АроА-IF порівняно з InsF. Цей диференційований відгук свідчить про білок-специфічні механізми взаємодії та вказує на можливість розробки цілеспрямованих терапевтичних підходів. Отримані результати надають нові уявлення про складну взаємодію між поліфенолами, амілоїдними фібрилами та ліпідними мембранами, що сприяє фундаментальному розумінню амілоїдогенезу та відкриває нові шляхи для створення терапевтичних стратегій на основі поліфенолів у лікуванні амілоїд-асоційованих захворювань.

**Ключові слова:** амілоїдні фібрили; ліпідний бішар; поліфеноли; Фьорстерівський резонансний перенос енергії

## TO THE THEORY OF INTRABAND SINGLE-PHOTON ABSORPTION OF LIGHT IN SEMICONDUCTORS WITH ZINC-BLENDE STRUCTURE

✉ **Rustam Y. Rasulov<sup>a</sup>**, ✉ **Voxob R. Rasulov<sup>a\*</sup>**, **Forrukh U. Kasimov<sup>b</sup>**, **Makhliyo A. Mamatova<sup>a</sup>**

<sup>a</sup> *Fergana State University, Fergana, Uzbekistan*

<sup>b</sup> *Andijan State University, Andijan, Uzbekistan*

\*Corresponding Author e-mail: [vrrasulov83@gmail.com](mailto:vrrasulov83@gmail.com)

Received August 6, 2024; revised October 11, 2024; accepted October 27, 2024

A theoretical analysis of the frequency-temperature dependence of the coefficient of single-photon absorption of polarized radiation in narrow- and wide-bandgap semiconductors has been conducted, considering intraband optical transitions and the temperature dependence of band parameters. It has been shown that with a fixed frequency, the single-photon absorption coefficient initially increases with temperature, reaches a maximum, and then decreases. The maximum value shifts towards lower frequencies for both narrow- and wide-bandgap semiconductors when considering the temperature dependence of the bandgap width and the effective mass of holes. It was determined that in semiconductors with a zinc-blende lattice structure, the consideration of the temperature dependence of the band parameters leads to a decrease in the amplitude value of the frequency and temperature dependence of the single-photon absorption coefficient. As the temperature increases, the absorption threshold decreases, which is noticeably observed when taking into account the Passler formula. Each type of optical transition contributes differently to the frequency, temperature, and polarization dependencies of  $K_{SO,th}^{(1)}(\omega, T)$ .

**Keywords:** *Temperature dependence of band parameters; Bandgap width; Effective mass of holes; Passler and Varshni formula; Narrow- and wide-bandgap semiconductor; Single-photon absorption coefficient; Coherent saturation effect*

**PACS:** 71.20. – b, 71.28. + d

### INTRODUCTION

Intraband light absorption, caused by vertical inter-subband optical transitions in diamond-like semiconductors, has been studied for quite some time [1-3].

In works [4-9], theoretical studies have been conducted on one- and multiphoton absorption associated with both interband and intersubband optical transitions. Specifically, in [4, 6-9], the spectral-temperature dependencies of the multiphoton absorption coefficient and its linear-circular dichroism in semiconductors with cubic symmetry were investigated. In [10, 11], the saturation of photocurrent in topological insulators induced by direct optical transitions in regions of high intensity was discovered. In [12], a quantum-mechanical theory of the intensity-dependent edge photocurrent in graphene was developed; in [13], the polarization dependencies of one- and multiphoton interband transitions in two-dimensional monomolecular transition metal dichalcogenides were calculated.

The analysis of the theoretical calculations of the single-photon absorption coefficient of polarized light presented below indicates that considering the coherent saturation effect will lead to a unique frequency-temperature dependence. Therefore, it is of interest to theoretically study the light absorption caused by single-photon transitions from the branches of heavy and light holes to the spin-orbit split-off subband, taking into account the coherent saturation effect [5-9].

### ABSORPTION OF LIGHT CAUSED BY SINGLE-PHOTON TRANSITIONS FROM THE HEAVY AND LIGHT HOLE BRANCHES TO THE SPIN-ORBIT SPLIT-OFF SUBBAND.

The spectral, polarization, and temperature dependencies of the absorption coefficient due to single-photon transitions from the heavy and light hole branches of the valence band to the spin-orbit split-off subband are determined by the expression:

$$K^{(1)} = \frac{2\pi \hbar \omega}{\hbar} \frac{1}{I} \sum_{\vec{k}} \left( f_{lh,\vec{k}}^{(1)} - f_{SO,\vec{k}}^{(1)} \right) \left| \sum_{lh,m=\pm 1/2; SO,m'=\pm 1/2} M_{lh,m; SO,m'}^{(2)}(\vec{k}) \right|^2 \delta(E_{SO,\vec{k}} - E_{lh,\vec{k}} - \hbar \omega), \quad (1)$$

Considering the coherent saturation effect [5-9, 14], we obtain:

$$K^{(1)} = \frac{2\pi}{\hbar} \hbar \omega \frac{1}{I} \rho(\hbar \omega) f(T, \omega) (\langle \mathfrak{R}_+ \rangle + \langle \mathfrak{R}_- \rangle), \quad (2)$$

where

$$\mathfrak{R}_{\pm} = \frac{\left| M_{SO,+1/2,lh,\pm 1/2}^{(1)}(\vec{k}) + M_{SO,-1/2,lh,\pm 1/2}^{(1)}(\vec{k}) \right|^2}{\sqrt{1 + 4 \frac{\alpha \omega}{\hbar^2 \omega^2} \left| M_{SO,+1/2,lh,\pm 1/2}^{(1)}(\vec{k}) + M_{SO,-1/2,lh,\pm 1/2}^{(1)}(\vec{k}) \right|^2}}, \quad (3)$$

$\rho(\hbar\omega) = \mu_- k_\omega^{(1)} / (\pi^2 \hbar^2)$  is the density of states,  $k_\omega^{(1)} = (2\mu_- [\hbar\omega - \Delta_{SO}] / \hbar^2)^{1/2}$ ,  $\left\langle |M_{n\vec{k}, n\vec{k}}^{(1)}|^2 \right\rangle$  is the square of the matrix element of the optical transition type  $M_{n\vec{k}, n\vec{k}}^{(1)}$  is the optical transition matrix element for the transition of type  $|n\vec{k}\rangle \rightarrow |n'\vec{k}'\rangle$  averaged over the solid angles of the wave vector  $\vec{k}$ . The parameter  $\alpha_\omega = 6\omega^2 T_1^{(1)} T_2^{(1)} \frac{I}{I_0}$ , where  $I_0 = \frac{cn_\omega \hbar^3 \omega^3}{2\pi|B|}$ , and  $I(\omega)$  is the intensity (frequency) of the light. The functions  $f_{L\vec{k}}^{(1)}$  represent the distribution functions of charge carriers (where  $L=1$  ( $hh$ ) corresponds to heavy holes,  $L=2$  ( $lh$ ) corresponds to light holes, and  $L=SO$  corresponds to holes in the spin-orbit split-off subband). The energy dispersion of holes in branch  $L$  is given by  $E_{L\vec{k}} = -\hbar^2 k^2 / 2m_L$  [15,16]. The parameters  $e'_\pm = e_{x'} \pm e_{y'}$ ,  $e_{x'}$ ,  $e_{y'}$  are the projections of the polarization vector  $\vec{e}$  onto the  $Ox'$  and  $Oy'$  axes, perpendicular to the wave vector  $\vec{k}$  of the holes. The reduced effective mass of the holes is  $\mu_{-}^{(SO,L)} = m_{SO} m_L / (m_{SO} - m_L)$ . In particular, for single-photon transitions from the light hole branch to the spin-orbit split-off subband, the value  $\mathfrak{R}_\pm$  is written as:

$$\mathfrak{R}_+ = 3 \left( \frac{eA_0}{ch} \right)^2 B^2 k^2 |e'_{-}|^2 \left[ 1 + 4 \frac{\alpha_\omega}{\hbar^2 \omega^2} \left( \frac{eA_0}{ch} \right)^2 B^2 k^2 3 |e'_{-}|^2 \right]^{-1/2}, \tag{4}$$

$$\mathfrak{R}_- = \left( \frac{eA_0}{ch} \right)^2 B^2 k^2 (9e'^2_{\perp} + 4e'^2_z) \left[ 1 + 4 \frac{\alpha_\omega}{\hbar^2 \omega^2} \left( \frac{eA_0}{ch} \right)^2 B^2 k^2 (9e'^2_{\perp} + 4e'^2_z) \right]^{-1/2}, \tag{5}$$

where  $4B = \hbar^2 m_{lh} m_{hh} / (m_{hh} - m_{lh})$ . If the contribution of the coherent saturation effect to light absorption is neglected ( $\alpha_\omega = 0$ ) and averaging is performed over the solid angles of  $\vec{k}$  from (4, 5), then the expression becomes polarization-independent:

$$\langle \mathfrak{R}_+^{(0)} \rangle + \langle \mathfrak{R}_-^{(0)} \rangle = \left( \frac{eA_0}{ch} \right)^2 B^2 k^2 \langle 9e'^2_{\perp} + 4e'^2_z \rangle = \frac{22}{3} \left( \frac{eA_0}{ch} \right)^2 B^2 k^2. \tag{6}$$

Then (1) takes the form:

$$K^{(1)} = \frac{44\pi}{3\hbar} \left( \frac{eA_0}{ch} \right)^2 \frac{\hbar\omega}{I} \rho(\hbar\omega) f(\beta, \omega) B^2 k^2. \tag{7}$$

From Table 1, it can be seen that the reduced effective mass of holes  $\mu_{-}^{(SO, hh)} = \frac{m_{SO} m_{hh}}{m_{SO} - m_{hh}}$ , involved in optical transitions from the heavy hole branch to the spin-orbit split-off subband takes a negative value for several A3B5 semiconductors. This, in turn, leads to the wave vector of the charge carriers  $k_{SO, hh}^{(1\omega)} = [2\mu_{-}^{(SO, hh)} \hbar^{-2} (\hbar\omega - \Delta_{SO})]^{1/2}$  involved in such optical transitions becoming an imaginary quantity. For this reason, unlike the optical transitions from the light hole branch, transitions from the heavy hole branch to the spin-orbit split-off subband are forbidden.

Since optical transitions are allowed from the light hole branch to the spin-orbit split-off subband of the valence band, we will further analyze the frequency and temperature dependencies of the single-photon absorption coefficient. Then, according to the law of energy conservation:  $\frac{\hbar^2 k^2}{2m_{SO}} + \Delta_{SO} - \frac{\hbar^2 k^2}{2m_L} - \hbar\omega = 0$  the wave vector is determined by the expression  $k_{SO, L}^{(1\omega)} = [2\mu_{-}^{(SO, L)} \hbar^{-2} (\hbar\omega - \Delta_{SO})]^{1/2}$ .

From (6) and (7), it can be seen that the single-photon absorption coefficient does not depend on the degree of light polarization; therefore, linear-circular dichroism is not observed during single-photon absorption. To account for the effect of coherent saturation on absorption, it is necessary to perform calculations based on (2) and (3).

**Table 1.** Numerical values of band parameters for some semiconductors [17]

Quantities	GaAs	InSb	InAs
$E_g, eV$	1.519	0.235	0.417
$\Delta_{SO}, eV$	0.341	0.81	0.39
$m_c/m_0$	0.067	0.0135	0.026
$m_{SO}/m_0$	0.172	0.11	0.14
$\Delta_{SO}/E_g$	0.24b	4.65	1.1
$m_{lh}/m_0$	0.09009	0.0152	0.027027
$m_{hh}/m_0$	0.34965	0.26316	0.33333
$\alpha_T, meV/K$	0.5405	0.32	0.276
$\beta_T, K$	204	170	93
$F$	-1.94	-0.23	-2.90

Now, we will calculate the frequency-temperature dependencies of the single-photon absorption coefficient using the following expression for the single-photon absorption coefficient, associated with optical transitions from the light hole branch to the spin-orbit split-off subband:

$$K^{(1)} = \frac{4\pi e^2}{c\omega m_0^2 n_\omega} \sum_{nn'\vec{k}} |\vec{e}\vec{p}_{SO, lh}(\vec{k})|^2 (f_{lh, \vec{k}} - f_{SO, \vec{k}}) \delta(E_{SO}(\vec{k}) - E_{lh}(\vec{k}) - \hbar\omega). \tag{8}$$

Next, we assume the energy dispersion of light and heavy holes as  $E_{lh}(\vec{k}) = -\hbar^2 k^2 / (2m_{lh})$  and  $E_{hh}(\vec{k}) = -\hbar^2 k^2 / (2m_{hh})$ , while in the spin-orbit split-off subband it is  $E_{SO}(\vec{k}) = -\Delta_{SO} - \hbar^2 k^2 / (2m_{SO})$ , where  $m_{lh}$  ( $m_{hh}$ ) are the effective masses of light and heavy holes, respectively, and  $\Delta_{SO}$  is the spin-orbit splitting energy, with numerical values for various semiconductors provided in [17]. Then, from (8), we obtain:

$$K_{SO,lh}^{(1)} = \frac{22}{3} \frac{e^2}{c \hbar n_\omega} \frac{\mu_-}{\hbar \omega} \frac{1}{\hbar^2} B^2 (k_\omega^{(1)})^3 f_{lh,k_\omega^{(1)}} [1 - \exp(-\hbar \omega / k_B T)]$$

or

$$K_{SO,lh}^{(1)} = \frac{11}{12} \frac{e^2}{c \hbar n_\omega} \left( \frac{m_{hh} - m_{lh}}{m_{SO} - m_{lh}} \frac{m_{SO}}{m_{lh}} \right)^2 \frac{\hbar \omega - \Delta_{SO}}{\hbar \omega} \left( \frac{m_{hh} - m_{lh}}{m_{hh}} \right)^2 k_\omega^{(1)} f_{lh,k_\omega^{(1)}} (1 - e^{-\hbar \omega / k_B T}), \quad (9)$$

where  $k_\omega^{(1)} = [2\mu_-^{(SO,lh)} \hbar^{-2} (\hbar \omega - \Delta_{SO})]^{1/2}$ ,  $f_{lh,k_\omega^{(1)}} = \exp\left(\frac{E_F}{k_B T}\right) \cdot \exp\left[-\frac{m_{SO}}{m_{SO} - m_{lh}} \frac{\hbar \omega - \Delta_{SO}}{k_B T}\right]$  (see Fig. 1).

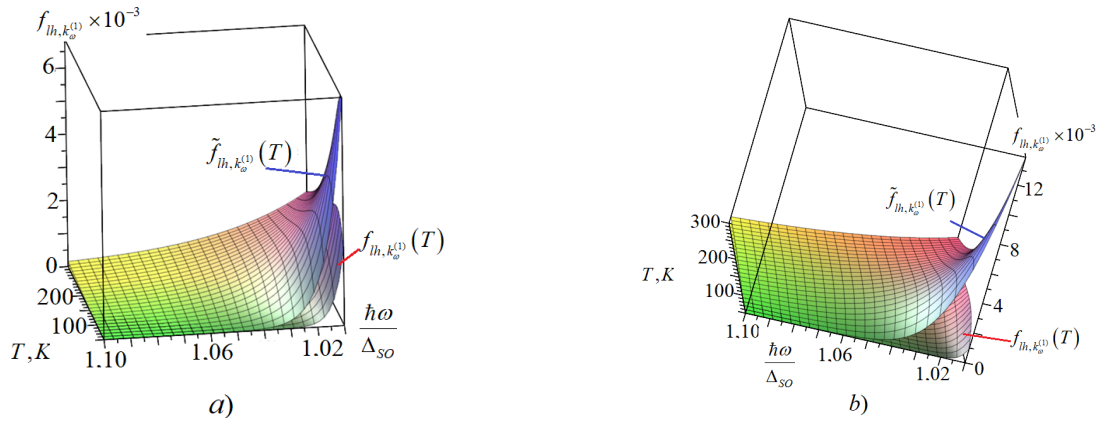


**Figure 1.** The frequency-temperature dependence of the distribution function of light holes  $f_{lh,k_\omega^{(1)}}(T)$ , involved in single-photon transitions in GaAs (a) and InAs (b), considering the temperature dependence of the bandgap width  $E_g(T)$  and the effective mass of charge carriers using the Varshni formula. The function  $\tilde{f}_{lh,k_\omega^{(1)}}(T)$  represents the distribution function of light holes at  $E_g(T = 0)$ .

The Fermi energy  $E_F$  is determined by the relation:

$$e^{\frac{E_F}{k_B T}} = \frac{1}{2} p \left( \frac{k_B T}{2\pi \hbar^2} \right)^{-3/2} \left( m_{hh}^{3/2} + m_{lh}^{3/2} + m_{SO}^{3/2} e^{-\frac{\Delta_{SO}}{k_B T}} \right)^{-1}, \quad (10)$$

where  $p$  is the hole concentration. Note that in our case,  $\hbar \omega \gg k_B T$ , so  $e^{-\hbar \omega / k_B T} \ll 1$ .

Thus, the frequency ( $x = \hbar \omega / \Delta_{SO}$ ) and temperature ( $y = k_B T / \Delta_{SO}$ ) dependencies of the single-photon absorption coefficient can be written as:

$$K_{SO,lh}^{(1)}(\omega, T) = K_0^{(1)} \frac{x-1}{x} (x-1)^{1/2} \frac{\exp\left[-\frac{m_{SO}}{m_{SO} - m_{lh}} \frac{x-1}{y}\right]}{y^{3/2} (m_{hh}^{3/2} + m_{lh}^{3/2} + m_{SO}^{3/2} e^{-1/y})}, \quad (11)$$

where

$$K_0^{(1)} = \frac{11}{6} \frac{\pi^{3/2} e^2}{c \hbar n_\omega} \frac{(m_{hh} - m_{lh})^4}{(m_{SO} - m_{lh})^{5/2}} \frac{m_{SO}^{5/2}}{m_{lh}^{3/2} m_{hh}^2} \frac{\hbar^2 p}{\Delta_{SO}}.$$

In further calculations, we assert that the temperature dependence of the bandgap width is determined by the Varshni formula [17]:

$$E_g(T) = E_g(T = 0) - \gamma_T \frac{T^2}{T + T_V}, \quad (12)$$

and by the Passler formula [18]:

$$E_g(T) = E_g(T = 0) - \frac{\alpha \theta_p}{2} \left[ \left( 1 + \left( \frac{2T}{\theta_p} \right)^p \right)^{1/p} - 1 \right]. \quad (13)$$

According to the multiband Kane model, the effective masses of electrons in the conduction band ( $m_c$ ) and holes in the spin-orbit split-off subband ( $m_{SO}$ ) depend on temperature and are expressed as [17]:

$$m_0 / m_c = \left[ 1 + 2F + \frac{E_P}{3} \left( E_{g0} - \frac{\alpha T}{\beta + T} + \frac{2}{3} \Delta_{SO} \right) \left( E_{g0} - \frac{\alpha T}{\beta + T} \right)^{-1} \left( E_{g0} - \frac{\alpha T}{\beta + T} + \Delta_{SO} \right)^{-1} \right], \quad (14)$$

$$m_0/m_{SO} = \left[ \gamma_1 - \frac{E_P}{3} \Delta_{SO} \left( E_{g0} - \frac{\alpha T}{\beta + T} \right)^{-1} \left( E_{g0} - \frac{\alpha T}{\beta + T} + \Delta_{SO} \right)^{-1} \right], \quad (15)$$

where  $E_{g0} = E_g(T = 0)$ . For quantitative calculations, the numerical values of the parameters  $\gamma_T$ ,  $T_V$ ,  $\alpha$ ,  $\Theta_p$ ,  $p$  are taken from [18].

Using the numerical values of the band parameters for GaAs and InAs (see Table 1), when the temperature changes from 10 K to 300 K, the effective mass of electrons in the conduction band decreases by 0.053% and 0.051%, respectively, and the effective mass of holes in the spin-orbit split-off subband decreases by 0.01% and 0.04%, respectively. Although these changes are minor, considering  $E_g(T)$  leads to significant changes in the frequency-temperature dependence of the absorption coefficient.

As seen from equation (8), the temperature dependence of  $K_{SO,lh}^{(1)}$  is determined by the temperature dependence of  $f_{lh,k_\omega^{(1)}}(T)$ , while the frequency dependence is determined by the term  $\frac{\hbar\omega - \Delta_{SO}}{\hbar\omega} k_\omega^{(1)} \rho(\hbar\omega) \exp\left(-\frac{m_{SO}}{m_{SO} - m_{lh}} \frac{\hbar\omega - \Delta_{SO}}{k_B T}\right)$ . In this context, Figure 1 presents the frequency-temperature dependence of the distribution function of light holes involved in single-photon transitions in GaAs and InAs. It shows that, at a fixed frequency, the distribution function  $f_{lh,k_\omega^{(1)}}$  initially increases with temperature, reaches a maximum, and then decreases. Specifically, at  $\hbar\omega = 1,01\Delta_{SO}$  in GaAs (InAs), the function  $f_{lh,k_\omega^{(1)}}$  reaches its maximum at a temperature of 90 K (60 K). Figure 1 also shows that the functions  $f_{lh,k_\omega^{(1)}}(T, E_g(T))$  and  $\tilde{f}_{lh,k_\omega^{(1)}}(T) = f_{lh,k_\omega^{(1)}}(T, E_g(T) = 0)$  differ significantly at low frequencies across all temperatures, but converge at high frequencies. Furthermore, the temperature dependence of the band parameters is prominently observed at low frequencies. The calculations do not account for the contribution of the coherent saturation effect in  $f_{lh,k_\omega^{(1)}}(T)$  and  $\tilde{f}_{lh,k_\omega^{(1)}}(T)$ .

The frequency-temperature dependence of the single-photon absorption coefficient  $K_{SO,lh}^{(1)}(\omega, T)$  ( $\tilde{K}_{SO,lh}^{(1)}(\omega, T)$ ) in InSb (a, b) GaAs (c, d) (see Figure 2) was calculated according to (14), using the Varshni formula (plots a, c) and the Passler formula (plots b, d), where  $K_{SO,lh}^{(1)}(\omega, T)$  ( $\tilde{K}_{SO,lh}^{(1)}(\omega, T)$ ) is the absorption coefficient with (without) considering the temperature dependence of  $E_g(T)$  and the effective masses of holes. The contribution of the coherent saturation effect is not accounted for, and the amplitude value of  $\tilde{K}_{SO,lh}^{(1)}(\omega, T)$  was normalized to unity.

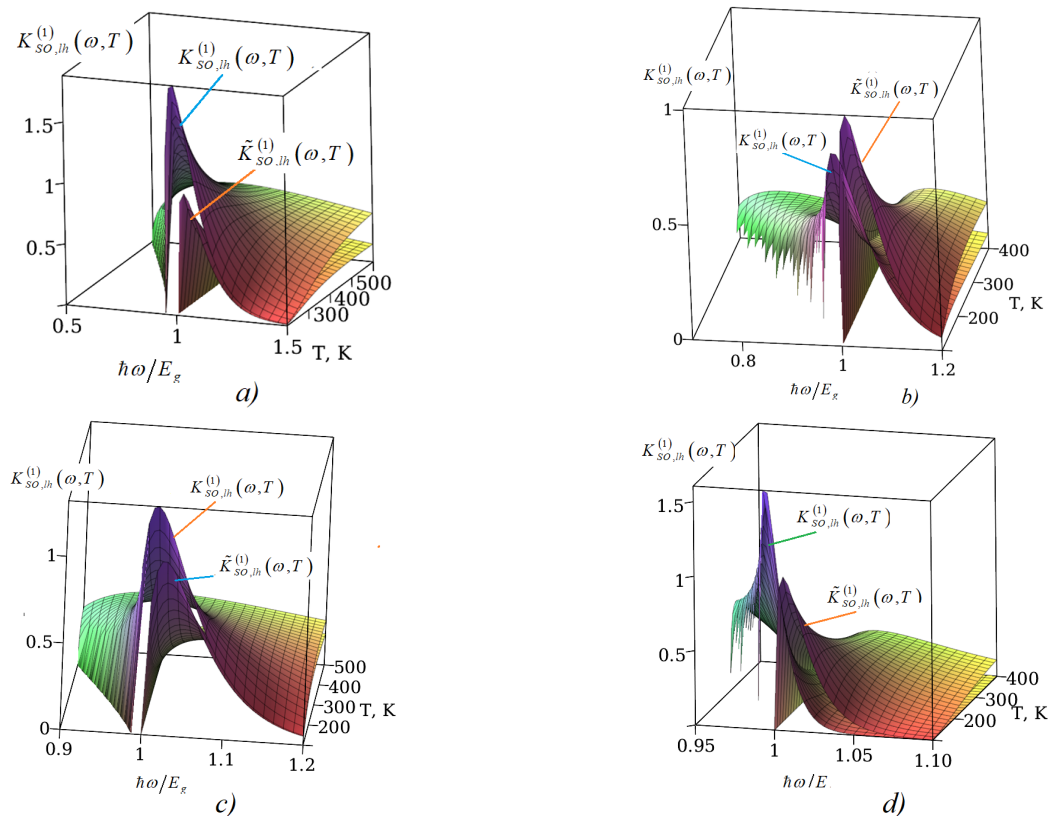


**Figure 2.** Frequency-temperature dependence of  $K_{SO,lh}^{(1)}(\omega, T)$  in InSb (a, b) and GaAs (c, d), where  $K_{SO,lh}^{(1)}(\omega, T)$  was calculated using the Varshni (plots a, c) and Passler (plots b, d) formulas.  $K_{SO,lh}^{(1)}(\omega, T)$  ( $\tilde{K}_{SO,lh}^{(1)}(\omega, T)$ ) is the absorption coefficient with (without) accounting for the temperature dependence of  $E_g(T)$  and the effective masses of holes.

From Fig. 2, it is evident that at a fixed frequency,  $K_{SO,lh}^{(1)}(T)$  increases with temperature, reaches a maximum, and then decreases. This temperature-dependent behavior of  $K_{SO,lh}^{(1)}(\omega, T)$  ( $\tilde{K}_{SO,lh}^{(1)}(\omega, T)$ ) is described by the analogous behavior of the corresponding distribution function. It is noted that in the frequency range  $\Delta_{SO} \leq \hbar\omega \leq 1,3\Delta_{SO}$  the absorption coefficient  $K_{SO,lh}^{(1)}(\omega, T)$  is greater than  $\tilde{K}_{SO,lh}^{(1)}(\omega, T)$ , whereas for  $\hbar\omega > 1,3\Delta_{SO}$  the plots of  $K_{SO,lh}^{(1)}(\omega, T)$  and  $\tilde{K}_{SO,lh}^{(1)}(\omega, T)$  merge.

It is worth noting that in narrow-gap crystals, if the dependencies  $E_g(T)$ ,  $m_{SO}(T)$ ,  $m_c(T)$ , are considered, the dependence  $K_{SO,lh}^{(1)}(\omega, T)$  increases sharply (see Fig. 2). This can be explained by the sharp increase in the quantity  $\left(\frac{m_{hh}-m_{lh}}{m_{SO}-m_{lh}}\right)^2 \left(\frac{m_{hh}-m_{lh}}{m_{hh}}\right)^2 \left(\frac{m_{SO}-m_{lh}}{m_{SO}-m_{lh}} \cdot \Delta_{SO}\right)^{1/2}$  with increasing temperature (particularly in InSb, this quantity increases up to 10 times).

### 3. CONCLUSIONS

From the above-mentioned results and Figures 1-2, it is evident that, at a fixed frequency, the coefficient of one-photon absorption in the semiconductors GaAs and InAs initially increases with temperature, reaches a maximum, and then decreases. The maximum value, considering the temperature dependence of  $E_g(T)$ ,  $m_{SO}(T)$ ,  $m_c(T)$  shifts towards lower frequencies, and this shift is sensitive when accounting for (13) for both narrow-gap and wide-gap semiconductors.

It is also noted that considering the temperature dependence of band parameters leads to a reduction in the frequency and temperature dependence of the one-photon absorption coefficient  $K_{SO,lh}^{(1)}(\omega, T)$ .

As the temperature increases, the absorption threshold (edge) decreases, which is noticeably observed when considering the Passler formula. It has been shown that each type of optical transition contributes differently to the frequency, temperature, and polarization dependencies of  $K_{SO,lh}^{(1)}(\omega, T)$ , as some optical transitions are forbidden.

### ORCID

✉ **Rustam Y. Rasulov**, <https://orcid.org/0000-0002-5512-0654>; ✉ **Voxob R. Rasulov**, <https://orcid.org/0000-0001-5255-5612>

### REFERENCES

- [1] E.L. Ivchenko, "Two-photon absorption of light and optical orientation of free carriers," *Physics*, St. Petersburg, **14**(12), 3489-3496 (1972).
- [2] R.Ya. Rasulov, Polarization optical photovoltaic effects in semiconductors with linear and nonlinear absorption of light," Sc.D. Thesis, Ioffe Institute, 1993.
- [3] R.Ya. Rasulov, "Linear-circular dichroism in multiphoton intersubband absorption in semiconductors," *Semiconductors*, **35**(6), 1674-1678 (1993). <https://journals.ioffe.ru/articles/viewPDF/14966> (in Russian).
- [4] S.D. Ganichev, E.L. Ivchenko, R. Ya. Rasulov, I.D. Yaroshetsky, and B.Ya. Averbukh, "Linear-circular dichroism of the drag current during nonlinear intersubband absorption of light in p-Ge," *FTT*, **35**(1), 198-207 (1993). <https://journals.ioffe.ru/articles/viewPDF/14762> (in Russian).
- [5] R.Ya. Rasulov, G.Kh. Khoshimov, and Kh. Kholitdinov, "Linear-circular dichroism of nonlinear light absorption in n-GaP," *Semiconductors*, **30**(2), 274-272 (1996). <https://journals.ioffe.ru/articles/viewPDF/18345>
- [6] V.R. Rasulov, R.Ya. Rasulov, I. Eshboltaev, "Linearly and Circular Dichroism in a Semiconductor with a Complex Valence Band with Allowance for Four-Photon Absorption of Light," *Physics of the Solid State*, **59**, 463 (2017). <https://doi.org/10.1134/S1063783417030283>
- [7] R.Y. Rasulov, V.R. Rasulov, I. Eshboltaev, and R.R. Sultonov, "Two- and Three-Photon Linear Circular Dichroism in Semiconductors of Cubic Symmetry," *Russian Physics Journal*, **63**(11), 2025–2030 (2021).
- [8] R.Ya. Rasulov, V.R. Rasulov, M.Kh. Kuchkarov, and I.M. Eshboltaev, "Interband multiphoton absorption of polarized radiation and its linear circular dichroism in semiconductors in the Kane approximation," *Russian Physics Journal*, **65**(10), (2023). <https://doi.org/10.1007/s11182-023-02825-3>
- [9] R.Ya. Rasulov, V.R. Rasulov, N.U. Kodirov, and U.M. Isomaddinova, "Interband one photon absorption of light and its linear-circular dichroism in crystals with coherent saturation effect included," *Physics of the Solid State*, **65**(7), 1173-1179 (2023). <https://doi.org/10.61011/PSS.2023.07.56410.77>
- [10] N.V. Leppenen, E.L. Ivchenko, and L.E. Golub, "Nonlinear optical absorption and photocurrents in topological insulators," *Phys. Rev. B*, **105**, 115306 (2022). <https://doi.org/10.1103/PhysRevB.105.115306>
- [11] S.N. Danilov, L.E. Golub, T. Mayer, A. Beer, S. Binder, E. Mönch, J. Minár, *et al.*, "Superlinear Photogalvanic Effects in (Bi<sub>0.3</sub>Sb<sub>0.7</sub>)<sub>2</sub>(Te<sub>0.1</sub>Se<sub>0.9</sub>)<sub>3</sub>: Probing Three-Dimensional Topological Insulator Surface States at Room Temperature," *Phys. Rev. Applied*, **15**, 064030 (2021). <https://doi.org/https://doi.org/10.1103/PhysRevApplied.16.064030>
- [12] S. Candussio, L.E. Golub, S. Bernreuter, T. Jötten, T. Rockinger, K. Watanabe, T. Taniguchi, *et al.*, "Nonlinear intensity dependence of terahertz edge photocurrents in graphene," *Phys. Rev. B*, **104**, 155404 (2021). <https://doi.org/10.1103/PhysRevB.104.155404>
- [13] R.Y. Rasulov, V.R. Rasulov, K.K. Urinova, M.A. Mamatova, and B.B. Akhmedov, "Single and multiphoton optical transitions in atomically thin layers of transition metal dichalcogenides," *East European Journal of Physics*, (1), 393–397 (2024). <https://doi.org/10.26565/2312-4334-2024-1-40>
- [14] D.A. Parshin, and A.R. Shabaev, "Theory of linear IR absorption by semiconductors with degenerate bands," *Zh. Exp. Teor. Fiz.* **92**(4), 1471-1484 (1987). [http://jetp.ras.ru/cgi-bin/dn/e\\_065\\_04\\_0827.pdf](http://jetp.ras.ru/cgi-bin/dn/e_065_04_0827.pdf)

- [15] G.L. Bir, and G.E. Pikus, *Symmetry and Strain-induced Effects in Semiconductors*, (Wiley, New York, 1972).
- [16] E.L. Ivchenko, and R.Ya. Rasulov, *Symmetry and real band structure of semiconductors*, (Tashkent, Fan, 1989). <https://koha.lib.tsu.ru/cgi-bin/koha/opac-detail.pl?biblionumber=125752>
- [17] I. Vurgaftman, J.R. Meyer, and L.R. Ram-Mohan, "Band parameters for III–V compound semiconductors and their alloys," *Journal of Applied Physics*, **89**, 5815-5875 (2001). <https://doi.org/10.1063/1.1368156>
- [18] R. Paessler, "Parameter Sets Due to Fittings of the Temperature Dependencies of Fundamental Bandgaps in Semiconductors," *Phys. Stat. Sol. (b)*, **216**, 975-1007 (1999). [https://doi.org/10.1002/\(SICI\)1521-3951\(199912\)216:23.3.CO;2-E](https://doi.org/10.1002/(SICI)1521-3951(199912)216:23.3.CO;2-E)

## ДО ТЕОРІЇ ВНУТРІШНЬОГО ОДНОФОТОННОГО ПОГЛИНАННЯ СВІТЛА У НАПІВПРОВІДНИКАХ ІЗ СТРУКТУРОЮ ЦИНКОВОЇ ОБМАНКИ

Рустам Ю. Расулов<sup>а</sup>, Воксоб Р. Расулов<sup>а</sup>, Форрух У. Касимов<sup>б</sup>, Махліїо А. Маматова<sup>а</sup>

<sup>а</sup>Ферганський державний університет, Фергана, Узбекистан

<sup>б</sup>Андижанський державний університет, Андижан, Узбекистан

Проведено теоретичний аналіз частотно-температурної залежності коефіцієнта однофотонного поглинання поляризованого випромінювання у вузько- та широкозонних напівпровідниках з урахуванням внутрішньозонних оптичних переходів та температурної залежності зонних параметрів. Показано, що при фіксованій частоті коефіцієнт однофотонного поглинання спочатку зростає з температурою, досягає максимуму, а потім зменшується. Максимальне значення зміщується в бік нижчих частот як для вузькозонних, так і для широкозонних напівпровідників при розгляді температурної залежності ширини забороненої зони та ефективної маси дірок. Визначено, що в напівпровідниках зі структурою ґратки цинкової обманки врахування температурної залежності параметрів зони призводить до зменшення амплітудного значення частотної та температурної залежності коефіцієнта однофотонного поглинання. З підвищенням температури поріг поглинання знижується, що помітно спостерігається при врахуванні формули Пасслера. Кожен тип оптичного переходу по-різному впливає на частоту, температуру та поляризаційні залежності  $K_{SO,th}^{(1)}(\omega, T)$ .

**Ключові слова:** температурна залежність параметрів зони; ширина забороненої зони; ефективна маса дірок; формула Пасслера та Варшні; вузько- та широкозонний напівпровідник; коефіцієнт однофотонного поглинання; ефект когерентного насичення

## ENHANCEMENT OF MOLECULAR STRUCTURAL AND LINEAR/NONLINEAR OPTICAL FEATURES OF CHITOSAN/TITANIUM DIOXIDE NANOCOMPOSITE FILMS FOR FOOD PACKAGING AND OPTOELECTRONIC APPLICATIONS

 Osiris W. Guirguis<sup>a\*</sup>, Najlaa D. Alharbi<sup>b</sup>

<sup>a</sup>*Biophysics Department, Faculty of Science, Cairo University, Giza, Egypt*

<sup>b</sup>*Department of Physical Sciences, College of Science, University of Jeddah, Jeddah, Saudi Arabia*

\*Corresponding Author e-mail: [osiris@sci.cu.edu.eg](mailto:osiris@sci.cu.edu.eg)

Received July 2, 2024; revised September 18, 2024; accepted October 9, 2024

The current study aims to synthesize and characterize nanocomposite films of chitosan and titanium dioxide in terms of molecular structure, thermal and optical properties for use in food packaging and optoelectronic applications. The Fourier-transform infrared (FTIR) spectroscopy was used to study the interaction between the TiO<sub>2</sub>-NPs and chitosan and the analysis confirmed that TiO<sub>2</sub>-NPs interacted with chitosan and demonstrated good compatibility. Differential scanning calorimetry and thermogravimetric analysis revealed that increasing the concentration of TiO<sub>2</sub>-NPs improved the thermal stability of the nanocomposites. The linear optical properties in the UV-Vis range (200–800 nm) were measured spectrophotometrically. Below 400 nm, the transmittance spectra of the nanocomposites show decreased degrees of transparency, indicating their capacity to entirely block UV-light transmission. Tauc's model was used to identify the types of electronic transitions in the samples. The single-oscillator model was utilized to investigate the dispersion energy and parameters. Nonlinear optical properties were also investigated. UV-Vis in the region (360-410 nm), the analysis revealed that increasing the concentration of TiO<sub>2</sub>-NPs from 0 to 12 wt% reduced the absorption edge from 2.716 to 2.043 eV, decreased the direct (3.282 to 2.798 eV) and indirect (2.417 to 1.581 eV) energy band gaps, increased the Urbach energy from 0.692 to 1.295 eV, decreased the dispersion energy from 11.324 to 5.621 eV, decreased the single oscillator energy from 6.308 to 5.393 eV, and improved the other linear and nonlinear parameters. The findings support the usage of CS/TiO<sub>2</sub> nanocomposite films in the packaging industry and a variety of optical applications.

**Keywords:** Chitosan; TiO<sub>2</sub> Nanoparticles; Chitosan/TiO<sub>2</sub> Nanocomposites; FTIR Analysis; Thermal Stability; Linear/nonlinear Optical Properties

**PACS:** 78.20.Ci; 36.20.Kd; 73.50.Gr; 77.22.\_d; 78.30.Jw

### 1. INTRODUCTION

Polymers and nanocomposites have grown in importance due to their wide range of applications, including photonics, biotechnology, packaging, drug delivery, and optoelectronics [1,2]. Overuse of synthetic polymers and nanocomposites in the packaging sector has become a severe global environmental problem in recent decades due to their nonbiodegradability [3,4]. The increasing concern about the environment has prompted the industry to try to replace non-biodegradable petrochemical-based plastics with biodegradable ones. Strategies for improving biopolymer characteristics involve matrix reinforcement. Some package optimization solutions have been proposed, including altering pack sizes and constructing active and intelligent packaging that preserves food quality while increasing shelf life [5,6]. Polymer/biopolymer composites, on the other hand, have been shown to function as passive or active optical components in optoelectronics [7,8]. Furthermore, nanocomposites are useful and have been used in a variety of sectors, including physical, biological, biomedical, and pharmacological applications. They can be utilized in films having a high index of refraction, thin film transistors, solar cells, light-emitting diodes, optical waveguides, and photochromic materials. Biopolymers derived from biomass, including proteins, polysaccharides, and biodegradable polymers, are commonly employed in the fabrication of bio-based films and thin membranes [9-11]. The combination of diverse polymers, organic and/or inorganic particles, and polymers is a strategic approach to improving material performance and enabling the creation of unique composite systems that increase the performance of the parent polymer. One way for creating a novel material with diverse properties is to mix solutions of several polymers together. These qualities are primarily determined by the properties of the original homopolymers as well as the compound makeup. Recently, there has been a hunt for newer materials for sophisticated technology that have fixed properties. Organic and polymeric materials have been the subject of much research as promising candidate media for optical information transmission, optical data storage, optical switching, and processing [12]. The organic compound has special applications, particularly in nonlinear optics (NLO), electronic/optoelectronic materials, and optical communication. All nonlinear optics research works to develop a material with good nonlinear optical (NLO) properties while also meeting all technological requirements [12,13]. NLO materials, which have a large nonlinear absorption coefficient that is primarily determined by the imaginary part of the third-order nonlinear susceptibility and a higher nonlinear refractive index that is directly related to the real part of the third-order nonlinear susceptibility, are used in optical limiting and optical switching technology [14].

Polysaccharides utilized to make edible films include cellulose, starch derivatives, pectin derivatives, seaweed extracts, microbial fermentation gums, and chitosan [15]. The future potential of biopolymers, particularly those derived from renewable resources, has long been recognized. These biopolymers are predominantly employed in the food industry. Biopolymers used as coatings in food packaging offer the benefits of being biocompatible, biodegradable, and increasing the quality of fresh foods while also being environmentally friendly packaging. Chitosan, a deacetylated derivative of chitin, is a well-known biopolymer and the second most abundant linear polysaccharide after cellulose [16-19]. Chitosan is a renewable substance derived from crustacean skeletons (crab, shrimp, and lobster), molluscan organs, the exoskeleton of marine zooplankton species such as coral and jellyfish, insect cuticles (butterflies and ladybugs), yeast cell walls, some mushroom envelopes, and fungi [20,21]. Chitosan's main-chain contains highly reactive hydroxyl ( $-OH$ ) and high-density amine ( $-NH_2$ ) groups, which can donate a free pair of electrons, make it soluble in diluted aqueous acetic solvents, and make it useful in a variety of applications and readily available for chemical reactions. Chitosan biopolymer is an attractive substance that is thought to be a great adsorbent due to its high nitrogen and oxygen content [22]. Chitosan can be made in a variety of geometries, including films, microspheres, nanospheres, and sponges. Chitosan's chemical and biological properties include being biocompatible with living tissues, biodegradable, bioadhesive, absorbable, nontoxic, a good film-forming biopolymer, naturally decomposed by body enzymes, and capable of binding to metal ions [23-26]. Chitosan's unique qualities make it useful in a wide range of biotechnological applications, including medical and environmental protection. It has been discovered in industrial and agricultural fields, either alone or in combination with other natural polymers [27-31]. Chitosan's polycationic structure makes it effective for immunoadjuvant, anti-thrombogenic, immunoenhancing, antitumoral, antiviral, antibacterial, antifungal, non-allergic, and anti-cholesteric properties [26,31,32]. Chitosan has been thoroughly researched for various potential uses including pharmaceutical, drug and gene delivery, dressings for wounds, treatment for cancer, burned skin, skin natural regeneration, functional coatings, beauty products, biological engineering, surgical tools, food industries, filtration of water for heavy metal adsorption, juice clarification and deacidification, food extended shelf life and preserving from microbial deterioration, food quality advancement, additives for food, and biodegradable packaging films formation [32-35]. Pieklarz and Modrzejewska [36] suggested that chitosan-based treatments could be used to prevent and treat viral infections, including COVID-19, due to their antiviral properties. The US-Food and Drug Administration (US-FDA) has designated chitosan as a generally recognized as safe (GRAS) food additive [28]. The hydrophilic characteristics of chitosan and other biopolymer films may limit their practical applications. Composite chitosan films exhibited superior hydrophobic properties compared to pure films [37]. Chitosan-based films, made through casting, can be utilized as active food packaging with added components and are considered safe food preservatives globally [28,32]. Combining chitosan with other biopolymers can increase its packaging material characteristics [38,39].

Nanoparticles (NPs) research has increased dramatically in recent years. Nanotechnology is concerned with the production and application of metal and metal oxide nanoparticles up to 100 nm in size. Because of their small size and unique features, metal and metal oxide nanoparticles have gained popularity in recent years. Nanoparticles have unique properties based on their size, shape, and morphology, allowing them to interact with plants, animals, and microbes [40-42]. Nanoparticles (NPs) are widely used in a variety of applications, including materials science, paints, agriculture, food industries, cosmetics, medicine delivery, and diagnostics [43,44]. They are also finding use in biomedicine, electronics, photography, optical electronics, optical data storage, information technology, biological sensing, and catalysis [21,43,45,46]. Inorganic metal NPs such as Fe, Cu, Ti, Ag, Au, Pt, and Zn, as well as metal oxide NPs such as CaO, CuO, ZnO, FeO, SiO<sub>2</sub>, and TiO<sub>2</sub>, have been shown to be potentially useful compounds due to their appealing characteristics [28,44,47,48]. The dispersion of nanoparticles in the polymer matrix is critical for increasing structural, optical, and mechanical properties. TiO<sub>2</sub> is a flexible and chemically inert metal oxide that has shown promise due to its photocatalytic activity, high chemical stability, cheap cost, biocompatibility, and antibacterial properties [5,49,50]. TiO<sub>2</sub> is commonly employed in a variety of applications, including medicinal, biomedical, antibacterial, ethylene scavenger, ecological, and clean energy [28,51]. In addition, the US-FDA has approved TiO<sub>2</sub> for use in human food, medicines, and products that contact food [52]. When being subjected to UV-light at wavelengths <385 nm, TiO<sub>2</sub> produces reactive oxygen species like hydroxyl radicals ( $\cdot OH$ ), and superoxide ions ( $O_2^{\cdot -}$ ), capable of destroying microbial cells and killing microorganisms, as well as ethylene ultraviolet degradation [28]. According to Mohammad et al. [43], TiO<sub>2</sub>-NPs and ZnO-NPs effectively scatter UV radiation and have been found to be particularly useful as UV blockers, which assist in protecting against skin cancer caused primarily by UV radiation, as well as photocatalysts in solar cells, exhibits and detectors, photosynthesis, and sunlight protection. Numerous research has reported that TiO<sub>2</sub> nanoparticles at low content ( $\leq 5\%$ ) can enhance the physical-thermal properties of biocomposite films [28,31,53]. TiO<sub>2</sub>-NPs have attracted consideration in the oil and gas industry because of their potential for purifying water and, more recently, as additives in recovery fluids to improve current improved oil recovery methods by modifying the surface tension or interfacial interactions [54-57]. One of the main downsides of TiO<sub>2</sub>-NPs is their propensity to agglomerate, which reduces their photocatalytic ability [28]. According to Anaya Esparza et al. [51], the interaction of TiO<sub>2</sub>-NPs with biopolymers such as starch, gums, and chitosan can aid to minimize TiO<sub>2</sub> spontaneous agglomeration, hence improving the functional aspects of composites.

On the other hand, the antibacterial, moisturizing, mechanical, and antioxidant capabilities of pure chitosan film have been deemed inadequate in practical applications. To overcome these limitations, metal oxide NPs were added

during film creation to create chitosan-based composite films with good physicochemical and biological properties [5,58,59]. Thus, composite films made of chitosan reinforced with nanoparticles have received a lot of attention for a variety of applications [11,15]. Recently, there has been a surge of interest in hybrid composites and their prospective applications, particularly CS/TiO<sub>2</sub> nanocomposites, which have intriguing technical characteristics as well as potential applications [5,24,51]. A number of research studies have reported that incorporating TiO<sub>2</sub>-NPs into chitosan raised hydrophilicity, enhanced the mechanical characteristics of the composite film, reduced the transmission of light in the range of visible light, and indicated to be announcing composites in a variety of applications [5,28,51,60-63]. These CS/TiO<sub>2</sub> nanocomposites have applications in the biomedical field as scaffolding compounds for liver tissue engineering, clinical skincare as functional antimicrobial substances such as photobacteriocidal and artificial skin alternatives, restored tissues, healing of wounds, cancer detection and therapy, developed delivery of drugs, operating aids, and biological sensors for extracted fruits [31,43,51,64]. Razzaz et al. [65] and Spoyală et al. [66] observed that CS functionalized with TiO<sub>2</sub> nanoparticles displayed adsorbent properties for treating wastewater for the elimination of heavy metal ions; Saravanan et al. [67] reported that CS/TiO<sub>2</sub> nanocomposites showed great effectiveness in degrading against methyl orange dye; Kaewklin et al. [17] achieved success in fabricating CS/TiO<sub>2</sub> nanocomposite films for tomato conservation; and Siripatrawan and Kaewklin [64] created and analyzed multifunctional active packaging for food using CS/TiO<sub>2</sub> nanocomposites for use as an antibacterial film in postharvest uses for preserving fresh produce.

In order to achieve the current study's objective, and in continuation of previous studies, especially by the same author(s), which were published previously, and with the addition of some theoretical analyses of the results obtained for the possibility of applying these compounds in many medical and industrial fields, the solution casting process was used for preparing pure CS and CS/TiO<sub>2</sub> nanocomposite films with various TiO<sub>2</sub>-NP concentrations (4, 8, and 12 wt%). The molecular structure of the films was examined with the FTIR technique. DSC and TGA/DTGA thermograms were used to assess the thermal stability of the films. The kinetic parameters were evaluated using the Coat-Reffdern method. The optical characteristics of the produced nanocomposite films were measured spectroscopically in the UV-Vis range (200-800 nm). The linear optical parameters, including absorption coefficient ( $\alpha$ ), extinction coefficient ( $K$ ), and refractive index ( $n$ ), as well as dispersion parameters such as dispersion energy ( $E_d$ ) and average energy gap ( $E_o$ ), were determined. The films' nonlinear optical properties, including third-order susceptibility ( $\chi^{(3)}$ ), refractive index ( $n_2$ ), and absorption coefficient ( $\beta_c$ ), were also evaluated. The results were discussed, and the potential for employing the produced nanocomposite films in biodegradable food packaging and optoelectronic applications was investigated.

## 2. EXPERIMENTAL PART

### Materials and preparation of CS and CS/TiO<sub>2</sub> nanocomposite films

Chitosan (CS) powder with a molecular weight of 900 kg.mol<sup>-1</sup>, particle size >100 mesh, deacetylation >75%, free of *E. coli* and *Salmonella*, creamy white color, odorlessness, and purity >98% was acquired from Avondale Laboratories Supplies & Services Ltd. Titanium dioxide (TiO<sub>2</sub>) nanopowder with a particle size <100 nm (catalog number 718467), white color, and purity >99% was supplied from Sigma-Aldrich (China). Glacial acetic acid was obtained from Avondale Laboratories Supplies & Services Ltd. (Banbury, UK).

The film casting technique was used to manufacture pure chitosan (CS) and CS/TiO<sub>2</sub> nanocomposite films [5,8,50]. To prepare the chitosan (CS) film, dissolve 1 g of chitosan powder in 100 mL of a 1% (v/v) acetic acid aqueous solution. Stir continuously with a magnetic stirrer (100 rpm) for 24 hours at room temperature (~25°C). Filtration was used to remove the insoluble masses from the dissolved solution. CS thin films were produced by casting the solution onto Petri dishes and drying in an oven at 40°C for 48 hours before peeling off from the plate. For the preparation of the CS/TiO<sub>2</sub> nanocomposite films, various weights of TiO<sub>2</sub>-NPs (0.04 g, 0.08 g, and 0.12 g) were added to the as-prepared CS solutions. The solutions were thoroughly mixed before being sonicated for 1 hour using a digital ultrasonic cleaner (CD-4820 170W/42 kHz, China) to eliminate agglomeration and achieve homogeneous solutions [5,8]. The solutions were then poured into Petri dishes and dried in an oven at 40°C for 48 hours. After drying, the films were gently removed from the plates and stored in vacuum desiccators at room temperature until

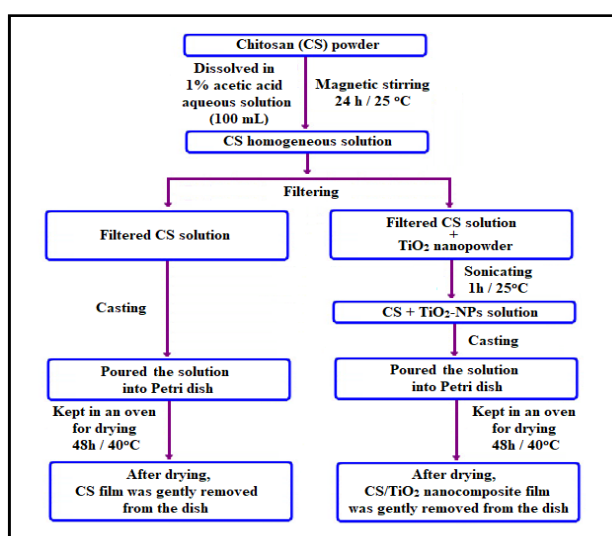


**Figure 1.** Flowchart of the process used to prepare CS and CS/TiO<sub>2</sub> nanocomposite films by casting technique

used. The thicknesses of the films were measured using an Insize 3109-25A Digital External Micrometer (China) with an accuracy of  $\pm 2 \mu\text{m}$ , covering a range of 0-25 mm. Figure 1 depicts a schematic of the casting technique employed in the current study to produce pure chitosan (CS) and CS/TiO<sub>2</sub> nanocomposite films.

### Characterization methods

FTIR absorption spectra of CS and CS/TiO<sub>2</sub> nanocomposite films were measured using a Fourier transform infrared spectrometer (Nicolet-380, UK). Spectra were acquired in the 4000-400 cm<sup>-1</sup> range at room temperature using 32 scans, with a resolution of 4 cm<sup>-1</sup> and an accuracy of ±1%.

The differential scanning calorimetry (DSC) of the manufactured films was carried out with a differential scanning calorimeter (Shimadzu DSC-50, Japan) with a measuring temperature range of 25 to 650°C. Thermogravimetric analysis (TGA/DTGA) of the films was performed using a thermogravimetric analyzer (Shimadzu TGA-50H, Japan) with a measuring temperature range of 25-750°C. The thermograms were recorded in an atmosphere of nitrogen with a flow rate of 30 cm<sup>3</sup>·min<sup>-1</sup> and a heating rate of 10°C·min<sup>-1</sup>. The starting sample weight was around 6.5 mg. The temperature at the maximum decomposition rate (T<sub>m</sub>) and weight loss (%) were estimated for each decomposition stage for the samples using TGA and DTGA thermograms. Each sample was packed snugly into an aluminum pan, with an empty pan acting as a reference. Prior to analysis, the equipment was calibrated with calcium oxalate as a standard reference.

The UV-Vis optical absorbance, transmittance, and reflectance spectra of the prepared films were recorded at room temperature using a UV-Vis-NIR double beam spectrophotometer (Shimadzu V-530, Japan) covering the range 200–2500 nm with standard illumination "C" and a 2 nm bandwidth with accuracy ±0.05%. The collected spectra were used to determine linear and nonlinear optical characteristics, as well as related parameters.

## 3. RESULTS AND DISCUSSION

### Fourier transform infrared (FTIR) spectroscopy

To determine the potential interaction between the TiO<sub>2</sub>-NPs and the CS chains, FTIR spectra have been recorded in the 4000-400 cm<sup>-1</sup> region. A comparison of the FTIR absorption spectra of pure CS and CS/TiO<sub>2</sub> nanocomposite films is shown in Figure 2.

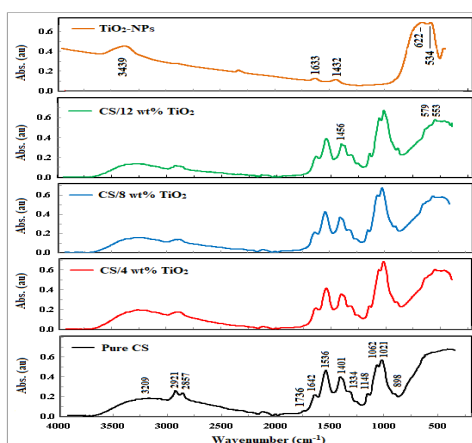


**Figure 2.** FTIR absorbance spectra of pure CS and CS/TiO<sub>2</sub> nanocomposite films

The FTIR spectra were in agreement with those previously reported by other researchers [32,37,39,45,51,55,64,66,68]. The broad absorption peak centered at around 3209 cm<sup>-1</sup> was assigned to stretching vibrations of the hydroxyl (–OH) and amine (–NH) groups. The two peaks between 3000 and 2800 cm<sup>-1</sup> (asymmetric at ~2921 cm<sup>-1</sup> and symmetric at ~2857 cm<sup>-1</sup>) were due to the C–H stretching vibration of the methyl group. The peak at ~1642 cm<sup>-1</sup> was corresponded to C=O stretching vibration (amide I). The peak at ~1536 cm<sup>-1</sup> was due to in plane N–H bending vibration (amide II). The peak at ~1401 cm<sup>-1</sup> was assigned to deformation vibrations of C–H and –OH groups. The peaks in the range of 1150–1000 cm<sup>-1</sup> were corresponded to asymmetric of C–O–C (at ~1148 cm<sup>-1</sup>) and symmetric C–O (at ~1062 cm<sup>-1</sup>) stretching vibrations. The peak at ~1021 cm<sup>-1</sup> was assigned to C–O stretching vibration, and also indicated bending vibration of Ti–O–C. The weak peak at ~898 cm<sup>-1</sup> was due to C–H stretching of the glycoside linkage and N–H (amide III). A shoulder corresponding to C–N stretching (amide III) at around 1334 cm<sup>-1</sup> was observed. Furthermore, Hussein et al. [50] and Filippo et al. [69] identified two characteristic absorption peaks at approximately 1532 and 1456 cm<sup>-1</sup>, corresponding to the symmetric and asymmetric stretching vibrations of the carboxyl groups, respectively. The figure also showed that all of the produced nanocomposite films had remarkably similar spectra, with mostly of the peak characteristic of the CS film. The FTIR spectra of pure CS and CS/TiO<sub>2</sub> nanocomposites show separate peaks for both CS and TiO<sub>2</sub>-NPs in the composite. The spectra of the nanocomposites showed that the broader and stronger peak shifted somewhat to lower wavenumbers. The changes in spectra between the pure CS sample and the CS/TiO<sub>2</sub> nanocomposites revealed the interaction between CS and TiO<sub>2</sub>-NPs due to minor differences in angles, bonding energies, internal stresses, and crystal level during the formation of the nanocomposites. As the concentration of TiO<sub>2</sub>-NPs in the film increased, so did the small peaks at low wavenumbers in the range 700-500 cm<sup>-1</sup> (at about 523-504 cm<sup>-1</sup> and at ~680 cm<sup>-1</sup>), indicating the bending vibration of Ti–O–Ti for the interactions of CS–TiO<sub>2</sub> [50,64,66]. A new shoulder was appeared at around 579 cm<sup>-1</sup> belongs to the amide group and a new peak at ~553 cm<sup>-1</sup> was formed corresponding to the

stretching group. This demonstrated that that –OH and/or –NH<sub>2</sub> from the CS chains can interact with the acidic groups of the TiO<sub>2</sub>-NPs to establish covalent bonds or hydrogen bonds, hence improving TiO<sub>2</sub> nanoparticle incorporation in the CS matrix [5,28,70]. The findings suggest that TiO<sub>2</sub>-NPs are primarily incorporated into the CS matrix in the amorphous area of chitosan [51,64].

The degree of structural organization of the films under study was evaluated using the following IR indices [71,72]: (1) the total crystallinity index (TCI), which provides the crystallinity ratio; (2) the lateral order index (LOI), which correlates the number of crystalline components and amorphous regions in the sample; and (3) the hydrogen bond intensity (HBI), which connects the crystalline structure and the degree of homogeneity of the molecules as measured by chain movement and bonding distance. TCI, LOI, and HBI can be assessed using the following relationships [73,74]:

$$\text{TCI} = \frac{H_{1336}}{H_{2896}}, \quad \text{LOI} = \frac{Ar_{1427}}{Ar_{896}}, \quad \text{and} \quad \text{HBI} = \frac{A_{3333}}{A_{1336}} \quad (1)$$

where  $H_{1336}$  and  $H_{2896}$  are the band heights of the O–H bending and C–H stretching vibrations, respectively, at 1336 and 2896  $\text{cm}^{-1}$ ;  $Ar_{1427}$  and  $Ar_{896}$  are the areas of the bands at 1427 and 896  $\text{cm}^{-1}$ , respectively, which correspond to O–H, C–H bending, –CH<sub>2</sub> deformation, C–O deformation, and –CH<sub>2</sub> rocking;  $A_{3333}$  and  $A_{1336}$  are the absorbance of the bands at 3333 and 1336  $\text{cm}^{-1}$ , which correspond to the O–H stretching and bending vibration modes, respectively. Furthermore, the energy of the hydrogen bond ( $E_H$ ) of the –OH stretch group was determined with the following formula [71,72,74]:

$$E_H = \left( \frac{1}{K} \right) \left( \frac{\nu_o - \nu}{\nu_o} \right) \quad (2)$$

where  $K$  is a constant ( $= 3.8095 \times 10^{-6} \text{J}^{-1}$ ),  $\nu_o$  is the standard frequency of the free –OH group at 3650  $\text{cm}^{-1}$ , and  $\nu$  is the frequency of the bound –OH group of the sample. Table 1 shows the calculated values for the IR indices (TCI, LOI, and HBI), as well as  $E_H$ . It was discovered that the CS/12 wt% TiO<sub>2</sub> nanocomposite exhibited greater TCI and HBI values and a lower LOI value than other nanocomposites when compared to the pure CS sample, indicating decreased crystallinity. This observed tendency can be related to the differences in accessibility of the discrete crystalline and amorphous areas of the film, as well as its key chemical components. The table shows no discernible change (~5%) in  $E_H$  values between nanocomposites and pure CS samples. The presence of TiO<sub>2</sub>-NPs on the CS network, as well as the formation of hydrogen bonds between CS and TiO<sub>2</sub>-NPs, which increase the extent of hydrogen bonding between molecules in the CS, can be attributed to changes in the IR indices and  $E_H$  of the prepared nanocomposites [71,72].

**Table 1.** Values of TCL, LOI, HBI, and  $E_H$  for pure CS and CS/TiO<sub>2</sub> nanocomposites

Sample	TCL	LOI	HBI	$E_H$ (kJ)
Pure CS	0.8293	48.3333	0.5751	31.6986
CS/4wt% TiO <sub>2</sub>	1.1515	14.9608	0.5859	30.4212
CS/8wt% TiO <sub>2</sub>	1.2074	12.2963	0.6226	30.3583
CS/12wt% TiO <sub>2</sub>	1.4520	8.0494	0.7641	30.2668

### Thermal properties

One of the most practical techniques for determining the miscibility and thermal properties of composite polymers was differential scanning calorimetry (DSC) [50]. Figure 3 depicts the DSC thermograms obtained to investigate the thermal behavior of pure CS and CS/TiO<sub>2</sub> nanocomposites. It was obvious that all films disintegrated in similar way up to 600°C.

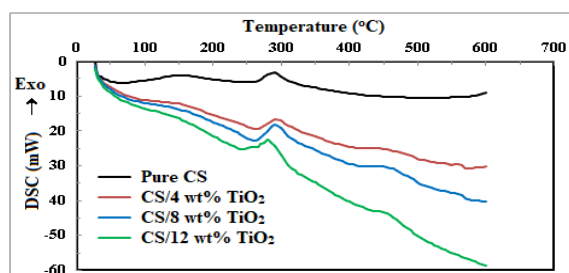


**Figure 3.** DSC thermograms of pure CS and CS/TiO<sub>2</sub> nanocomposite films

The thermogram for pure CS can be analyzed as follows: a broad endothermic peak between 25 and 125°C and an exothermic peak between 260 and 320°C [50,66]. The endothermic peak at ~65°C may be owing to the evaporation of water absorbed by the hydrophilic groups of chitosan [24]. The exothermic peak had a decomposition temperature of around 290°C, may be due to thermal decomposition of CS [24,66,75]. Furthermore, the thermograms of the

nanocomposite samples revealed one endothermic peak between 25 and 125°C and two exothermic peaks. The exothermic maxima ranged from 240 to 320°C and 420 to 480°C. The endothermic initial stage resulted in the loss of largely adsorbed water molecules. When TiO<sub>2</sub>-NPs are dispersed in the CS matrix, the intensities of the exothermic peaks increase, which may correspond to weight loss caused by polysaccharide disintegration and loss of the hydroxyl group [50,76]. The area under the peak rose, indicating that the enthalpy of melting decreased as the amount of TiO<sub>2</sub>-NPs increased. The decomposition temperature of the second stage shifts toward lower temperatures, showing the establishment of an intermolecular interaction and variation in internal mechanisms caused by the induced influence of TiO<sub>2</sub>-NPs on the CS structure of the network.

Thermogravimetric analysis (TGA) is an extremely useful tool for determining the heat stability of polymers and nanocomposites [50,77,78]. Chitosan is highly sensitive to several types of degradation, including heat decomposition [11,24]. Figure 4 shows the TGA (a) and DTGA (b) thermograms of pure CS and CS/TiO<sub>2</sub> nanocomposite films at temperatures ranging from 25 to 750°C.

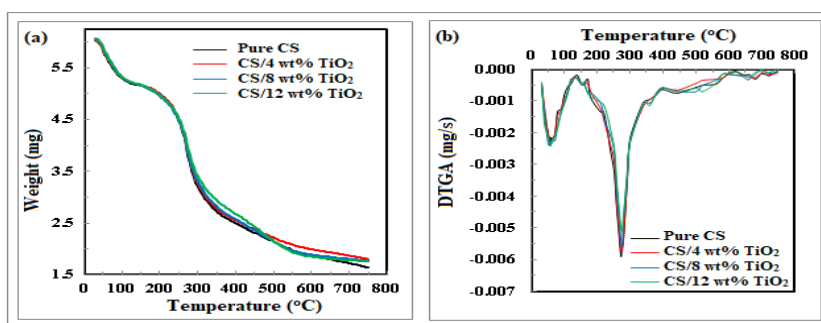


**Figure 4.** (a) TGA and (b) DTGA thermograms of pure CS and CS/TiO<sub>2</sub> nanocomposite films

DTGA curves represent the rate of weight loss during thermal degradation. Pure TiO<sub>2</sub>-NPs in powder form remain stable up to 750°C (no curve depicted) [79]. As shown in Figure 4a, all films followed a similar decomposition approach, and the TGA thermograms reveal three stages of weight change [5,50,77,78]. A small weight loss was observed between 25 and 110°C, followed by a steady weight loss above 150 to 750°C. When the temperature reached 110°C, the weight loss during the first decomposition stage was approximately 13 to 10% of the original weight, which could be attributed to the vaporization of absorbed water and residual acetic acid in the polymer matrix [24,77,78,80]. Water absorption in the CS/TiO<sub>2</sub> nanocomposite was related to the presence of hydroxyl and amino groups, which interact with water molecules via hydrogen bonding. The second decomposition stage is more intense thermal deposition, which occurs at temperatures ranging from 150 to 400°C and results in a rapid weight loss of 44 to 42%, which could be attributed to the thermal and oxidative decomposition of the CS matrix (the main component of the nanocomposite) [66,80]. At temperatures above 400 to 750°C, films incorporating TiO<sub>2</sub>-NPs experienced a third degradation step, resulting in a weight loss of around 16%. As previously described by Corazzari et al. [75], a crucial process connected with the pyrolytic disintegrate of chitosan was demonstrated in the temperature range of 200–450°C and entailed the release of H<sub>2</sub>O, NH<sub>3</sub>, CO, CO<sub>2</sub>, and CH<sub>3</sub>COOH. The second and third thermal stages may be caused by chain fragmentation, saccharide ring degradation, depolymerization, and the disintegration of acetylated and/or deacetylated chitosan units [8,80,81]. DTGA curves in Figure 4b show more accurate differences in the thermal behavior of CS and CS/TiO<sub>2</sub> nanocomposite films. Nearly no remarkable variation exists in the DTGA peak positions. The DTGA peak temperature of the pure CS sample was ~273°C [24], while the CS/TiO<sub>2</sub> nanocomposite had a peak temperature of ~274°C. Table 2 summarizes the maximum temperature (T<sub>M</sub>), weight loss (%), total weight loss (%), and residual weight (%) values for CS and CS/TiO<sub>2</sub> nanocomposites at the three degradation stages. The residual weight of nanocomposites rose as the concentration of TiO<sub>2</sub>-NPs increased, indicating that the presence of TiO<sub>2</sub>-NPs changes the degradation mechanism of the CS matrix. Additionally, the nanocomposite films were more thermally stable than the CS sample. Many earlier studies have reported similar behavior [8,24,50,80]. In general, these findings validated the inclusion of TiO<sub>2</sub>-NPs in the CS matrix of the produced films, which increases the thermal stability of the nanocomposite, and revealed that thermal stability was directly proportional to nanoparticle concentration.

**Table 2.** Maximum temperature (T<sub>M</sub>), the weight loss (%) for the three decomposition stages, the total weight loss (%), and the residual weight (%) of pure CS and CS/TiO<sub>2</sub> nanocomposites

Sample	First stage (25–110 °C)		Second stage (110–400 °C)		Third stage (400–750 °C)	Total weight loss (%)	Residue (%)
	T <sub>M</sub> (°C)	Weight loss (%)	T <sub>M</sub> (°C)	Weight loss (%)	Weight loss (%)		
Pure CS	58.054	12.633	273.084	43.539	16.460	72.632	27.368
CS/4 wt% TiO <sub>2</sub>	58.054	11.008	273.934	42.845	16.270	70.123	29.877
CS/8 wt% TiO <sub>2</sub>	58.054	10.328	273.934	42.747	16.755	69.830	30.170
CS/12 wt% TiO <sub>2</sub>	57.044	10.192	273.934	41.710	16.258	68.160	31.840

**Kinetics of thermal decomposition**

There is a growing interest in producing thermoplastic biopolymers, particularly those generated from renewable sources, for use in a variety of applications, including food packaging and optoelectronic devices. The TGA/DTGA technique plays an essential role for determining the decomposition processes, temperature, and kinetic characteristics of solid materials. The kinetics of thermal degradation processes were represented using different equations that took into account the unique properties of their mechanisms [8,82]. The activation energy for the primary thermal decomposition for TGA measurements can be calculated using the Coats and Redfern equation as follows [8,83]:

$$\ln\left(\frac{-\ln(1-g)^{1-n}}{T^2}\right) = -\frac{E_a}{RT} + \ln\left(\frac{fR}{qE_a}\right), \tag{3}$$

where T is the absolute temperature, g is the fractional weight loss at the specific temperature (T), n is the order of reaction, E<sub>a</sub> is the activation energy, R is the universal gas constant (= 8.31445 J.K<sup>-1</sup>.mol<sup>-1</sup>), q is the linear heating rate (dT/dt), and f is the frequency factor. The values of f and g can be estimated using the following formulae [8,82]:

$$g = \frac{w_i - w_T}{w_i - w_f}, \tag{4}$$

$$f = \frac{\gamma e k_b T_M}{h} \exp\left(\frac{\Delta S}{R}\right), \tag{5}$$

where w<sub>i</sub>, w<sub>T</sub>, and w<sub>f</sub> are the initial mass, current mass at temperature T, and final mass of the sample, respectively, T<sub>M</sub> is the maximum temperature of the decomposition stage, γ is the transmission coefficient (=1 for monomolecular reaction), e is the Neper number (=2.7183), h is the Planck's constant (=6.6261×10<sup>-34</sup> J.s), k<sub>B</sub> is the Boltzmann's constant (=1.3806×10<sup>-23</sup> J.K<sup>-1</sup>), and ΔS is the entropy activation. For n ≠ 1, Eq. 3 can be rewritten as [8,82,83]:

$$\ln\left(\frac{-\ln(1-g)}{T^2}\right) = -\frac{E_a}{RT} + \ln\left(\frac{fR}{qE_a}\right). \tag{6}$$

Using Equation 5, ΔS can be estimated as follows [8]:

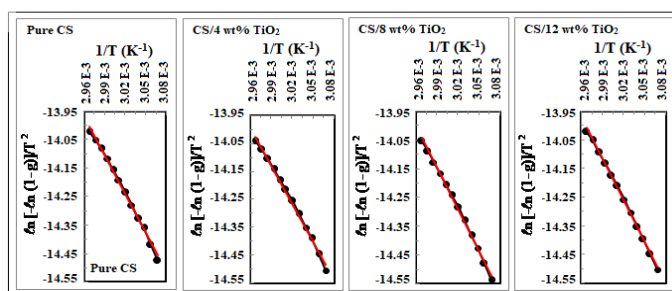
$$\Delta S = R \ln\left(\frac{fh}{\gamma e k_b T_M}\right). \tag{7}$$

The thermodynamic equations are used to compute the enthalpy activation (ΔH) for total thermal motion and the Gibbs free energy (ΔG) for system stability as follows [8]:

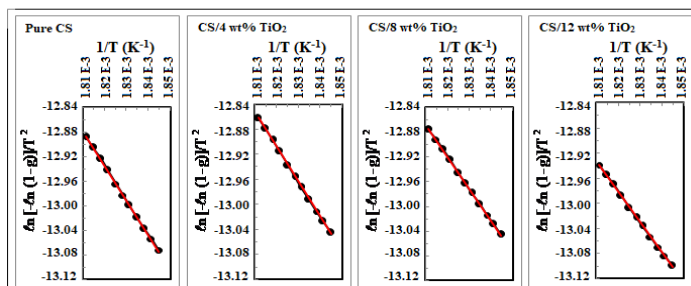
$$\Delta H = E_a - RT_M, \tag{8}$$

$$\Delta G = \Delta H - T_M \Delta S. \tag{9}$$

Figures 5 and 6 show the fluctuation of  $\ln[-\ln(1-g)]/T^2$  against 1/T for pure CS and CS/TiO<sub>2</sub> nanocomposites throughout the first and second breakdown stages.



**Figure 5.**  $\ln[-\ln(1-g)]/T^2$  against 1/T in the first decomposition stage for pure CS and CS/TiO<sub>2</sub> nanocomposite films



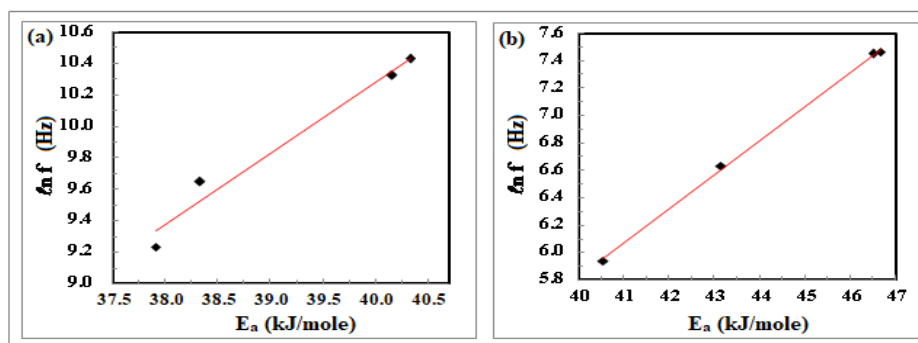
**Figure 6.**  $\ln[-\ln(1-g)]/T^2$  against 1/T in the second decomposition stage for pure CS and CS/TiO<sub>2</sub> nanocomposite films

Table 3 summarizes the values of activation energy ( $E_a$ ) and frequency factor ( $f$ ) for all films based on the slope, intercept, and regression ( $r^2$ ) of the fitted straight lines of each degradation stage. The values of  $\Delta S$ ,  $\Delta H$ , and  $\Delta G$  were computed using Equations. 7-9 and were listed in the table. The data in the table showed that the calculated activation energy values ( $E_a$ ) of the nanocomposite samples increased in the first decomposition stage and decreased in the second as the TiO<sub>2</sub>-NPs content increased, indicating that the nanocomposite sample had some form of chemical and/or physical rearrangement of the initial structure, bringing it into thermodynamic equilibrium.

**Table 3.** The kinetic parameters for of pure CS and CS/TiO<sub>2</sub> nanocomposites based on CR approach

Sample	$E_a$ (kJ.mol <sup>-1</sup> )	$f$ (Hz)	$r^2$	$\Delta S$ (kJ.mol <sup>-1</sup> .K <sup>-1</sup> )	$\Delta H$ (kJ.mol <sup>-1</sup> )	$\Delta G$ (kJ.mol <sup>-1</sup> )
First decomposition stage						
CS	37.906	$1.023 \times 10^4$	0.995	-0.177	35.145	94.049
CS/4wt% TiO <sub>2</sub>	38.330	$1.546 \times 10^4$	0.995	-0.174	35.577	93.151
CS/8wt% TiO <sub>2</sub>	40.159	$3.057 \times 10^4$	0.996	-0.168	37.406	93.1041
CS/12wt% TiO <sub>2</sub>	40.334	$3.379 \times 10^4$	0.998	-0.167	37.581	93.002
Second decomposition stage						
CS	46.669	$1.748 \times 10^3$	0.999	-0.196	42.129	149.269
CS/4wt% TiO <sub>2</sub>	46.503	$1.724 \times 10^3$	0.999	-0.197	41.956	149.332
CS/8wt% TiO <sub>2</sub>	43.1439	$0.759 \times 10^3$	0.999	-0.203	38.596	149.706
CS/12wt% TiO <sub>2</sub>	40.542	$0.380 \times 10^3$	0.999	-0.209	35.994	150.251

According to the kinetic data from the DTGA curves (Figure 4b) and the data in Table 3, all of the nanocomposites exhibit negative activation entropy values, confirming that the generation of activated complexes is directly related to entropy variation. The association between  $E_a$  and  $f$  values in Table 3 verified the existence of the compensating phenomena, also known as the isokinetic effect [82] as illustrated in Figure 7a and b.



**Figure 7.** Frequency factor ( $f$ ) versus the activation energy ( $E_a$ ) in (a) first and (b) second decomposition stages for pure CS and CS/TiO<sub>2</sub> nanocomposite films

Figure 8a and b demonstrates a linear relationship between ( $\Delta S$ ) and ( $\Delta H$ ), indicating the presence of the compensating phenomena in CS/TiO<sub>2</sub> nanocomposites. This linear relation may be due to structural changes that occur when increasing the temperature of the polymeric material to achieve equilibrium. A similar tendency has already been seen for other polymer composites [8,84,85]. The acquired results could be employed in thermal degradation optimization, as well as to improve the thermal stability of the nanocomposite under examination, potentially leading to intriguing technological applications.

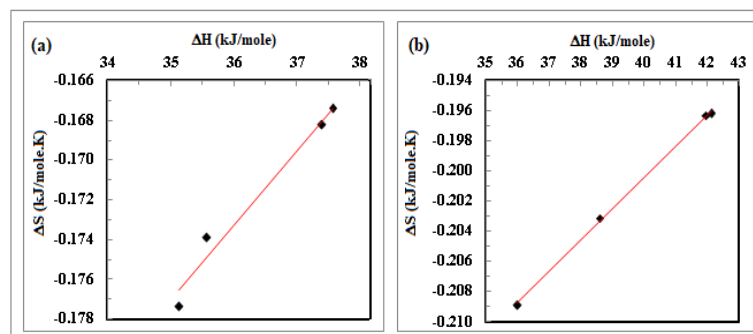


**Figure 8.**  $\Delta S$  versus  $\Delta H$  in (a) first and (b) second decomposition stages for pure CS and CS/TiO<sub>2</sub> nanocomposite films

#### UV-Vis optical characterization

The study of optical properties has significance for understanding the nature of materials utilized in food packaging and electrooptical applications. UV-Vis optical absorption spectra are one of the most effective tools for

revealing significant information about the films under investigation. Figure 9a depicts the absorption spectra of pure CS and CS/TiO<sub>2</sub> nanocomposites in the UV-Vis range of 200 to 800 nm.

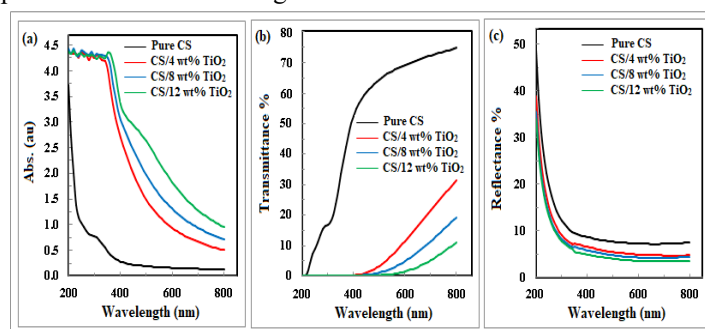


**Figure 9.** (a) Absorbance, (b) transmittance, and (c) reflectance spectra against wavelength for pure CS and CS/TiO<sub>2</sub> nanocomposite films

The absorption spectra for the films may be separated into two regions: 1) the first zone of significant absorption occurs between 200 and 360 nm, and 2) the second region of the absorption edge begins between 360 and 800 nm. The absorption spectra of pure CS decrease rapidly in the UV region as the wavelength increases, with an absorption shoulder centered at ~290 nm, corresponding to the forbidden  $n \rightarrow \pi^*$  transition. The absorbance decreases slightly in the visible range. As the amount of TiO<sub>2</sub>-NPs in the nanocomposite film grows, the UV absorbance rises significantly, and the shoulder shifts to a longer wavelength. A new peak of TiO<sub>2</sub>-NPs was identified at ~352 nm in the CS/12 wt% TiO<sub>2</sub> nanocomposite sample. This observation implies that the TiO<sub>2</sub>-NPs and CS matrix are complexed via hydrogen bonding via OH groups [45]. In the visible region, absorbance increased as compared to pure CS film. This improvement is due in significant part to the addition of TiO<sub>2</sub>-NPs at a concentration of 12 weight %. These observed increases in absorbance across the entire UV-Vis range (200-800 nm) can be attributed to an increase in composite film density, which leads to an increase in refractive index due to increased polarization. Figure 9b and c shows the spectrum characteristics of the optical transmittance and reflectance, respectively, of the produced films. Figure 9b indicates that the CS spectrum in the UV zone has transmittance values ranging from ~0.02 at 200 nm to ~38% at 360 nm. According to Souza et al. [3], chitosan film is an effective UV light barrier and they reported that T% values at 200 and 360 nm were approximately 0.02 and 38%, respectively. The spectra of the CS/TiO<sub>2</sub> nanocomposites show transmittance values close to 0% in the UV spectrum. The inclusion of TiO<sub>2</sub>-NPs changed the barrier block at longer wavelengths. The optical transparency of the CS/12wt% TiO<sub>2</sub> nanocomposite decreased to ~0.005% at 360 nm, and UV light was nearly completely blocked. One of the most essential features of films designed for various food packaging categories is their UV-visible light barrier [3,86]. The acquired data reveal that all of the nanocomposite films under research have UV-blocking properties, making them suitable barriers against UV radiation and enhancing the shelf-life of light-sensitive foods by avoiding photo-oxidation [28,64]. Additionally, Figure 9a and b shows a considerable rise in absorption and decrease in transmittance across the whole spectrum as the concentration of TiO<sub>2</sub>-NPs increased. This result could be attributable to a decrease in film transparency caused by variations in molecular composition [50]. Incorporating TiO<sub>2</sub>-NPs with CS in the film matrix resulted in increased adsorption capacity in the visible region. As a whole, including TiO<sub>2</sub>-NPs into the CS network dramatically reduces UV transmission, making them extremely useful for applications that require UV protection, photocatalytic characteristics, and antibacterial effects when exposed to UV light. In the visible range (400-800 nm), the decrease in transmittance as TiO<sub>2</sub>-NPs concentration increases may be explained by the possibility of increasing TiO<sub>2</sub>-NPs agglomeration, which may prevent light transformation throughout the film due to TiO<sub>2</sub>-NPs incorporation into the CS matrix [18,87]. Figure 9c displays the reflectance spectra of the prepared films. The reflectance values declined as the amount of TiO<sub>2</sub>-NPs increased. This could be attributed to the inclusion of TiO<sub>2</sub>-NPs in the CS network, which resulted in reduced reflection due to the smaller sizes of the nanoparticles relative to the wavelength of visible light, indicating low light scattering ability [28,50].

The opacity and transparency of composite films possess important characteristics, particularly when they are intended for use as food packaging materials. The opacity and transparency of pure CS and CS/TiO<sub>2</sub> nanocomposites can be determined using the following relationships [3,18,86]:

$$\text{Opacity} = \frac{A_{600}}{d}, \quad (10)$$

$$\text{Transparency} = \frac{-\log(\%T_{600})}{d}, \quad (11)$$

where  $A_{600}$  is the absorbance at 600 nm,  $\%T_{600}$  is the percentage transmittance at 600 nm, and  $d$  is the film thickness in millimeters. Table 4 presents a comparison of the opacity and transparency values of pure CS and CS/TiO<sub>2</sub> nanocomposites. As noted, the higher the opacity value, the lower the transparency of the film. The opacity value of pure CS film is  $1.601 \text{ mm}^{-1}$ , which increases considerably as the amount of TiO<sub>2</sub>-NPs increases, reaching a maximum of  $18.336 \text{ mm}^{-1}$  for the CS/12 wt% TiO<sub>2</sub> nanocomposite. Transparency values reduced dramatically from  $30.666$  to  $2.774 \text{ mm}^{-1}$  when the concentration of TiO<sub>2</sub>-NPs was raised from 0 to 12 wt%. This rise in opacity (reduction in

transparency) values was caused by the interaction of TiO<sub>2</sub>-NPs with the CS matrix, which is responsible for the compact and higher polymeric chain network that prevents the passage of UV and visible light. These findings can be explained by the fact that when TiO<sub>2</sub>-NPs interacted with CS chains, a discontinuity formed in the CS matrix, resulting in a more disordered structure [3,18,86].

Measurements of optical transmittance (T) and reflectance (R) were utilized to evaluate optical parameters, including absorption coefficient ( $\alpha$ ), extinction coefficient (K), and refractive index (n). The absorption coefficient ( $\alpha$ ) is a crucial optical characteristic that determines how far light can travel within a film before absorption. It is also an important parameter for determining the absorption edge, kind of transition, and energy gap. The absorption coefficient of the manufactured films has been calculated using the following formula [88,89]:

$$\alpha = \frac{1}{d} \ln \frac{(1-R)^2}{T}, \quad (12)$$

where d is the thickness of the film.

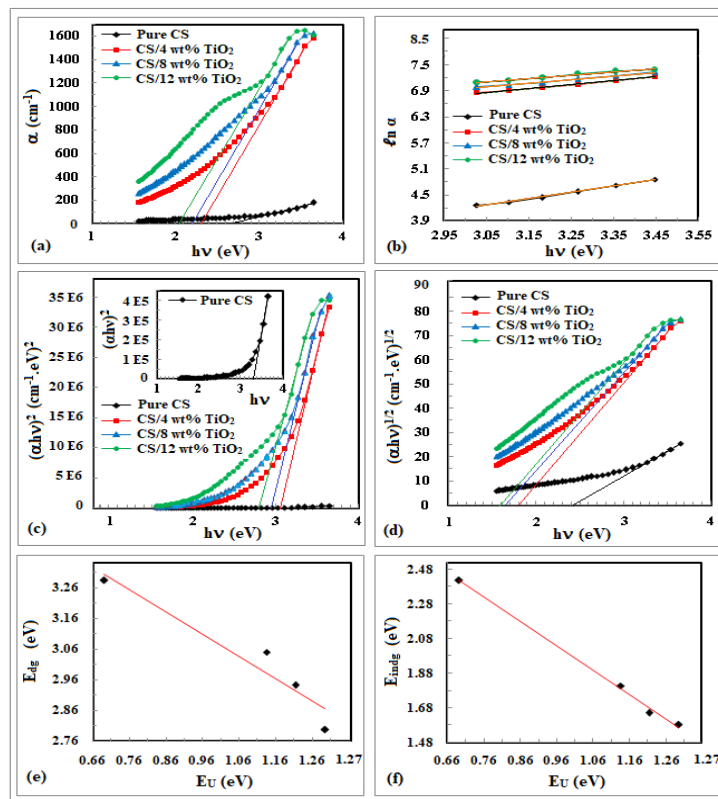


**Figure 10.** (a)  $\alpha$ , (b)  $\ln \alpha$ , (c)  $(\alpha h\nu)^2$ , and (d)  $(\alpha h\nu)^{1/2}$  against  $h\nu$ ; (e)  $E_U$  versus  $E_{dg}$  and (f)  $E_U$  versus  $E_{indg}$  for pure CS and CS/TiO<sub>2</sub> nanocomposite films

Figure 10a shows a plot of the absorption coefficient ( $\alpha$ ) versus incident photon energy ( $h\nu$ ) for pure CS and CS/TiO<sub>2</sub> nanocomposite films. Increasing the photon energy and TiO<sub>2</sub>-NP concentration to 12 wt% leads to an increase in  $\alpha$  value. To calculate the absorption edge ( $E_{cd}$ ) values, extrapolate the linear parts to  $\alpha = 0$  on the  $h\nu$ -axis and the computed values are listed in Table 4. The  $E_{cd}$  value for pure CS was shown to decrease toward lower energy values (higher wavelengths) as the concentration of TiO<sub>2</sub>-NPs increased.  $E_{cd}$  values decrease from 2.716 to 2.043 eV as the concentration of TiO<sub>2</sub>-NPs increases from 0 to 12 wt%. This was closely correlated with the production of charge-transfer complexes in nanocomposite films [21]. The observed decrease in  $E_{cd}$  value could be related to the enhancement of the amorphous phase, resulting in changes in the structure of the CS/TiO<sub>2</sub> nanocomposites [8,90]. Further, the decrease in  $E_{cd}$  may imply the presence of intra- or inter-molecular interaction between Ti<sup>4+</sup> ions and neighboring OH groups in the CS matrix [50]. Also, this observation suggests that the electronic polarization values of the nanocomposites change, demonstrating the decrease in the optical energy band gap values and changes occurring in the band structure of the CS/TiO<sub>2</sub> nanocomposites [8,90,91].

The Urbach energy ( $E_U$ ) describes the order of a matter system by calculating the width of the tail of local states in the forbidden gap. It can be determined using the Urbach empirical formula as follows [92,93]:

$$\ln \alpha = \ln \alpha_0 + \frac{h\nu}{E_U}, \quad (13)$$

$\alpha_0$  represents a pre-exponential factor. Figure 10b shows a plot of  $\ln \alpha$  against  $h\nu$  for pure CS and CS/TiO<sub>2</sub> nanocomposites. Table 4 lists the calculated Urbach energy ( $E_U$ ) values based on the reciprocal slopes of the fitted lines.

The  $E_U$  values rise from 0.692 eV for pure CS to 1.295 eV for the CS/12 wt% TiO<sub>2</sub> nanocomposite. This increase in  $E_U$  values indicates that a disruption in the band structure occurred, increasing structural disorder and enhancing the amorphous phase of the film. In addition, detailed information on the density of defects (DOF) and relaxation of the distorted bonds can be obtained by computing the steepness parameter (S) and electron-phonon interaction strength ( $E_{e-p}$ ) using the following relations [92,93]:

$$S = \frac{k_B T}{E_U}, \text{ and } E_{e-p} = \frac{2}{3S}, \quad (14)$$

where  $k_B$  and T represent Boltzmann's constant and room temperature (=298 K), respectively. Table 4 gives the computed values for S and  $E_{e-p}$ . The steepness parameter (S) values decreased from 0.037 to 0.020, while the electron-phonon interaction strength ( $E_{e-p}$ ) values increased from 17.929 to 33.583 as the concentration of TiO<sub>2</sub>-NPs increased from 0 to 12 wt%. Thus, the inclusion of TiO<sub>2</sub>-NPs into the CS network may be responsible for the inverse change between S and  $E_{e-p}$ , causing the ionicity and anion valence of the CS/TiO<sub>2</sub> nanocomposite change. Additionally, these variations in S and  $E_{e-p}$  show that the density of defects (DOF) increases around the absorption edge, confirming the improvement of the amorphous phase of CS with increasing TiO<sub>2</sub>-NP concentration [8,92,93].

**Table 4.** Optical parameter values: opacity, transparency,  $E_{ed}$ ,  $E_U$ , S,  $E_{e-p}$ ,  $E_{dg}$ ,  $E_{indg}$  and  $N_{cc}$  of pure CS and CS/TiO<sub>2</sub> nanocomposites

Sample	Opacity (mm <sup>-1</sup> )	Transparency (mm <sup>-1</sup> )	$E_{ed}$ (eV)	$E_U$ (eV)	S	$E_{e-p}$	$E_{dg}$ (eV)	$E_{indg}$ (eV)	$N_{cc}$
Pure CS	1.601	30.666	2.716	0.692	0.037	17.929	3.282	2.417	110
CS/4 wt%TiO <sub>2</sub>	9.421	17.633	2.303	1.135	0.023	29.428	3.050	1.807	127
CS/8 wt%TiO <sub>2</sub>	13.153	11.411	2.206	1.214	0.021	31.463	2.943	1.651	137
CS/12wt%TiO <sub>2</sub>	18.336	2.774	2.043	1.295	0.020	33.583	2.798	1.581	151

The energy band gap of a material is determined by its greater absorption spectra (first region), which is strongly influenced by the absorption coefficient ( $\alpha$ ). Tauc's relation was used to compute the optical energy band gap ( $E_g$ ) as follows [45,94,95]:

$$(\alpha h\nu)^p = B(h\nu - E_g), \quad (15)$$

where B is a constant known as the band-tailing parameter (Tauc's slope) and p is the power factor that describes the sort of electronic transition. Exponent p can have values of 2 or 1/2, corresponding to direct or indirect allowed transitions, respectively. Figure 10c and d show graphs of  $(\alpha h\nu)^2$  and  $(\alpha h\nu)^{1/2}$  versus  $h\nu$  for pure CS and CS/TiO<sub>2</sub> nanocomposites, respectively. The direct ( $E_{dg}$ ) and indirect ( $E_{indg}$ ) energy band gaps can be calculated by extending the linear portions to  $(\alpha h\nu)^2 = 0$  and  $(\alpha h\nu)^{1/2} = 0$  on the  $h\nu$ -axis. Table 4 summarizes the computed values of  $E_{dg}$  and  $E_{indg}$ . As TiO<sub>2</sub>-NP concentrations increase, the  $E_{dg}$  and  $E_{indg}$  values decrease. As the TiO<sub>2</sub>-NPs content increases from 0 to 12 wt%,  $E_{dg}$  values decrease from 3.282 to 2.798 eV and  $E_{indg}$  values decrease from 2.417 to 1.581 eV. The decrease in energy band gap could be due to an excessive amount of localized states in the band structure. These declines in the values of  $E_{dg}$  and  $E_{indg}$  could be attributed to increased disorder within the nanocomposite film's structure. This disorder creates new vacant energy levels in the band gap, allowing electrons to move more easily between the valence and conduction bands [45]. It may also be related to the existence of electronic interaction between TiO<sub>2</sub>-NPs and CS polymer, resulting in an increase in absorption intensity [90]. The decreases in  $E_{ed}$ ,  $E_{dg}$  and  $E_{indg}$  values of nanocomposite films suggest changes to the CS microstructure and band structure, possibly due to the formation of new optical transition clusters. Figure 10e and f shows the variance of  $E_{dg}$  and  $E_{indg}$  versus  $E_U$ , respectively. The energy band gap reduces as the value of  $E_U$  increases, indicating a direct correlation with  $E_{dg}$  and  $E_{indg}$ . These findings are consistent with previous research, as band gap lowering can lead to the formation of localized states in the optical band gap as a result of defects forming in the CS matrix [93,96]. Using these two approaches, the following linear fitting relationships can be estimated:

$$E_{dg} = 3.804 - 0.725E_U, \quad (16a)$$

$$E_{indg} = 3.391 - 1.409E_U. \quad (16b)$$

It was discovered that increasing the Urbach energy of the film indicates a decrease in the values of the optical energy band gap. This observation supports the assumption that introducing TiO<sub>2</sub>-NPs will enhance the number of traps.

The following equation can be used to compute the number of carbon atoms per cluster ( $N_{cc}$ ) in pure CS and CS/TiO<sub>2</sub> nanocomposites using the direct optical energy band gap ( $E_{dg}$ ) values [97,98]:

$$N_{cc} = \frac{1.1834 \times 10^3}{E_{dg}^2}. \quad (17)$$

The calculated  $N_{cc}$  values are shown in Table 4. The  $N_{cc}$  values increased from 110 for pure CS to 151 for the CS/12 wt% TiO<sub>2</sub> nanocomposite. The rise in  $N_{cc}$  values may be due to the resultant conjugation between CS matrix monomer units following the incorporation of TiO<sub>2</sub>-NPs. This result can be related to the existence of more defects in the CS matrix as the TiO<sub>2</sub>-NP content increases, resulting in the formation of additional low energy levels, lowering the optical band gap and improving  $N_{cc}$  values. Abdelfattah et al. [8] and Ahmed et al. [98] reported a similar trend. As a result, the observed variations confirm the increasing disorder degree in nanocomposite samples where the optical band

gap is compositionally dependent [97,98]. The decreased energy gap values of CS following the incorporation of TiO<sub>2</sub>-NPs make it a promising material for optoelectronic devices. Moreover, based on the results, it is clear that CS/TiO<sub>2</sub> nanocomposites could be used in the design and manufacture of custom packaging materials to block sunlight and prevent the formation of toxic substances, unpleasant odors, and flavors, preserve food color, and prevent photo-oxidation of fats in food products if used as active food packaging materials [28].

### Linear optical parameters

Many of the optical parameters that contribute to the effective use of polymeric nanocomposites in a variety of industrial, medical, and optoelectronic applications are directly related to the extinction coefficient (K) and refractive index (n) parameters [8,91,98,106]. The optical parameters K and n were determined to obtain an understanding of the polarization and optical variations in the produced nanocomposite films. The extinction coefficient (K), a parameter that represents the fraction of energy lost as a result of absorbing or scattering due to the interaction between the incident photon and the charge of the medium, can be described as follows [50,90]:

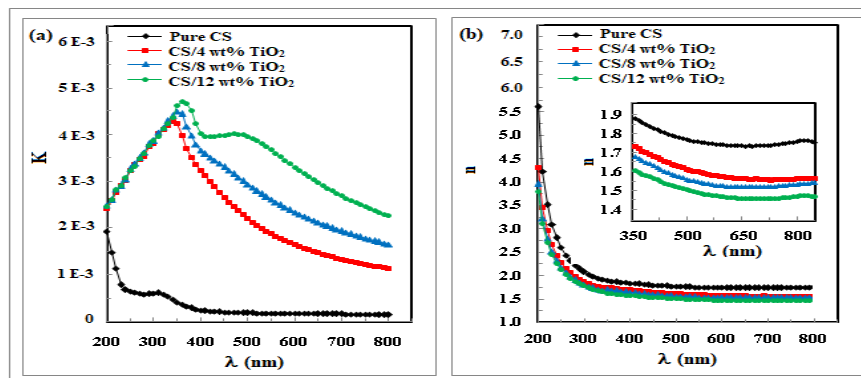
$$K = \frac{\alpha\lambda}{4\pi} \tag{18}$$

Figure 11a shows the relationship between the extinction coefficient (K) and wavelength (λ) in pure CS and CS/TiO<sub>2</sub> nanocomposites. The behavior of K varied significantly across all nanocomposite samples as compared to the pure CS film. It was demonstrated that K values altered on the order of 10<sup>-3</sup>. K values in nanocomposite films increase with rising UV wavelengths. This increase in K value reveals that electromagnetic waves cannot pass through this region, which can be explained by the fact that some of the energy was scattered or reflected by these nanocomposites, causing damping and decay. In contrast, as seen in Figure 11a, the K value decreased in the visible range and the extinction coefficient (K) behaves similarly to the absorption coefficient (α); see Figure 3a. Furthermore, as noted in Equation 18, K is directly proportional to α, which explains the reduction in values of K as the wavelength increases. On the other hand, increasing the concentration of TiO<sub>2</sub>-NPs incorporated into chitosan in the nanocomposite film to 12 wt% resulted in a significant rise in K values as the absorbance of the manufactured nanocomposites was enhanced. This indicates that the extinction coefficient is determined by the defects in structure and free electron densities present in the nanocomposite under consideration. This discovery verifies the results of the transmittance spectra, as well as the previously indicated opacity and transparency values. As a result, the acquired K values show that the manufactured films have no surface imperfections that enhance roughness, making them a good choice for optoelectronic devices [99].

The refractive index reveals how an incoming photon persuades molecules to polarize. The improved design of optoelectronic devices necessitates a thorough examination of the material's refractive index behavior. The refractive index (n) can be determined using Fresnel's relation as follows [14,50]:

$$n = \frac{1 + R}{1 - R} + \sqrt{\frac{4R}{(1 - R)^2} - K^2} \tag{19}$$

Figure 11b illustrates the relationship between refractive index (n) and wavelength (λ) in pure CS and CS/TiO<sub>2</sub> nanocomposites. It was found that the refractive index decreases significantly in the UV zone while remaining rather steady as the wavelength increases. This unremarkable decrease in the visible region could be explained to the fact that the molecules in the sample do not obey the applied electromagnetic field alternations due to their inertia [87]. Furthermore, increasing the TiO<sub>2</sub>-NPs content in the CS matrix reduces the nanocomposite's refractive index values, which can be attributed to a decrease in the free charge carrier concentration and polarizability of the nanocomposite samples [100]. The interaction of TiO<sub>2</sub>-NPs with CS molecules may modify the CS refractive index, and the variations in the refractive indices of the film components may affect the film's transparency (opacity) [50].



**Figure 11.** (a) The extinction coefficient, K, and (b) the refractive index, n, versus wavelength, λ, for pure CS and CS/TiO<sub>2</sub> nanocomposite films

### Wemple and Di-Domenico dispersion parameters

Dispersion parameters are useful in assessing the optical properties of any material for use in the construction of photoelectronic devices [8,91]. The observed dispersion in the refractive index in Figure 11b can be applied to determine the dispersion energies using the Wemple-DiDomenico model (single-oscillator model). The following relation relates the refractive index ( $n$ ) and photon energy ( $h\nu$ ) [8,92,98,101]:

$$(n^2 - 1)^{-1} = \frac{E_o}{E_d} - \frac{(h\nu)^2}{E_o E_d}, \quad (20)$$

where  $E_d$  is the effective energy of dispersion, which quantifies the average strength of inter-band transitions in the film, and  $E_o$  is the single effective oscillator energy (the WDD-gap), which provides quantitative information about the film's overall band structure. Figure 12a displays the graphical relationship between  $(n^2-1)^{-1}$  and  $(h\nu)^2$  for pure CS and CS/TiO<sub>2</sub> nanocomposites. The WDD parameters ( $E_d$  and  $E_o$ ) can be determined using the  $(n^2-1)^{-1}$ -axis intercept ( $E_o/E_d$ ) and the negative slope ( $1/E_o E_d$ ) of the straight line fit, as can be seen in Table 5. The following equations were used to calculate dispersive parameters based on  $E_d$  and  $E_o$ , such as oscillation field strength ( $f$ ), Wemple-DiDomenico optical energy band gap ( $E_g^{WDD}$ ), static refractive index ( $n_0$ ), and static dielectric constant at infinite wavelength ( $\epsilon_s$ ) [102,103]:

$$f = E_o E_d, \quad E_g^{WDD} = \frac{E_o}{2}, \quad n_0 = \sqrt{1 + \frac{E_d}{E_o}}, \quad \text{and} \quad \epsilon_s = n_0^2 \quad (21)$$

Table 5 shows the computed oscillator parameters for CS and nanocomposite films. The table demonstrates that the values of  $E_d$ ,  $E_o$ ,  $f$ ,  $n_0$ , and  $\epsilon_s$  decrease when TiO<sub>2</sub>-NPs concentration increases. By increasing the percentage of TiO<sub>2</sub>-NPs from 0 to 12 wt%, the  $E_d$  values reduce gradually from 11.324 to 5.621 eV, while the  $E_o$  values decrease from 6.308 to 5.393 eV, resulting in a decrease in direct band gap energy ( $E_{dg}$ ) values and being compatible with increases in Urbach energy ( $E_U$ ). To establish a correlation between direct band gap energy ( $E_{dg}$ ) and effective oscillator energy ( $E_o$ ), the table revealed that the ratio  $E_o/E_{dg}$  was found to be in the range 1.922–1.828 ( $E_o \approx 1.9 E_{dg}$ ), which coincides with the prediction of the Wemple-DiDomenico model for the current CS and CS/TiO<sub>2</sub> nanocomposite films. This finding in the  $E_o/E_g$  ratio shows thermally created defects that produce localized states around energy band gaps, which have a significant impact on the optical characteristics of nanocomposite films [91,92,102]. The table shows that increasing the content of TiO<sub>2</sub>-NPs from 0 to 12 wt% reduced the oscillation field strength ( $f$ ) –  $f$  represents the interaction strengths between the material and the electromagnetic radiation – values from 71.429 to 29.412 (eV)<sup>2</sup>, indicating a weaker composition of the nanocomposite film. The  $E_g^{WDD}$  values decrease from 3.154 to 2.697 eV when the TiO<sub>2</sub>-NPs concentration is increased from 0 to 12 wt%, which could be attributable to variations in atom diffusion rates in the nanocomposites and imply that the number of atoms in the previously identified interstitial has altered. The values of  $E_g^{WDD}$  are consistent with the values of the direct energy band gap ( $E_{dg}$ ) (see Table 4). This result suggests that the inclusion of TiO<sub>2</sub>-NPs reduces the system's average bonding strength or cohesive energy while increasing the disorder degree in the CS matrix [102,104]. The computed static refractive index ( $n_0$ ) values decreased from 1.672 to 1.418 as the concentration of TiO<sub>2</sub>-NPs increased from 0 to 12 wt%. The static dielectric constant ( $\epsilon_s$ ) values decreased from 3.642 to 2.702 as the amount of TiO<sub>2</sub>-NPs increased from 0 to 12 wt%. These observations could indicate an increase in structural disorder, which alters the optical properties of the film.

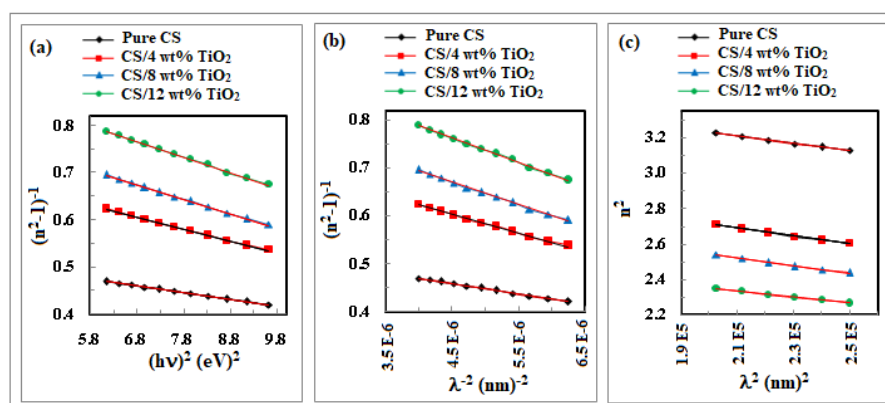


**Figure 12.** (a)  $(n^2-1)^{-1}$  versus  $(h\nu)^2$ , (b)  $(n^2-1)^{-1}$  versus  $\lambda^{-2}$  and (c)  $n^2$  versus  $\lambda^2$  for pure CS and CS/TiO<sub>2</sub> nanocomposite films

The first optical moment ( $M_{-1}$ ) and second optical moment ( $M_{-3}$ ) of CS and CS/TiO<sub>2</sub> nanocomposite films, which measure the process of light-material interaction, were computed using the estimated  $E_d$  and  $E_o$  values from the following equations [8,98]:

$$M_{-1} = \frac{E_d}{E_o}, \quad \text{and} \quad M_{-3} = \frac{M_{-1}}{E_o^2}. \quad (22)$$

Table 5 also included the computed  $M_{-1}$  and  $M_{-3}$  values for all samples. It has been found that while the transition moments  $M_{-1}$  and  $M_{-3}$  are mainly determined by the values of  $E_d$  and  $E_o$ , their values follow similar trends and decrease as the  $\text{TiO}_2$ -NPs content increases. When the concentration of  $\text{TiO}_2$ -NPs was increased from 0 to 12 wt%,  $M_{-1}$  reduced from 1.795 to 1.011, and  $M_{-3}$  decreased from 0.045 to 0.035 (eV)<sup>-2</sup>. This result validates the structural dependency of the optical properties of the nanocomposites under study, as well as the enhancement of the amorphous phase of the CS/ $\text{TiO}_2$  nanocomposite [8,98].

**Table 5.** The evaluated values of  $E_d$ ,  $E_o$ ,  $E_o/E_{dg}$  ratio,  $f$ ,  $E_g^{WDD}$ ,  $n_o$ ,  $\epsilon_s$ ,  $M_{-1}$ ,  $M_{-3}$ ,  $\lambda_o$ ,  $S_o$ ,  $\epsilon_L$ ,  $N/m^*$ ,  $N$  and  $\omega_p$ , for pure CS and CS/ $\text{TiO}_2$  nanocomposites

Dispersion parameters	Samples			
	Pure CS	CS/4wt% $\text{TiO}_2$	CS/8wt% $\text{TiO}_2$	CS/12wt% $\text{TiO}_2$
$E_d$ (eV)	11.324	7.179	6.148	5.621
$E_o$ (eV)	6.308	5.575	5.422	5.393
$E_o/E_{dg}$ ratio	1.922	1.828	1.842	1.928
$f$ (eV) <sup>2</sup>	71.429	39.999	33.333	29.412
$E_g^{WDD}$ (eV)	3.154	2.788	2.711	2.697
$n_o$	1.672	1.512	1.461	1.418
$\epsilon_s$	2.795	2.287	2.134	2.011
$M_{-1}$	1.795	1.287	1.134	1.011
$M_{-3}$ (eV) <sup>-2</sup>	0.045	0.041	0.039	0.035
$\lambda_o$ (m)	$1.988 \times 10^{-7}$	$2.230 \times 10^{-7}$	$2.307 \times 10^{-7}$	$2.258 \times 10^{-7}$
$S_o$ (m <sup>-2</sup> )	$4.541 \times 10^{13}$	$2.588 \times 10^{13}$	$2.131 \times 10^{13}$	$1.982 \times 10^{13}$
$\epsilon_L$	3.642	3.163	2.982	2.702
$N/m^*$ (m <sup>-3</sup> .kg <sup>-1</sup> )	$8.840 \times 10^{56}$	$8.789 \times 10^{56}$	$8.557 \times 10^{56}$	$7.584 \times 10^{56}$
$N$ (m <sup>-3</sup> )	$3.543 \times 10^{26}$	$3.523 \times 10^{26}$	$3.430 \times 10^{26}$	$3.040 \times 10^{26}$
$\omega_p$ (Hz)	$1.601 \times 10^{15}$	$1.596 \times 10^{15}$	$1.571 \times 10^{15}$	$1.483 \times 10^{15}$

The average oscillator wavelength ( $\lambda_o$ ) and average oscillator strength ( $S_o$ ) were determined using the following Wemple-Didomenico formulae [8,98,101]:

$$(n^2 - 1)^{-1} = (n_o^2 - 1)^{-1} - \frac{\lambda_o^2}{(n_o^2 - 1)} \lambda^{-2}, \quad \text{and} \quad S_o = \frac{(n_o^2 - 1)}{\lambda_o^2}. \quad (23)$$

Graphing the relationship between  $(n^2 - 1)^{-1}$  and  $\lambda^{-2}$  yields a negative slope ( $-1/S_o$ ) line that intersects the  $\lambda^{-2}$ -axis at  $(1/S_o \lambda_o^2)$  (Figure 12b). The parameters  $\lambda_o$  and  $S_o$  were computed and shown in Table 5. As  $\text{TiO}_2$ -NPs concentration increases from 0 to 12 wt%,  $\lambda_o$  values increase from 198.8 to 225.8 nm, while  $S_o$  values decrease from  $4.541 \times 10^{13}$  to  $1.982 \times 10^{13}$  m<sup>-2</sup>. According to Hassanein [105],  $\lambda_o$  is inversely proportional to  $E_o$ , and since  $E_o$  is directly proportional to  $E_g$ ,  $\lambda_o$  will be inversely proportional to  $E_g$ . However,  $S_o$  is directly proportional to  $E_d$ , therefore  $S_o$  will be directly proportional to  $E_g$ .

The refractive index ( $n$ ) data can be examined to calculate the lattice dielectric constant at a longer wavelength ( $\epsilon_L$ ), taking into account dispersion vibrations and free carriers. The following equation represents the relationship between the refractive index ( $n$ ) and wavelength ( $\lambda$ ) [8,98]:

$$n^2 = \epsilon_L - \frac{e^2}{4\pi\epsilon_o c^2} \left( \frac{N}{m^*} \right) \lambda^2, \quad (24)$$

where  $\epsilon_L$  is the lattice dielectric constant,  $\epsilon_o$  is the free space permittivity ( $= 8.854 \times 10^{-12}$  F·m<sup>-1</sup> or C<sup>2</sup>·N<sup>-1</sup>·m<sup>-2</sup>),  $c$  is the speed of light in space ( $= 3 \times 10^8$  m·s<sup>-1</sup>),  $e$  is the electron charge ( $= 1.602 \times 10^{-19}$  C), and  $(N/m^*)$  is the ratio of charge carrier concentration ( $N$ ) and effective mass ( $m^*$ ). Figure 12c depicts the graphical representations of  $n^2$  and  $\lambda^2$  for pure CS and CS/ $\text{TiO}_2$  nanocomposites. Table 5 summarizes the calculated  $\epsilon_L$  and  $N/m^*$  values based on the intersection and slope of fitted lines. Assuming  $m^* = 0.44 m_e$  ( $m_e$  is the electron's rest mass  $= 9.109 \times 10^{-31}$  kg), the value of  $N$  is computed and listed in Table 5. The table reveals that increasing the  $\text{TiO}_2$ -NPs concentration from 0 to 12 wt% decreases  $\epsilon_L$  from 3.642 to 2.702,  $N/m^*$  ratio from  $8.840 \times 10^{56}$  to  $7.584 \times 10^{56}$  m<sup>-3</sup>.kg<sup>-1</sup>, and  $N$  values from  $3.543 \times 10^{26}$  to  $3.040 \times 10^{26}$  per m<sup>3</sup>. Table 5 indicates that  $\epsilon_s$  values are lower than  $\epsilon_L$  values, possibly due to the polarization process caused by light and decreased charge carrier concentrations [8,106,107].

The plasma frequency ( $\omega_p$ ); corresponds to the typical electrostatic oscillation frequency in response to a small charge separation; of CS and CS/ $\text{TiO}_2$  nanocomposite films was calculated using the classical Drude dispersion model and the ratio  $N/m^*$  as follows [8]:

$$\omega_p = \sqrt{\frac{e^2 N}{\epsilon_o m^*}}. \quad (25)$$

Table 5 lists the computed  $\omega_p$  values. Increasing TiO<sub>2</sub>-NPs content from 0 to 12 wt% causes a decrease in  $\omega_p$  values from  $1.601 \times 10^{15}$  to  $1.483 \times 10^{15}$  Hz. High  $\omega_p$  values were attributed to high free carrier concentrations, as  $\omega_p$  is mainly determined by charge carrier concentration (N). Adding more TiO<sub>2</sub>-NPs reduces the time-variation of the electric field caused by resonance effects, resulting in lower frequency values [98,105].

### Nonlinear optical parameters

The study of nonlinear optical properties of materials such as nanocomposites is crucial for predicting their ability to be used in a wide range of optical applications, including internet access, optical regulators, optical networks, optical switching equipments and frequency conversion devices [8,93,102]. The nonlinear optical polarizability (P) within the material was obtained by expanding the power sequence of the entire applied optical field (E) [8,93]:

$$P = \chi^{(1)}E + \chi^{(2)}E^2 + \chi^{(3)}E^3 + \dots \quad (26)$$

where  $\chi^{(1)}$  is the first-order linear susceptibility,  $\chi^{(2)}$  is the second-order nonlinear susceptibility, and  $\chi^{(3)}$  is the third-order nonlinear optical susceptibility. The following semi-empirical relation was used to calculate the first-order linear susceptibility ( $\chi^{(1)}$ ) based on the linear refractive index (n) [12,95]:

$$\chi^{(1)} = \frac{(n^2 - 1)}{4\pi} \quad (27)$$

Using WDD-dispersion energies ( $E_d$  and  $E_o$ ) and Equation 20,  $\chi^{(1)}$  can be expressed as:

$$\chi^{(1)} = \frac{E_o E_d}{4\pi [E_o^2 - (h\nu)^2]} \quad (28)$$

At the limit  $h\nu \rightarrow 0$  ( $n = n_0$ ), using Equations 27 and 28 one obtains:

$$\chi^{(1)} = \frac{(n_0^2 - 1)}{4\pi} = \frac{E_d}{4\pi E_o} \quad (29)$$

The nonlinear optical (NLO) properties of a material are expressed by its third-order nonlinear susceptibility ( $\chi^{(3)}$ ) and nonlinear refractive index ( $n_2$ ). According to Miller's principle and WDD model,  $\chi^{(3)}$  can be approximated using the following expression [14,95,102]:

$$\chi^{(3)} = A \left( \chi^{(1)} \right)^4 \quad (30)$$

where A is a constant factor independent of photon energy (about  $1.7 \times 10^{-10}$  esu for all materials). For  $h\nu \rightarrow 0$ ,  $\chi^{(3)}$  can be expressed as:

$$\chi^{(3)}(esu) = A \left( \frac{n_0^2 - 1}{4\pi} \right)^4 = 6.8 \times 10^{-15} \left( \frac{E_d}{E_o} \right)^4 \quad (31)$$

The nonlinear refractive index ( $n_2$ ) and nonlinear absorption coefficient ( $\beta_c$ ) were calculated using the following equations [12,98,102]:

$$n_2 = \frac{12\pi\chi^{(3)}}{n_0} \quad (32)$$

$$\beta_c = \frac{48\pi^3\chi^{(3)}}{n^2 c \lambda} \quad (33)$$

Figure 13a-d shows the spectrum distributions of  $\chi^{(1)}$ ,  $\chi^{(3)}$ ,  $n_2$ , and  $\beta_c$  versus wavelength ( $\lambda$ ) for pure CS and CS/TiO<sub>2</sub> nanocomposites, respectively. The values of  $\chi^{(1)}$ ,  $\chi^{(3)}$ ,  $n_2$ , and  $\beta_c$  decrease dramatically with increasing wavelength (decreasing photon energy) and TiO<sub>2</sub>-NP concentration. As the percentage weight of TiO<sub>2</sub>-NPs increased, the refractive index (n) decreased, resulting in decreases in  $\chi^{(1)}$ ,  $\chi^{(3)}$ ,  $n_2$ , and  $\beta_c$  values. This suggests that using a higher concentration of TiO<sub>2</sub>-NPs may help to change the local polarization and reduce the number of free charge carriers in the nanocomposite film. Table 6 gives the computed values of  $\chi^{(1)}$ ,  $\chi^{(3)}$ , and  $n_2$  at  $h\nu \rightarrow 0$ , for pure CS and CS/TiO<sub>2</sub> nanocomposites. The predicted value of  $\chi^{(1)}$  decreases from 0.143 for the pure CS sample to 0.080 for the CS/12 wt% TiO<sub>2</sub>-NP nanocomposite. The table shows a significant decrease in  $\chi^{(3)}$  values from  $70.826 \times 10^{-15}$  esu for pure CS to  $7.126 \times 10^{-15}$  esu for a CS/12 wt% TiO<sub>2</sub>-NPs nanocomposite, which is strongly associated with other parameters. As TiO<sub>2</sub>-NPs concentration increased from 0 to 12 wt%,  $n_2$  values reduced from  $15.970 \times 10^{-13}$  to  $1.894 \times 10^{-13}$  esu. The reduction in  $n_2$  values supports the decrease in static refractive index ( $n_0$ ) values of the CS/TiO<sub>2</sub> nanocomposite samples as the TiO<sub>2</sub>-NP concentration increases. The observed changes in susceptibility and nonlinear index of refraction values were considered to be caused by variations in the samples' band gap values and densities. Because  $n_2$  values are on the order of  $10^{-12}$ - $10^{-13}$ , intense light beams were required to make a substantial influence. The acquired results revealed a

substantial association with the other linear parameters evaluated for the prepared samples. The nonlinear parameter results show that the investigated CS/TiO<sub>2</sub> nanocomposites can serve as a good advancer in a variety of optical applications [8,98,109].

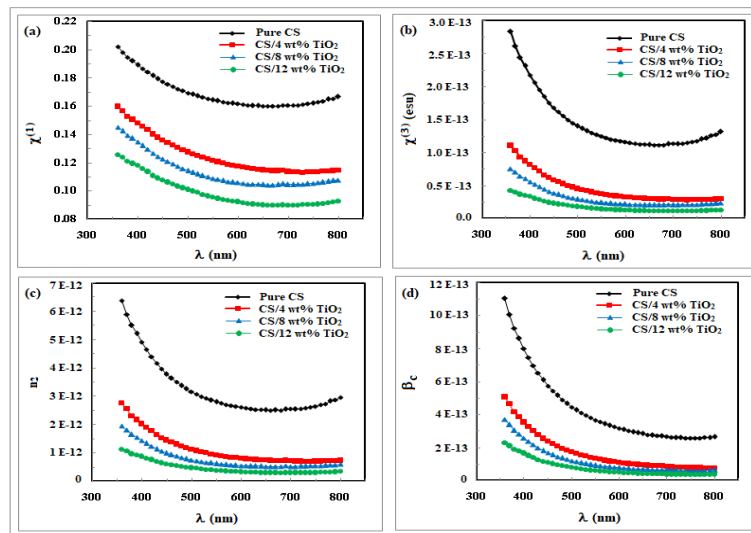


Figure 13. Plots of: (a)  $\chi^{(1)}$  and (b)  $\chi^{(3)}$  against  $h\nu$ ; (c)  $n_2$  and (d)  $\beta_c$  versus  $\lambda$ , for pure CS and CS/TiO<sub>2</sub> nanocomposite films

Table 6. Values of  $\chi^{(1)}$ ,  $\chi^{(3)}$ , and  $n_2$  for pure CS and CS/TiO<sub>2</sub> nanocomposites

Dispersion parameters	Samples			
	Pure CS	CS/4 wt% TiO <sub>2</sub>	CS/8 wt% TiO <sub>2</sub>	CS/12 wt% TiO <sub>2</sub>
$\chi^{(1)}$	0.143	0.102	0.090	0.081
$\chi^{(3)}$ (esu)	$70.826 \times 10^{-15}$	$18.704 \times 10^{-15}$	$11.265 \times 10^{-15}$	$7.126 \times 10^{-15}$
$n_2$ (esu)	$15.970 \times 10^{-13}$	$4.663 \times 10^{-13}$	$2.907 \times 10^{-13}$	$1.894 \times 10^{-13}$

### Optical dielectric constants and optical conductivities

When a material is electronically activated by UV-Vis radiation, the optical dielectric constant can be explained using the electronic excitation spectrum of any material [84,98,98]. The complex dielectric constant ( $\epsilon^*$ ) and its components [real part ( $\epsilon_r$ ) and imaginary part ( $\epsilon_i$ )] represent the decrease in the speed of light and the absorption energy of the electric field caused by the dipole movement of molecules in films. The complex dielectric constant ( $\epsilon^*$ ) and its components ( $\epsilon_r$  and  $\epsilon_i$ ) can be calculated using the refractive index ( $n$ ) and extinction coefficient ( $K$ ) data as follows [93,98]:

$$\epsilon^* = \epsilon_r + i \epsilon_i, \quad \epsilon_r = n^2 - K^2 \quad \text{and} \quad \epsilon_i = 2nK. \quad (34)$$

Figure 14 shows how the real,  $\epsilon_r$  (a) and imaginary,  $\epsilon_i$  (b) dielectric constants for pure CS and CS/TiO<sub>2</sub> nanocomposites vary with wavelength ( $\lambda$ ). As demonstrated in Figure 14a,  $\epsilon_r$  increased with photon energy, corresponding to the behavior of the refractive index (see Figure 11b). The polar nature of CS/TiO<sub>2</sub> nanocomposites causes fluctuations in the incident electromagnetic wave field, resulting in a dispersion region in the photon energy range of 3.6–6.2 eV (<350 nm) for all samples. The observed higher  $\epsilon_r$  values were attributable to the high contribution of the free charge carrier. The spectra, on the other hand, tend to behave consistently at lower photon energies (i.e., in the visible region). Due to inertia, molecules in this region are unable to follow oscillations in the incident field, resulting in nearly constant  $\epsilon_r$  values. The dispersion region of a nanocomposite plays an important role for optical networking and device design, as the real dielectric constant ( $\epsilon_r$ ) affects electron mobility during light transformation and slows photon propagation. Figure 14a shows that when the amount of TiO<sub>2</sub>-NPs in the nanocomposite film of the CS matrix increased, the values of  $\epsilon_r$  decreased. This indicates that the incorporation of TiO<sub>2</sub>-NPs into the CS/TiO<sub>2</sub> nanocomposite enhanced the energy dissipative and disruptive rates of incident light on the film, indicating a reduction in the speed of light propagation within the films. The imaginary dielectric constant part ( $\epsilon_i$ ) reflects energy absorption from dipole motion and measures the disruptive rate of light waves through the material. Figure 14b indicates that  $\epsilon_i$  values steadily increase in the visible region as photon energy and TiO<sub>2</sub>-NPs content increase. The variance in  $\epsilon_i$  values was related to the dipolar polarization of the nanocomposite [108]. Because of the direct relationship between  $\epsilon_i$  and  $K$ , the trend of  $\epsilon_i$  in prepared films mimics the behavior of  $K$ . Additionally, Figure 14a and b shows that  $\epsilon_r$  values are significantly higher than  $\epsilon_i$ . The discrepancy in  $\epsilon_r$  and  $\epsilon_i$  values indicates interactions between free electrons and photons in the nanocomposite films under investigation. Furthermore, the observed differences in the optical dielectric constant values of the CS/TiO<sub>2</sub> nanocomposite samples compared to pure CS verify the presence of more density of states (DOS), resulting in increased polarization and higher dielectric constant values [90,98].

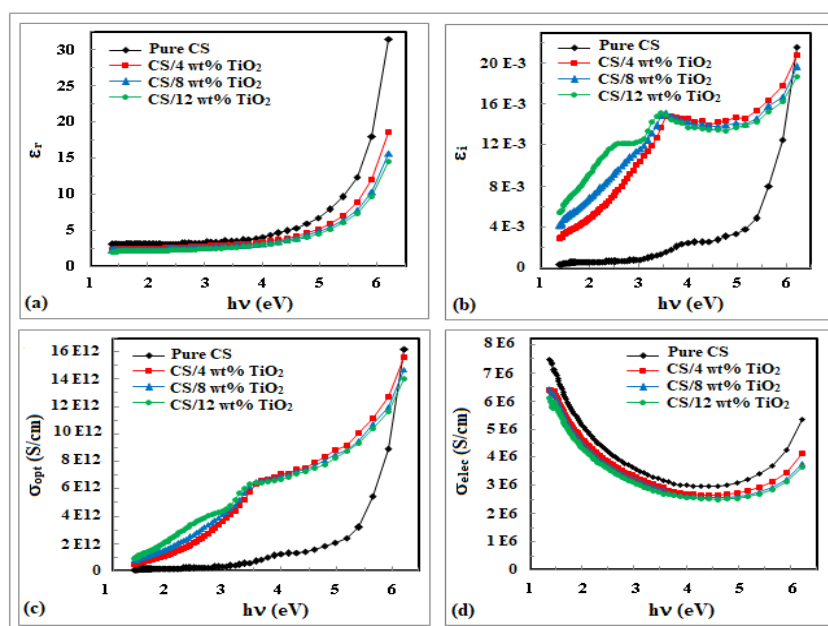


**Figure 14.** Plots of: (a)  $\epsilon_r$ , (b)  $\epsilon_i$ , (c)  $\sigma_{opt}$ , and (d)  $\sigma_{elec}$  against  $h\nu$  for pure CS and CS/TiO<sub>2</sub> nanocomposite films

The optical and electrical conductivities of the manufactured films were determined in order to understand more about their optical response. The optical ( $\sigma_{opt}$ ) and electric ( $\sigma_{elec}$ ) conductivities of the produced films were estimated using the following equations [93,102]:

$$\sigma_{opt} = \frac{\alpha nc}{4\pi}, \quad \text{and} \quad \sigma_{elec} = \frac{2\lambda\sigma_{opt}}{\alpha} \quad (35)$$

Figure 14 displays graphs of  $\sigma_{opt}$  (c) and  $\sigma_{elec}$  (d) versus photon energy ( $h\nu$ ). It was found that both  $\sigma_{opt}$  and  $\sigma_{elec}$  behave differently. Figure 14c shows that increasing the photon energy and TiO<sub>2</sub>-NPs content in the CS/TiO<sub>2</sub> nanocomposite improves the  $\sigma_{opt}$  of the films. Additionally, the spectral behavior of  $\sigma_{opt}$  in the films is comparable to that of  $\epsilon_i$  (Figure 14b).

High photon energy (low wavelength) in the UV range causes a dramatic increase in  $\sigma_{opt}$  for all films, indicating a strong interaction between charge carriers and energetic photons. In addition, nanocomposite films exhibit higher optical conductivity and absorbance than pure CS film. The produced nanocomposites exhibit high photoresponsiveness, with  $\sigma_{opt}$  values of the order of  $10^{12}$ . This suggests that the band gap has decreased while conductivity increased, indicating that the composite film has a longer conjugation length. This finding indicates that the concentration of charge carriers in the CS/TiO<sub>2</sub> nanocomposites has increased, as well as the enhancement of electron excitation due to an increase in film absorption coefficients and incident photon energy [98,102]. Figure 14d reveals that the electrical conductivity ( $\sigma_{elec}$ ) values of the samples are on the order of  $10^6$ .  $\sigma_{elec}$  values decrease with increasing photon energy up to  $\sim 4.1$  eV ( $\sim 300$  nm), then increase with increasing photon energy to  $\sim 6.2$  eV ( $\sim 200$  nm). Furthermore, increasing the concentration of TiO<sub>2</sub>-NPs in the nanocomposite film to 12 wt% reduces  $\sigma_{elec}$  values. This observed behavior could be attributed to the variance in charge carriers generated by the rising amount of TiO<sub>2</sub>-NPs in the produced nanocomposite. The results for optical and electrical conductivities were matched, indicating potential for optical applications.

#### 4. CONCLUSION

In the current study, innovative pure chitosan and chitosan/TiO<sub>2</sub> nanocomposite thin films with differed TiO<sub>2</sub>-NP concentrations (4, 8, and 12 wt%) were successfully created applying the solution casting method. The produced films were analyzed using FTIR, thermal analysis, and UV-Vis optical spectroscopy methods. FTIR examination confirmed that there is an interaction between CS and TiO<sub>2</sub>-NPs, as well as alterations in the structure of CS caused by the presence of TiO<sub>2</sub>-NPs. These changes were observed in the intensities and positions of the absorption peaks of CS/TiO<sub>2</sub> nanocomposites as compared to the pure CS sample. Analysis of DSC data revealed that when the amount of TiO<sub>2</sub>-NPs increased, there was an intense interaction between the -OH groups of CS and TiO<sub>2</sub> nanoparticles, confirming the miscibility of the nanocomposites. TGA and DTGA results showed that increasing TiO<sub>2</sub>-NP concentrations increased the thermal stability of the nanocomposite due to chemical interactions between the CS-polymer and TiO<sub>2</sub>-NPs. Spectroscopy was used to investigate the linear and nonlinear optical properties of pure CS and CS/TiO<sub>2</sub> nanocomposites films in the UV-Vis range between 200 and 800 nm. According to the data, all of the nanocomposite films contain UV-blocking characteristics that are below 360 nm, making them ideal UV light barriers. The Tauc equation and the Urbach postulate were used to calculate the allowed energy band gaps, both direct ( $E_{dg}$ ) and indirect

( $E_{indg}$ ), as well as the Urbach energy ( $E_U$ ). The absorption edge values ( $E_{cd}$ ) of the CS/12 wt% TiO<sub>2</sub> nanocomposite were determined to be 2.043 eV, less than 2.716 eV for pure CS. The  $E_{dg}$  values reduced dramatically from 3.282 eV for pure CS to 2.798 eV for the CS/12 wt% TiO<sub>2</sub> nanocomposite.  $E_{indg}$  values decreased from 2.417 to 1.581 eV when the TiO<sub>2</sub>-NPs content increased from 0 to 12 wt%.  $E_U$  values increased from 0.692 to 1.295 eV as TiO<sub>2</sub>-NP concentrations increased from 0 to 12 wt%. The observed alterations in  $E_{cd}$ ,  $E_{dg}$ ,  $E_{indg}$ ,  $E_U$ ,  $S$ ,  $E_{c-p}$ , and  $N_{cc}$  might be attributed to internal domain differences caused by structure disorder and a decrease in the crystallinity degree of CS. These changes can alter the overall number of potential states. Furthermore, the decrease in direct and indirect energy band gaps was explained in terms of localized states and defects, as confirmed by the Urbach energy. Increasing the concentration of TiO<sub>2</sub>-NPs in CS nanocomposite significantly improved optical parameters such as extinction coefficient ( $K$ ), refractive index ( $n$ ), real ( $\epsilon_r$ ) and imaginary ( $\epsilon_i$ ) optical dielectric constant parts, and optical and electrical conductivities ( $\sigma_{opt}$  and  $\sigma_{elec}$ ). In addition, the dispersion properties of the nanocomposites were investigated using the theoretical single oscillator model. The nanocomposites' both nonlinear and linear properties [ $\chi^{(1)}$ ,  $\chi^{(3)}$ ,  $n_2$  and  $\beta_c$ ] were increased. The observed innovative results of the linear and nonlinear optical characteristics of the examined nanocomposites indicate that CS/TiO<sub>2</sub> nanocomposite films are promising materials for further investigation for usage as packaging materials for food and in a variety of applications involving optical electronics.

#### ORCID

Osiris W. Guirguis, <https://orcid.org/0000-0003-3670-2904>

#### REFERENCES

- [1] Y. Kamari, and M. Ghiaci, "Preparation and characterization of ibuprofen/modified chitosan/TiO<sub>2</sub> hybrid composite as a controlled drug-delivery system", *Microporous and Mesoporous Mater.* **234**, 361–369 (2016). <https://doi.org/10.1016/j.micromeso.2016.07.030>
- [2] S. Kumar, K. Prasad, J.M. Gil, A.J.F.N. Sobral, and J. Koh, "Mesoporous zeolite-chitosan composite for enhanced capture and catalytic activity in chemical fixation of CO<sub>2</sub>", *Carbohydr. Polym.* **198**, 401–406 (2018). <https://doi.org/10.1016/j.carbpol.2018.06.100>
- [3] V.G.L. Souza, A.L. Fernando, J.R.A. Pires, P.F. Rodrigues, A.A.S. Lopes, and F.M.B., Fernandes, "Physical properties of chitosan films incorporated with natural antioxidants", *Ind. Crop. Prod.* **107**, 565–572 (2017). <http://dx.doi.org/10.1016/j.indcrop.2017.04.056>
- [4] J. Salvada, B. Alke, C. Brazinha, V.D. Alves, and I.M. Coelho, "Development and characterisation of arabinoxylan-based composite films", *Coatings*, **12**, 813 (2022). <https://doi.org/10.3390/coatings12060813>
- [5] Y. Xing, X. Li, X. Guo, W. Li, J. Chen, Q. Liu, Q. Xu, Q. Wang, H. Yang, Y. Shui, and X. Bi, "Effects of different TiO<sub>2</sub> nanoparticles concentrations on the physical and antibacterial activities of chitosan-based coating film", *Nanomaterials* **10**, 1365 (2020). <https://doi.org/10.3390/nano10071365>
- [6] V.-B. Hoa, D.-H. Song, K.-H. Seol, S.-M. Kang, H.-W. Kim, J.-H., Kim, S.-S. Moon, and S.-H. Cho, "Application of a newly developed chitosan/oleic acid edible coating for extending shelf-life of fresh pork", *Foods*, **11**, 1978 (2022). <https://doi.org/10.3390/foods11131978>
- [7] S.B. Aziz, M.M. Nofal, H.O. Ghareeb, E.M.A. Dannoun, S.A., Hussien, J.M. Hadi, K.K. Ahmed, and A.M. Hussein, "Characteristics of poly(vinyl alcohol) (PVA) based composites integrated with green synthesized Al<sup>3+</sup>-metal complex: structural, optical, and localized density of state analysis", *Polymers*, **13**, 1316 (2021). <https://doi.org/10.3390/polym13081316>
- [8] E.M. Abdelfattah, H. Elzanaty, W.B. Elsharkawy, M.A. Azzam, Z.M. Elqahtani, S. Alotibi, M. Alyami, and T. Fahmy, "Enhancement of the structure, thermal, linear/nonlinear optical properties, and antibacterial activity of poly(vinyl alcohol)/chitosan/ZnO nanocomposites for eco-friendly applications", *Polymers*, **15**, 4282 (2023). <https://www.mdpi.com/journal/polymers>
- [9] A. Nešić, G. Cabrera-Barjas, S. Dimitrijević-Branković, S. Davidović, N. Radovanović, and C. Delattre, "Prospect of polysaccharidebased materials as advanced food packaging", *Molecules*, **25**, 135 (2020). <https://doi.org/10.3390/molecules25010135>
- [10] T.M. Vieira, M., Moldão-Martins, and V.D. Alves, "Design of chitosan and alginate emulsion-based formulations for the production of monolayer crosslinked edible films and coatings", *Foods*, **10**, 1654 (2021). <https://doi.org/10.3390/foods10071654>
- [11] R.A. Ilyas, H.A. Aisyah, A.H. Nordin, N. Ngadi, M.Y.M. Zuhri, M.R.M. Asyraf, S.M. Sapuan, E.S. Zainudin, S. Sharma, H. Abrial, M. Asrofi, E. Syafri, N.H. Sari, M. Rafidah, S.Z.S. Zakaria, M.R. Razman, N. Abd Majid, Z. Ramli, A. Azmi, S.P. Bangar, and R. Ibrahim, "Natural-fiber-reinforced chitosan, chitosan blends and their nanocomposites for various advanced applications", *Polymers*, **14**, 874 (2022). <https://doi.org/10.3390/polym14050874>
- [12] E.F.M. El-Zaidia, M.S. Al-Kotb, and I.S. Yahia, "Deposition of nanostructured methyl violet-10B films/FTO: Optical limiting and optical linearity/nonlinearity", *Mater. Chem. Phys.* **240**, 122074 (2020). <https://doi.org/10.1016/j.matchemphys.2019.122074>
- [13] M.V. Vijisha, V.V. Sini, N.K. Siji Narendran, and K. Chandrasekharan, "Enhanced nonlinear optical response from dihydroxy(5,10,15,20-tetraphenyl porphyrinato)tin(IV) or SnTPP in a fully plastic photonic crystal microcavity", *Phys. Chem. Chem. Phys.* **19**, 29641–29646 (2017). <https://doi.org/10.1039/C7CP06455A>
- [14] M. Yaseen, Z. Farooq, M. Ahmad, M. Abdullah Sultan, M.A. Raza, J.-Y. Winum, M. Mustafa, M.H.R. Mahmood, M. Tayyab, M.A. Iqbal, and M.S. Mahr, "Synthesis and investigation of linear and nonlinear optical properties of an octahedral metalloporphyrin", *Opt. Mater.* **149**, 115092 (2024). <https://doi.org/10.1016/j.optmat.2024.115092>
- [15] M.A. Neves, J. Hashemi, T. Yoshino, K. Uemura, and M. Nakajima, "Development and characterization of chitosan-nanoclay composite films for enhanced gas barrier and mechanical properties", *J. Food Sci. Nutr.* **2**, 100007 (2016). <https://www.researchgate.net/publication/299488601>

- [16] G. Xiao, X. Zhang, W. Zhang, S. Zhang, H. Su, and T. Tan, "Visible-light-mediated synergistic photocatalytic antimicrobial effects and mechanism of Ag-nanoparticles@chitosan-TiO<sub>2</sub> organic-inorganic composites for water disinfection", *Appl. Catal. B*, **170**, 255–262 (2015). <https://doi.org/10.1016/j.apcatb.2015.01.042>
- [17] P. Kaewklin, U. Siripatrawan, A. Suwanagul, and Y.S. Lee, "Active packaging from chitosan-titanium dioxide nanocomposite film for prolonging storage life of tomato fruit", *Biol. Macromol.* **112**, 523–529 (2018). <https://doi.org/10.1016/j.ijbiomac.2018.01.124>
- [18] H. Haghighi, S. Biard, F. Bigi, R. De Leo, E. Bedin, F. Pfeifer, H.W. Siesler, F. Licciardello, and A. Pulvirenti, "Comprehensive characterization of active chitosan-gelatin blend films enriched with different essential oils", *Food Hydrocoll.* **95**, 33–42 (2019). <https://doi.org/10.1016/j.foodhyd.2019.04.019>
- [19] S. Yadav, G.K. Mehrotra, P. Bhartiya, A. Singh, and P.K. Dutta, "Preparation, physicochemical and biological evaluation of quercetin-based chitosan-gelatin film for food packaging", *Carbohydr. Polym.* **227**, 115348 (2020). <https://doi.org/10.1016/j.carbpol.2019.115348>
- [20] M. Islam, S. Masum, M.M. Rahman, A.I. Molla, A.A. Shaikh, and S.K. Roy, "Preparation of chitosan from shrimp shell and investigation of its properties", *Int. J. Basic Appl. Sci.* **11**, 116–130 (2011).
- [21] S.B. Aziz, O.Gh. Abdullah, and M.A. Rasheed, "A novel polymer composite with a small optical band gap: New approaches for photonics and optoelectronics", *J. Appl. Polym. Sci.* **134**, 44847 (2017). <https://doi.org/10.1002/app.44847>
- [22] S.F. Hamza, M.M. El-Sawy, N.A. Alian, and N.O. Shaker, "Synthesis and evaluation of performance characteristics green composites from sustainable fatty chitosan graft copolymer with acrylic acid for wastewater treatment", *Egypt. J. Chem.* **64**, 6007–6015 (2021). <https://doi.org/10.21608/EJCHEM.2021.73857.3656>
- [23] Q. Cao, Y. Zhang, W. Chen, X. Meng, and B. Liu, "Hydrophobicity and physicochemical properties of agarose film as affected by chitosan addition", *Int. J. Biol. Macromol.* **106**, 1307–1313 (2018). <https://doi.org/10.1016/j.ijbiomac.2017.08.134>
- [24] S. Mafirad, M.R. Mehrnia, P. Zahedi, and S.-N. Hosseini, "Chitosan-based nanocomposite membranes with improved properties: Effect of cellulose acetate blending and TiO<sub>2</sub> nanoparticles incorporation", *Polym. Compos.* **39**, 4452–4466 (2018). <https://doi.org/10.1002/pc.24539>
- [25] M. Mujtaba, R.E. Morsi, G. Kerch, M.Z. Elsabee, M. Kaya, J. Labidi, and K.M. Khawar, "Current advancements in chitosan-based film production for food technology; A review", *Int. J. Biol. Macromol.* **121**, 889–904 (2019). <https://doi.org/10.1016/j.ijbiomac.2018.10.109>
- [26] M.E. Ergun, E. Ozen, N. Yildirim, B. Dalkilic, and E. Baysal, "Mechanical and thermal properties of polyvinyl acetate foams reinforced with biopolymers", *Cell. Polym.* **42**, 156–173 (2023). <https://doi.org/10.1177/02624893231193501>
- [27] Z. Hu, P. Hong, M. Liao, S. Kong, N. Huang, C. Ou, and S. Li, "Preparation and characterization of chitosan-agarose composite films", *Materials*, **9**, 816 (2016). <https://doi.org/10.3390/ma9100816>
- [28] X. Zhang, G. Xiao, Y. Wang, Y. Zhao, H. Su, and T. Tan, "Preparation of chitosan-TiO<sub>2</sub> composite film with efficient antimicrobial activities under visible light for food packaging applications", *Carbohydr. Polym.* **169**, 101–107 (2017). <http://dx.doi.org/10.1016/j.carbpol.2017.03.073>
- [29] B. Cheba, "Chitosan: Properties, modifications and food nanobiotechnology", *Procedia Manuf.* **46**, 652–665 (2020). <https://doi.org/10.1016/j.promfg.2020.03.093>
- [30] S.F. Hamza, N.A. Alian, M.M. Elsayy, and N. Shaker, "Preparation, characterization and antimicrobial activity of chitosan-fatty acid derivatives as a drug delivery system: intercalation and in vitro release of ciprofloxacin", *Al-Azhar Bull. Sci.* **32**, 47–56 (2021). <https://doi.org/10.21608/absb.2021.72129.1110>
- [31] M.S. Hanafy, W.M. Desoky, E.M. Hussein, N.H. El-Shaer, M. Gomaa, A.A. Gamal, M.A. Esawy, and O.W. Guirguis, "Biological applications study of bio-nanocomposites based on chitosan/TiO<sub>2</sub> nanoparticles polymeric films modified by oleic acid", *J. Biomed. Mater. Res.* **109**, 232–247 (2021). doi:10.1002/jbm.a.37019
- [32] M. Bajić, T. Ročnik, A. Oberlintner, F. Scognamiglio, U. Novak, and B. Likozar, "Natural plant extracts as active components in chitosan-based films: A comparative study", *Food Packag. Shelf Life*, **21**, 100365 (2019). <https://doi.org/10.1016/j.fpsl.2019.100365>
- [33] B. Tian, and Y. Liu, "Chitosan-based biomaterials: From discovery to food application", *Polym. Adv. Technol.* **31**, 2408–2421 (2020). <https://doi.org/10.1002/pat.5010>
- [34] S. Moradi, H. Hamed, A.E. Tonelli, and M.W. King, "Chitosan/graphene oxide composite films and their biomedical and drug delivery applications: A review", *Appl. Sci.* **11**, 7776 (2021). <https://doi.org/10.3390/app1117776>
- [35] S.M. Bashir, G.A. Rather, A. Patricio, Z. Haq, A.A. Sheikh, M.Z.H. Shah, H. Singh, A.A. Khan, S. Imtiyaz, S.B. Ahmad, S. Nabi, R. Rakhshan, S. Hassan, and P. Fonte, "Chitosan nanoparticles: A versatile platform for biomedical applications", *Materials*, **15**, 6521–6529 (2022). <https://doi.org/10.3390/ma15196521>
- [36] K. Piekłarz, and K. Modrzejewska, "SARS-CoV-2 – The latest global threat and the prospect of COVID-19 therapy with the use of chitosan", *Prog. Chem. Appl. Chitin Deriv.* **26**, 41–60 (2021).
- [37] S. Valizadeh, M. Naseri, S. Babaei, S.M.H. Hosseini, and A. Imani, "Development of bioactive composite films from chitosan and carboxymethyl cellulose using glutaraldehyde, cinnamon essential oil and oleic acid", *Int. J. Biol. Macromol.* **134**, 604–612 (2019). <https://doi.org/10.1016/j.ijbiomac.2019.05.071>
- [38] L.A.M. van den Broek, R.J.I. Knoop, F.H.J. Kappen, and C.G. Boeriu, "Chitosan films and blends for packaging material", *Carbohydr. Polym.* **116**, 237–242 (2015). <https://doi.org/10.1016/j.carbpol.2014.07.039>
- [39] E. Le Goué, C. Gardrat, M. Romain, M. Rollini, C. Moresoli, and V. Coma, "Effect of oleic acid on the release of tetrahydrocurcumin in chitosan-based films", *Food Hydrocoll.* **124**, 107202 (2022). <https://doi.org/10.1016/j.foodhyd.2021.107202>
- [40] K.S. Siddiqi, A. Rahman, Tajuddin, and A. Husen, "Biogenic fabrication of iron/iron oxide nanoparticles and their application", *Nanoscale Res. Lett.* **11**, 498 (2016). <https://doi.org/10.1186/s11671-016-1714-0>
- [41] K.S. Siddiqi, and A. Husen, "Recent advances in plant-mediated engineered gold nanoparticles and their application in biological system", *J. Trace Elements Med. Biol.* **40**, 10–23 (2017). <https://doi.org/10.1016/j.jtemb.2016.11.012>

- [42] I. Khan, K. Saeed, and I. Khan, "Nanoparticles: Properties, applications and toxicities", *Arab. J. Chem.* **12**, 908–931 (2019). <https://doi.org/10.1016/j.arabjc.2017.05.011>
- [43] F. Mohammad, H.A. Al-Lohedan, and H.N. Al-Haque, "Chitosan-mediated fabrication of metal nanocomposites for enhanced biomedical applications", *Adv. Mater. Lett.* **8**, 89–100 (2017). <https://doi.org/10.5185/amlett.2017.6925>
- [44] K.S. Siddiqi, A. Husen, and R.A.K. Rao, "A review on biosynthesis of silver nanoparticles and their biocidal properties", *J. Nanobiotechnol.* **16**, 14 (2018). <https://doi.org/10.1186/s12951-018-0334-5>
- [45] F. Gami, N. Algethami, H.M. Ragab, A. Rajah, and A.E. Tarabiah, "Structural, optical and electrical studies of chitosan/polyacrylamide blend filled with synthesized selenium nanoparticles", *J. Mol. Struct.* **1257**, 132631 (2022). <https://doi.org/10.1016/j.molstruc.2022.132631>
- [46] S. Sau, and S. Kundu, "Variation in structure and properties of poly(vinyl alcohol) (PVA) film in the presence of silver nanoparticles grown under heat treatment", *J. Mol. Struct.* **1250**, 131699 (2022). <https://doi.org/10.1016/j.molstruc.2021.131699>
- [47] N.R. Saha, G. Sarkar, I. Roy, D. Rana, A. Bhattacharyya, A. Adhikari, A. Mukhopadhyay, and D. Chattopadhyay, "Studies on methylcellulose/pectin/montmorillonite nanocomposite films and their application possibilities", *Carbohydr. Polym.* **136**, 1218–1227 (2016). <https://doi.org/10.1016/j.carbpol.2015.10.046>
- [48] M. Yang, Y. Xia, Y. Wang, X. Zhao, Z. Xue, F. Quan, C. Geng, and Z. Zhao, "Preparation and property investigation of crosslinked alginate/silicon dioxide nanocomposite films", *J. Appl. Polym. Sci.* **133**, 43489 (2016). <https://doi.org/10.1002/app.43489>
- [49] W. Ma, J. Li, Y. Liu, X. Ren, Z.G. Gu, Z. Xie, and J. Liang, "Preparation and characterization of excellent antibacterial TiO<sub>2</sub>/N-halamines nanoparticles", *Colloids Surf. A Physicochem. Eng. Asp.* **506**, 284–290 (2016). <https://doi.org/10.1016/j.colsurfa.2016.06.055>
- [50] E.M. Hussein, W.M. Desoky, M.F. Hanafy, and O.W. Guirguis, "Effect of TiO<sub>2</sub> nanoparticles on the structural configurations and thermal, mechanical, and optical properties of chitosan/TiO<sub>2</sub> nanoparticle composites", *J. Phys. Chem. Solids*, **152**, 109983 (2021). <https://doi.org/10.1016/j.jpcs.2021.109983>
- [51] L.M. Anaya-Esparza, J.M. Ruvalcaba-Gómez, C.I. Maytorena-Verdugo, N. González-Silva, R. Romero-Toledo, S. Aguilera-Aguirre, A. Pérez-Larios, and A.E. Montalvo-González, "Chitosan-TiO<sub>2</sub>: A versatile hybrid composite", *Materials*, **13**, 811 (2020). <https://doi.org/10.3390/ma13040811>
- [52] V.K. Yemmireddy, G.D. Farrell, and Y.C. Hung, "Development of titanium dioxide (TiO<sub>2</sub>) nanocoatings on food contact surfaces and method to evaluate their durability and photocatalytic bactericidal property", *J. Food Sci.* **80**, 1903–1911 (2015). <https://doi.org/10.1111/1750-3841.12962>
- [53] S.A. Oleyaei, H. Almasi, B. Ghanbarzadeh, and A.A. Moayedi, "Synergistic reinforcing effect of TiO<sub>2</sub> and montmorillonite on potato starch nanocomposite films: Thermal, mechanical and barrier properties", *Carbohydr. Polym.* **152**, 253–262 (2016). <https://doi.org/10.1016/j.carbpol.2016.07.040>
- [54] A. Khalilnezhad, H. Rezvani, P. Ganji, and Y. Kazemzadeh, "A Complete experimental study of oil/water interfacial properties in the presence of TiO<sub>2</sub> nanoparticles and different ions", *Oil Gas Sci. Technol.* **74**, 39 (2019). <https://doi.org/10.2516/ogst/2019007>
- [55] Q. Chen, Z. Ye, L. Tang, T. Wu, Q. Jiang, and N. Lai, "Synthesis and solution properties of a novel hyperbranched polymer based on chitosan for enhanced oil recovery", *Polymers*, **12**, 2130 (2020). <https://doi.org/10.3390/polym12092130>
- [56] G.S. Negi, S. Anirbid, and P. Sivakumar, "Applications of silica and titanium dioxide nanoparticles in enhanced oil recovery: Promises and challenges", *Petroleum Res. B*, 224–246 (2021). <https://doi.org/10.1016/j.ptlrs.2021.03.001>
- [57] A.D. Dos Santos Francisco, K.C.B. Maia, J.G. Vieira Moura, R.S. Veiga Nascimento, F. da Silva Lima, and D. Grasseschi, "Chitosan derivatives as surfactant carriers for enhanced oil recovery – Experimental and molecular dynamic evaluations of polymer-surfactant interactions", *Colloids Surf. A Physicochem. Eng. Asp.* **671**, 131644 (2023). <https://doi.org/10.1016/j.colsurfa.2023.131644>
- [58] Y.H. Yun, J.W. Yun, S.D. Yoon, and H.S. Byun, "Physical properties and photocatalytic activity of chitosan-based nanocomposites added titanium oxide nanoparticles", *Macromol. Res.* **24**, 51–59 (2016). <https://doi.org/10.1007/s13233-016-4008-6>
- [59] K.T. Karthikeyan, A. Nithya, and K. Jothivenkatachalam, "Photocatalytic and antimicrobial activities of chitosan-TiO<sub>2</sub> nanocomposite", *Int. J. Biol. Macromol.* **104**, 1762–1773 (2017).
- [60] T. Kamal, Y. Anwar, S.B. Khan, M.T.S. Chani, and A.M. Asiri, "Dye adsorption and bactericidal properties of TiO<sub>2</sub>/Chitosan coating layer", *Carbohydr. Polym.* **148**, 153–160 (2016). <https://doi.org/10.1016/j.carbpol.2016.04.042>
- [61] H. Chang, J. Lv, H. Zhang, B. Zhang, W. Wei, and Y. Qiao, "Photoresponsive colorimetric immunoassay based on chitosan modified AgI/TiO<sub>2</sub> heterojunction for highly sensitive chloramphenicol detection", *Biosens. Bioelectron.* **87**, 579–586 (2017). <https://doi.org/10.1016/j.bios.2016.09.002>
- [62] W. Xu, W. Xie, X. Huang, X. Chen, N. Huang, X. Wang, and J. Liu, "The graphene oxide and chitosan biopolymer loads TiO<sub>2</sub> for antibacterial and preservative research", *Food Chem.* **221**, 267–277 (2017). <https://doi.org/10.1016/j.foodchem.2016.10.054>
- [63] A. Mohandas, S. Deepthi, R. Biswas, and R. Jayakuma, "Chitosan based metallic nanocomposite scaffolds as antimicrobial wound dressings", *Bioact. Mater.* **3**, 267–277 (2018). <https://doi.org/10.1016/j.bioactmat.2017.11.003>
- [64] U. Siripatrawan, and P. Kaewklin, "Fabrication and characterization of chitosan-titanium dioxide nanocomposite film as ethylene scavenging and antimicrobial active food packaging", *Food Hydrocoll.* **84**, 125–134 (2018). <https://doi.org/10.1016/j.foodhyd.2018.04.049>
- [65] A. Razzaz, S. Ghorban, L. Hosayni, M. Irani, and M. Aliabadi, "Chitosan nanofibers functionalized by TiO<sub>2</sub> nanoparticles for the removal of heavy metal ions", *J. Taiwan Inst. Chem. Eng.* **58**, 333–343 (2015). <https://doi.org/10.1016/j.jtice.2015.06.003>
- [66] A. Spoială, C.-I. Ilie, G. Dolete, A.-M. Croitoru, V.-A. Surdu, R.-D. Truşcă, L. Motelica, O.-C. Oprea, D. Ficaï, A. Ficaï, E. Andronescu, and L.-M. Diţu, "Preparation and characterization of chitosan/TiO<sub>2</sub> composite membranes as adsorbent materials for water purification", *Membranes* **12**, 804 (2022). <https://doi.org/10.3390/membranes12080804>
- [67] R. Saravanan, J. Aviles, F. Gracia, E. Mosquera, and V.K. Gupta, "Crystallinity and lowering band gap induced visible light photocatalytic activity of TiO<sub>2</sub>/CS (Chitosan) nanocomposites", *Int. J. Biol. Macromol.* **109**, 1239–1245 (2018). <https://doi.org/10.1016/j.ijbiomac.2017.11.125>

- [68] H.H. Ibrahim, A.M. Abdelghany, M.H. Gaber, and S.A. Ali, "Optical and physical characteristics of chitosan/silver vanadate nanocomposites", *Opt. Quantum Electron.* **56**, 435 (2024). <https://doi.org/10.1007/s11082-023-05979-z>
- [69] E. Filippo, C. Carlucci, A.L. Capodilupo, P. Perulli, F. Conciauro, G.A. Corrente, G. Gigli, and G. Ciccarella, "Enhanced photocatalytic activity of pure anatase TiO<sub>2</sub> and Pt-TiO<sub>2</sub> nanoparticles synthesized by green microwave assisted route", *Mater. Res.* **18**, 473–481 (2015). <http://dx.doi.org/10.1590/1516-1439.301914>
- [70] P. Mujeeb Rahman, V.M. Abdul Mujeeb, K. Muraliedharan, and S.K. Thomas, "Chitosan/nano ZnO composite films: enhanced mechanical, antimicrobial and dielectric properties", *Arab J. Chem.* **11**, 120 (2018). <https://doi.org/10.1016/j.arabjc.2016.09.008>
- [71] N.D. Alharbi, "Synthesis of composites from hydroxypropyl cellulose:iron (III) oxide nanoparticles", *Polym. Polym. Compos.* **31**, 1–12 (2023). <https://doi.org/10.1177/09673911221149548>
- [72] N.D. Alharbi, H.H. Amer, N.A. El-Zaher, and O.W. Guirguis, "Saudi cotton fabrics treated with chitosan and different concentrations of ZnO nanoparticles: Preparation, characterization, and demonstration", *Fiber. Polym.* **24**, 537–554 (2023). <https://doi.org/10.1007/s12221-023-00035-9>
- [73] A. Olaru, T. Măluțan, U.C. Marta, M. Geba, and L. Stratulat, "Structural changes in hemp fibers following temperature, humidity and UV or gamma-ray radiation exposure", *Cellulose Chem. Technol.* **50**, 31–39 (2016).
- [74] N.A. El-Zaher, G.T. El-Bassyouni, M.A. Esawy, and O.W. Guirguis, "Amendments of the structural and physical properties of cotton fabrics dyed with natural dye and treated with different mordants", *J. Nat. Fibers*, **18**, 1247–1260 (2021). <https://doi.org/10.1080/15440478.2019.1689884>
- [75] I. Corazzari, R. Nisticò, F. Turci, M.G. Faga, F. Franzoso, S. Tabasso, and G. Magnacca, "Advanced physico-chemical characterization of chitosan by means of TGA coupled on-line with FTIR and GCMS: Thermal degradation and water adsorption capacity", *Polym. Degrad. Stab.* **112**, 1–9 (2015). <https://doi.org/10.1016/j.polymdegradstab.2014.12.006>
- [76] I. Ozsoy, A. Demirkol, A. Mimaroglu, H. Unal, and Z. Demir, "The influence of micro- and nano-filler content on the mechanical properties of epoxy composites", *Stroj. Vestn. J. Mech. E.* **61**, 601 (2015). <https://doi.org/10.5545/SV-JME.2015.2632>
- [77] L. Cui, S. Gao, X. Song, L. Huang, H. Dong, J. Liu, F. Chen, and S. Yu, "Preparation and characterization of chitosan membranes", *RSC Adv.* **8**, 28433–28439 (2018). <https://doi.org/10.1039/c8ra05526b>
- [78] A. Al-Harrasi, S. Bhtaia, M.S. Al-Azri, H.A. Makeen, M. Albratty, H.A. Alhazmi, S. Mohan, A. Sharma, and T. Behl, "Development and characterization of chitosan and porphyrin based composite edible films containing ginger essential oil", *Polymers*, **14**, 2518 (2022). <https://doi.org/10.3390/polym14091782>
- [79] N.A. El-Zaher, M.S. Melegy, and O.W. Guirguis, "Thermal and structural analyses of PMMA/TiO<sub>2</sub> nanoparticles composites", *Nat. Sci.* **6**, 859 (2014). <https://doi.org/10.4236/NS.2014.611083>
- [80] V.G.L. Souza, J.R.A. Pires, C. Rodrigues, P.F. Rodrigues, A. Lopes, R.J. Silva, J. Caldeira, M.P. Duarte, F.B. Fernandes, I.M. Coelho, and A.L. Fernando, "Physical and morphological characterization of chitosan/montmorillonite films incorporated with ginger essential oil", *Coatings*, **9**, 700 (2019). <https://doi.org/10.3390/coatings9110700>
- [81] V. Alizadeh, H. Barzegar, B. Nasehi, and V. Samavati, "Development of a chitosan-montmorillonite nanocomposite film containing Satureja hortensis essential oil", *Iran. Food Sci. Technol. Res. J.* **13**, 131–143 (2018). <https://doi.org/10.22067/iftstr.v1396i13.64248>
- [82] E.M. Abdelrazek, I.S. Elashmawi, and S. Labeeb, "Chitosan filler effects on the experimental characterization, spectroscopic investigation and thermal studies of PVA/PVP blend films", *Physica B*, **405**, 2021–2027 (2010). <https://doi.org/10.1016/j.physb.2010.01.095>
- [83] A.W. Coats, and J.P. Redfern, "Kinetic parameters from thermogravimetric data", *Nature*, **201**, 68–69 (1964).
- [84] T. Fahmy, E.O. Abdelmutlib, M.I. Abdelhamid, W.B. Elsharkawy, Z.M. Elqahtani, and M.T. Ahmed, "TSDC of irradiated and non-irradiated cellulose acetate", *Egypt. J. Chem.* **64**, 2453–2468 (2021). <https://doi.org/10.21608/EJCHEM.2021.57068.3228>
- [85] W.B. Elsharkawy, M.T. Ahmed, E.O. Abdelmutlib, Z.M. Elqahtani, M.A. Azzam, and T. Fahmy, "Effect of  $\gamma$ -irradiation on thermally stimulated depolarization current spectra of polyethylenegrafted-poly(acrylic acid)", *Radiat. Eff. Defects Solids*, **177**, 671–687 (2022). <https://doi.org/10.1080/10420150.2022.2073880>
- [86] Y. Amaregouda, K. Kamanna, and T. Gasti, "Biodegradable polyvinyl alcohol/carboxymethyl cellulose composite incorporated with l-alanine functionalized MgO nanoplates: Physico-chemical and food packaging features", *J Inorg Organomet Polym Mater.* **32**, 2040–2055 (2022). <https://doi.org/10.1007/s10904-022-02261-9>
- [87] A.M. El-naggar, Z.K. Heiba, M.B. Mohamed, A.M. Kamal, G. Lakshminarayana, and M. Ali Shar, "Structural, linear and nonlinear optical properties of poly (vinyl alcohol) (PVA)/polyethylene glycol (PEG)/SnS<sub>2</sub>:Y nanocomposite films", *Optik*, **258**, 168941 (2022). <https://doi.org/10.1016/j.ijleo.2022.168941>
- [88] N.A. Abdel-Zaher, G.T. El-Bassyouni, M.T.H. Moselhey, and O.W. Guirguis, "Structural, thermal and optical modifications of chitosan due to UV-ozone irradiation", *Egypt. J. Chem.* **61**, 447–460 (2018). <https://doi.org/10.21608/ejchem.2018.2904.1241>
- [89] N.D. Alharbi, and O.W. Guirguis, "Macrostructure and optical studies of hydroxypropyl cellulose in pure and nano-composites forms", *Results Phys.* **15**, 102637 (2019). <https://doi.org/10.1016/j.rinp.2019.102637>
- [90] S.B. Aziz, "Morphological and optical characteristics of chitosan<sub>(1-x)</sub>:Cu<sup>x</sup> (4 ≤ x ≤ 12) based polymer nano-composites: Optical dielectric loss as an alternative method for Tauc's model", *Nanomaterials*, **7**, 444 (2017). <https://doi.org/10.3390/nano7120444>
- [91] A.S. Hassanien, and I. Sharma, "Synthesis, analysis, and characterization of structural and optical properties of thermally evaporated chalcogenide a-Cu-Zn-Ge-Se thin films", *Mater. Chem. Phys.* **311**, 128524 (2024). <https://doi.org/10.1016/j.matchemphys.2023.128524>
- [92] D.J. Borah, and A.T.T. Mostako, "Investigation on dispersion parameters of Molybdenum Oxide thin films via Wemple-DiDomenico (WDD) single oscillator model", *Appl. Phys. A* **126**, 818–825 (2020). <https://doi.org/10.1007/s00339-020-03996-3>
- [93] D.A. Nasrallah, T.H. AlAbdulaal, H.Y. Zahran, I.S. Yahia, and M.I. Mohammed, "Investigation of linear and nonlinear optical characterization of triple blended polymers incorporated with varying content of eriochrome black T dye for low-cost optical technologies and limiting absorption", *Mater. Sci. Semicond. Process.* **175**, 108179 (2024). <https://doi.org/10.1016/j.mssp.2024.108179>

- [94] J. Tauc, *Optical Properties of Amorphous Semiconductors, Amorphous and Liquid Semiconductors*, (Plenum Press, New York, 1979).
- [95] F.M. Amin, H. Abdel-Khalek, A.M. El-Sagheer, M. Abd-El Salam, and A.M. El-Mahalawy, "Detailed investigations on structural, spectroscopic, and optoelectronic properties of Ethyl Nile Blue thin films", *Phys. B: Condens. Matter*, **642**, 414141 (2022). <https://doi.org/10.1016/j.physb.2022.414141>
- [96] A.M. Ismail, M.I. Mohammed, and E.G. El-Metwally, "Influence of gamma irradiation on the structural and optical characteristics of Li ion-doped PVA/PVP solid polymer electrolytes", *Indian J. Phys.* **93**, 175–183 (2019). <https://doi.org/10.1007/s12648-018-1286-1>
- [97] O.Gh. Abdullah, S.B. Aziz, and M.A. Rasheed, "Structural and optical characterization of PVA:KMnO<sub>4</sub> based solid polymer electrolyte", *Results Phys.* **6**, 1103–1108 (2016). <https://doi.org/10.1016/j.rinp.2016.11.050>
- [98] M.T. Ahmed, A. Sarhan, Z.M. Elqahtani, W.B. Elsharkawy, M.A. Azzam, and T. Fahmy, "Linear and non-linear optical parameters of copper chloride doped poly (vinyl alcohol) for optoelectronic applications", *Egypt. J. Chem.* **65**, 99–108 (2022). <https://doi.org/10.21608/ejchem.2022.105927.4878>
- [99] M. Shkir, V. Ganesh, S. AlFaify, I.S. Yahia, and H.Y. Zahran, "Tailoring the linear and nonlinear optical properties of NiO thin films through Cr<sup>3+</sup> doping", *J. Mater. Sci.: Mater. Electron.* **29**, 6446–6457 (2018). <https://doi.org/10.1007/s10854-018-8626-y>
- [100] F.M. Ali, "Structural and optical characterization of [(PVA:PVP)-Cu<sup>2+</sup>] composite films for promising semiconducting polymer devices", *J. Mol. Struct.* **1189**, 352–359 (2019). <https://doi.org/10.1016/j.molstruc.2019.06.055>
- [101] S.H. Wemple, and M.D. DiDomenico Jr., "Behavior of the electronic dielectric constant in covalent and ionic materials", *Phys. Rev. B*, **3**, 1338–1351 (1971). <https://doi.org/10.1103/PHYSREVB.3.1338>
- [102] H.Y.S. Al-Zahrani, "Synthesis, optical and optoelectrical analysis of the Cu<sub>2</sub>CoSnS<sub>4</sub> thin films as absorber layer for thin-film solar cells", *J. Mater. Sci. Mater. Electron.* **31**, 6900–6909 (2020). <https://doi.org/10.1007/s10854-020-03252-7>
- [103] L.M. El Radaf, and A.S. Hassanien, "Effect of thickness on structural, optical, and optoelectrical properties of sprayed CuInSnS<sub>4</sub> thin films as a new absorber layer for solar cells", *Physica B*, **659**, 414867 (2023). <https://doi.org/10.1016/j.physb.2023.414867>
- [104] T.S. Soliman, S.A. Vshivkov, and S.I. Elkalashy, "Structural, linear and nonlinear optical properties of Ni nanoparticles-polyvinyl alcohol nanocomposite films for optoelectronic applications", *Opt. Mater.* **107**, 110037 (2020). <https://doi.org/10.1016/j.optmat.2020.110037>
- [105] A.S. Hassanien, "Intensive linear and nonlinear optical studies of thermally evaporated amorphous thin Cu-Ge-Se-Te films", *J. Non-Cryst. Solids*, **586**, 121563 (2022). <https://doi.org/10.1016/j.jnoncrysol.2022.121563>
- [106] S.H. Alotaibi, A.S. Radwan, Y.K. Abdel-Monem, and M.M. Makhlof, "Synthesis, thermal behavior and optical characterizations of thin films of a novel thiazole azo dye and its copper complexes", *Spectrochimica Acta Part A: Molecular and Biomolecular Spectroscopy*, **205**, 364–375 (2018). <https://doi.org/10.1016/j.saa.2018.07.043>
- [107] T.A. Taha, A.A. Azab, and M.A., Sebak, "Glycerol-assisted sol-gel synthesis, optical, and magnetic properties of NiFe<sub>2</sub>O<sub>4</sub> nanoparticles", *J. Mol. Struct.* **1181**, 14–18 (2019). <https://doi.org/10.1016/j.molstruc.2018.12.075>
- [108] M. Aslam, M. Ali Kalyar, and Z. Ali Raza, "Graphene oxides nanosheets mediation of poly(vinyl alcohol) films in tuning their structural and opto-mechanical attributes", *J. Mater. Sci. Mater. Electron.* **28**, 13401-13413 (2017). <https://doi.org/10.1007/s10854-017-7177-y>
- [109] Z.K. Heiba, A.M. El-naggar, A.M. Kamal, O.H. Abd-Elkader, and M.B. Mohamed, "Optical and dielectric properties of PVC/TiO<sub>2</sub>/TBAI ionic liquid polymer electrolyte", *Opt. Mater.* **139**, 113764 (2023). <https://doi.org/10.1016/j.optmat.2023.113764>

**ПОКРАЩЕННЯ МОЛЕКУЛЯРНО-СТРУКТУРНИХ ТА ЛІНІЙНИХ/НЕЛІНІЙНИХ ОПТИЧНИХ  
ХАРАКТЕРИСТИК НАНОКОМПЗИТНИХ ПЛІВОК ХІТОЗАНУ/ДІОКСИДУ ТИТАНУ ДЛЯ ПАКУВАННЯ  
ТА ОПТОЕЛЕКТРОННИХ ЗАСТОСУВАНЬ**

**Осіріс В. Гіргіс<sup>а</sup>, Найлаа Д. Алхарбі<sup>б</sup>**

<sup>а</sup>*Відділ біофізики, Факультет природничих наук, Каїрський університет, Гіза, Єгипет*

<sup>б</sup>*Відділ фізичних наук, Науковий коледж, Університет Джидди, Джидда, Саудівська Аравія*

Поточне дослідження спрямоване на синтез та характеристику нанокмпозитних плівок хітозану та діоксиду титану з точки зору молекулярної структури, теплових та оптичних властивостей для використання в упаковці продуктів та оптоелектронних застосувань. Інфрачервона спектроскопія з перетворенням Фур'є (FTIR) була використана для вивчення взаємодії між TiO<sub>2</sub>-NPs і хітозаном, і аналіз підтвердив, що TiO<sub>2</sub>-NPs взаємодіяли з хітозаном і продемонстрували хорошу сумісність. Диференціальна скануюча калориметрія та термогравіметричний аналіз показали, що збільшення концентрації TiO<sub>2</sub>-NP покращує термічну стабільність нанокмпозитів. Лінійні оптичні властивості в діапазоні UV-Vis (200–800 нм) вимірювали спектрофотометрично. Нижче 400 нм спектри пропускання нанокмпозитів демонструють знижений ступінь прозорості, що вказує на їх здатність повністю блокувати пропускання УФ-світла. Модель Таука була використана для ідентифікації типів електронних переходів у зразках. Модель одного осцилятора була використана для дослідження енергії та параметрів дисперсії. Також були досліджені нелінійно-оптичні властивості. UV-Vis в області (360–410 нм), аналіз показав, що збільшення концентрації TiO<sub>2</sub>-NPs від 0 до 12 мас. % зменшує край поглинання з 2,716 до 2,043 eV, зменшує пряме (3,282 до 2,798 eV) і непряме (від 2,417 до 1,581 eV) енергетичні заборонені зони, збільшили енергію Урбаха з 0,692 до 1,295 eV, зменшили енергію дисперсії з 11,324 до 5,621 eV, зменшили енергію одного осцилятора з 6,308 до 5,393 eV і покращили інші лінійні та нелінійні параметри. Результати підтверджують використання нанокмпозитних плівок CS/TiO<sub>2</sub> в пакувальній промисловості та різноманітних оптичних застосуваннях.

**Ключові слова:** хітозан; наночастинки TiO<sub>2</sub>; нанокмпозити хітозан/TiO<sub>2</sub>; FTIR аналіз; термостабільність; лінійні/нелінійні оптичні властивості

## FIRST-PRINCIPLES STUDY: THE OPTOELECTRONIC PROPERTIES OF THE WURTZITE ALLOY $In_xGa_{1-x}N$ BASED SOLAR CELLS, WITHIN MODIFIED BECKE-JOHNSON (MBJ) EXCHANGE POTENTIAL

✉ **Amina Benzina**<sup>a,b,\*</sup>, ✉ **Abdel-Djawad Zebentout**<sup>a,b</sup>, ✉ **Lakhdar Benahmedi**<sup>c</sup>, ✉ **Taieb Seddik**<sup>d</sup>,  
**Abdelhadi Lachabi**<sup>c</sup>, ✉ **Hamza Abid**<sup>e</sup>

<sup>a</sup>Faculty of Sciences and Technology (FST), University of Ain Temouchent, 46000, Algeria

<sup>b</sup>Applied Materials Laboratory (AML), Research Center, Djillali Liabes, University of Sidi Bel Abbes, 22000, Algeria

<sup>c</sup>Technology and Solids Properties Laboratory, University of Mostaganem Abdelhamid ibn Badis (UMAB), 27000, Algeria

<sup>d</sup>Laboratory of Quantum Physics of Matter and Mathematical Modeling (LPQ3M), Faculty of Sciences and Technology, Mustapha Stambouli University of Mascara, 29000, Algeria.

<sup>e</sup>Applied Materials Laboratory (AML), Research Center, Djillali Liabes, University of Sidi Bel Abbes, 22000, Algeria

\*Corresponding Author e-mail: [benzina.amina@gmail.com](mailto:benzina.amina@gmail.com), [amina.benzina@univ-temouchent.edu.dz](mailto:amina.benzina@univ-temouchent.edu.dz)

Received July 20, 2024; revised November 15, 2024; accepted November 18, 2024

Numerical simulation based on Full Potential-Linearized Augmented Plane Wave calculations (FP-LAPW) is implemented in WIEN2K code to study the fundamental structural and optoelectronic properties of the Wurtzite ternary alloy structure  $In_xGa_{1-x}N$  ( $x = 0.125, 0.375, 0.625$  and  $0.875$ ) matched on  $GaN$  substrate using a 16-atom supercell. The generalized gradient approximation of Wu and Cohen, the standard local density approach, and the Tran-Blaha modified Becke–Johnson potential was applied to improve the band structure and optical properties of the concerning compounds. Whenever conceivable, we compare the obtained results by experiments and computations performed with diverse computational scheme. In those alloys, the essential points in the optical spectra display the passage of electrons from the valance band to the unoccupied states in the conduction band. The results lead that Becke-Johnson potential will be a promising potential for the bandgaps engineering of III-V compounds which supplied that those materials had crucial absorption coefficients that lead to the application for optoelectronics components, especially solar cells.

**Keywords:** Full Potential-Linearized Augmented Plane Wave (FP-LAPW);  $In_xGa_{1-x}N$ ; Tran and Blaha modified Becke-Johnson potential (TB-mBJ); Wurtzite; Solar cells

**PACS:** 71.15.m, 71.15.Ap, 71.15.Mb, 71.20.b, 71.55.Eq, 78.20.Ci

### 1. INTRODUCTION

III-Nitrides elements such as  $AlN$ ,  $GaN$ ,  $InN$  and their alloys, have all the coveted physical properties for prodigious of tomorrow's optoelectronic devices [1], which developed one of the numerous studied subjects of semiconductors, essentially due to their diverse applications in optoelectronics and high-power/high-temperature electronics.

Significant III-V semiconductors are in the Zinc-blende structure; however, the III-nitrides exist in the Wurtzite phase; though, their metastable Zinc-blende structures were more described and studied [2]. The  $AlN$ ,  $GaN$  and  $InN$  crystallize in the stable structure Wurtzite (Wz) [3], this structure is broadly employed because of the band gap nature (direct) in III-nitride semiconductors [4].

In contrast, III-nitrides (III-Ns) have started to accomplish significant consideration toward the photovoltaic application [5].  $InN$  is a suited semiconductor material since its base temperature necessity, enormous carrier mobility and little electron effective mass that affords the application in photovoltaic devices [6]. The band gap of  $InN$  was lately found to be 0.7 eV rather than the previous considered 1.3 eV. Since the band gap of  $In_xGa_{1-x}N$  comprising the whole spectrum variation, tunable by 0.7 eV for  $InN$  to 3.4 eV for  $GaN$ . Therefore, permitting the design of multi-junction solar cell with ideal band gap for maximum efficiency [7].

The Wurtzite structure is suitable for growing most III-nitride semiconductors [8]. Growth of  $InGaN$  with adequate elevate  $In$  incorporation (in fact to attain green emission) has established problematic, while: The lattice mismatch among  $GaN$  and  $InN$  equal approximate 11% [9].  $InN$  and  $In$ -rich  $InGaN$  alloys have not been investigated thoroughly because of difficulties associated with the growth of these compound [10]. By expanding the thickness of  $InGaN$  layer with high indium ( $In$ ) content to absorbing light, the material quality turns out to be much more dreadful [11]. Indium gallium nitride ( $InGaN$ ) based alloys are widely applied in the domain of optoelectronics, such as light-emitting diodes (LEDs) and laser diodes (LDs). Recently,  $InGaN$ -based alloys concerned much research attention in solar cell application [11]. To date, the  $InGaN$  heterojunction solar cells using a semi-bulk absorber (multi-layered  $InGaN/GaN$  structure) [12]. Textured surface has been performed on  $InGaN$ -based solar cells [13].  $In_xGa_{1-x}N/GaN$  double heterojunction solar cells [7].

To supplement the existing experimental and theoretical studies and to afford a basis [14] for explaining notions for new components and their applications, the calculations of the structural, electronic properties and the optical spectra of Wz  $In_xGa_{1-x}N$  ternary alloys in this framework are presented using first-principles calculations.

The recent theoretical calculations and studies now a day are done utilizing DFT (density functional theory), it has become an important tool in the treatment of many-body problems in atomic, molecular, solid state, and nuclear physics including optical properties of many-body systems [15].

Toward deeper knowledge, slightly extensive experimental and first-principles calculations studies for the ternary alloys  $In_xGa_{1-x}N$  with  $x$  varying  $0 \leq x \leq 1$  have accomplished in the research to perform a significant matching, [4, 16-18]. Therefore, our study could provide as a source of perspective for future searches.

The most prominent interest of DFT lies in its ability to execute computations without empirical parameters as inputs, whose relieves up application exceedingly from constraints set by experiments [19], the first-principles calculations based on DFT was performed in the WIEN2k code [20].

After the introduction, the paper has been arranged in three sections. In Section 2, we concisely illustrate the computational method applied in this study. The important results accomplished for the structural, electronic, and optical properties of  $In_xGa_{1-x}N$  ternary alloys are exhibited and discussed in Section 3. Subsequently, the conclusions in Section 4.

## 2. COMPUTATIONAL DETAIL

The precise and important theoretical solution of the structural, electronic, optical, and magnetic properties of metals and semiconductors is the Kohn-Sham formation [21-23].

The nitrides compounds crystallize in Zinc-blende (space group  $F43m$ ) and Wurtzite structure (space group  $P63mc$ ), Fig. 1 illustrate the stable structure Wurtzite of the binary  $InN$  and  $GaN$  obtained by the WIEN 2k code.

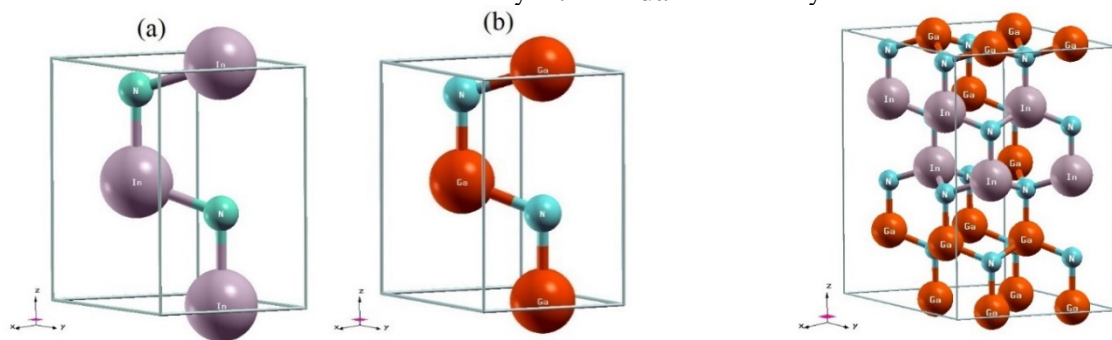


**Figure 1.** Illustration of a  $1 \times 1 \times 1$  conventional hexagonal cell- Wurtzite: (a)  $InN$  and (b)  $GaN$ .

**Figure 2.** Illustration of a  $2 \times 2 \times 2$  Wurtzite  $In_{0.375}Ga_{0.625}N$  supercell

The current calculations in this study of the physical properties of the Wurtzite ternary alloy  $A_xB_{1-x}N$  ( $In_xGa_{1-x}N$ ), so that  $x$  signifies  $In$  composition, were performed by the FP-LAPW method based on the DFT executed in the WIEN2k package [24]. To model  $A_xB_{1-x}N$  Wurtzite alloy, we used a 16-atom  $A_nB_{8-n}N_8$  supercell, ( $2 \times 2 \times 2$ ) that is twice the size of a primitive Wurtzite unit cell in base plane direction [4]. The realized model of crystal structures of ternary  $In_xGa_{1-x}N$  alloys is shown in Fig. 2.

The exchange and correlation effects were handled applying three different approximations: the Wu and Cohen Generalized Gradient Approximation (GGA-WC) functional [25,26], the Standard Local Density Approach (LDA), and the Tran and Blaha modified Becke-Johnson exchange potential (TB-mBJ) [25,27,28] is performed to procure a larger band gap value that is generally underestimated by LDA and GGA [25]. For the total and partial Densities Of States (DOS) we considered the orbitals of  $In$  ( $4d^{10}5s^25p^1$ ),  $Ga$  ( $3d^{10}4s^24p^1$ ) and  $N$  ( $2s^22p^3$ ) as valence electrons.

An entirely relativistic calculation moreover scalar relativistic approximation for core and valence state, respectively, without spin-orbit interaction, were employed. In the interstitial region, the plane wave cut-off value of  $RMT \cdot K_{max} = 7$  was used [6], where  $RMT$  is the minimum radius of the Muffin-Tin spheres are set to 2.04, 1.84, 1.70 atomic units (a.u) for  $In$ ,  $Ga$  and  $N$  respectively, and  $K_{max}$  provides the magnitude of the largest  $K$  vector in the plane wave basis [29]. The maximum  $l$  quantum number of the wave function expansion inside the atomic sphere was defined to  $l_{max} = 10$  [24], for the Fourier expansion the charge density was extended to  $G_{max} = 12$  ( $a.u$ )<sup>-1</sup>. The Brillion Zone (BZ) integration has been formed applying Monkhorst-Pack Special K-points approach [30].

## 3. RESULTS AND DISCUSSION

### 3.1 Structural properties

First, we performed the structural properties of the binary compounds  $InN$  and  $GaN$  in the both structures Wurtzite (Wz) and Zinc-blende (Zb). The  $InN$  and  $GaN$  are reported by ( $1 \times 1 \times 1$ ) conventional hexagonal cell (Wurtzite) and face centered cubic (Zinc-blende).

The computed total energies within GGA as a function of the volume were employed for the perception of theoretical lattice constant and bulk modulus. The equilibrium energy  $E_0$ , the Bulk modulus  $B_0$ , its first derivative  $B_0'$ , and the balance volume at zero pressure  $V_0$ , by fitting the calculated total energy to the Murnaghan's equation of state (EOS) [31], which is allowed with WIEN2k package.

From Fig. 3 we noticed that the Wz phase was found to be more stable than the Zinc-blende phase for the *InN* and *GaN* compounds. The calculated lattice constants and bulk modulus are arranged in Table I.

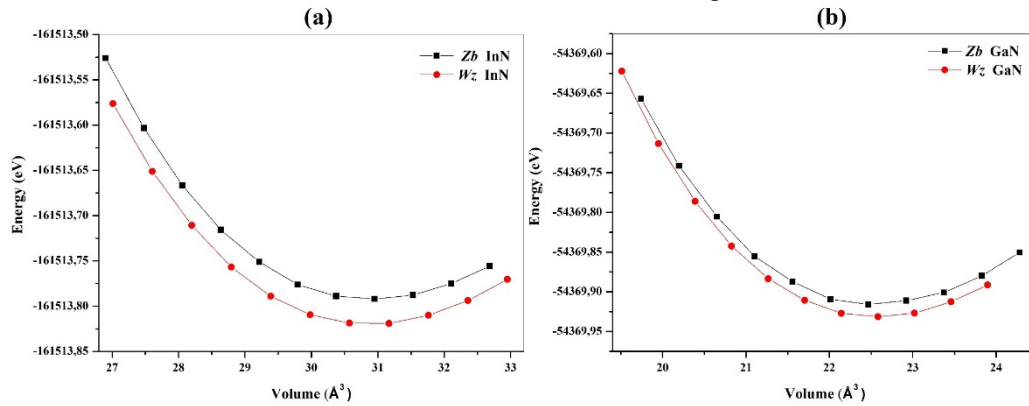


**Figure 3.** Total energies as a function of volume for the (a) *InN* and (b) *GaN* for Zb and Wz phases.

**Table I.** Lattice constant  $a$  and  $c$ , bulk modulus  $B$  and its first derivative  $B'$  of *InN* and *GaN*, compared to other experimental or theoretical data, the lattice mismatch  $\Delta(a_o)$  and  $\Delta(c_o)$  are indicated in the table.

Material	$a(\text{\AA})$			$c(\text{\AA})$			$\Delta(a_o)$	$\Delta(c_o)$	$B(\text{GPa})$		$B'$	
	Our	Other	Exp	Our	Other	Exp			Our	Other	Our	Other
<i>InN</i>	3.57	3.59 <sup>a</sup>	3.53 <sup>a</sup>	5.80	5.78 <sup>a</sup>	5.69 <sup>a</sup>	0.04	0.11	123.41	--	4.18	--
		3.54 <sup>d</sup>	3.51 <sup>c</sup>		5.70 <sup>d</sup>	5.66 <sup>c</sup>	0.06	0.14				
		3.54 <sup>f</sup>	3.55 <sup>e</sup>		5.71 <sup>f</sup>	5.74 <sup>e</sup>	0.02	0.06				
<i>GaN</i>	3.21	3.23 <sup>a</sup>	3.19 <sup>a</sup>	5.24	5.26 <sup>a</sup>	5.18 <sup>a</sup>	0.02	0.06	176.80	--	4.20	--
		3.18 <sup>b</sup>	3.15 <sup>c</sup>		5.18 <sup>b</sup>	5.14 <sup>c</sup>	0.06	0.10				
		3.19 <sup>d</sup>	3.18 <sup>e</sup>		5.18 <sup>d</sup>	5.18 <sup>e</sup>	0.03	0.06				
		3.18 <sup>f</sup>			5.18 <sup>f</sup>							

<sup>a</sup>Ref [32], <sup>b</sup>Ref [33], <sup>c</sup>Ref [34], <sup>d</sup>Ref [35], <sup>e</sup>Ref [36], <sup>f</sup>Ref [37]

The obtained lattice constant parameters  $a$  and  $c$  for the Wurtzite *InN* and *GaN* were somewhat bigger than the experimental lattice constant parameters, the shift in lattice parameter set as  $\Delta(a_o)$  and  $\Delta(c_o)$ . For further details, no experimental data were possible for the Bulk modulus  $B_0$  and its first derivative  $B_0'$ .

The element configuration of ternary alloy  $In_xGa_{1-x}N$  acts a notable part in both physical properties and the epitaxial growth process. To study the fundamental structural properties of the ternary alloys  $In_xGa_{1-x}N$  matched on *GaN* substrate for composition of  $0 \leq x \leq 1$ , we have considered all studied of the ternary alloys in Wz phase which is the stable compared with Zinc-blende whereas the ternary alloys  $In_xGa_{1-x}N$  with 16 atoms with 25% intervals of  $x$ .

Reviewing the Vegard's law validity for the Wurtzite ternary alloy  $In_xGa_{1-x}N$ , the lattice constant is commonly denoted as a linear function depend on  $x$  concentration of the compounds. The Vegard's law [38] is applicable for the both  $a$  and  $c$  lattice parameters as below:

$$a_{In_xGa_{1-x}N} = xa_{InN} + (1-x)a_{GaN}, \quad (1)$$

$$c_{In_xGa_{1-x}N} = xc_{InN} + (1-x)c_{GaN}. \quad (2)$$

The obtained lattice constants of  $In_xGa_{1-x}N$  are summarized in Table II, its clearly observed that the lattice constant  $a$  and  $c$  are in inversely proportional relation with the Indium incorporation.

**Table II.** Lattice constant  $a$  and  $c$  calculated by The Vegard's law of  $In_xGa_{1-x}N$ , compared to other experimental work results.

Materials	$a(\text{\AA})$		$c(\text{\AA})$	
	Our	Exp	Our	Exp
$In_{0.125}Ga_{0.875}N$	3.24	3.20 <sup>a</sup>	5.31	5.21 <sup>a</sup>
$In_{0.375}Ga_{0.625}N$	3.33	3.30 <sup>a</sup>	5.45	5.35 <sup>a</sup>
$In_{0.625}Ga_{0.375}N$	3.43	3.38 <sup>a</sup>	5.59	5.49 <sup>a</sup>
$In_{0.875}Ga_{0.125}N$	3.52	3.47 <sup>a</sup>	5.73	5.64 <sup>a</sup>

<sup>a</sup>Ref [4]

### 3.2 Electronic properties

The energy band gap of a semiconductor is an essential key which is extremely useful for their efficient employment in optoelectronic and different photonic devices. Its small variation can completely modify the utilization in the optoelectronic devices. Therefore, the knowledge of the character of the band gaps of the current materials and their

precise values whether by experiments or calculations are not only significant for their technological applications as well as their band gap tailoring [2].

It is entirely comprehended that the most accurate GGA and LDA undervalue the band gap of semiconductors, the reason is the regardless of the quasiparticle excitations in DFT. To defeat this obstacle, the mBJ approach was employed to produce a band gap approaching the experiment value.

The bandgap energy formula of the  $In_xGa_{1-x}N$  is depicted as below:

$$E_g(x) = x \cdot E_g(InN) + (1 - x) \cdot E_g(GaN) - b \cdot x \cdot (1 - x), \quad (3)$$

where  $E_g(x)$ ,  $E_g(InN)$ ,  $E_g(GaN)$  are the bandgap energy for the respective  $In_xGa_{1-x}N$ ,  $InN$  and  $GaN$ , and  $b$  is the bandgap bowing parameter [39], the Vegard's law is convenient for the lattice constants of relaxed  $InGaN$ . Recent studies propose that the bowing parameter values depend to the indium incorporation, so that for  $0 \leq x \leq 0.5$  the bowing is 1.4 eV, and for  $0 \leq x \leq 1$ , the bowing be 1.15 eV or 2.5 eV [4].

Accordingly, the calculated results completed of energy at the point  $\Gamma$  of high-symmetry on the Brillouin zone for the studied binary and ternary compounds using the WC-GGA, LDA, TB-mBJ are summarized in Table III, together with previous experimental results.

**Table III.** Energy band gap  $E_g$  of  $GaN$ ,  $InN$  and  $In_xGa_{1-x}N$  calculated with WC-GGA, LDA, TB-mBJ and Vegard's law compared to other experimental or theoretical data.

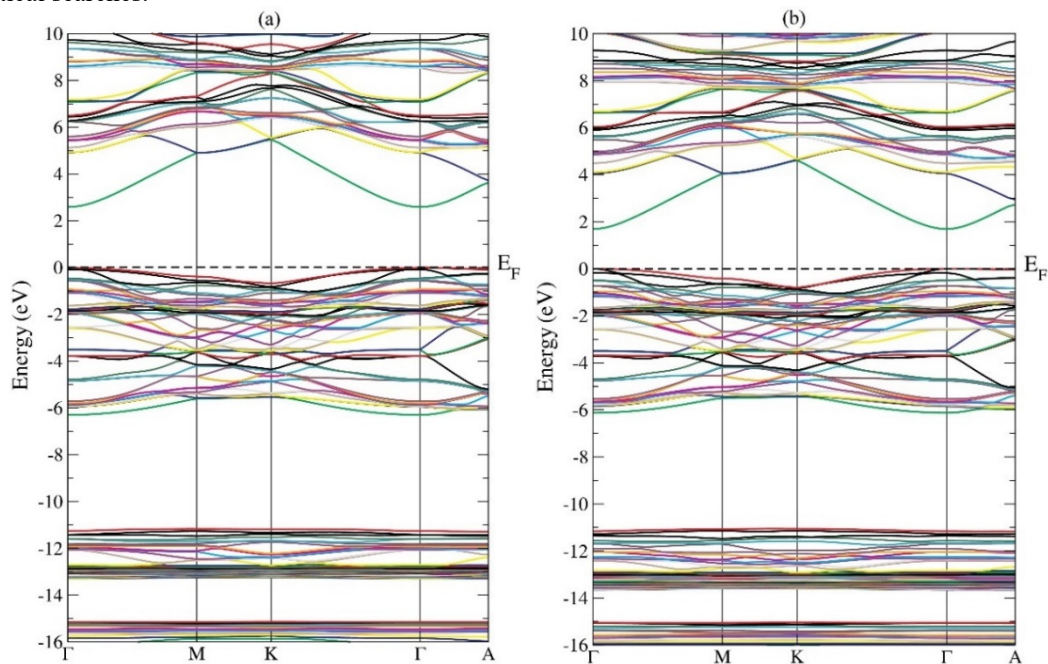
Materials	$E_g$ (eV)					
	WC-GGA	LDA	TB-mBJ	Vegard's law bowing 1.11	Calculations bowing 2.5	Exp
$InN$	0.00	0.00	0.77	--	--	0.70 <sup>a</sup> - 0.77 <sup>b</sup>
$In_{0.125}Ga_{0.875}N$	1.24	1.31	2.58	2.61	2.46	2.88 <sup>b</sup> - 3.10 <sup>c</sup>
$In_{0.375}Ga_{0.625}N$	0.49	0.55	1.68	1.91	1.58	1.95 <sup>b</sup> - 2.62 <sup>c</sup>
$In_{0.625}Ga_{0.375}N$	0.03	0.08	1.17	1.35	1.02	1.38 <sup>b</sup>
$In_{0.875}Ga_{0.125}N$	0.00	0.00	0.82	0.93	0.77	0.85 <sup>b</sup>
$GaN$	1.67	1.75	3.01	--	--	3.50 <sup>a</sup> - 3.42 <sup>b</sup> - 3.42 <sup>c</sup>

<sup>a</sup> Ref [16]. <sup>b</sup> Ref [4]. <sup>c</sup> Ref [18].

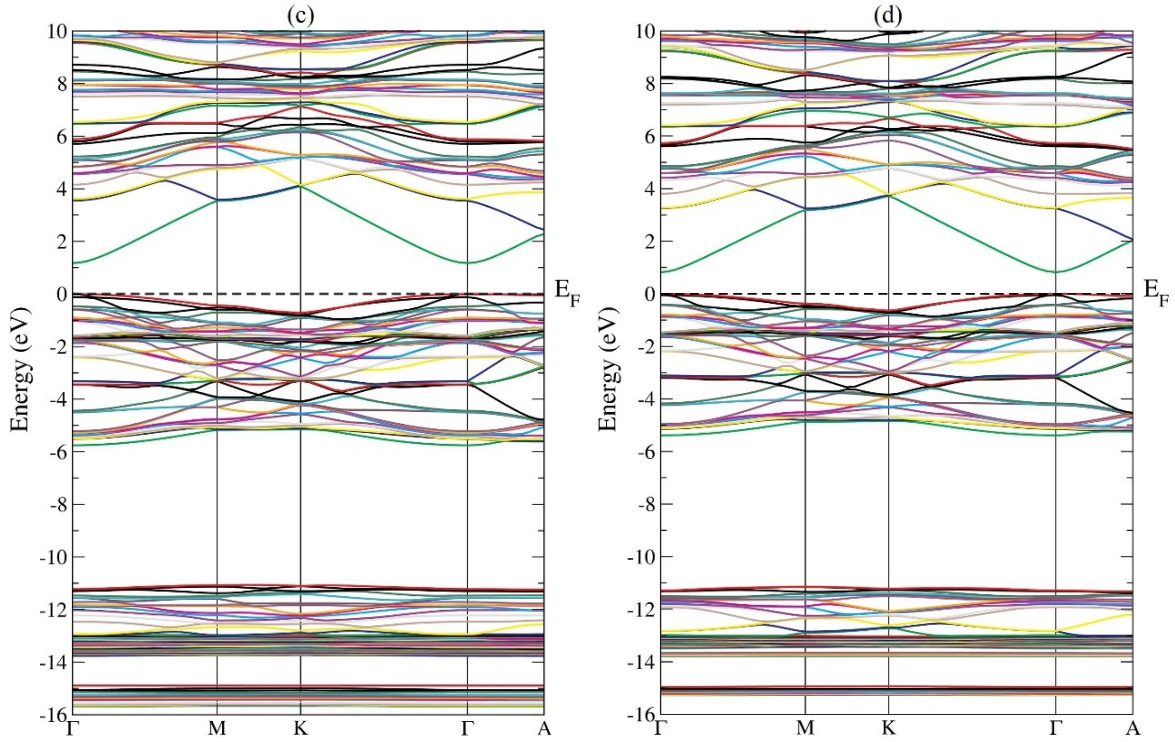
It is obviously noticed that the calculated band gap values (Table III) with TB-mBJ display a clear improvement over the previously calculated values using Vegard's law.

Fig. 4 present the band structure of the considered ternary alloy  $In_xGa_{1-x}N$ , the high-symmetry lines through the first irreducible Brillouin zone estimated within mBJ approach.

The Valance Band Maximum (VBM) and the Conduction Band Minimum (CBM) appear at the  $\Gamma$  point showing that the studying materials have a direct band gap. Those results correspond properly through the precedent experimental and theoretical searches.



**Figure 4.** Band structures within TB-mBJ for (a)  $In_{0.125}Ga_{0.875}N$ , (b)  $In_{0.375}Ga_{0.625}N$ , (c)  $In_{0.625}Ga_{0.375}N$  and (d)  $In_{0.875}Ga_{0.125}N$  (continued on the next page)



**Figure 4.** Band structures within TB-mBJ for (a)  $In_{0,125}Ga_{0,875}N$ , (b)  $In_{0,375}Ga_{0,625}N$ , (c)  $In_{0,625}Ga_{0,375}N$  and (d)  $In_{0,875}Ga_{0,125}N$ .

The data of energy band gap using the WC-GGA, LDA and TB-mBJ approximations depicted in Table III are plotted in Fig. 5.

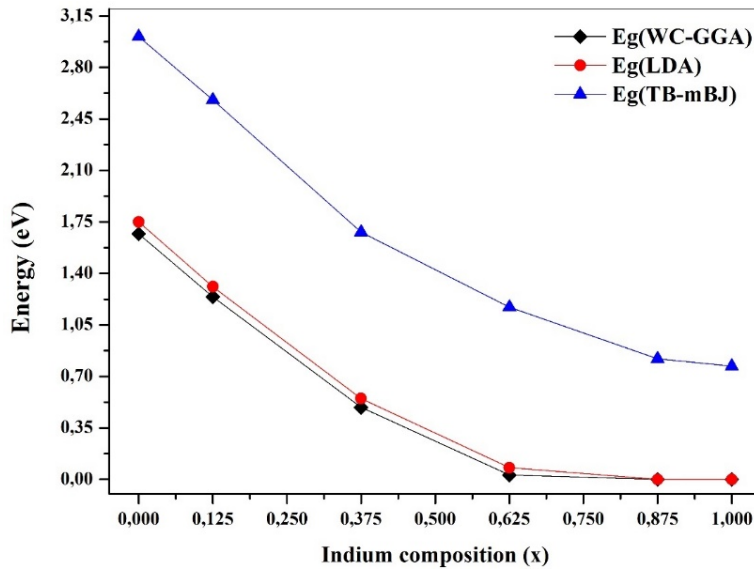


**Figure 5.** Band gap energy as a function of Indium concentration.

This last one displays that at small Indium composition, a notable bowing can be achieved however at huge indium composition, the bowing could be negligible.

Therefore, the Band gap energy can be characterized as a function of the Indium composition, the  $E_g$  is fitted and expressed by the following equations:

$$E_g^{WC-GGA}(x) = 1.68 - 4.13x + 2.46x^2, \tag{4}$$

$$E_g^{LDA}(x) = 1.76 - 4.15x + 2.39x^2, \tag{5}$$

$$E_g^{TB-mBJ}(x) = 3.03 - 4.25x + 1.98x^2. \tag{6}$$

These equations are related to the formula (3), where the bowing  $b = 2.46, 2.39$  and  $1.98$  corresponding the respective approximations WC-GGA, LDA and Tb-mBJ.

The information of the electron density of states (DOS) is wanted to comprehend and simplify, the calculated band structure to know the contributing atomic states, the total and the partial DOS of the studied ternary  $In_{0,125}Ga_{0,875}N$ ,  $In_{0,375}Ga_{0,625}N$ ,  $In_{0,625}Ga_{0,375}N$  and  $In_{0,875}Ga_{0,125}N$  respectively are plotted in Fig. 6, which are estimated using the TB-mBJ scheme. We have considered the inner-shell electrons in the valence electrons of  $In$  ( $4d^{10}5s^25p^1$ ),  $Ga$  ( $3d^{10}4s^24p^1$ ), and  $N$  ( $2s^22p^3$ ) shells [40].

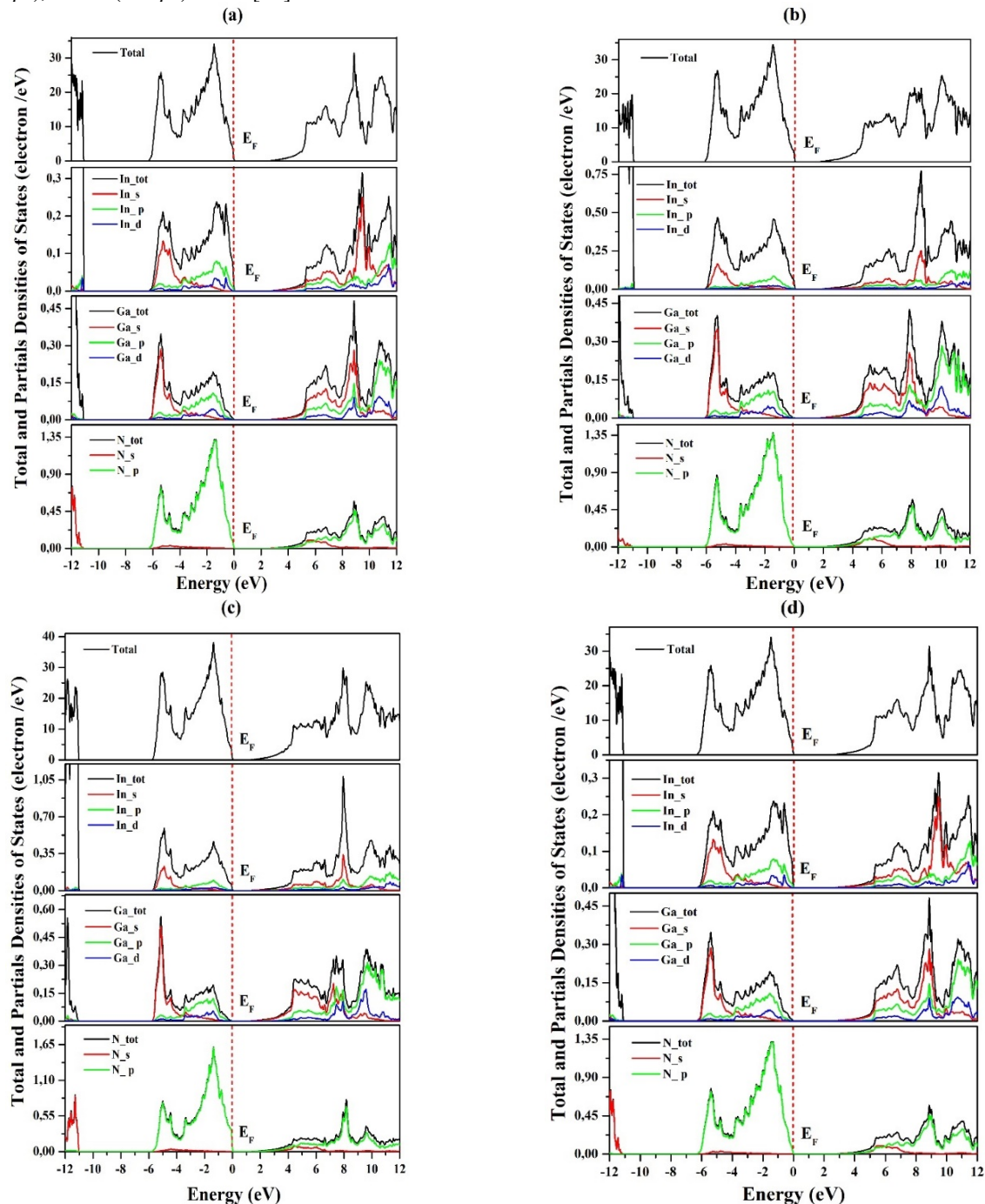


**Figure 6.** Total and partial densities of states for (a)  $In_{0,125}Ga_{0,875}N$ , (b)  $In_{0,375}Ga_{0,625}N$ , (c)  $In_{0,625}Ga_{0,375}N$  and (d)  $In_{0,875}Ga_{0,125}N$  compounds

It is obviously shown from Fig. 6, the state's lesser  $E_F$  the valence band be divided by two region the narrow range between  $-13.08$  eV to  $-11.06$  eV, mainly originates from the hybridization of  $In$  s/p,  $Ga$  s/p and  $N$  /s states. The wider region from  $-6.08$  eV to Fermi level contain two peaks, the first between  $-6.08$  to  $-4.10$  eV is mainly occupied by  $N$  /p,  $Ga$  /s and  $In$  /s states while the second from  $-4.10$  eV approaching to fermi level is densely dominated by  $N$  /p,  $Ga$  P/d and  $In$  p/d states.

The studied ternary compounds note a definite energy gap among the valance and the conduction energy bands of 2.58, 1.68, 1.17 and 0.82 eV for the  $In_{0.125}Ga_{0.875}N$ ,  $In_{0.375}Ga_{0.625}N$ ,  $In_{0.625}Ga_{0.375}N$  and  $In_{0.875}Ga_{0.125}N$  respectively, the alloys system preserving its semiconductor character. Hence, the dominant conduction electron states possess a composition from several  $N$  /p,  $Ga$  s/p/d and  $In$  s/p.

### 3.3 Optical properties

The optical properties are straightly correlated to the electronic band gap of a semiconductor, characterizing the interaction of electromagnetic radiations with a material. The dielectric function  $\varepsilon(\omega)$  acts an essential part in exploring the optical properties of a compound.

To provide an excellent optical properties of the WZ semiconductors, a 480  $k$ -points was achieved into the irreducible part of Brillouin zone ( $BZ$ ) integration using the TB-mBJ exchange potential for the  $In_{0.125}Ga_{0.875}N$ ,  $In_{0.375}Ga_{0.625}N$ ,  $In_{0.625}Ga_{0.375}N$  and  $In_{0.875}Ga_{0.125}N$ .

The dielectric function can be written as  $\varepsilon(\omega) = \varepsilon_1(\omega) + i\varepsilon_2(\omega)$ , illustrates the material response to the photon spectrum, where the imaginary part of the dielectric function  $\varepsilon_2(\omega)$  signifies the optical absorption in the crystal, those able to acquire from the momentum matrix elements through the occupied and unoccupied eigenstates. It signifies the diversity of inter-band transitions in a semiconductor and the real part  $\varepsilon_1(\omega)$  of the dielectric function is related to the imaginary part  $\varepsilon_2(\omega)$  by employing the Kramers Kronig (KK) relations [41].

$$\varepsilon_1(\omega) = 1 + \frac{2}{\pi} P \int_0^{\infty} \frac{\omega' \varepsilon_2(\omega')}{\omega'^2 - \omega^2} d\omega'. \quad (7)$$

Different optical properties can be determined from the dielectric function, selected the refractive index  $n(\omega)$ , the extinction coefficient  $k(\omega)$ , the reflectivity  $R(\omega)$ , and the absorption coefficient  $\alpha(\omega)$ , within the following relations [42]:

$$n(\omega) = \sqrt{\frac{|\varepsilon(\omega)| + \varepsilon_1(\omega)}{2}}, \quad (8)$$

$$K(\omega) = \sqrt{\frac{|\varepsilon(\omega)| - \varepsilon_1(\omega)}{2}}, \quad (9)$$

$$R(\omega) = \frac{(n(\omega)-1)^2 + k(\omega)^2}{(n(\omega)+1)^2 + k(\omega)^2}, \quad (10)$$

$$\alpha(\omega) = \frac{4\pi}{\lambda} k(\omega). \quad (11)$$

Where,  $\lambda$  is the wavelength of light in the vacuum.

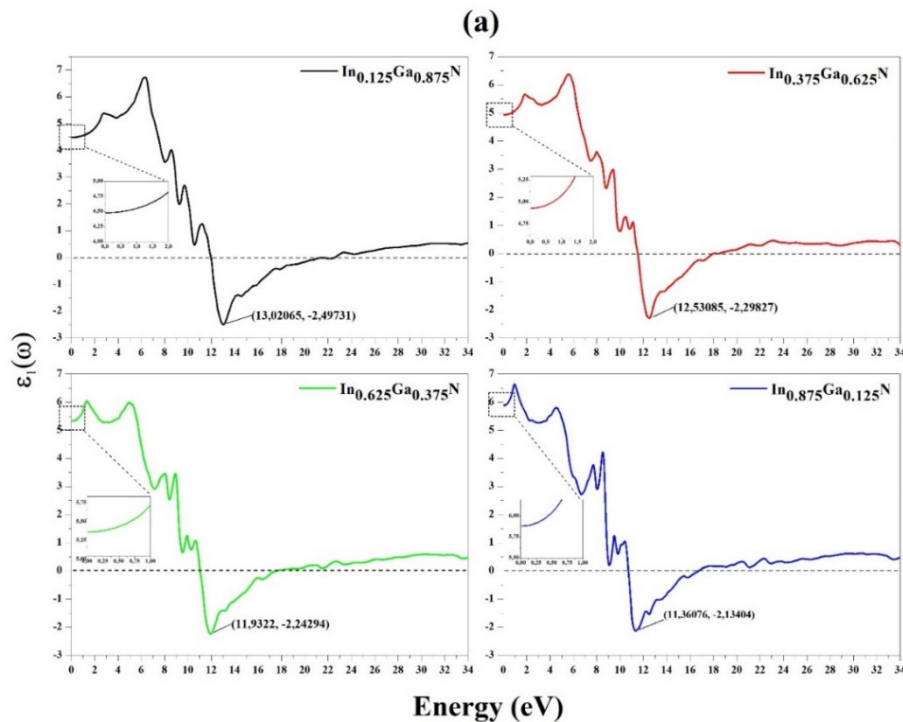


**Figure 7.** Real part  $\varepsilon_1(\omega)$  (a) and imaginary part  $\varepsilon_2(\omega)$  (b) for  $In_{0.125}Ga_{0.875}N$ ,  $In_{0.375}Ga_{0.625}N$ ,  $In_{0.625}Ga_{0.375}N$  and  $In_{0.875}Ga_{0.125}N$  (continued on the next page)

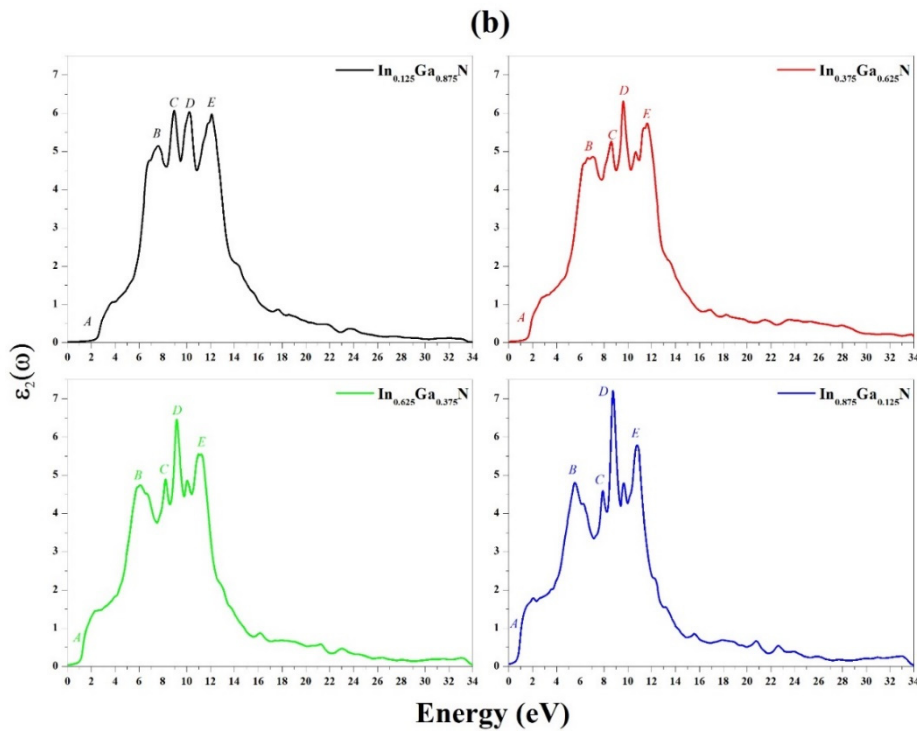


**Figure 7.** Real part  $\epsilon_1(\omega)$  (a) and imaginary part  $\epsilon_2(\omega)$  (b) for  $In_{0.125}Ga_{0.875}N$ ,  $In_{0.375}Ga_{0.625}N$ ,  $In_{0.625}Ga_{0.375}N$  and  $In_{0.875}Ga_{0.125}N$

Fig.7 (a) show the real part of dielectric function  $\epsilon_1(\omega)$ , afford the static dielectric constant  $\epsilon_1(0)$  presented in Table IV. The inversely proportional relation between the  $\epsilon_1(0)$  and  $E_g$  can be defined by the Penn model [43],

$$\epsilon \approx 1 + (\hbar\omega_p/E_g)^2. \quad (12)$$

Where,  $\omega_p$  is the plasma frequency, and  $\hbar = h/2\pi$  ( $h$  is the Planck constant).

**Table IV.** Collected the peak positions of  $\epsilon_2(\omega)$ , static dielectric constant  $\epsilon_1(0)$ , refractive index  $n(0)$  and Static reflectivity  $R(0)$  for  $In_{0.125}Ga_{0.875}N$ ,  $In_{0.375}Ga_{0.625}N$ ,  $In_{0.625}Ga_{0.375}N$  and  $In_{0.875}Ga_{0.125}N$ .

Materials	Critical points					Static dielectric constant $\epsilon_1(0)$	Static refractive index $n(0)$	Static reflectivity $R(0)$
	A	B	C	D	E			
$In_{0.125}Ga_{0.875}N$	2.58	7.55	8.93	10.22	12.05	4.49	2.11	0.128
$In_{0.375}Ga_{0.625}N$	1.68	7.07	8.64	9.60	11.65	4.93	2.22	0.144
$In_{0.625}Ga_{0.375}N$	1.17	6.06	8.24	9.19	11.11	5.33	2.30	0.156
$In_{0.875}Ga_{0.125}N$	0.82	5.56	7.89	8.71	10.75	5.88	2.42	0.172

$\epsilon_1(\omega)$  rises within a small energy margin, then decreases for values less than one, the lower values of  $\epsilon_1(\omega)$  occurs at 13.02, 12.53, 11.93 and 11.36 eV for the  $In_{0.125}Ga_{0.875}N$ ,  $In_{0.375}Ga_{0.625}N$ ,  $In_{0.625}Ga_{0.375}N$  and  $In_{0.875}Ga_{0.125}N$ , respectively. These values correspond to the higher values of the reflectivity shown in Fig.7 (a). Furthermore, when  $\epsilon_1(\omega)$  attains a stability when getting energy more than (>22, 18, 17 and 16) eV for the respective ternary  $In_{0.125}Ga_{0.875}N$ ,  $In_{0.375}Ga_{0.625}N$ ,  $In_{0.625}Ga_{0.375}N$  and  $In_{0.875}Ga_{0.125}N$ , designating that the incident photons cross the material without any notable interaction.

From Fig.7 (b), the calculated  $\epsilon_2(\omega)$  spectra reveal that the first crucial point A, further set as optical's absorption edge occurs at 2.58 eV, 1.68 eV, 1.17 eV and 0.82 eV which represent the direct optical transitions for the respective compounds  $In_{0.125}Ga_{0.875}N$ ,  $In_{0.375}Ga_{0.625}N$ ,  $In_{0.625}Ga_{0.375}N$  and  $In_{0.875}Ga_{0.125}N$ . The electronic optical transitions (represented by peaks B, C, D and E given in Table IV among the valence band and conduction band at  $\Gamma_{15v}-\Gamma_{1c}$  symmetry point, originate the absorption region.

As provides in Fig. 8 (a), the reflectivity reached the maximum in the photon energy range (12.53 to 16.55) eV, (11.84 to 15.40) eV, (11.51 to 15.06) eV and (10.88 to 14.56) eV for the compounds  $In_{0.125}Ga_{0.875}N$ ,  $In_{0.375}Ga_{0.625}N$ ,  $In_{0.625}Ga_{0.375}N$  and  $In_{0.875}Ga_{0.125}N$ , respectively.

This Prominent reflectance is explained to the resonance plasmon rising in the Ultraviolet range. Furthermore, the  $In$  integration decrease proportionally the maximum value of the reflectivity as below 0.48, 0.46, 0.45 and 0.44 (a.u) for the respective  $In$  concentration ( $x = 0.125, 0.375, 0.625$  and  $0.875$ ).

The refractive index follows the pattern of  $\epsilon_1(\omega)$ , It is seen from the Fig.8(b) that  $n(\omega)$  spectra increase and reach a peak value of 2.67 at 6.48 eV, 2.60 at 5.72 eV, 2.52 at 5.23 eV and 2.57 at 0.93 eV for the respective  $In_{0.125}Ga_{0.875}N$ ,  $In_{0.375}Ga_{0.625}N$ ,  $In_{0.625}Ga_{0.375}N$  and  $In_{0.875}Ga_{0.125}N$  compounds. Beyond the maximum, the spectra decrease inferior to 1. As the bandgap is decreased when we increase the In amount, while  $n(0)$  alter vice versa with the band gap of the compounds as mentioned in the Table III. The Refractive index inferior than unity ( $vg = c/n$ ) exhibits that the group velocity of the incident radiation is bigger than the lightspeed  $c$  [44,45]. It signifies that the group velocity shift to negative domain and the material turn into superluminal for high energy photons.

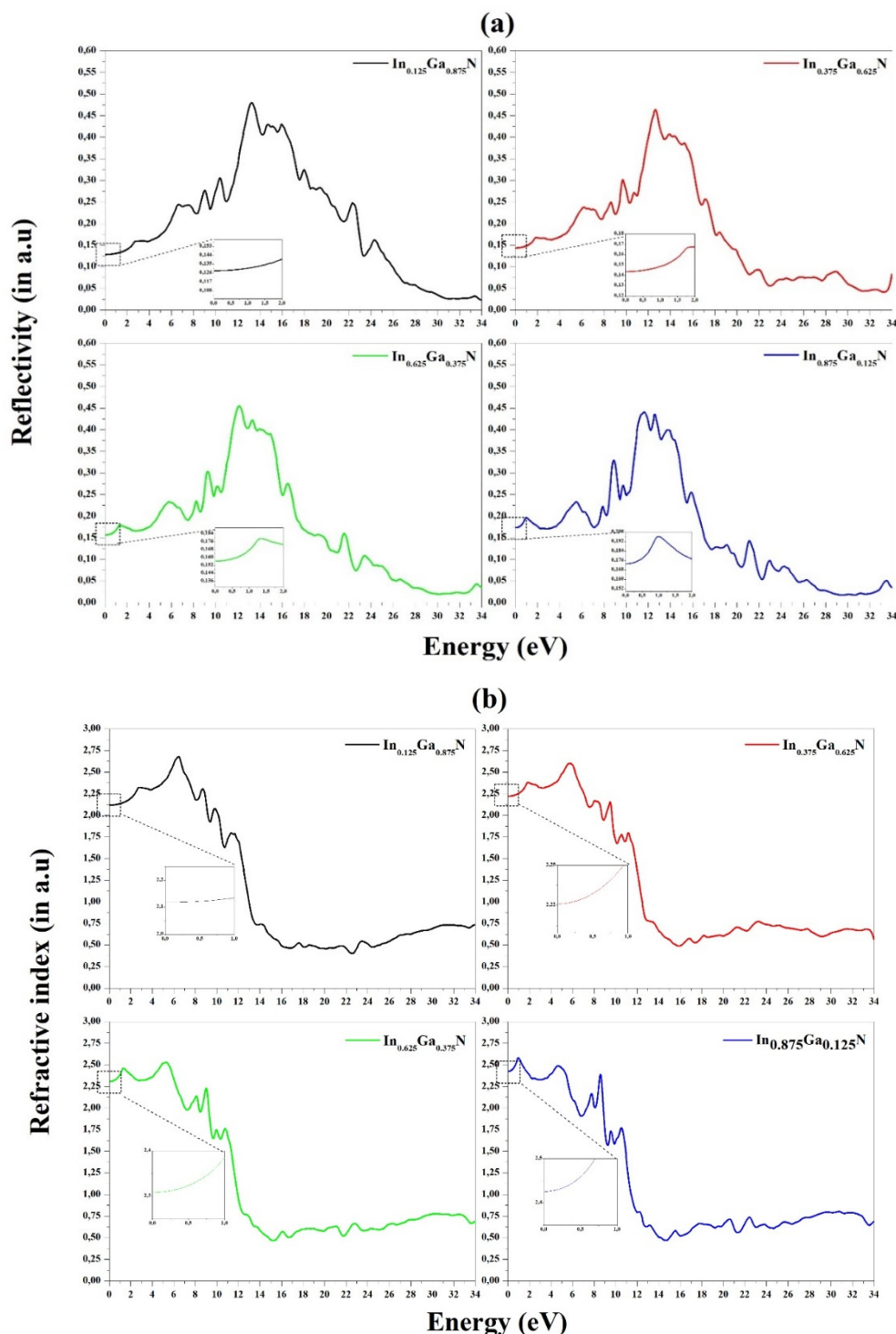


**Figure 8.** Reflectivity  $R(\omega)$  (a) and (b) Refractive index  $n(\omega)$  for  $In_{0.125}Ga_{0.875}N$ ,  $In_{0.375}Ga_{0.625}N$ ,  $In_{0.625}Ga_{0.375}N$  and  $In_{0.875}Ga_{0.125}N$ .

It is clearly from the absorption  $\alpha(\omega)$  spectra plotted in Fig. 9, that the absorption edge occurs at the energy values 2.58, 1.68, 1.17 and 0.82 eV for the compounds  $In_{0.125}Ga_{0.875}N$ ,  $In_{0.375}Ga_{0.625}N$ ,  $In_{0.625}Ga_{0.375}N$  and

$In_{0,875}Ga_{0,125}N$ , respectively. These previous values are identical to the energy gaps of  $\Gamma v - \Gamma c$ . The absorption coefficient is the most important characterizing the solar cells, the maximum  $\alpha(\omega)$  is 248.41, 231.96, 219.30 and 211.55 for  $In$  concentration of ( $x = 0.125, 0.375, 0.625$  and  $0.875$ ), therefore confirm [46] study, that for  $In$  poor region ( $x$  less or equal 25%) of the  $In_xGa_{1-x}N$  may allow the possibility of appropriate bandgap engineering for solar cell utilization.

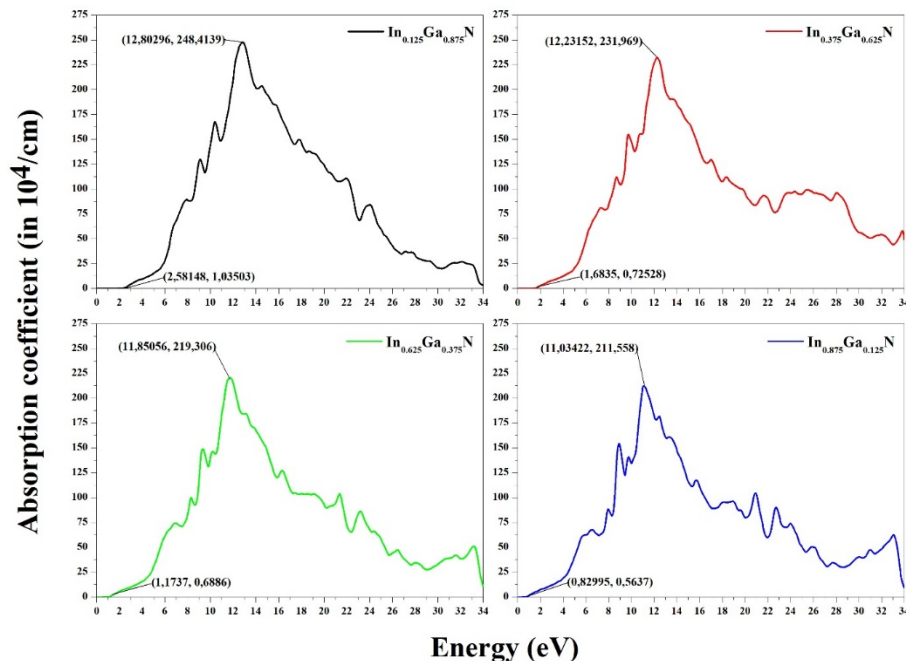


Figure 9. Absorption coefficient  $\alpha(\omega)$  for  $In_{0,125}Ga_{0,875}N$ ,  $In_{0,375}Ga_{0,625}N$ ,  $In_{0,625}Ga_{0,375}N$  and  $In_{0,875}Ga_{0,125}N$

#### 4. CONCLUSIONS

Theoretical study of structural, electronic and optical properties of III-Nitrides alloys based on “FP-LAPW” calculation method, implementing LDA, GGA and mBJ approximations. These ternary compounds  $In_{0,125}Ga_{0,875}N$ ,  $In_{0,375}Ga_{0,625}N$ ,  $In_{0,625}Ga_{0,375}N$  and  $In_{0,875}Ga_{0,125}N$  have Wurtzite structure. The bandgaps nature of these materials is direct  $\Gamma v - \Gamma c$ . It is inferred that mBJ is an adequate theoretical method for the computation of the band structures of III/V materials. The findings require that mBJ will be a favorable potential for the bandgaps engineering of III/V compounds. In those alloys, the critical points in the optical spectra reveal the passage of electrons from valance band to the unoccupied states in the conduction band. The zero-frequency edge of  $\epsilon_1(0)$  and  $n(0)$  show a reversed link with the bandgaps. From the interpretation of optical graphs, it is provided that those materials are implemented for optoelectronics components [ $In$  poor region ( $x$  less or equal 25%) of the  $In_xGa_{1-x}N$ ] in ultraviolet energy ranges and for solar cells application.

#### Acknowledgements

The authors are grateful to the Directorate-General for Scientific Research and Technological Development (DGRSDT) for the supplied support to perform this research.

#### ORCID

© Amina Benzina, <https://orcid.org/0000-0002-9375-3006>; © Abdel-Djawad Zebentout, <https://orcid.org/0000-0002-9503-7716>  
 © Lakhdar Benahmedi, <https://orcid.org/0009-0008-0895-6820>; Taieb Seddik, <https://orcid.org/0000-0002-5777-1338>  
 © Hamza Abid, <https://orcid.org/0000-0001-9647-7425>

#### REFERENCES

- [1] Liu, F., Wang, T., Gao, X., Yang, H., Zhang, Z., Guo, Y., ... & Wang, X. “Determination of the preferred epitaxy for III-nitride semiconductors on wet-transferred graphene,” *Science Advances*, **9**(31), eadf8484 (2023). <https://doi.org/10.1016/j.commsci.2024.113264>
- [2] G. Rehman, et al., “Electronic Band Structures of the Highly Desirable III-V Semiconductors: TB-mBJ DFT Studies,” *J. Electron. Mater.* **45**, 3314 (2016). <https://doi.org/10.1007/s11664-016-4492-7>
- [3] Benbedra, A., Meskine, S., Boukortt, A., & Abbassa, H. “Polarization Properties of Wurtzite III-Nitride Alloys Using the Hexagonal Reference Structure,” *ECS Journal of Solid-State Science and Technology*, **12**(10), 103008 (2023). <https://doi.org/10.1149/2162-8777/acfe9a>
- [4] B.-T. Liou, S.-H. Yen, and Y.-K. Kuo, “Vegard’s law deviation in band gaps and bowing parameters of the wurtzite III-nitride ternary alloys,” in: *Semiconductor Lasers and Applications II*, vol. 5628, edited by J.Q. Yao, Y.J. Chen, and S. Lee, (International Society for Optics and Photonics, SPIE, 2005), pp. 296–305, <https://doi.org/10.1117/12.575300>

- [5] C.J. Praharaaj, *Group III-Nitride Semiconductor Optoelectronics*, (John Wiley & Sons, 2023).
- [6] M. Aslan, *et al.*, “Structural and electronic properties of  $\text{In}_x\text{P}_{1-x}$  alloy in full range ( $0 \leq x \leq 1$ ),” *Philosophical Magazine*, **96**, 991 (2016). <https://doi.org/10.1080/14786435.2016.1149248>
- [7] Chouchen, B., Ducroquet, F., Nasr, S., Alzahrani, A. Y., Hajjiah, A. T., & Gazzah, M. H.  $\text{In}_x\text{Ga}_{1-x}\text{N}/\text{GaN}$  double heterojunction solar cell optimization for high temperature operation. *Solar Energy Materials and Solar Cells*, **234**, 111446 (2022). <https://doi.org/10.1016/j.solmat.2021.111446>
- [8] Giorgi, G., Amato, M., Ossicini, S., Cartoixa, X., Canadell, E., & Rurali, R. “Doping of III–V arsenide and phosphide wurtzite semiconductors,” *The Journal of Physical Chemistry C*, **124**(49), 27203-27212 (2020). <https://dx.doi.org/10.1021/acs.jpcc.0c09391>
- [9] Imran, A., Sulaman, M., Yousaf, M., Anwar, M. A., Qasim, M., Dastgeer, G., ... & Wang, X. “Growth of High Mobility InN Film on Ga-Polar GaN Substrate by Molecular Beam Epitaxy for Optoelectronic Device Applications,” *Advanced Materials Interfaces*, **10**(20), 2200105 (2023). <https://doi.org/10.1002/admi.202200105>
- [10] Reilly, C. E., Keller, S., Nakamura, S., & DenBaars, S. P. “InN quantum dots by metalorganic chemical vapor deposition for optoelectronic applications,” *Frontiers in Materials*, **8**, 647936 (2021). <https://doi.org/10.3389/fmats.2021.647936>
- [11] H. Abboudi, H. EL Ghazi, R. En-nadir, M.A. Basyooni-M. Kabatas, A. Jorio, I. Zorkani, “Efficiency of InN/InGaN/GaN Intermediate-Band Solar Cell under the Effects of Hydrostatic Pressure, In-Compositions, Built-in-Electric Field, Confinement, and Thickness,” *Nanomaterials*, **14**, 104 (2024). <https://doi.org/10.3390/nano14010104>
- [12] R. Belghouthi, A. Rached, M. Aillerie, et al., “N-Face Semi-Bulk Absorber Boosts Conversion Efficiency of InGaN Solar Cell,” *J. Electron. Mater.* **52**, 7566–7575 (2023). <https://doi.org/10.1007/s11664-023-10662-w>
- [13] A. Bouadi, H. Naim, A. Djelloul, Y. Benkrima, R. Fares, “Enhancing the efficiency of the gallium indium nitride (InGaN) solar cell by optimizing the effective parameters,” *Chalcogenide Letters*, **19**(9), 611-619 (2022). <https://doi.org/10.15251/CL.2022.199.611>
- [14] Benahmedi, L., Besbes, A., & Djelti, R. “Structural, magnetic, elastic, and thermoelectric properties of  $\text{Ba}_2\text{InOsO}_6$  double perovskite in the cubic phase: A DFT+ U study with spin-orbit-coupling,” *Journal of Magnetism and Magnetic Materials*, **611**, 172629. (2024). <https://doi.org/10.1016/j.jmmm.2024.172629>
- [15] Lakhdar, B., Anissa, B., Radouan, D., Al Bouzieh, N., & Amrane, N. “Structural, electronic, elastic, optical and thermoelectric properties of  $\text{ASiCl}_3$  (A= Li, Rb and Cs) chloroperovskites: a DFT study,” *Optical and Quantum Electronics*, **56**(3), 313 (2024). <https://doi.org/10.1007/s11082-023-06045-4>
- [16] L.C. de Carvalho, *et al.*, “Ab initio calculation of optical properties with excitonic effects in wurtzite  $\text{In}_x\text{Ga}_{1-x}\text{N}$  and  $\text{In}_x\text{Al}_{1-x}\text{N}$  alloys,” *Physical Review B*, **87**, 195211 (2013). <https://doi.org/10.1103/PhysRevB.87.195211>
- [17] S. A. Hashemizadeh, and S. V. Mohammadi, “First-Principles Investigation of Density of States and Electron Density in Wurtzite  $\text{In}_{0.5}\text{Ga}_{0.5}\text{N}$  Alloys with GGA-PBESol Method,” *Journal of Nanostructures*, **6**, 273 (2016) <https://doi.org/10.22052/jns.2016.40758>
- [18] W.-W. Lin and Y.-K. Kuo, “Band structures and bandgap bowing parameters of wurtzite and zincblende III-nitrides,” in: *Semiconductor Lasers and Applications*, vol. 4913, edited by Y. Luo and Y. Nakano, (International Society for Optics and Photonics, SPIE, 2002), pp. 236-247. <https://doi.org/10.1117/12.482239>
- [19] N. N. Anua, *et al.*, “DFT Investigations of the Optical Properties of Gallium Arsenide”, in: *Advanced Materials Research*, vol. 895, (Trans. Tech. Publications Ltd, 2014), pp. 429–438, <https://doi.org/10.4028/www.scientific.net/AMR.895.429>
- [20] K. Schwarz, and P. Blaha, “Solid state calculations using WIEN2k,” *Computational Materials Science*, **28**, 259 (2003). [https://doi.org/10.1016/S0927-0256\(03\)00112-5](https://doi.org/10.1016/S0927-0256(03)00112-5)
- [21] B. Amin, and I. Ahmad, “Theoretical investigation of half metallicity in Fe/Co/Ni doped ZnSe material systems,” *Journal of Applied Physics*, **106**, 093710 (2009). <https://doi.org/10.1063/1.3256186>
- [22] P. Hohenberg, and W. Kohn, “Inhomogeneous Electron Gas,” *Physical Review*, **136**, B864 (1964). <https://doi.org/10.1103/PhysRev.136.B864>
- [23] W. Kohn, and L. J. Sham, “Self-Consistent Equations Including Exchange and Correlation Effects,” *Physical Review*, **140**, A1133 (1965). <https://doi.org/10.1103/PhysRev.140.A1133>
- [24] M. Dadsetani, B. Kianisadr, and H. Nejatipour, “First Principles Investigation of the Optical Properties of  $\text{BN}_x\text{P}_{1-x}$  ( $0 \leq x \leq 1$ ) Boron Ternary Alloys,” *J. Electron. Mater.* **44**, 2699-2711 (2015). <https://doi.org/10.1007/s11664-015-3691-y>
- [25] B.-T. Liou, and C.-W. Liu, “Electronic and Structural Properties of zincblende  $\text{Al}_x\text{In}_{1-x}$ ,” *Optics Communications*, **274**, 361 (2007). <https://doi.org/10.1016/j.optcom.2007.02.040>
- [26] B. Amin, et al., “Ab initio study of the bandgap engineering of  $\text{Al}_{1-x}\text{Ga}_x\text{N}$  for optoelectronic applications,” *Journal of Applied Physics*, **109**, 023109 (2011). <https://doi.org/10.1063/1.3531996>
- [27] A. Benzina, *et al.*, “First-principles calculation of structural, optoelectronic properties of the cubic  $\text{Al}_x\text{Ga}_y\text{In}_{1-x-y}\text{N}$  quaternary alloys matching on AlN substrate, within modified Becke–Johnson (mBJ) exchange potential,” *Optik*, **127**, 11577 (2016). <https://doi.org/10.1016/j.ijleo.2016.09.014>
- [28] D. Koller, F. Tran, and P. Blaha, “Merits and limits of the modified Becke–Johnson exchange potential,” *Physical Review B*, **83**, 195134 (2011). <https://doi.org/10.1103/PhysRevB.83.195134>
- [29] M. B. Asfia, and M. A. Rashid, “First-Principles Study of Half Metallic Ferromagnetic and Optical Properties of Nb Doped Cubic ZnS using TB-mBJ Approximation,” *Dhaka University Journal of Science*, **69**, 194–201 (2022). <https://doi.org/10.3329/dujs.v69i3.60030>
- [30] S. Berri, “Theoretical analysis of the structural, electronic, optical and thermodynamic properties of trigonal and hexagonal  $\text{Cs}_3\text{Sb}_2\text{I}_9$  compound,” *The European Physical Journal B*, **93**, 1-12 (2020). <https://doi.org/10.1140/epjb/e2020-10143-1>
- [31] V. Tyuterev, and N. Vast, “Murnaghan’s equation of state for the electronic ground state energy,” *Computational Materials Science*, **38**, 350 (2006). <https://doi.org/10.1016/j.commatsci.2005.08.012>
- [32] R. Nunez-Gonzalez, *et al.*, “First-principles calculation of the band gap of  $\text{Al}_x\text{Ga}_{1-x}\text{N}$  and  $\text{In}_x\text{Ga}_{1-x}\text{N}$ ,” *Revista Mexicana de fisica*, **54**, 111 (2008). <https://www.redalyc.org/pdf/570/57019061017.pdf>
- [33] S. Stepanov, *et al.*, “Influence of Poisson’s ratio uncertainty on calculations of the bowing parameter for strained InGaN layers,” *MRS Internet Journal of Nitride Semiconductor Research*, **6**, e6 (2001). <https://doi.org/10.1557/S1092578300000181>

- [34] A. I. Duff, L. Lymperakis, and J. Neugebauer, "Understanding and controlling indium incorporation and surface segregation on  $\text{In}_x\text{Ga}_{1-x}\text{N}$  surfaces: An ab initio approach," *Physical Review B*, **89**, 085307 (2014). <https://doi.org/10.1103/PhysRevB.89.085307>
- [35] P. Rinke, et al., "Consistent set of band parameters for the group-III nitrides AlN, GaN, and InN," *Physical Review B*, **77**, 075202 (2008). <https://doi.org/10.1103/PhysRevB.77.075202>
- [36] A. Belabbes, et al., "Cubic inclusions in hexagonal AlN, GaN, and InN: Electronic states," *Physical Review B*, **84**, 125108 (2011). <https://doi.org/10.1103/PhysRevB.84.125108>
- [37] S.-H. Wei, et al., "Breakdown of the band-gap-common-cation rule: The origin of the small band gap of InN," *Physical Review B*, **67**, 165209 (2003). <https://doi.org/10.1103/PhysRevB.67.165209>
- [38] Tian, Z., Zhang, P., Sun, W., Yan, B., & Sun, Z. "Vegard's law deviating  $\text{Ti}_2$  ( $\text{Sn}_x\text{Al}_{1-x}$ ) C solid solution with enhanced properties," *Journal of Advanced Ceramics*, **12**(8), 1655-1669 (2023). <http://dx.doi.org/10.26599/JAC.2023.9220779>
- [39] E. Sakalauskas, et al., "Dielectric function and bowing parameters of InGaN alloys," *Physica Status Solidi (b)*, **249**, 485 (2012). <https://doi.org/10.1002/pssb.201100334>
- [40] Waack, J. M., Schäfer, N. A., Czerner, M., & Heiliger, C. "Structural, elastic, and electronic properties of cubic zinc-blende  $\text{In}_x\text{Ga}_{1-x}\text{N}$  alloys," *Physical Review B*, **110**(19), 195201 (2024). <https://doi.org/10.1103/PhysRevB.110.195201>
- [41] M. O'Donnell, E.T. Jaynes, and J.G. Miller, "Kramers–Kronig relationship between ultrasonic attenuation and phase velocity," *The Journal of the Acoustical Society of America*, **69**, 696 (1981). <https://doi.org/10.1121/1.385566>
- [42] Z.-Y. Jiao, S.-H. Ma, and Y.-L. Guo, "Simulation of optical function for phosphide crystals following the DFT band structure calculations," *Computational and Theoretical Chemistry*, **970**, 79 (2011). <https://doi.org/10.1016/j.comptc.2011.05.030>
- [43] Resendiz-Hernandez, G., Leal-Perez, J. E., Herrera-Basurto, R., Mercader-Trejo, F. E., Auciello, O., & Hurtado-Macias, A. "Structural properties, bandgap, and complex dielectric function in  $\text{Bi}_2\text{Te}_3$  thermoelectric by valence electron energy loss spectroscopy (VEELS) analysis," *Journal of Alloys and Compounds*, **965**, 171420 (2023). <https://doi.org/10.1016/j.jallcom.2023.171420>
- [44] R. Ali, et al., "The structural, electronic and optical response of IIA–VIA compounds through the modified Becke–Johnson potential," *Physica B: Condensed Matter*, **410**, 93 (2013). <https://doi.org/10.1016/j.physb.2012.09.050>
- [45] G. Murtaza, et al., "First principle study of cubic perovskites:  $\text{AgTF}_3$  ( $T=\text{Mg, Zn}$ )," *Physica B: Condensed Matter*, **406**, 4584 (2011). <https://doi.org/10.1016/j.physb.2011.09.026>
- [46] A. Khetrou, I. Zeydi, M. Chellali, M.B. Arbia, Mansouri, S., Helal, H., & Maaref, H. "Simulation and optimization of InGaN Schottky solar cells to enhance the interface quality," *Superlattices and Microstructures*, **142**, 106539 (2020). <https://doi.org/10.1016/j.spmi.2020.106539>

#### БАЗОВІ ДОСЛІДЖЕННЯ: ОПТОЕЛЕКТРОННІ ВЛАСТИВОСТІ СОНЯЧНИХ ЕЛЕМЕНТІВ НА ОСНОВІ СПЛАВУ ВЮРЦИТА $\text{In}_x\text{Ga}_{1-x}\text{N}$ В МЕЖАХ МОДИФІКОВАНОГО ОБМІННОГО ПОТЕНЦІАЛУ БЕКЕ–ДЖОНСОНА (МВJ)

Аміна Бензіна<sup>a,b</sup>, Абдель-Джавад Зебентут<sup>a,b</sup>, Лахдар Бенахмеді<sup>c</sup>, Тайєб Седік<sup>d</sup>, Абдельхаді Лачабі<sup>e</sup>, Хамза Абід<sup>e</sup>

<sup>a</sup>Факультет наук і технологій (FST), Університет Айн-Темушент, 46000, Алжир

<sup>b</sup>Лабораторія прикладних матеріалів (AML), дослідницький центр, Джілалі Ліабес, Університет Сіді-Бель-Аббес, Алжир

<sup>c</sup>Лабораторія технологій і властивостей твердих тіл, Університет Мосаганем Абдельхамід ібн Бадіс (UMAB), Алжир

<sup>d</sup>Лабораторія квантової фізики матерії та математичного моделювання (LPQ3M), факультет природничих наук і технологій, Мустафа Стамбулі Університет Маскара, Алжир

<sup>e</sup>Лабораторія прикладних матеріалів (AML), дослідницький центр, Джілалі Ліабес, Університет Сіді-Бель-Аббес, Алжир

Чисельне моделювання на основі розрахунків повної лінеаризованої розширеної плоскої хвилі (FP-LAPW) реалізовано в коді WIEN2K для вивчення фундаментальних структурних і оптоелектронних властивостей потрібної структури сплаву Wurtzite  $\text{In}_x\text{Ga}_{1-x}\text{N}$  ( $x = 0,125, 0,375, 0,625$  і  $0,875$ ) узгоджено на підкладці GaN за допомогою 16-атомної суперкомірки. Узагальнене градієнтне наближення Ву та Коена, стандартний підхід локальної щільності та Тран-Блаха модифікований потенціал Бекке–Джонсона, були застосовані для покращення зонної структури та оптичних властивостей відповідних сполук. Коли це можливо, ми порівнюємо отримані результати за допомогою експериментів і обчислень, виконаних за різними обчислювальними схемами. У цих сплавах основні точки в оптичних спектрах відображають перехід електронів із валентної зони до незаповнених станів у зоні провідності. Результати свідчать про те, що потенціал Беке Джонсона буде багатообіцяючим потенціалом для розробки заборонених зон сполук III-V, які показали, що ці матеріали мають вирішальні коефіцієнти поглинання, які призводять до застосування для компонентів оптоелектроніки, особливо сонячних елементів.

**Ключові слова:** повна потенційно-лінеаризована доповнена плоска хвиля (FP-LAPW);  $\text{In}_x\text{Ga}_{1-x}\text{N}$ ; Тран і Блаха модифікований потенціал Беке-Джонсона (ТВ-мВJ); вюрцит; сонячні елементи

## MASS TRANSFER AND MHD FREE CONVECTION FLOW ACROSS A STRETCHING SHEET WITH A HEAT SOURCE AND CHEMICAL REACTION

 Sunmoni Mudoi<sup>a</sup>,  Satyabhushan Roy<sup>a</sup>,  Dipak Sarma<sup>a</sup>,  Ankur Kumar Sarma<sup>a,b\*</sup>

<sup>a</sup>Department of Mathematics, Cotton University, Guwahati-781001, India

<sup>b</sup>Department of Mathematics, Baosi Banikanta Kakati College, Nagaon, Barpeta-781311, India

\*Corresponding Author e-mail: [ankurkumarsarma44@gmail.com](mailto:ankurkumarsarma44@gmail.com)

Received June 30, 2024; revised October 4, 2024; in final form November 20, 2024; accepted November 25, 2024

This work examines mass transfer and MHD free convective flow across a stretching sheet in the presence of a heat source and a chemical reaction. The sheet's stretching action propels the flow, while a magnetic field applied perpendicular to the flow direction influences it. The effects of gradients in temperature and concentration on buoyant forces are also taken into account. The continuity, momentum, energy, and concentration equations are among the coupled nonlinear partial differential equations that regulate the system. Similarity transformations are used to convert these equations into a system of ordinary differential equations, which are then numerically solved using *bvp4c* techniques. In this investigation, magnetic, buoyancy, chemical reaction rate, and heat source factors are the main parameters of interest. The outcomes show the influence of these parameters on the boundary layer's temperature, concentration, and velocity profiles. To quantify the mass transfer rate, heat transfer rate, and shear stress at the sheet surface, the skin friction coefficient, Nusselt number, and Sherwood number are calculated. By manipulating the magnetic field, chemical reactions, and heat generation, the work offers important new insights into how to best utilise MHD flows in industrial processes, such as polymer manufacturing, chemical reactors, and cooling systems.

**Keywords:** *MHD; Stretching Surface; Heat source; Chemical reaction; bvp4c*

**PACS:** 47.55.P-, 44.05.+e, 82.80.Dx, 44.40.+a

### INTRODUCTION

An intricate and crucial subject in fluid mechanics, especially for industrial and engineering applications, is the study of magnetohydrodynamic (MHD) free convective flow and mass transfer over a stretching sheet with a chemical reaction and heat source. Heat transfer, chemical processes, magnetic fields, fluid dynamics, and heat transfer are all intricately entwined in the study of MHD free convective flow and mass transfer across a stretching sheet and with a heat source [20-21]. These studies' main goal is to comprehend how these variables affect flow and transfer characteristics, which can help create industrial processes that are more productive and efficient. Improved heat and mass transfer rates, flow separation control, and overall engineering system performance are all aided by this research.

Stretching sheets are surfaces that extend in a specific direction and are frequently modelled as moving with either a linear or nonlinear velocity. Owing to its applications in industrial operations including metal processing, polymer extrusion, and electronic device cooling, the study of fluid flow over a stretching sheet is a significant problem in fluid mechanics [4-5]. When comparing the analysis of fluid flow across a stretching sheet with slip conditions to the traditional no-slip boundary condition, more intricacy is added. Where the premise of no-slip may not hold true, slip conditions are crucial to understanding different types of micro- and nanoscale fluxes [14-16]. Double stratification's impact on heat transmission and magnetohydrodynamic (MHD) Williamson fluid boundary layer flow over a stretching or contracting sheet submerged in a porous medium is a complicated topic with important implications in a range of industrial and technical operations [17-18]. It is a crucial procedure to investigate how radiation affects flow and heat transfer across an unstable, stretched sheet. The interplay of radiative heat transfer, fluid flow, and heat transfer in the boundary layer that forms over a stretching sheet whose velocity varies with time is the subject of the problem [23].

A fluid's density, viscosity, and electrical conductivity can all change as a result of a chemical reaction occurring within it. The heat source and chemical kinetics may be coupled if the reaction rate is temperature-dependent. It is examined how a chemical reaction magnetohydrodynamics (MHD) viscous fluid flows steadily over a two-dimensional boundary layer with suction and injection over a diminishing sheet by Y. Khan [2]. Mahabaleswar et al [12] studied the influence of a magnetic field on mixed convection heat transfer through Casson fluid flow across a porous material when thermo-diffusion mechanisms involving carbon nanotubes are present. Examining the interaction between molecules and the dissipation of viscosity in MHD convection flow across an infinite vertical plate embedded in a porous material using the Soret effect by Goud et al [19]. The temperature distribution inside the fluid is impacted by the presence of a heat source. This in turn may affect the fluid's electrical conductivity, density (by thermal expansion), and pace of chemical reaction [3]. K. Raghunath et al [7] examine the effects of radiation absorption and thermos diffusion on an unsteady magnetohydrodynamic flow past a moving plate that is infinitely vertical and permeable while thermal radiation, heat absorption, and a homogenous chemical reaction are present and the suction is varied. The steady free convection of an electrically conducting viscous and incompressible fluid in the coexistence of magnetic and suction/injection parameters

is studied in a vertically oriented porous channel with a line/point heat source/sink (point/line heat generation/absorption) at various channel positions by Jha et al [8]. Ramudu [9] investigates how a constant convective magnetohydrodynamic shear-thickening liquid stream across a vertically extended sheet is affected by viscous dissipation stimuli.

Studying the movement of a species (solute) inside a fluid is known as mass transfer in the context of MHD free convective flow over a stretching sheet with a chemical reaction and heat source. Reaction kinetics, convection, and diffusion all work together to control this process. Applications in industrial and technical processes, such as material processing, chemical reactors, and cooling systems, require a thorough understanding of these interactions. The behaviour of the concentration, temperature, and flow fields under different circumstances can be predicted by numerically solving these equations [1]. Aspects of mass and heat transport in MHD flow across an exponentially stretched sheet involving chemical reactions was studied by Paul and Das [13]. In the presence of a steady transverse magnetic field, the impact of a chemical reaction on the free convective flow and mass transfer of a viscous, incompressible, and electrically conducting fluid over a stretching surface is examined by Afify [22].

The novelty of this study is that it looks into 2D, steady flow, heat and mass transfer over a stretched sheet that has a heat source and a chemical process going on. According to the author's best knowledge, no researcher has earlier studied the combined effects of heat source and chemical reaction with the boundary conditions used in this article. Additionally, the hall effect is not taken into account since only a weak magnetic field is being addressed. To do the analysis, we usually have to solve a set of linked partial differential equations that control the flow, concentration, and temperature of the fluid while taking magnetic fields, gravity, chemical processes, and heat generation into account. Additionally, the new findings are thought to be pretty good when compared to earlier research.

### MATHEMATICAL FORMULATION

We examine the mass transfer and steady free convective flow of an electrically conducting, viscous, and incompressible fluid across a stretching sheet. The sheet is being stretched at a rate proportionate to the distance from the fixed origin,  $x=0$ , by applying two equal and opposing forces along the  $x$ -axis. Figure 1 illustrates the imposition of the uniform transverse magnetic field  $B_0$  along the  $y$ -axis. There is very little magnetic field created by the electrically conductive fluid moving. For tiny magnetic Reynolds numbers, this assumption is correct. Additionally, it is believed that there is no external electric field and that the electric field created by charge polarisation is very small. Neglect is given to the pressure gradient and viscous dissipations. Viscous dissipations and the pressure gradient are disregarded. It is believed that the species concentration and temperature will disappear far away from the sheet and are kept at specified constant values,  $T_w$  and  $C_w$ .

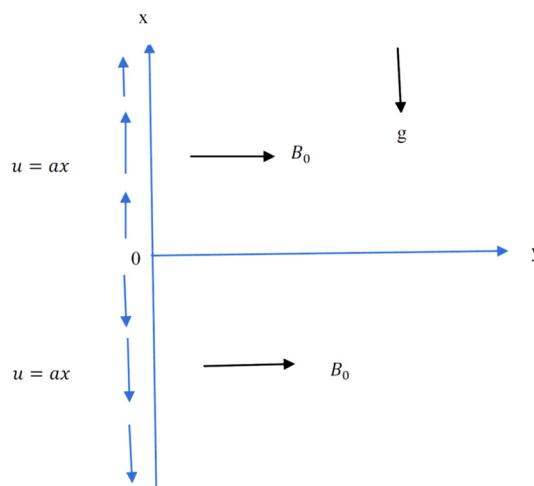


Figure 1. Coordinate system and Physical model of the problem

With the Boussinesq approximation and these presumptions in place, the governing equations for the laminar boundary layer flow's continuity, motion, energy, and species diffusion are as follows:

$$u \frac{\partial u}{\partial x} + v \frac{\partial u}{\partial y} = \nu \frac{\partial^2 u}{\partial y^2} + g\beta T + g\beta^* C - \frac{\sigma B_0^2}{\rho} u, \tag{1}$$

$$u \frac{\partial T}{\partial x} + v \frac{\partial T}{\partial y} = \frac{k}{\rho c_p} \frac{\partial^2 T}{\partial y^2} + \frac{Q}{\rho c_p} T, \tag{2}$$

$$u \frac{\partial C}{\partial x} + v \frac{\partial C}{\partial y} = D \frac{\partial^2 C}{\partial y^2} - k_0 C^n. \tag{3}$$

$$u \frac{\partial C}{\partial x} + v \frac{\partial C}{\partial y} = D \frac{\partial^2 C}{\partial y^2} - k_0 C^n. \tag{4}$$

The boundary conditions are

$$u(x, 0) = ax, v(x, 0) = 0, T(x, 0) = constant = T_w, C(x, 0) = constant = C_w \tag{5}$$

$$u(x, \infty) = 0, T(x, \infty) = 0, C(x, \infty) = 0. \tag{6}$$

Stream function is:

$$u = \frac{\partial \psi}{\partial y'}, v = -\frac{\partial \psi}{\partial x}. \tag{7}$$

Similarity transformations are:

$$\psi(x, y) = (av)^{\frac{1}{2}} xf(\eta), \quad \eta = \left(\frac{a}{v}\right)^{\frac{1}{2}} y, \quad \theta = \frac{T}{T_w}, \quad \phi = \frac{C}{C_w}. \tag{8}$$

The non-dimensional equations are:

$$f''' + ff'' - f'^2 + Gr\theta + Gc\phi - M^2f' = 0, \tag{9}$$

$$\theta'' + Prf\theta' - PrS\theta = 0, \tag{10}$$

$$\phi'' + Sc(f\phi' - \gamma\phi^n) = 0. \tag{11}$$

Boundary conditions are:

$$f(0) = 0, \quad f'(0) = 1, \quad \theta(0) = 1, \quad \phi(0) = 1 \quad \text{at } \eta = 0, \tag{12}$$

$$f'(\infty) = 0, \quad \theta(\infty) = 0, \quad \phi(\infty) = 0 \quad \text{at } \eta \rightarrow \infty. \tag{13}$$

**Solution Method**

The dimensionless quantities are used to convert the equations (1) to (4) with boundary conditions (5) to (6) into non-dimensional equations (9) to (11) with boundary conditions (12) to (13) that may then be solved in MATLAB using the BVP4C method. Numerical values for the fluid's temperature, velocity, and species concentration can also be found using this method. Analysis is also done on the different skin friction, Nusselt, and Sherwood numbers.

**RESULTS AND DISCUSSION**

The paper provides a thorough examination of how different parameters affect mass transfer and MHD free convective flow across a stretching sheet that has a heat source and a chemical reaction. By improving our knowledge of the intricate relationships between mass transfer across a stretching sheet and MHD free convective flow, this research will help build more effective and regulated industrial and chemical processing methods. Below is a discussion of the various impacts of these distinct parameters.

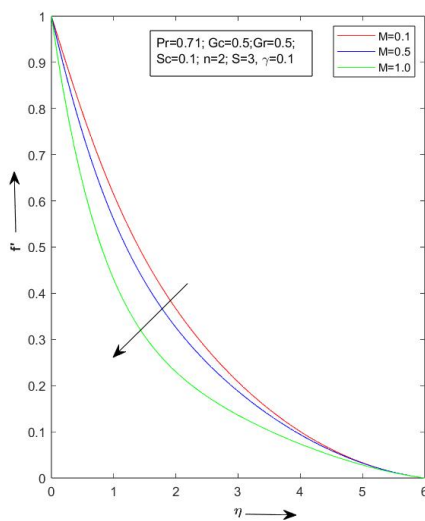


**Figure 2.** Velocity variation for *M*

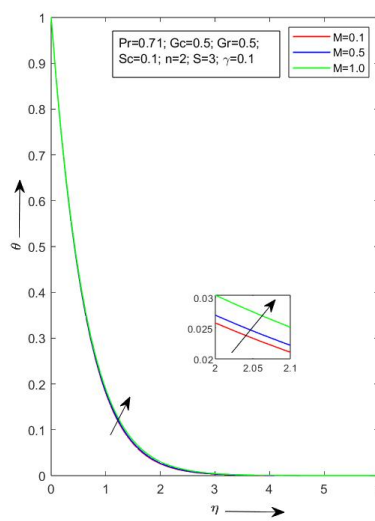


**Figure 3.** Temperature variation for *M*

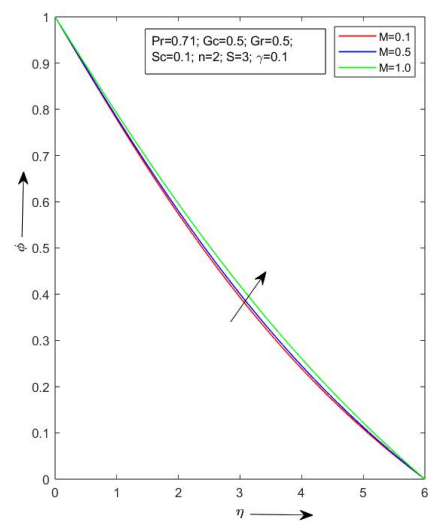


**Figure 4.** Concentration variation for *M*

Figures 2-4 illustrate how various fluid distributions vary in relation to the magnetic parameter. With increasing *M*, the temperature and fluid concentration will rise while the velocity will fall. Increases in *M* also result in increases in the Lorentz force opposing the flow, which accelerates the flow's deceleration. The fluctuation of various fluid distributions for the Prandtl number is shown in Figures 5-7.

With an increase in  $Pr$ , the fluid's concentration will rise, but its velocity and temperature will fall. In comparison to thermal diffusivity, momentum diffusivity becomes increasingly prominent as the Prandtl number rises. The velocity profile close to the shrinking sheet decreases as a result of the thinner velocity barrier layer. A rise in the Prandtl number signifies a comparatively low thermal diffusivity. As a result, there is a thinner thermal barrier layer and a lower temperature profile due to less effective heat conduction. As the thermal boundary layer gets thinner in concentration profiles, an increase in the Prandtl number may cause the concentration boundary layer to get bigger. This may lead to a rise in the chemical species concentration in the vicinity of the surface.

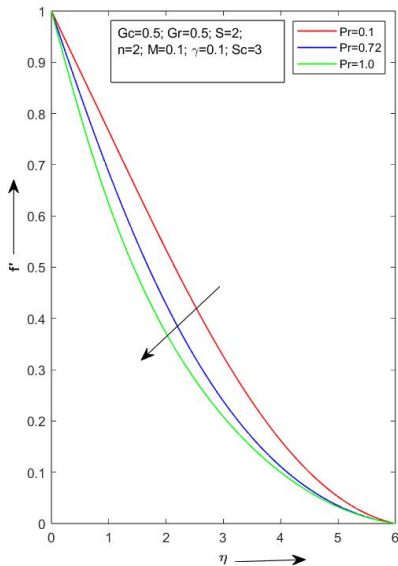


Figure 5. Velocity variation for  $Pr$

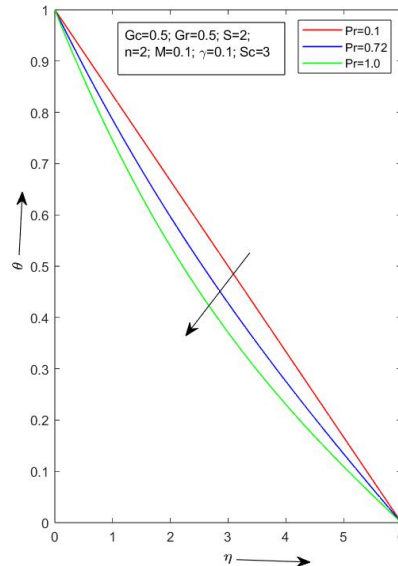


Figure 6. Temperature variation for  $Pr$

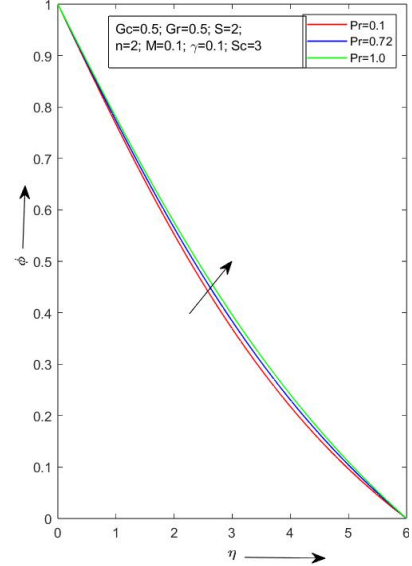


Figure 7. Concentration variation for  $Pr$

Variations for the different fluid distributions for the heat source parameter are described in Figures 8-10. When a heat source is present, the fluid's temperature tends to rise. This can lower the fluid's density and, consequently, the buoyant forces that propel the flow. Convective heat transfer, which extracts heat from the boundary layer more effectively, may be the cause of the temperature profile's drop. The changed diffusion processes are responsible for the increase in the concentration profile. By altering the local temperature gradients, the heat source can have an impact on the diffusion of chemical species, which in turn affects the concentration boundary layer. The concentration of the chemical species close to the surface may rise as a result of this impact. When considering the effect of the chemical reaction parameter ( $\gamma$ ), it describes the rate of chemical reaction within the fluid are shown in Figs. 11-13. The velocity profile often decreases as the chemical reaction parameter increases because of the increased reactant consumption, which might lessen the flow's overall driving forces. More heat is produced when the chemical reaction parameter is increased, which raises the temperature profile inside the boundary layer. Reactant consumption rate increases are indicated by increases in the chemical reaction parameter. Because the chemical species are being transformed into products more quickly, the concentration of those species within the boundary layer decreases as a result.

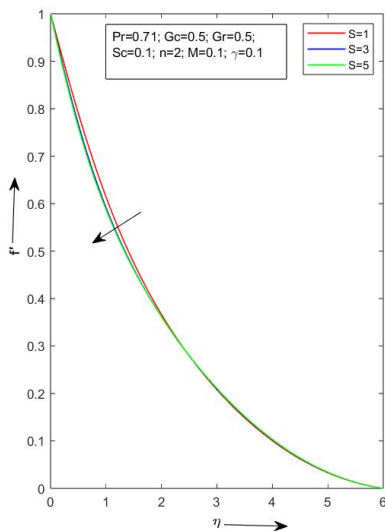


Figure 8. Velocity variation for  $S$

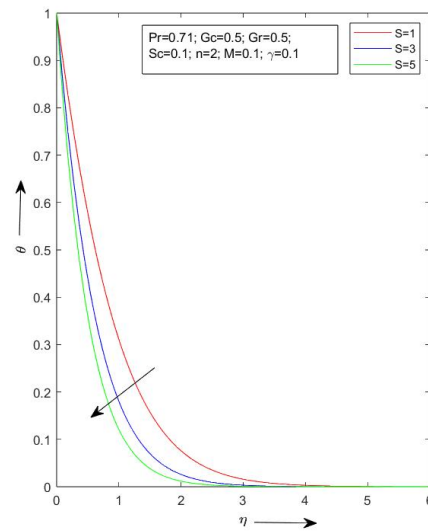


Figure 9. Temperature variation for  $S$

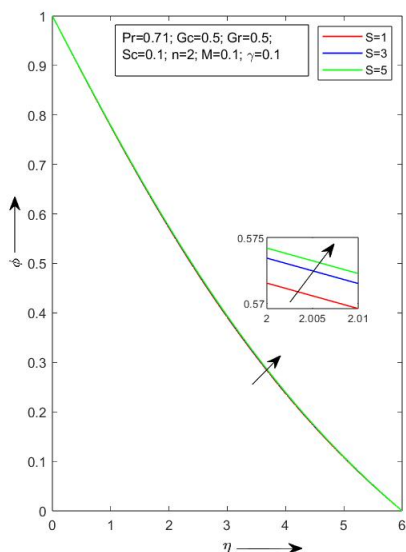


Figure 10. Concentration variation for  $S$

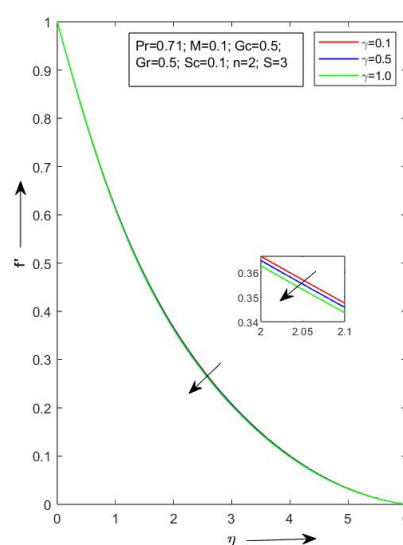


Figure 11. Velocity variation for  $\gamma$

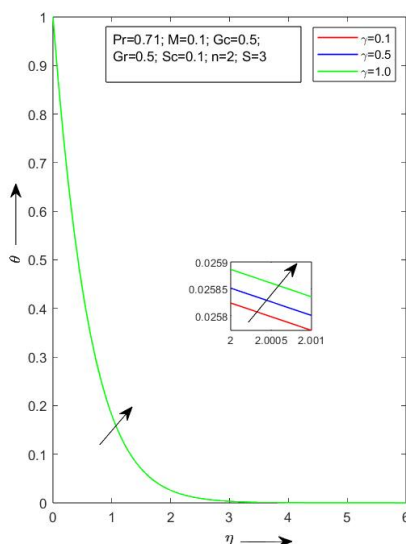


Figure 12. Temperature variation for  $\gamma$

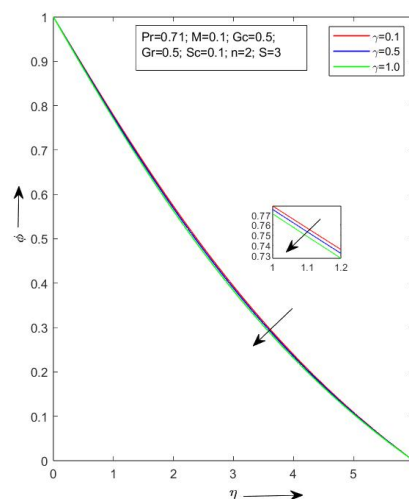


Figure 12. Concentration variation for  $\gamma$

Table 1 explains the validity of our work. Given that the Nusselt number values are identical to those of previously published studies, our study is validated, taking all factors into account.

Table 1. Comparison of  $-\theta'(0)$  value with previously published papers

$M$	$\gamma$	Afify [22]	Present study
0.1		0.2940	0.2941
0.5		0.2261	0.2263
1.0		0.1081	0.1082
	0.1	0.4826	0.4826
	0.5	0.4518	0.4518
	1.0	0.4231	0.4231

Table 2. Variations of  $f''(0)$ ,  $-\theta'(0)$  and  $-\phi'(0)$  for different parameters

$S$	$n$	$Pr$	$\gamma$	$M$	$Sc$	$f''(0)$	$-\theta'(0)$	$-\phi'(0)$
1	2	0.71	0.1	0.1	0.1	0.3963	1.0181	0.2197
2						0.4344	1.5672	0.2186
5						0.4543	1.9692	0.2181
	1					0.4344	1.5672	0.2186
	2					0.4366	1.5671	0.2252
	3					0.4368	1.5671	0.2239
		0.1				0.3279	0.5836	0.2236
		0.72				0.4351	1.5783	0.2185

$S$	$n$	$Pr$	$\gamma$	$M$	$Sc$	$f''(0)$	$-\theta'(0)$	$-\phi'(0)$
		1.0				0.4514	1.8623	0.2181
			0.1			0.4344	1.5672	0.2186
			0.5			0.4271	1.5675	0.1971
			1.0			0.4182	1.5679	0.1721
				0.1		0.4344	1.5672	0.2186
				0.5		0.5707	1.5638	0.2147
				1.0		0.9332	1.5552	0.2053
					0.1	0.4344	1.5672	0.2186
					5	0.6719	1.5583	1.3022
					10	0.7055	1.5574	1.7409

The fluctuation of physical parameters for various parameters is displayed in the Table 2. The skin friction parameter will go down with  $G$  but will increase with  $S, n, Pr, M, and Sc$ . as  $S, Pr, and G$  The Nusselt number grows but falls as  $n, M, and Sc$  increase. The Sherwood number goes down with  $S, Pr, G, and M$  but goes up with  $n and Sc$ . Because of the increased Lorentz force, the skin friction coefficient usually increases as  $M$  increases. Depending on how much the magnetic field promotes or inhibits the formation of thermal boundary layers, the Nusselt number may go down or up. Since the Sherwood number is dependent on convective mass transfer, which is controlled by the magnetic field, it fluctuates similarly to the Nusselt number. Changes in the concentration profile can impact the Sherwood number when a chemical reaction is taking place. The kind of response can also affect the Nusselt number and, consequently, the thermal boundary layer. Friction on the skin Increased viscosity brought on by the heat source parameter's influence causes the coefficient to rise. Because of variations in the surface temperature gradient, the heat source parameter directly affects the Nusselt number. A stronger temperature gradient causes the Nusselt number to rise, although thermal saturation might cause it to fall. Sherwood numbers may rise if the boundary layer stabilises but may drop with less mass diffusion.

### CONCLUSIONS

A magnetic field has been used to study the effects of a heat source, chemical reaction, and mass transfer on free convective flow and the mass transfer of a viscous, incompressible, and electrically conducting fluid over a stretching surface. A similarity transformation has been used to translate the governing equations with the boundary conditions into a system of non-linear ordinary differential equations with the necessary boundary conditions. The bvp4c approach has also been utilised to obtain numerical solutions for the similarity equations. It can be inferred from the current study that

- The fluid's temperature and velocity are both lowered by the heat source parameter, but its concentration profile is also raised.
- The fluid's temperature profile rises when the chemical reaction parameter is increased, but the fluid's velocity and concentration drop.
- The fluid's temperature and concentration profile rise along with the fluid's decreased velocity when the magnetic parameter is raised.
- Skin-friction increases with increasing  $S, n, Pr, M and Sc$ ; but it decreases with increasing  $\gamma$ .
- With increasing  $S, Pr and \gamma$ , the coefficients of Nusselt number increases; it decreases with  $n and Sc$ .
- Sherwood number drop with growing  $S, Pr, \gamma and M$ ; but it increases with  $n and Sc$ .

The expansion of this field's theoretical, computational, and applied aspects may be the main focus of future research prospects. For other applications that are important to industry, expand the research to non-Newtonian fluid models like Casson or viscoelastic fluids. To investigate coupled effects, incorporate Hall currents and heat radiation into the MHD equations. Expand the research to include turbulent flow regimes and look at the system's stability analysis. Examine how adding nanoparticles such as metallic oxides or graphene to nanofluids might improve mass and heat transmission. Investigate three-dimensional stretching sheets to more accurately simulate intricate systems, including industrial sheets or biological membranes.

#### List of symbols

$B_o$ : imposed magnetic field  
 $a$ : stretching rate constant  
 $C_p$ : specific heat  
 $C$ : concentration  
 $D$ : diffusion coefficient  
 $S$ : Heat source parameter  
 $Gc$ : local modified Grashof number  
 $f$ : similarity function  
 $n$ : order of reaction  
 $k_o$ : reaction rate constant  
 $g$ : acceleration due to gravity  
 $Gr$ : local Grashof number

#### Subscripts

$w$ : wall condition  
 $o$ : constant condition  
 $\infty$ : free stream condition

#### Greek symbols

$\vartheta$ : kinematic viscosity  
 $\beta$ : coefficient of thermal expansion  
 $\psi$ : stream function  
 $\rho$ : density  
 $\sigma$ : electric conductivity  
 $\theta$ : dimensionless temperature  
 $\beta^*$ : coefficient of expansion with concentration

$k$ :	thermal conductivity	$\phi$ :	dimensionless concentration
$Sc$ :	Schmidt number	$\eta$ :	similarity variable
$T$ :	temperature	$\gamma$ :	non-dimensional chemical reaction parameter
$M$ :	magnetic parameter		
$Pr$ :	Prandtl number		
$(x, y)$ :	Cartesian coordinates		
$(u, v)$ :	velocity components along $(x, y)$ –axes		

#### ORCID

 **Sunmoni Mudoi**, <https://orcid.org/0009-0000-2170-5235>; 
  **Satyabhushan Roy**, <https://orcid.org/0009-0005-7899-7351>  
 **Dipak Sarma**, <https://orcid.org/0009-0007-1463-242X>; 
  **Ankur Kumar Sarma**, <https://orcid.org/0009-0003-6209-8859>

#### REFERENCES

- [1] R. Kandasamy, K. Periasamy, and S. Prabhu, "Chemical reaction, heat and mass transfer on MHD flow over a vertical stretching surface with heat source and thermal stratification effects," *International Journal of Heat and Mass Transfer*, **48**(21–22), 4557–4561 (2005). <https://doi.org/10.1016/j.ijheatmasstransfer.2005.05.006>
- [2] Y. Khan, "Two-Dimensional Boundary Layer Flow of Chemical Reaction MHD Fluid over a Shrinking Sheet with Suction and Injection," *Journal of aerospace engineering*, **27**(5), (2014). [https://doi.org/10.1061/\(asce\)as.1943-5525.0000274](https://doi.org/10.1061/(asce)as.1943-5525.0000274)
- [3] S. Mishra, G. Dash, and M. Acharya, "Mass and heat transfer effect on MHD flow of a visco-elastic fluid through porous medium with oscillatory suction and heat source," *International Journal of Heat and Mass Transfer*, **57**(2), 433–438 (2013). <https://doi.org/10.1016/j.ijheatmasstransfer.2012.10.053>
- [4] M. Gnaneswara Reddy, P. Padma, and B. Shankar, "Effects of viscous dissipation and heat source on unsteady MHD flow over a stretching sheet," *Ain Shams Engineering Journal*, **6**(4), 1195–1201 (2015). <https://doi.org/10.1016/j.asej.2015.04.006>
- [5] K. Bhattacharyya, "Effects of heat source/sink on MHD flow and heat transfer over a shrinking sheet with mass suction," *Chemical Engineering Research Bulletin*, **15**(1), (2011). <https://doi.org/10.3329/ceerb.v15i1.6524>
- [6] P. Jalili, S.M.S. Mousavi, B. Jalili, P. Pasha, and D.D. Ganji, "Thermal evaluation of MHD Jeffrey fluid flow in the presence of a heat source and chemical reaction," *International journal of modern physics B/International journal of modern physics b*, **38**(08), 2450113 (2024). <https://doi.org/10.1142/s0217979224501133>
- [7] K. Raghunath, M. Obulesu, and K.V. Raju, "Radiation absorption on MHD free conduction flow through porous medium over an unbounded vertical plate with heat source," *International journal of ambient energy*, **44**(1), 1712–1720 (2023). <https://doi.org/10.1080/01430750.2023.2181869>
- [8] B.K. Jha, M.M. Altine, and A.M. Hussaini, "MHD steady natural convection in a vertical porous channel in the presence of point/line heat source/sink: An exact solution," *Heat transfer*, **52**(7), 4880–4894 (2023). <https://doi.org/10.1002/htj.22903>
- [9] A.C.V. Ramudu, K.A. Kumar, and V. Sugunamma, "Application of heat transfer on MHD shear thickening fluid flow past a stretched surface with variable heat source/sink," *Heat Transfer*, **52**(2), 1161–1177 (2023). <https://doi.org/10.1002/htj.22734>
- [10] N.J. Mishra, and N.T. Samantara, "Effect of Non-Linear Radiation and Non-Uniform Heat Source/Sink on Flow over a Linear Stretching Sheet with Fluid Particle Suspension," *CFD Letters*, **15**(2), 42–53 (2023). <https://doi.org/10.37934/cfdl.15.6.4253>
- [11] S.A. Lone, A. Khan, H. Alrabaiah, S. Shahab, Zehba Raizah, and I. Ali, "Dufour and Soret diffusions phenomena for the chemically reactive MHD viscous fluid flow across a stretching sheet with variable properties," *International journal of heat and fluid flow*, **107**, 109352–109352 (2024). <https://doi.org/10.1016/j.ijheatfluidflow.2024.109352>
- [12] U.S. Mahabaleshwar, K.N. Sneha, and A. Wakif, "Significance of thermo-diffusion and chemical reaction on MHD Casson fluid flows conveying CNTs over a porous stretching sheet," *Waves in random and complex media*, 1–19, (2023). <https://doi.org/10.1080/17455030.2023.2173500>
- [13] A. Paul, and T. K. Das, "Thermal and mass transfer aspects of MHD flow across an exponentially stretched sheet with chemical reaction," *International Journal of Ambient Energy*, 1–27 (2023). <https://doi.org/10.1080/01430750.2023.2179110>
- [14] C.A. Nandhini, S. Jothimani, and A.J. Chamkha, "Effect of chemical reaction and radiation absorption on MHD Casson fluid over an exponentially stretching sheet with slip conditions: ethanol as solvent," *European Physical Journal Plus*, **138**(1), (2023). <https://doi.org/10.1140/epjp/s13360-023-03660-8>
- [15] M.P. Preetham, and S. Kumbinarasaiah, "A numerical study of two-phase nanofluid MHD boundary layer flow with heat absorption or generation and chemical reaction over an exponentially stretching sheet by Haar wavelet method," *Numerical heat transfer. Part B, Fundamentals/Numerical heat transfer. Part B. Fundamentals*, **85**(6), 706–735 (2023). <https://doi.org/10.1080/10407790.2023.2253364>
- [16] Z. Khan, E.N. Thabet, A.M. Abd-Alla, and F.S. Bayones, "Investigating the effect of bio-convection, chemical reaction, and motile microorganisms on Prandtl hybrid nanofluid flow across a stretching sheet," *Zeitschrift für angewandte Mathematik und Mechanik*, (2023). <https://doi.org/10.1002/zamm.202300509>
- [17] R. Geetha, B. Reddappa, N. Tarakaramu, B.R. Kumar, and M.I. Khan, "Effect of Double Stratification on MHD Williamson Boundary Layer Flow and Heat Transfer across a Shrinking/Stretching Sheet Immersed in a Porous Medium," *International journal of chemical engineering*, **2024**, 1–12 (2024). <https://doi.org/10.1155/2024/9983489>
- [18] R.M. Kumar, R.S. Raju, M.A. Kumar, and B. Venkateswarlu, "A numerical study of thermal and diffusion effects on MHD Jeffrey fluid flow over a porous stretching sheet with activation energy," *Numerical heat transfer. Part A. Applications/Numerical heat transfer. Part A, Applications*, 1–22 (2024). <https://doi.org/10.1080/10407782.2024.2319344>
- [19] B.S. Goud, Y.D. Reddy, and K.K. Asogwa, "Inspection of chemical reaction and viscous dissipation on MHD convection flow over an infinite vertical plate entrenched in porous medium with Soret effect," *Biomass Conversion and Biorefinery*, (2022). <https://doi.org/10.1007/s13399-022-02886-3>
- [20] B.M. Cham, N. Shams-ul-Islam, M. Saleem, S. Talib, and S. Ahmad, "Unsteady, two-dimensional magnetohydrodynamic (MHD) analysis of Casson fluid flow in a porous cavity with heated cylindrical obstacles," *AIP advances*, **14**(4), (2024). <https://doi.org/10.1063/5.0178827>

- [21] M. Mahboobtosi, et al., "Investigate the Influence of Various Parameters on MHD Flow characteristics in a Porous Medium," Case studies in thermal engineering, 104428–104428 (2024). <https://doi.org/10.1016/j.csite.2024.104428>
- [22] A.A. Afify, "MHD free convective flow and mass transfer over a stretching sheet with chemical reaction," Heat and Mass Transfer, **40**(6-7), (2004). <https://doi.org/10.1007/s00231-003-0486-0>
- [23] M.A. El-Aziz, "Radiation effect on the flow and heat transfer over an unsteady stretching sheet," International communications in heat and mass transfer, **36**(5), 521–524 (2009). <https://doi.org/10.1016/j.icheatmasstransfer.2009.01.016>

### МАСОПЕРЕНОС ТА ВІЛЬНИЙ МГД КОНВЕКЦІЙНИЙ ПОТІК ЧЕРЕЗ ЛИСТ ЩО РОЗТЯГУЄТЬСЯ З ДЖЕРЕЛОМ ТЕПЛА ТА ХІМІЧНОЮ РЕАКЦІЄЮ

Сунмоні Мудой<sup>a</sup>, Сатъябхушан Рой<sup>a</sup>, Діпак Сарма<sup>a</sup>, Анкур Кумар Сарма<sup>a,b</sup>

<sup>a</sup>Факультет математики, Університет Коттон, Гувахаті-781001, Індія

<sup>b</sup>Факультет математики, Коледж Баосі Баніканта Какаті, Нагаон, Барнета-781311, Індія

У цій роботі розглядається масообмін і МГД вільний конвективний потік через лист ЩО розтягується за наявності джерела тепла та хімічної реакції. Дія розтягування листа прискорює потік, тоді як магнітне поле, прикладене перпендикулярно напрямку потоку, впливає на нього. Також враховується вплив градієнтів температури та концентрації на виштовхувальні сили. Рівняння безперервності, імпульсу, енергії та концентрації належать до пов'язаних нелінійних диференціальних рівнянь у частинних похідних, які регулюють систему. Перетворення подібності використовуються для перетворення цих рівнянь у систему звичайних диференціальних рівнянь, які потім чисельно розв'язуються за допомогою методів *bvp4c*. У цьому дослідженні основними параметрами, що представляють інтерес, є магнітне поле, плавучість, швидкість хімічної реакції та джерело тепла. Результати показують вплив цих параметрів на температуру, концентрацію та профілі швидкості прикордонного шару. Для кількісного визначення швидкості масообміну, швидкості теплообміну та напруги зсуву на поверхні листа розраховують коефіцієнт шкірного тертя, число Нуссельта та число Шервуда. Маніпулюючи магнітним полем, хімічними реакціями та виділенням тепла, робота пропонує нове важливе уявлення про те, як найкраще використовувати потоки МГД у промислових процесах, таких як виробництво полімерів, хімічні реактори та системи охолодження.

**Ключові слова:** МГД; поверхня, що розтягується; джерело тепла; хімічна реакція; *bvp4c*

## INTERACTION OF HEAVY METALS WITH $\beta$ -LACTOGLOBULIN: MOLECULAR DYNAMICS STUDY

**O. Zhytniakivska\***, **U. Tarabara**, **K. Vus**, **V. Trusova**, **G. Gorbenko**

*Department of Medical Physics and Biomedical Nanotechnologies, V.N. Karazin Kharkiv National University  
4 Svobody Sq., Kharkiv, 61022, Ukraine*

*\*Corresponding Author e-mail: [olga.zhytniakivska@karazin.ua](mailto:olga.zhytniakivska@karazin.ua)*

Received September 15, 2024; revised November 12, 2024; accepted November 22, 2024

$\beta$ -Lactoglobulin ( $\beta$ -lg), the predominant whey protein, is renowned for its nutritional and functional attributes, including its ability to bind hydrophobic and charged molecules. These properties make  $\beta$ -lg a promising candidate for applications such as drug delivery systems, nutraceutical carriers, and nanocomposites for environmental remediation, particularly in detecting and removing heavy metals. Despite its potential, the impact of heavy metal binding on  $\beta$ -lg's structure and stability remains insufficiently explored, posing challenges for its advanced applications. In this study, molecular dynamics (MD) simulations were employed to investigate the structural and dynamic responses of  $\beta$ -lg to the binding of heavy metal ions— $\text{Cd}^{2+}$ ,  $\text{Ni}^{2+}$ ,  $\text{Co}^{3+}$ ,  $\text{Pb}^{2+}$ , and  $\text{Pt}^{2+}$ . A series of 200-ns MD simulations for the metal-protein complexes was conducted at 300 K using GROMACS software and the CHARMM General Force Field. Key structural parameters analyzed included backbone root-mean-square deviation (RMSD), radius of gyration (Rg), solvent-accessible surface area (SASA), and root-mean-square fluctuations (RMSF). The results demonstrated that binding of  $\text{Cd}^{2+}$ ,  $\text{Ni}^{2+}$ ,  $\text{Co}^{3+}$ ,  $\text{Pb}^{2+}$ , and  $\text{Pt}^{2+}$  destabilized the protein's structure, with notable effects observed in critical regions such as the EF loop, H-strand, and AB loop. The extent of destabilization varied depending on the specific heavy metal ion. These findings emphasize the need for detailed residue-level analyses to fully elucidate the structural changes induced by metal binding and their implications for  $\beta$ -lg's functional properties. This work provides valuable insights into the behavior of  $\beta$ -lg under heavy metal binding and lays the groundwork for developing  $\beta$ -lg-based nanosystems for environmental and biomedical applications.

**Keywords:** *Protein-metal interaction; Heavy metals; Molecular dynamics*

**PACS:** 87.14.Cc, 87.16.Dg

Rapid industrialization and urbanization have significantly increased the discharge of heavy metals into global water resources. Even at trace concentrations, heavy metals pose serious health risks by damaging bones, nerves, and enzymes, and contributing to various severe health conditions [1,2]. To address this issue, a range of methods has been developed over the years for the removal of toxic heavy metals, including ion exchange [3,4], reverse osmosis [5], complexation precipitation [6,7], and adsorption [8,9]. Among these, adsorption stands out as an efficient, environmentally sustainable, and cost-effective solution, particularly when low-cost adsorbents are utilized [8,9]. Within the realm of adsorption, biosorption has gained prominence. This approach employs biopolymer-based biomass—such as chitosan, alginate, cellulose, starch—to bind and remove pollutants passively from aqueous solutions [10,11]. Among various biosorbents, protein-based nanomaterials have emerged as particularly promising candidates for heavy metal adsorption, owing to their diverse amino acid functional groups, which exhibit strong metal-binding properties [12-21]. The ability to induce the supramolecular assembly of protein molecules and tailor the structural properties of newly formed two- or three-dimensional structures at the molecular level opens new avenues for designing customized materials for various applications. A wide range of structures, including fibrils, spherical condensates, and gels, can be generated, spanning sizes from the nanoscale to the macroscopic scale. These supramolecular assemblies' structure, mechanical properties, charge, polarity, water accessibility, and stability can be precisely adjusted by controlling the growth conditions [12-21]. Recent advancements in protein-based adsorbents, including proteins and peptides functionalized derivatives and protein-derived nanomaterials have demonstrated exceptional removal efficiencies for a wide range of heavy metals [12-21]. To exemplify, Yu et al. developed a hybrid membrane for detecting and separating mercury ions by combining gold nanoclusters, bovine serum albumin (BSA) nanofibers, and graphene oxide with a mercury removal efficiency of up to 90.4% [13]. The soy protein-based polyethylenimine hydrogel was found can effectively adsorb Cu(II) ions from aqueous solution even in the presence of co-existing competitive heavy metal ions, such as Zn(II), Cd(II), and Pb(II) [14]. The excellent Pb(II) ions adsorption efficiency was previously observed for bovine serum albumin micro-sized amyloid-like spherical particles [15] and soy protein microsponges [16]. Costal et al demonstrated the efficiency of tunable biopolymers based on elastin-like polypeptides composed of either one or two hexahistidine clusters for Cd(II) removal [17]. In particular, hybrid membranes combining activated carbon and amyloid fibrils, self-assembled from various proteins such as  $\beta$ -lactoglobulin, soy protein, globulin, silk, and albumin, have shown exceptional effectiveness in purifying wastewater contaminated with heavy metals and radioactive compounds. [18-21]. More specifically, a hybrid membrane with activated carbon successfully removed over 99.5% of gold, mercury, lead, and palladium, both individually and in mixed aqueous solutions, and achieved 99% removal of arsenites and arsenates from prepared solutions and real contaminated water [18-21]. The isothermal thermal calorimetry (ITC) measurement performed by Peydayesh et al. also demonstrated

the more than 99% removal efficiencies of hybrid protein-carbon membranes also for chromium, nickel, silver, and platinum ions [18].

Among the various proteins employed in the composition of protein-based nanomaterials for heavy metal removal,  $\beta$ -lactoglobulin has emerged as a particularly promising, readily available, and low-cost candidate [18–20]. Numerous studies have highlighted  $\beta$ -lactoglobulin's ability to interact with various heavy metal ions, especially in the context of amyloid-carbon hybrid membranes [18–20]. However, to the best of our knowledge, little is known about the intermolecular interactions between heavy metal ions and  $\beta$ -lactoglobulin. Motivated by the protein's capacity to bind specific heavy metal ions, in our recent studies we identified the binding sites for heavy metal ions ( $\text{Cu}^{2+}$ ,  $\text{Fe}^{3+}$ ,  $\text{Mg}^{2+}$ ,  $\text{Mn}^{2+}$ ,  $\text{Zn}^{2+}$ ,  $\text{Cd}^{2+}$ ,  $\text{Fe}^{2+}$ ,  $\text{Ni}^{2+}$ ,  $\text{Hg}^{2+}$ ,  $\text{Co}^{2+}$ ,  $\text{Cu}^+$ ,  $\text{Au}^+$ ,  $\text{Ba}^{2+}$ ,  $\text{Pb}^{2+}$ ,  $\text{Pt}^{2+}$ ,  $\text{Sm}^{3+}$ , and  $\text{Sr}^{2+}$ ) on  $\beta$ -lactoglobulin and explored the possible interactions involved in protein-ion binding [22]. Building on our previous work, the present study employs molecular dynamics simulations to elucidate the influence of selected heavy metal ions ( $\text{Cd}^{2+}$ ,  $\text{Ni}^{2+}$ ,  $\text{Co}^{3+}$ ,  $\text{Pb}^{2+}$ ,  $\text{Pt}^{2+}$ ) on the structure and dynamics of  $\beta$ -lactoglobulin.

### MOLECULAR DYNAMICS SIMULATIONS

Molecular dynamics simulations and trajectory analyses were conducted using GROMACS software (version 5.1) with the CHARMM36m force field. The three-dimensional X-ray crystal structure of bovine  $\beta$ -lactoglobulin was obtained from the Protein Data Bank (<https://www.rcsb.org/>) under c. Input files for the MD simulations were prepared using the Solution Builder module of the web-based CHARMM-GUI interface [23]. The system was solvated using a TIP3P water rectangular solvation box, ensuring a minimum distance of 10 Å between the protein and the box edges. Six distinct ion-protein systems were prepared for simulation. The control system consisted of the protein and 7  $\text{Na}^+$  ions, added to neutralize the protein's net charge. Heavy metal ions were introduced into the system and randomly distributed according to the following scheme:

**Table 1.** The composition of systems containing bovine  $\beta$ -lactoglobulin and heavy metal ions

Metal	Number of metal ions	Number of Cl <sup>-</sup>
$\text{Cd}^{2+}$ :	4	1
$\text{Co}^{3+}$ :	3	2
$\text{Ni}^{2+}$ :	4	1
$\text{Pb}^{2+}$ :	4	1
$\text{Pt}^{2+}$ :	4	1

The molecular dynamics simulations and analysis of the trajectories were performed using the GROMACS software (version 2023.3) with the CHARMM36m force field in the NPT ensemble with the time step for MD simulations 2 fs. The calculations were performed at a temperature of 300 K. The minimization and equilibration of the systems were carried out during 50000 and 250000 steps, respectively. The Berendsen algorithm was used for thermostat and barostat during the equilibration phase. The LINCS algorithm was applied to constrain the lengths of hydrogen-containing bonds. The time interval for MD calculations was 200 ns. The GROMACS commands `gmx rms`, `gmx gyrate`, `gmx rmsf` were used to calculate the protein backbone root-mean-square deviation (RMSD), protein radius of gyration ( $R_g$ ), root-mean-square fluctuations of the C-alpha atoms (RMSF). Visualization of the snapshots of the MD runs and analysis of the protein secondary structures and protein solvent-accessible surface area (SASA) were performed in VMD.

### RESULTS AND DISCUSSION

#### $\beta$ -lactoglobulin

$\beta$ -Lactoglobulin, the predominant protein in whey, is highly valued in the food industry for its remarkable nutritional and functional properties. Each  $\beta$ -lactoglobulin monomer consists of 162 amino acids, has a molecular weight of 18.3 kDa, and features a hydrophobic core formed by eight anti-parallel  $\beta$ -strands, creating a characteristic calyx-shaped  $\beta$ -barrel [24]. These structural attributes, combined with its multiple high-affinity binding sites for hydrophobic and charged molecules, make  $\beta$ -lactoglobulin an excellent candidate for advanced applications. Notably, it shows great potential in the development of: i) nanocarriers for delivering drugs, nutraceuticals, and bioactive compounds; and ii) nanocomposites for detecting and removing heavy metal ions [18-20, 25]. The development of lactoglobulin-based nanosystems for environmental applications relies on a detailed understanding of the protein's metal-binding properties. Experimental approaches to identifying protein metal-binding sites, characterizing protein-metal interactions, and studying metal-induced changes in protein structure can be challenging. However, computational methods offer a relatively fast and efficient alternative for characterizing protein-ligand interactions.

In this study, molecular dynamics simulations were conducted to examine the influence of selected heavy metal ions ( $\text{Cd}^{2+}$ ,  $\text{Ni}^{2+}$ ,  $\text{Co}^{3+}$ ,  $\text{Pb}^{2+}$ , and  $\text{Pt}^{2+}$ ) on the structure and dynamics of  $\beta$ -lactoglobulin. Representative snapshots from a 200 ns simulation of heavy metal binding to  $\beta$ -lactoglobulin are presented in Figure 1. Notably, the binding propensity of these metals to the protein under identical simulation conditions differed significantly.  $\text{Cd}^{2+}$  and  $\text{Co}^{3+}$  exhibited a higher binding affinity for  $\beta$ -lactoglobulin compared to c ions added to the system formed stable interactions with the protein within the first 30 ns of the simulation and remained within the protein's binding pocket for the remainder of the

simulation time. In contrast, only two  $\text{Ni}^{2+}$  ions and one  $\text{Pb}^{2+}$  or  $\text{Pt}^{2+}$  ion established metal-protein contacts throughout the simulation. These findings align with previous experimental observations by Peydayesh et al., who demonstrated a stronger binding affinity of silver compared to chromium for similar protein systems [18]. Moreover, the higher binding propensity of  $\text{Cd}^{2+}$  relative to  $\text{Pb}^{2+}$  has also been reported for  $\beta$ -lactoglobulin dimers and  $\beta$ -lactoglobulin-carbon composite nanomaterials [26].

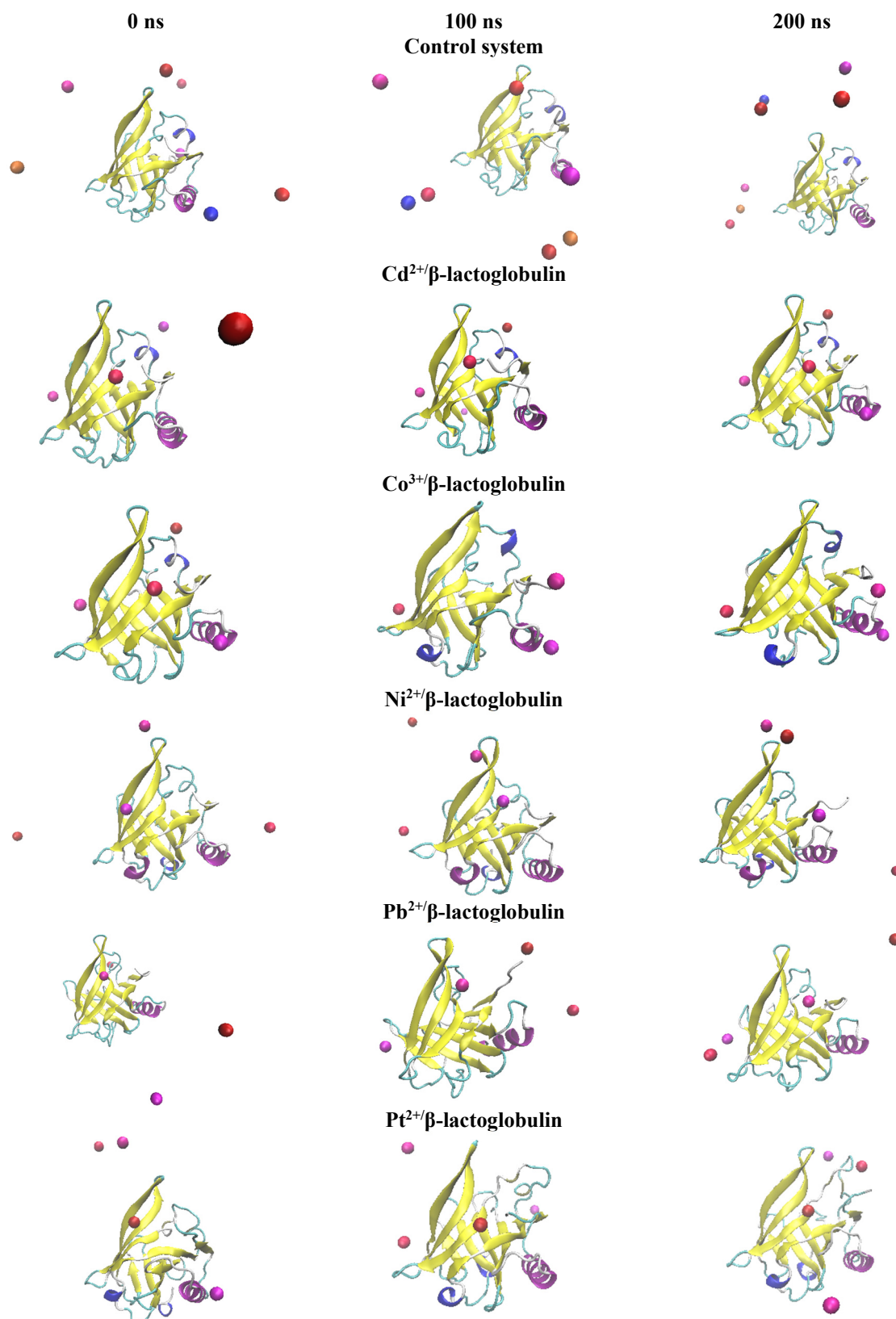


**Figure 1.** Representative snapshots of the metal-protein complexes

The selectivity and strength of interactions between metal ions and protein binding sites can be effectively explained using the Hard and Soft Acids and Bases (HSAB) theory [27]. According to HSAB theory, metal ions preferentially bind to protein sites that match their relative hardness or softness. In general, the interactions between hard acid metals and hard basic sites are predominantly ionic, whereas covalent bonds typically form between soft acid metals and soft basic sites. These distinct interaction types influence the structural integrity of proteins. For example, metal complexes interacting with bovine serum albumin (BSA) can disrupt disulfide bonds, leading to changes in the protein's secondary structure, including a significant loss of  $\alpha$ -helical content and eventual unfolding [29]. Furthermore, metal-protein interactions can alter the local polarity around exposed tryptophan residues due to molecular rearrangements, affecting the protein's structural and functional properties [29].

Therefore, in the initial stage of our study, we evaluated the overall stability of the protein over the simulation period by analyzing the time evolution of several structural parameters, including the protein backbone root-mean-square deviation (RMSD), radius of gyration (Rg), root-mean-square fluctuations (RMSF) of the C-alpha atoms, and solvent-accessible surface area (SASA). Figure 2 illustrates the temporal changes in the backbone RMSD, providing insight into the dynamic stability of the protein throughout the simulation.

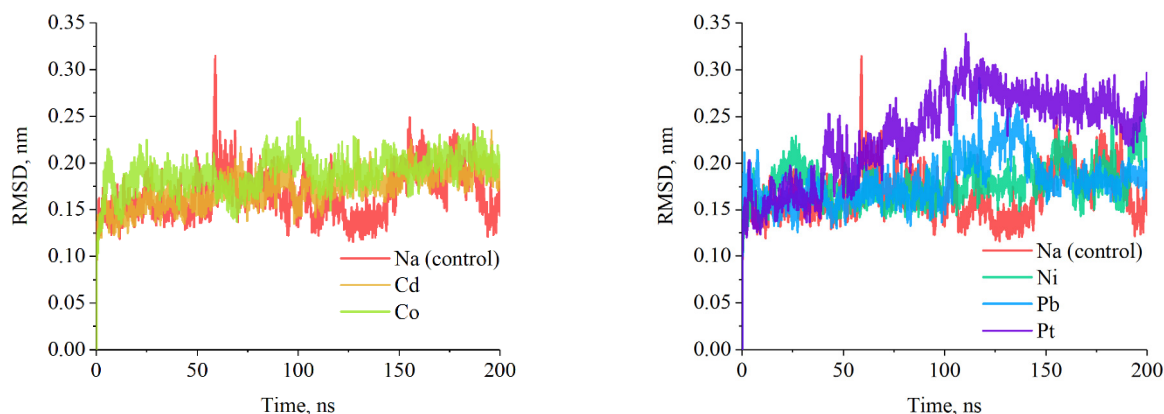


**Figure 2.** Time course evolution of the root-mean-square deviation

As shown in Figure 2, the calculated RMSD values for the  $\text{Cd}^{2+}$ ,  $\text{Ni}^{2+}$ , and  $\text{Co}^{3+}$ -containing systems remained below 0.2 nm, except for brief fluctuations observed in the  $\text{Ni}^{2+}$ /lactoglobulin system during the first 50 ns and in the  $\text{Co}^{3+}$ /lactoglobulin system between 80 ns and 115 ns. In contrast, the  $\text{Pb}^{2+}$  and  $\text{Pt}^{2+}$  ion-protein systems exhibited less stable trajectories compared to the other heavy metals studied. The RMSD time profile for the  $\text{Pb}^{2+}$ /lactoglobulin system reveals two distinct phases: i) slight fluctuations around 0.18 nm during the first 100 ns of the simulation and ii) a transient increase in RMSD values to 0.22–0.25 nm over the subsequent 30 ns, followed by a decrease back to approximately 0.17 nm, where it stabilized and fluctuated for the remainder of the simulation. For the  $\text{Pt}^{2+}$ /lactoglobulin system, a significant increase in RMSD values was observed starting at ~30 ns. The RMSD then converged and equilibrated, fluctuating around an average value of 0.26 nm for the remainder of the simulation. The higher RMSD values observed in the  $\text{Pt}^{2+}$ /lactoglobulin and  $\text{Pb}^{2+}$ /lactoglobulin systems relative to their initial structures suggest potential conformational changes in the protein, with these changes being more pronounced in the presence of  $\text{Pt}^{2+}$ . However, the minimal fluctuations (small standard deviation) in backbone RMSD during the final 50 ns of the simulation indicate that the systems ultimately reached equilibrium and remained stable under the simulation conditions.

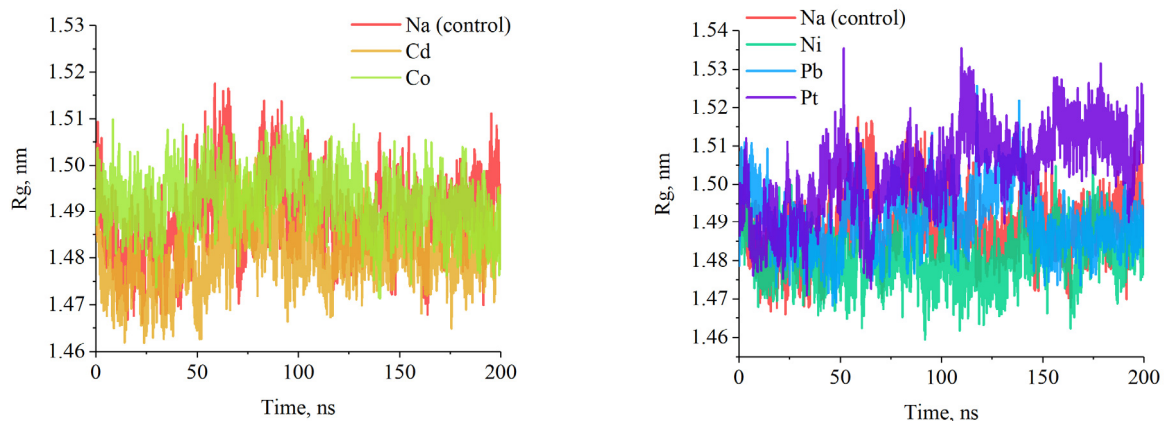


**Figure 3.** Time course evolution of the radius of gyration

The radius of gyration (Rg) is a key parameter for assessing a protein's structural compactness. Lower Rg values indicate a more tightly folded polypeptide chain, whereas higher Rg values reflect a more expanded or open protein

structure. The  $R_g$  for heavy metal/protein complexes was calculated and plotted over simulation time to evaluate changes in protein compactness, as illustrated in Figure 3. The results suggest that the protein structure remained relatively stable throughout the simulations, with an average  $R_g$  of 1.49 nm observed for all systems except for  $Pt^{2+}$ /lactoglobulin, which exhibited a slightly higher average  $R_g$  of 1.52 nm. However, specific trends in  $R_g$  patterns are noteworthy. The  $R_g$  values for  $Cd^{2+}$ ,  $Ni^{2+}$ ,  $Co^{3+}$ , and  $Pb^{2+}$  containing systems displayed a decreasing trend during the first 50 ns, indicating an initial increase in the structural compactness of lactoglobulin. Following this period, the  $R_g$  values stabilized, reflecting the preservation of compactness for the remainder of the simulation. A slight increase in  $R_g$  value was observed throughout the simulation for  $Pt^{2+}$ , suggesting the occurrence of potential Pt-induced spatial rearrangements in the side chains of amino acid residues and potentially within the secondary structures of  $\beta$ -lactalbumin.

The secondary structure of  $\beta$ -lactoglobulin ( $\beta$ -lg) consists of approximately 15%  $\alpha$ -helix, 50%  $\beta$ -sheet, and 15–20% reverse turns [24]. Its globular structure is formed by nine  $\beta$ -strands (A–I) arranged into two  $\beta$ -sheets, along with three turns of  $\alpha$ -helix. At neutral pH, these  $\beta$ -sheets form a conical barrel known as the calyx, with strand A linking the sheets on one side and strands D and E providing a secondary connection [24]. The  $\alpha$ -helix is situated between strands A and H, followed by strand I. The protein's structure is stabilized by disulfide bonds: Cys106–Cys119 linking strands G and H, and Cys66–Cys160 linking strand D to the C-terminal [24].

To determine the dynamic behavior of amino acid residues, the RMSF values of the C-alpha atoms of protein in the presence of heavy metal ions were calculated (Figure 4).

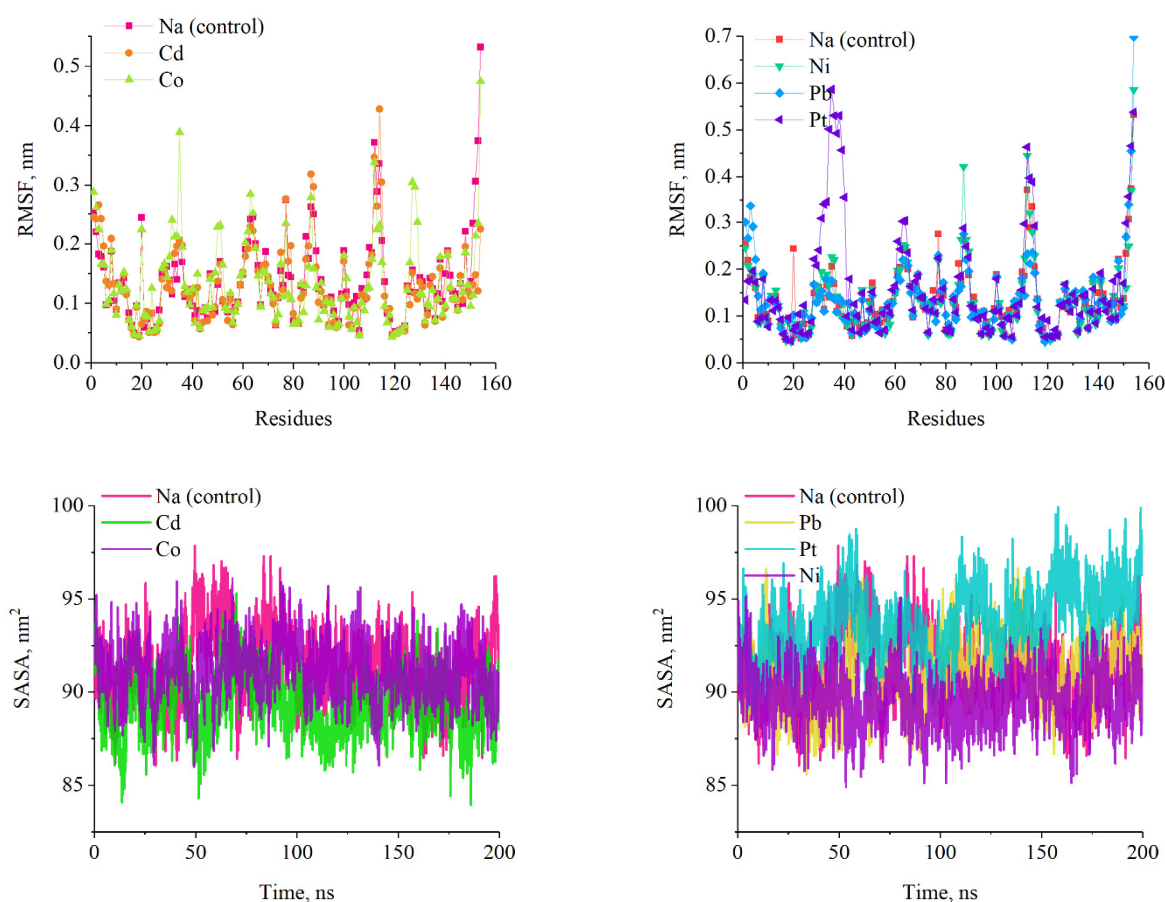


**Figure 4.** Time course evolution of the root-mean-square fluctuations and the solvent-accessible surface area for the metal-protein complexes

The RMSF analysis provided insights into the fluctuations of amino acid residues in all heavy-metal/protein systems under study, identifying regions of the protein that exhibited greater spatial fluctuations due to ion binding. Specifically, in the  $Pb^{2+}$ /lactoglobulin system, significant residue fluctuations were observed exclusively in the N-terminal region (residues V2–L10). Similar patterns of higher fluctuations in regions with minimal secondary structure were noted for other metal ions:  $Cd^{2+}$  (residues A86–E89),  $Co^{3+}$  (residues N63–C66 and P126–D130),  $Pt^{2+}$  (residues E62–D64 and E112–Q115), and  $Ni^{2+}$  (residues E112–Q115). Of particular interest is the EF loop (residues D85–E90), which acts as a gate regulating access to the binding site [24]. At low pH, this loop adopts a "closed" conformation, inhibiting or preventing ligand binding. Conversely, at high pH, the loop transitions to an "open" state, enabling ligands to penetrate the hydrophobic binding site [24]. The binding of all studied heavy metals, except  $Pb^{2+}$ , was associated with noticeable fluctuations in the H1 helical region (residues 30–36), with  $Pt^{2+}$  inducing the most significant changes. Interestingly, the

AB loop region plays a critical role in stabilizing the  $\beta$ -lactoglobulin structure through an ion pair interaction between Asp33 of one subunit and Arg40 of the other [24]. Thus, the observed increase in residue fluctuations within this region suggests that heavy metal ions may destabilize the tertiary protein structure by disrupting these key stabilizing interactions. Additionally, increased fluctuations in the amino acid residues of the H-strand region were observed in the presence of  $\text{Cd}^{2+}$ ,  $\text{Ni}^{2+}$ , and  $\text{Pt}^{2+}$ . This region includes the Cys119 residue, which forms a disulfide bond with Cys106—a critical interaction that stabilizes the overall protein structure [24]. In addition,  $\text{Co}^{3+}$  binding to the  $\beta$ -lactoglobulin caused an increase in fluctuations in the amino acid residues of the B strand (residue E45-P50).

A key factor influencing the interfacial properties of proteins is their solvent-exposed surface. To evaluate changes in the environment of  $\beta$ -lactoglobulin residues during the simulation, the solvent-accessible surface area (SASA) per residue was calculated (Figure 4). The analysis revealed no significant differences in SASA values across most protein-metal complexes. For the majority of systems studied, SASA fluctuated within the range of 87–95. However, a slight increase in SASA was observed for the  $\text{Pt}^{2+}$ /lactoglobulin complex during the simulation, suggesting a potential alteration in protein conformation specific to the presence of  $\text{Pt}^{2+}$ .

Molecular dynamics simulations of  $\beta$ -lactoglobulin in the presence of heavy metals ( $\text{Cd}^{2+}$ ,  $\text{Ni}^{2+}$ ,  $\text{Co}^{3+}$ ,  $\text{Pb}^{2+}$ , and  $\text{Pt}^{2+}$ ) reveal their partial destabilizing effects on the protein's tertiary structure, even at low concentrations. The integrity of the tertiary structure is highly sensitive to the dihedral angles of amino acid side chains, which can be significantly altered upon metal binding [30,31]. These alterations disrupt torsional angles, disturb hydrogen bonding networks, and may propagate changes to secondary structural elements such as  $\alpha$ -helices or  $\beta$ -sheets, ultimately affecting the protein's overall stability and conformation. Additionally, heavy metal binding has been shown to induce structural rearrangements by promoting the separation of non-polar groups from water, thereby encouraging the formation of new hydrophobic interactions [31,32]. While our results indicate that the secondary structure remains largely intact, the tertiary structure undergoes modifications due to metal interactions. However, further investigations are necessary to fully elucidate these structural changes and their implications for  $\beta$ -lactoglobulin functionality.

## CONCLUSIONS

The present study utilized molecular dynamics (MD) simulations to explore the effects of heavy metal ion binding ( $\text{Cd}^{2+}$ ,  $\text{Ni}^{2+}$ ,  $\text{Co}^{3+}$ ,  $\text{Pb}^{2+}$ , and  $\text{Pt}^{2+}$ ) on the structure and dynamics of  $\beta$ -lactoglobulin. The 200 ns MD simulation results performed at 300 K using GROMACS software and the CHARMM General Force Field indicate that  $\text{Cd}^{2+}$  and  $\text{Co}^{3+}$  exhibited the strongest binding affinity among the studied metals, forming stable interactions within the protein's binding pockets. In contrast,  $\text{Ni}^{2+}$ ,  $\text{Pb}^{2+}$ , and  $\text{Pt}^{2+}$  showed lower binding stability, with fewer ions maintaining contact throughout the trajectory. The analysis of root-mean-square deviation (RMSD) and radius of gyration (Rg) revealed varying degrees of structural destabilization upon metal binding.  $\text{Pt}^{2+}$  had the most pronounced destabilizing effect, as evidenced by increased RMSD and Rg values. Residue-level root-mean-square fluctuations (RMSF) analyses revealed that metal binding particularly affected regions important for  $\beta$ -lactoglobulin's stability including the EF loop, AB loop, H-strand, and H1 helix. Overall, the study underscores the sensitivity of  $\beta$ -lactoglobulin's tertiary structure to heavy metal binding. The destabilizing effects observed, particularly with  $\text{Pt}^{2+}$ , highlight the need for further residue-level investigations to fully elucidate the mechanisms underlying metal-induced structural changes.

## Acknowledgements

This work was supported by the Ministry of Education and Science of Ukraine (the project “Development of novel means of medical diagnostics by biomedical nanotechnologies and modern ultrasonic and fluorescence methods” and the project “Development of economically affordable nanosystems for rapid identification and purification of water from heavy metal ions based on carbon nanoallotropes and amyloids from organic waste”).

## ORCID

Olga Zhytniakivska, <https://orcid.org/0000-0002-2068-5823>; Uliana Tarabara, <https://orcid.org/0000-0002-7677-0779>  
Kateryna Vus, <https://orcid.org/0000-0003-4738-4016>; Valeriya Trusova, <https://orcid.org/0000-0002-7087-071X>  
Galyna Gorbenko, <https://orcid.org/0000-0002-0954-5053>

## REFERENCES

- [1] M. Balali-Mood, K. Naseri, Z. Tahergorabi, M. Reza Khazdair, and M. Sadeghi, *Front Pharmacol.* **12**, 643972 (2021). <https://doi.org/10.3389/fphar.2021.643972>
- [2] R. Singh, N. Gautam, A. Mishra, and R. Gupta, *Indian J. Pharmacol.* **43**, 246 (2011). <https://doi.org/10.4103/253-7613.81505>
- [3] S.A. Cavaco, S. Fernandes, M. Quina, and L.M. Ferreira. *J. Hazard. Mater.* **144**, 634 (2007). <https://doi.org/10.1016/j.jhazmat.2007.01.087>
- [4] A. Dąbrowski, Z. Hubicki, P. Podkościelny, and E. Robens, *Chemosphere*, **56**, 91 (2004). <https://doi.org/10.1016/j.chemosphere.2004.03.006>
- [5] V.L. Kapepula, and P. Luis, *Front. Chem. Eng.* **6**, 1334816 (2024). <https://doi.org/10.3389/fceng.2024.1334816>
- [6] J. Huang, J. *et al.*, *Colloids Surf. A Physicochem. Eng. Asp.* **520**, 361–368 (2017). <https://doi.org/10.1016/j.colsurfa.2017.02.001>
- [7] M.T. Alvarez, C. Crespo, B. Mattiasson. *Chemosphere*, **66**, 1677–1683 (2007). doi: 10.1016/j.chemosphere.2006.07.065.
- [8] R. Janani, G. Baskar, K. Sivakumar, V. Sunita, *et al.*, *Environmental Research*, **203**, 111815 (2022). <https://doi.org/10.1016/j.envres.2021.111815>
- [9] Z. Raji, A. Karim, A. Karam, and S. Khalloufi, *Waste*, **1**, 775-805 (2023). <https://doi.org/10.3390/waste1030046R>.

- [10] J. Wang, and C. Chen, *Biotechnology Advances*, **27**, 195-226 (2024). <https://doi.org/10.1016/j.biotechadv.2008.11.002>
- [11] L. Zhang, Y. Zeng, and Z. Cheng, *J. Mol. Liq.* **214**, 175-191 (2016). <https://doi.org/10.1016/j.molliq.2015.12.013>
- [12] Y. Luo, Y. Zhang, Z. Xiong, X. Chen, A. Sha et al. *Int J Mol Sci.* **25**(12), 6717 (2024). <https://doi.org/10.3390/ijms25126717>
- [13] X. Yu, W. Liu, X. Deng, S. Yan, and Z. Su, *Chemical Engineering Journal*, **335**, 176 (2017). <https://doi.org/10.1016/j.cej.2017.10.148>
- [14] J. Liu, D. Su, J. Yao, Y. Huang, J. Shao, and X. Chen, *J. Mater. Chem. A*, **5**, 4163 (2017). <https://doi.org/10.1039/C6TA10814H>
- [15] S. Anselmo, S. Cataldo, and T. Avola, *et al.*, *J. Colloid Interface Sci.* **610**, 347 (2022). [10.1016/j.jcis.2021.11.184](https://doi.org/10.1016/j.jcis.2021.11.184)
- [16] S. Anselmo, T. Avola, K. Kalouta, and S. Kataldo, *et al.*, *Int. J. Biol. Macr.*, **239**, 124276 (2023). <https://doi.org/10.1016/j.ijbiomac.2023.124276>
- [17] J. Kostal, A. Mulchandani, and W. Chen, *Macromolecules*, **34**, 7, 2257 (2001). <https://doi.org/10.1021/ma001973m>
- [18] M. Peydayesh, S. Bolisetty, T. Mohammadi, and R. Mezzenga, *Langmuir*, **35**, 4161 (2019). <https://doi.org/10.1021/acs.langmuir.8b04234>
- [19] S. Bolisetty, and R. Mezzenga, *Nat. Nanotechnol.*, **11**, 365 (2016) <https://doi.org/10.1038/nnano.2015.310>
- [20] S. Bolisetty, N. Reinhold, C. Zeder, M. Orozco, and R. Mezzenga, *Chem. Commun.* **53**, 5714 (2017) <https://doi.org/10.1039/C7CC00406K>
- [21] L.C. Ramírez-Rodríguez, L.E. Díaz Barrera, M.X. Quintanilla-Carvajal, *et al.*, *Membranes*, **10**, 386 (2020). <https://doi.org/10.3390/membranes10120386>
- [22] O. Zhytniakivska, U. Tarabara, K. Vus, V. Trusova, and G. Gorbenko, *East European Journal of Physics*, (1), 497 (2024). <https://doi.org/10.26565/2312-4334-2024-1-55>
- [23] S. Jo, T. Kim, V. G. Iyer, and W. Im, *J. Comp. Chem.* **29**, 1859 (2008), <https://doi.org/10.1002/jcc.20945>
- [24] G. Kontopidis, C. Holt, and L. Sawyer, *Journal of Dairy Science*, **87**, 785 (2004). [https://doi.org/10.3168/jds.S0022-0302\(04\)73222-1](https://doi.org/10.3168/jds.S0022-0302(04)73222-1)
- [25] Z. Shafaei, B. Ghalandari, A. Vaseghi, A. Divsalar, *et al.*, *Nanomedicine: Nanotechnology, Biology and Medicine*, **13**, 1685 (2017). <https://doi.org/10.1016/j.nano.2017.03.007>
- [26] K. Lilly, M. Wang, A.A. Orr, S. Bondos, *et al.*, *Ind. Eng. Chem. Res.* **63**(37), 16124 (2024). <https://doi.org/10.1021/acs.iecr.4c01774>
- [27] R. Pearson, *J. Chem. Educ.* **45**, 981 (1968). <https://doi.org/10.1021/ed045p581>
- [28] F. Samari, B. Hemmateenejad, M. Shamsipur, M. Rashidi, and H. Samouei, *Inorg. Chem.* **51**, 3454 (2012). <https://doi.org/10.1021/ic202141g>
- [29] T. Topala, A. Bodoki, L. Oprean, and R. Oprean, *Clujul Medical*, **87**, 215 (2014). <https://doi.org/10.15386/cjmed-357>
- [30] S. Tiwari, and S.R.K. Ainavarapu. *Chem Asian J.* e202400971 (2024). <https://doi.org/10.1002/asia.202400971>
- [31] K.D. McConnell, N.C. Fitzkee, and J.P. Emerson, *Inorg. Chem.* **61**(3), 1249 (2022). <https://doi.org/10.1021/acs.inorgchem.1c03271>
- [32] A.G. Moullick, and J. Chakrabarti, *Phys. Chem. Chem. Phys.* **24**, 21348 (2022). <https://doi.org/10.1039/D2CP02168D>

## ВЗАЄМОДІЯ ВАЖКИХ МЕТАЛІВ З $\beta$ -ЛАКТОГЛОБУЛІНОМ: ДОСЛІДЖЕННЯ МЕТОДОМ МОЛЕКУЛЯРНОЇ ДИНАМІКИ

О. Житняківська, У. Тарабара, К. Вус, В. Трусова, Г. Горбенко

*Кафедра медичної фізики та біомедичних нанотехнологій, Харківський національний університет імені В.Н. Каразіна м. Свободи 4, Харків, 61022, Україна*

$\beta$ -Лактоглобулін ( $\beta$ -Ig), основний білок сироватки молока, відомий своїми винятковими харчовими та функціональними властивостями, зокрема здатністю зв'язувати гідрофобні та заряджені молекули. Завдяки цим властивостям  $\beta$ -Ig є вкрай перспективним для розробки систем доставки лікарських препаратів і наноконструкцій для екологічної ремедіації, зокрема для виявлення та видалення важких металів. Попри його потенціал, вплив зв'язування важких металів на структуру та стабільність  $\beta$ -Ig залишається недостатньо вивченим, що створює труднощі для його практичних застосувань. У цьому дослідженні були використано метод молекулярної динаміки (MD) для аналізу структурних та динамічних реакцій  $\beta$ -Ig на зв'язування важких металів— $\text{Cd}^{2+}$ ,  $\text{Ni}^{2+}$ ,  $\text{Co}^{3+}$ ,  $\text{Pb}^{2+}$  та  $\text{Pt}^{2+}$ . Серія 200-нс симуляцій MD для комплексів метал-білок проводилася при 300 K за допомогою програмного забезпечення GROMACS та силового поля CHARMM. Основними проаналізованими структурними параметрами були середньоквадратичне відхилення остову ланцюга, радіус інерції, площа поверхні, доступна для розчинника та середньоквадратичні флуктуації. Результати показали, що зв'язування  $\text{Cd}^{2+}$ ,  $\text{Ni}^{2+}$ ,  $\text{Co}^{3+}$ ,  $\text{Pb}^{2+}$  та  $\text{Pt}^{2+}$  спричинило дестабілізацію структури білка, із помітним впливом на EF-петлю, H-ланцюг та АВ-петля білку. Ступінь дестабілізації залежав від конкретного іона важкого металу. Ці висновки підкреслюють необхідність детального аналізу на рівні залишків амінокислот для повного розуміння структурних змін, викликаних зв'язуванням металів, та їх впливу на функціональні властивості  $\beta$ -Ig. Отримані результати мають важливе значення у контексті розуміння механізмів взаємодії  $\beta$ -Ig з важкими металами і для розробки наносистем на основі  $\beta$ -Ig для екологічних та біомедичних застосувань.

**Ключові слова:** взаємодія білок-метал; важкі метали; молекулярна динаміка

# THE FORMATION OF ION-ACOUSTIC SOLITARY WAVES IN A PLASMA HAVING NONEXTENSIVE ELECTRONS AND POSITRONS

 Rafia Khanam<sup>a</sup>,  Satyendra Nath Barman<sup>b</sup>

<sup>a</sup>Department of Mathematics, Gauhati University, Guwahati -781014, Assam, India

<sup>b</sup>B. Borooah College, Guwahati-781007, Assam, India

\*Corresponding Author e-mail: [rafiakhanam353@gmail.com](mailto:rafiakhanam353@gmail.com)

Received June 4, 2024; revised October 6, 2024; in final form November 23, 2024; accepted November 25, 2024

In this plasma model, consisting of ions, electrons, and positrons have been theoretically investigated when both the electrons and positrons are obeying  $q$ -nonextensive velocity distribution. The reductive perturbation method is used to obtain Korteweg de Vries (KdV) equation describing the basic set of normalized fluid equations. The existence of ion-acoustic solitary waves depending on nonextensive parameter, electron to positron temperature ratio, ion to electron temperature ratio and streaming velocity are investigated numerically. It has been found that solely fast ion-acoustic modes can produce the coexistence of small amplitude rarefactive solitons.

**Keywords:**  $q$ -nonextensive distribution; Reductive perturbation method; KdV equation

**PACS:** 52.35.Fp, 52.35.Qz, 52.27.Ep

## 1. INTRODUCTION

The investigation of ion-acoustic solitary waves in a plasmas with nonextensive electrons [1] and positrons are tremendously described by Korteweg-de Vries equation. Almost all the systems behaved in statistical mechanics with Boltzmann-Gibbs(BG) statics have been generally extensive [2]. In extensivity, there are two obvious exceptions which are small system or clusters of particles and long range interparticle forces. Small system is consisting of a finite number particles and in this system thermodynamic limit is not used and for long range interparticles, nonextensivity holds for Coulomb electric or Newtonian gravitational forces. However, in recent years, numerous researcher have been showing their interest regarding the study of particle distribution in plasma using the Boltzmann Gibbs (BG) statistics. Renyi [3] was first recognized in generalization of the Boltzmann-Gibbs(BG) statistics and subsequently developed by Tsallis [4]. By citing this approach many researchers have worked nonextensive distribution for the number density of the particles in plasma [5–21]. Latter, this Boltzmann-Gibbs(BG) statistics is known as an additional parameter  $q$  and it is used to a number of nonextensive systems. The  $q$ -nonextensive distribution function shows distinct behaviors and it is based on the values of  $q$ , which determines the quantity of the nonextensivity of the system being recharged. If  $q < 1$  which is known as superextensivity and it indicates the plasma with higher number of superthermal particles compared to that of Maxwellian case. If  $q > 1$  which is known as subextensivity, the distribution function shows the plasma with large number of low-speed particles compared to that of Maxwellian case. It may be useful for  $q < -1$  where  $q$ -distribution is unnormalizable. Again, if  $q = 1$  then the distribution function is reduced to common Maxwellian-Boltzmann velocity distribution [22]. Numerous astrophysical plasma events include the formation of positrons in the plasma. In astrophysical objects electron-positron-ion plasma can be found such as in polar region of neutron stars, active galactic nuclei, the semiconductor plasmas, quasars and pulsar magnetosphere, the centre of Milky way galaxy, the early universe, intense laser fields *etc.* Moskalenko & Strong [23] studied in cosmic-ray nuclei interact with atoms in interstellar medium. Influence of Temperature and Positron Density on Large Amplitude Ion-acoustic Waves in an Electron-Positron-Ion Plasma was examined by Nejob [24]. In a nonextensive electron-positron-ion plasma, Ghosh *et al.* [25] have investigated the dynamic structures of nonlinear ion acoustic waves. Ion acoustic solitary waves in plasmas including relativistic thermal ions, positrons, and nonextensively distributed electrons have been investigated by Hafez *et al.* [26]. Danehkar [27] has investigated electrostatic solitary waves in a plasma of electron-positron pairs with suprathreshold electrons.

In this research, the propagation behavior of nonlinear ion-acoustic solitary waves in a three-component plasma made up of inertial ions, nonextensive electrons and positrons is investigated theoretically. In this paper, the nonlinear ion-acoustic waves are investigated using the reductive perturbation approach. The format of the paper is as follows: the Introduction is given in Section (1); the Basic Governing Equations in Section (2); Derivation of the Korteweg-de Vries equation and Its Solution in Section (3); and Results and Discussions in Section (4), and at the end References are included.

## 2. BASIC GOVERNING EQUATIONS

In this paper we consider one-dimensional collisionless three component plasma consisting of ions, electrons and positrons. We assume that ions are extensive but electrons and positrons both are nonextensive that means both are obeying

$q$ -nonextensive distribution. The nonlinear dynamics of the ion-acoustic waves is governed by the following normalized continuity and motion equations for ions, electrons, positrons and the poisson equations are

$$\frac{\partial n_i}{\partial t} + \frac{\partial(n_i v_i)}{\partial x} = 0 \tag{1}$$

$$\frac{\partial v_i}{\partial t} + v_i \frac{\partial v_i}{\partial x} + \frac{\sigma}{n_i} \frac{\partial p_i}{\partial x} + \frac{\partial \phi}{\partial x} = 0 \tag{2}$$

$$\frac{\partial p_i}{\partial t} + v_i \frac{\partial p_i}{\partial x} + 3p_i \frac{\partial v_i}{\partial x} = 0 \tag{3}$$

$$n_e = \alpha [1 + (q - 1)\phi]^{\frac{q+1}{2(q-1)}} \tag{4}$$

$$n_p = \beta [1 - \sigma_p (q - 1)\phi]^{\frac{q+1}{2(q-1)}} \tag{5}$$

$$\frac{\partial^2 \phi}{\partial x^2} = \alpha - \beta - n_i + (\alpha + \beta \sigma_p) s_1 \phi + (\alpha - \beta \sigma_p^2) s_2 \phi^2 + (\alpha + \beta \sigma_p^3) s_3 \phi^3 + \dots \tag{6}$$

where

$$\left. \begin{aligned} s_1 &= \frac{(1+q)}{2}, \quad s_2 = \frac{(1+q)(3-q)}{8}, \\ s_3 &= \frac{(1+q)(3-q)(5-3q)}{48} \end{aligned} \right\} \tag{7}$$

where parameter  $q$  is the real number greater than -1 and it stands for the strength of nonextensive ion;  $\alpha$  is the electron to ion density ratio;  $\beta$  is the positron to ion density ratio;  $n_e, n_p$  and  $n_i$  are the electron, positron and ion number density;  $v_i$  is the fluid velocity;  $p_i$  is the ion pressure and  $\phi$  is the electric potential. We, normalize  $n_i, n_e$  and  $n_p$  by their unperturbed densities  $n_{i0}, n_{e0}$  and  $n_{p0}$  respectively;  $v_i$  by the ion-acoustic speed  $C_{si} = \sqrt{K_B T_e / m_i}$ ; and  $\phi$  by  $K_B T_e / e$ . The space and time variables are in units of the ion Debye length  $\lambda_{Di} = \sqrt{K_B T_e / 4\pi n_i e^2}$ , and the ion plasma period  $\omega_{pi}^{-1} = \sqrt{m_i / 4\pi n_i e^2}$ , respectively. Here,  $K_b$  is the Boltzmann constant;  $\sigma = T_i / T_e$  is the ion to electron temperature ratio;  $\sigma_p = T_e / T_p$  is the electron to positron temperature ratio.

### 3. DERIVATION OF THE KORTEWEG-DE VRIES EQUATION AND ITS SOLUTION

To derive the KdV equation from the set of equations (1)-(6) we use the stretch variables:

$$\eta = \epsilon^{1/2}(x - Nt), \quad \tau = \epsilon^{3/2}t \tag{8}$$

where  $N$  represents the wave's phase velocity and the following flow variable expansions are expressed in terms of the smallness parameter  $\epsilon$

$$\left. \begin{aligned} n_i &= 1 + \epsilon n_{i1} + \epsilon^2 n_{i2} + \epsilon^3 n_{i3} + \dots \\ n_e &= 1 + \epsilon n_{e1} + \epsilon^2 n_{e2} + \epsilon^3 n_{e3} + \dots \\ n_p &= 1 + \epsilon n_{p1} + \epsilon^2 n_{p2} + \epsilon^3 n_{p3} + \dots \\ v_i &= v_{i0} + \epsilon v_{i1} + \epsilon^2 v_{i2} + \epsilon^3 v_{i3} + \dots \\ p_i &= 1 + \epsilon p_{i1} + \epsilon^2 p_{i2} + \epsilon^3 p_{i3} + \dots \\ \phi &= \epsilon \phi_1 + \epsilon^2 \phi_2 + \epsilon^3 \phi_3 + \epsilon^4 \phi_4 + \dots \end{aligned} \right\} \tag{9}$$

Following the standard perturbation method with the use of transformation (8), expansions (9) in the normalized set of equations (1)-(6) and the boundary conditions  $n_{i1} = 0, v_{i1} = 0, \phi_1 = 0$  at  $|\eta| \rightarrow \infty$ , we obtain the lowest order perturbation in  $\epsilon$  as

$$\left. \begin{aligned} n_{i1} &= \frac{\phi_1}{(N - v_{i0})^2 - 3\sigma}, \quad n_{e1} = \alpha s_1 \phi_1, \\ v_{i1} &= \frac{(N - v_{i0})\phi_1}{(N - v_{i0})^2 - 3\sigma}, \quad n_{p1} = -\beta \sigma_p s_1 \phi_1, \\ p_{i1} &= \frac{3\phi_1}{(N - v_{i0})^2 - 3\sigma} \end{aligned} \right\} \tag{10}$$

Again, using (8) and (9) in equation(6), we obtain the coefficient of  $\epsilon^0$  and  $\epsilon^1$  as

$$\alpha - \beta = 1 \tag{11}$$

$$n_{i1} - (\alpha + \beta \sigma_p) s_1 \phi_1 = 0 \tag{12}$$

Using the expression of  $n_{i1}$  from (10), the expression for phase velocity  $N$  is obtained as

$$N = v_{i0} \pm \sqrt{\frac{1 + 3\sigma(\alpha + \beta\sigma_p)s_1}{(\alpha + \beta\sigma_p)s_1}} \tag{13}$$

Again, equating the coefficients of second higher order terms of  $\epsilon$  from (1)-(6) we get,

$$\frac{\partial n_{i1}}{\partial \tau} - (N - v_{i0})\frac{\partial n_{i2}}{\partial \eta} + \frac{\partial v_{i2}}{\partial \eta} + \frac{\partial(n_{i1}v_{i1})}{\partial \eta} = 0 \tag{14}$$

$$\frac{\partial v_{i1}}{\partial \tau} - (N - v_{i0})\frac{\partial v_{i2}}{\partial \eta} - (N - v_{i0})n_{i1}\frac{\partial v_{i1}}{\partial \eta} + v_{i1}\frac{\partial v_{i1}}{\partial \eta} + \sigma\frac{\partial p_{i2}}{\partial \eta} + \frac{\partial \phi_2}{\partial \eta} + n_{i1}\frac{\partial \phi_1}{\partial \eta} = 0 \tag{15}$$

$$\frac{\partial p_{i1}}{\partial \tau} - (N - v_{i0})\frac{\partial p_{i2}}{\partial \eta} + 3\frac{\partial v_{i2}}{\partial \eta} + 3p_{i1}\frac{\partial v_{i1}}{\partial \eta} + v_{i1}\frac{\partial p_{i1}}{\partial \eta} = 0 \tag{16}$$

Now, putting the values of  $n_{i1}$ ,  $v_{i1}$  and  $p_{i1}$  in (14), (15) and (16) and eliminating  $\frac{\partial v_{i2}}{\partial \eta}$  and  $\frac{\partial p_{i2}}{\partial \eta}$ , we obtain the following equations

$$\frac{\partial n_{i2}}{\partial \eta} = \frac{2(N - v_{i0})}{[(N - v_{i0})^2 - 3\sigma]^2} \frac{\partial \phi_1}{\partial \tau} + \frac{1}{(N - v_{i0})^2 - 3\sigma} \frac{\partial \phi_2}{\partial \eta} + \frac{3(N - v_{i0})^2}{[(N - v_{i0})^2 - 3\sigma]^3} \phi_1 \frac{\partial \phi_1}{\partial \eta} \tag{17}$$

$$\frac{\partial n_{e2}}{\partial \eta} = 2\alpha s_2 \phi_1 \frac{\partial \phi_1}{\partial \eta} + \alpha s_1 \frac{\partial \phi_2}{\partial \eta} \tag{18}$$

$$\frac{\partial n_{p2}}{\partial \eta} = 2\beta s_2 \sigma_p^2 \phi_1 \frac{\partial \phi_1}{\partial \eta} - \beta s_1 \sigma_p \frac{\partial \phi_2}{\partial \eta} \tag{19}$$

$$\frac{\partial^2 \phi_1}{\partial \eta^2} = -n_{i2} + \alpha s_1 \phi_2 + \alpha s_2 \phi_1^2 + \beta s_1 \sigma_p \phi_2 - \beta s_2 \sigma_p^2 \phi_1^2 \tag{20}$$

$$\implies \frac{\partial^3 \phi_1}{\partial \eta^3} = -\frac{\partial n_{i2}}{\partial \eta} + \alpha s_1 \frac{\partial \phi_2}{\partial \eta} + 2\alpha s_2 \phi_1 \frac{\partial \phi_1}{\partial \eta} + \beta s_1 \sigma_p \frac{\partial \phi_2}{\partial \eta} - 2\beta s_2 \sigma_p^2 \phi_1 \frac{\partial \phi_1}{\partial \eta} \tag{21}$$

Using the relation (12) and entering the values of  $\frac{\partial n_{i2}}{\partial \eta}$ ,  $\frac{\partial n_{e2}}{\partial \eta}$  and  $\frac{\partial n_{p2}}{\partial \eta}$  in (21), we ultimately obtain the Korteweg-de Vries(KdV) equation as

$$\frac{\partial \phi_1}{\partial \tau} + A\phi_1 \frac{\partial \phi_1}{\partial \eta} + B\frac{\partial^3 \phi_1}{\partial \eta^3} = 0 \tag{22}$$

where the nonlinear coefficient  $A$  and the dispersion coefficient  $B$  are given by

$$A = \frac{3(N - v_{i0})^2 - 2s_2(\alpha - \beta\sigma_p^2) [(N - v_{i0})^2 - 3\sigma]^3}{2(N - v_{i0}) [(N - v_{i0})^2 - 3\sigma]} \quad \text{and} \quad B = \frac{[(N - v_{i0})^2 - 3\sigma]^2}{2(N - v_{i0})}$$

From the expressions of  $A$  and  $B$ , we have  $2(N - v_{i0}) [(N - v_{i0})^2 - 3\sigma] \neq 0$

In order to determine the stationary solitary wave solutions of the KdV equation (22), we introduce the variable  $\chi = \eta - C_1\tau$ , where  $C_1$  represents the wave's velocity in the linear  $\chi$ -space. With this, the solitary wave solution can be obtained by integrating the KdV equation (22) as

$$\phi_1 = \phi_0 \operatorname{sech}^2\left(\frac{\chi}{\Delta}\right) \tag{23}$$

Here,  $\phi_0 = 3C_1/A$  is the wave amplitude of the soliton and it is proportional to the soliton speed  $C_1$ ;  $\Delta = 2\sqrt{B/C_1}$  is the width, and is inversely proportional to the soliton speed  $C_1$ .

#### 4. RESULTS AND DISCUSSIONS

In this present plasma system, ion-acoustic solitary waves in plasma comprising  $q$ -nonextensive electrons and positrons through the KdV equation are discussed. In our investigations, only fast ion-acoustic mode is found to exist. We have examined numerically, the influences of plasma parameters such as nonextensive parameter ( $q$ ), the positron to ion density ratio ( $\beta$ ), electron to ion density ratio ( $\alpha$ ), electron to ion temperature ratio ( $\sigma$ ), positron to ion temperature ratio ( $\sigma_p$ ) and ion streaming velocities ( $v_{i0}$ ) on the variations of nonlinear term  $A$  and dispersion term  $B$  given in (22). In our

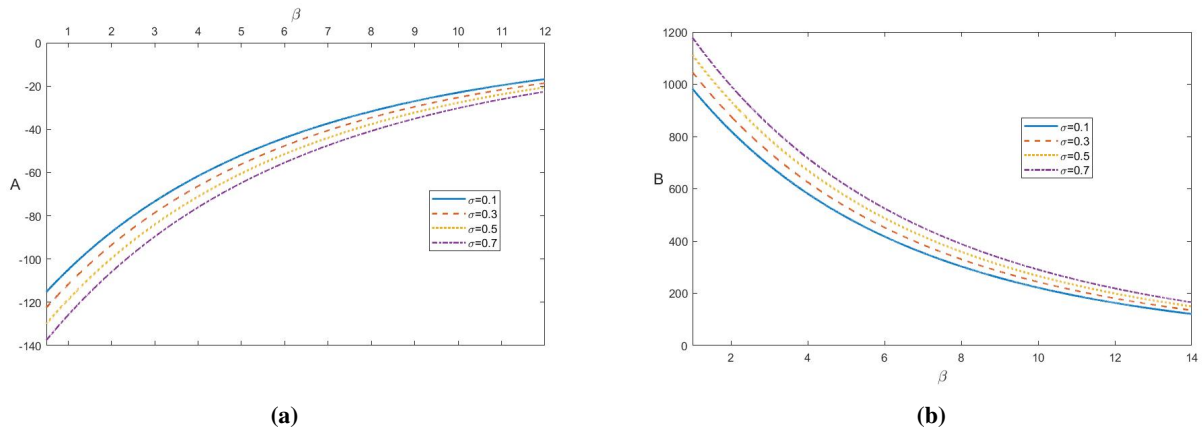


Figure 1. The variation of (a)  $A$  and (b)  $B$  versus  $\beta$  for different values of  $\sigma$ .

investigation, for all the cases, we consider  $-1 < q < 0$  and  $v_{i0} < 5$ ; otherwise no solitons found to exist in this model of plasma.

Fig. [1a-1b] shows the numerical analysis of the variation of the nonlinear term  $A$  and the dispersion term  $B$  versus  $\beta$  for various values of  $\sigma = 0.1, 0.3, 0.5, 0.7$ , for fixed  $\sigma_p = 0.05$ ,  $v_{i0} = 2.5$ ,  $q = -0.9$ ,  $C_1 = 0.5$  and  $\alpha = 1.1$ . In Fig. [1a], we observe that  $A$  is negative and grows as  $\sigma$  increases, while in Fig. [1b]  $B$  is positive, indicating that it increases as  $\sigma$  increases.

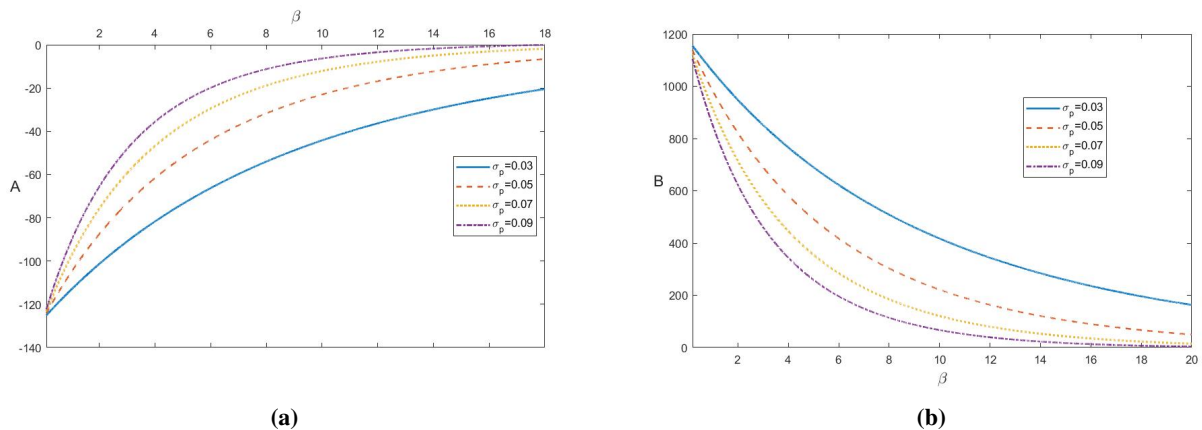


Figure 2. The variation of (a)  $A$  and (b)  $B$  versus  $\beta$  for different values of  $\sigma_p$ .

Fig. [2a-2b] reveals that the nonlinear term  $A$  and the dispersion term  $B$  are varying with  $\beta$  for various values of  $\sigma_p = 0.03, 0.05, 0.07, 0.09$  for fixed  $\sigma = 0.1$ ,  $v_{i0} = 2.5$ ,  $q = -0.9$ ,  $C_1 = 0.5$  and  $\alpha = 1.1$ . For all values of  $\sigma_p$ , the nonlinear term  $A$  is negative (Fig.[2a]), and dispersion term  $B$  is positive (Fig.[2b]).

The variation of (a)  $A$  and (b)  $B$  versus  $\alpha$  for various values of  $\sigma_p = 0.03, 0.05, 0.07, 0.09$  with  $\sigma = 0.1$ ,  $v_{i0} = 2.5$ ,  $q = -0.9$ ,  $C_1 = 0.5$ , and  $\beta = 0.1$  are plotted in Fig. [3a-3b]. Fig. [3a] shows that  $A$  is negative and decreases nonlinearly as  $\sigma_p$  increases, while Fig. [3b] shows a compressive reduction as  $\sigma_p$  increases.

In Fig.[4a-4b] we observe the variation of amplitude ( $\phi_0$ ) and width ( $\Delta$ ) versus nonextensive parameter  $q$  with different values of  $\sigma = 0.1, 0.3, 0.5, 0.7$  and  $\sigma_p = 0.05$ ,  $v_{i0} = 2.5$ ,  $q = -0.9$ ,  $C_1 = 0.5$  and  $\alpha = 1.1$ . In (Fig.4a) we find that amplitude is rarefactive and linearly decreasing as the increasing values of  $\sigma$ , and width (Fig.4b) is increasing linearly as well as  $\sigma$ .

In Fig.[5a-5b] we have seen the variation of amplitude ( $\phi_0$ ) and width ( $\Delta$ ) versus nonextensive parameter  $q$  with different values of  $\sigma_p = 0.03, 0.05, 0.07, 0.09$  with  $\sigma_p = 0.05$ ,  $v_{i0} = 2.5$ ,  $q = -0.9$ ,  $C_1 = 0.5$  and  $\alpha = 1.1$ . In (Fig.5a) we find that amplitude is rarefactive and linearly increasing for the increasing values of  $\sigma_p$ , and width (Fig.5b) is decreasing linearly as well as  $\sigma_p$ . In Fig.[6a-6b] we shown the variation of amplitude ( $\phi_0$ ) and width ( $\Delta$ ) versus streaming velocity  $v_{i0}$  with different values of  $\sigma = 0.1, 0.3, 0.5, 0.7$  and  $\sigma_p = 0.05$ ,  $v_{i0} = 2.5$ ,  $q = -0.9$ ,  $C_1 = 0.5$ ,  $\alpha = 1.1$ . In (Fig.6a) we observe that the amplitude is rarefactive and linearly decreasing as the increasing values of  $\sigma$  and width (Fig.6b) is increasing linearly as well as  $\sigma$ .

The variation of amplitude ( $\phi_0$ ) and width ( $\Delta$ ) versus streaming velocity  $v_{i0}$  with varying values of  $\sigma_p = 0.03, 0.05, 0.07, 0.09$  for fixed  $\sigma = 0.1$ ,  $v_{i0} = 2.5$ ,  $q = -0.9$ ,  $C_1 = 0.5$  and  $\alpha = 1.1$  are shown in Fig. [7a-7b].

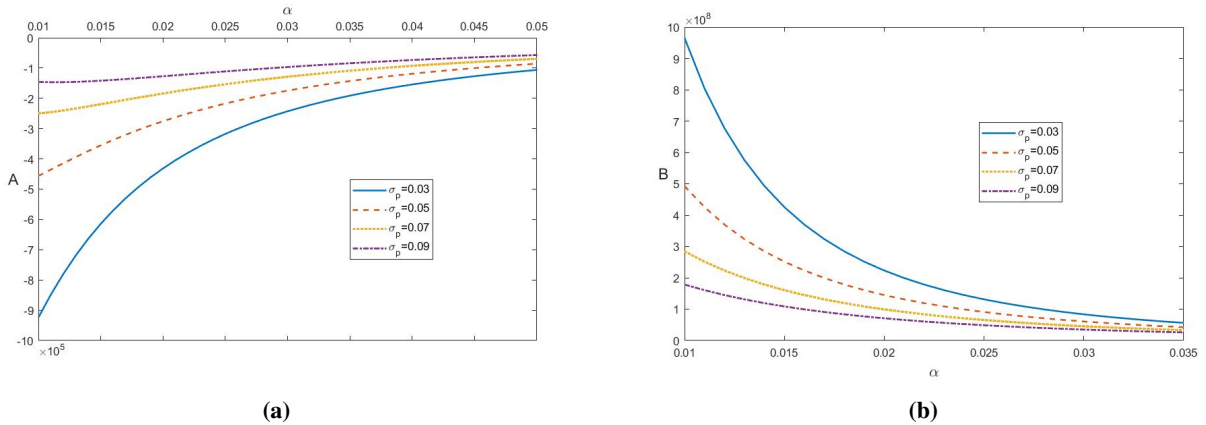


Figure 3. The variation of (a)  $A$  and (b)  $B$  versus  $\alpha$  for different values of  $\sigma_p$ .

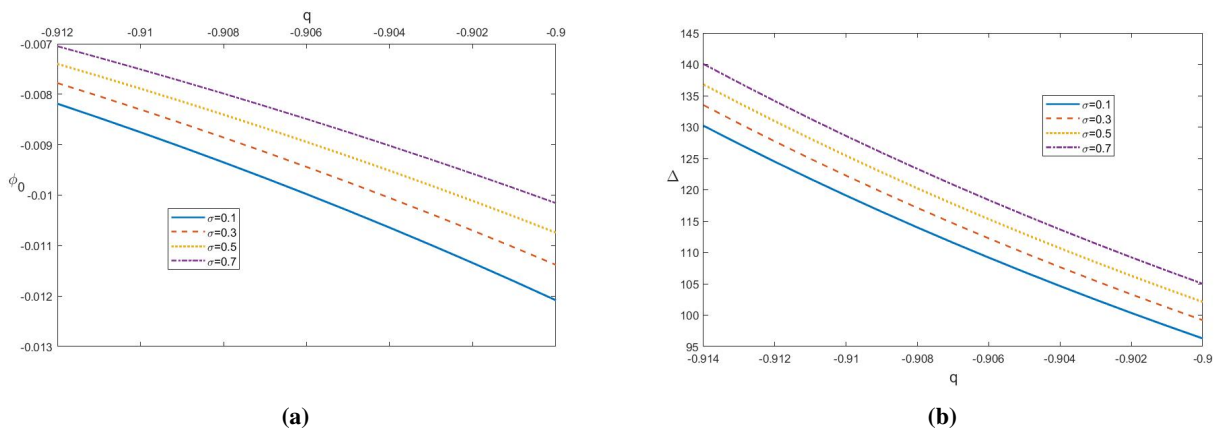


Figure 4. The variation of (a)  $\phi_0$  and (b)  $\Delta$  versus  $q$  for different values of  $\sigma$ .

The amplitude is rarefactive and increases linearly as  $\sigma_p$  increases, while the width decreases linearly as  $\sigma_p$  increases.

Again, the variation of solitary wave potential  $\phi_1(\chi)$  given in (23) versus  $\chi$  are plotted in the Fig.[8a-8b] with different values of (a)  $\sigma_p = 0.03, 0.05, 0.07, 0.09$  with  $\sigma = 0.1, v_{i0} = 2.5, q = -0.9, V = 0.5$  and (b)  $\sigma = 0.1, 0.3, 0.5, 0.7$  with  $\sigma_p = 0.05, v_{i0} = 2.5, q = -0.9, C_1 = 0.5$  and  $\alpha = 1.1$ . For both the positron to ion density ratio  $\beta$  and electron to ion density ratio  $\alpha$ , we have observed that the ion-acoustic soliton propagates rarefactively and that the amplitude of the solitary pulse increases (Fig.8a). We have also observed that as  $\sigma$  grows, the width of the solitary pulse increases slightly and the amplitude decreases.

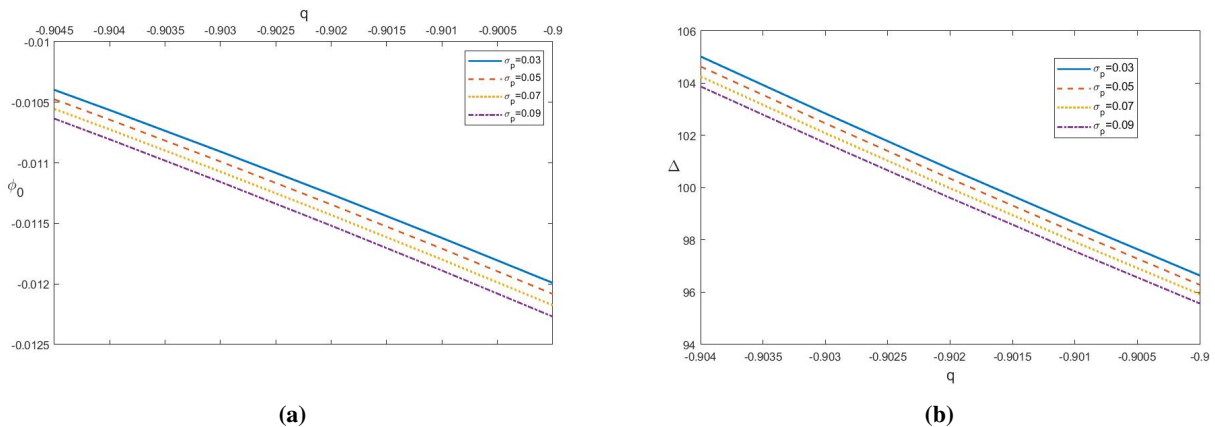


Figure 5. The variation of (a)  $\phi_0$  and (b)  $\Delta$  versus  $q$  for different values of  $\sigma_p$ .

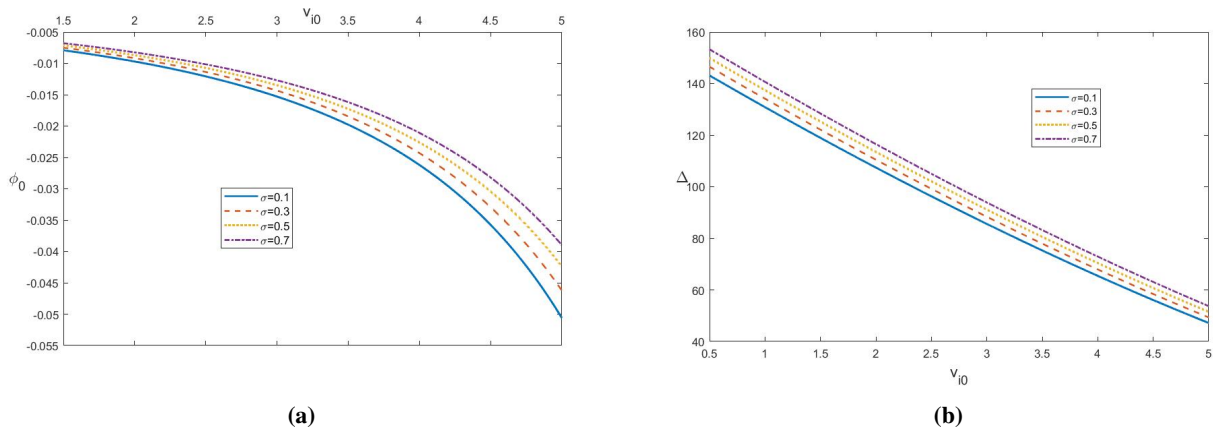


Figure 6. The variation of (a)  $\phi_0$  and (b)  $\Delta$  versus  $v_{i0}$  for different values of  $\sigma$ .

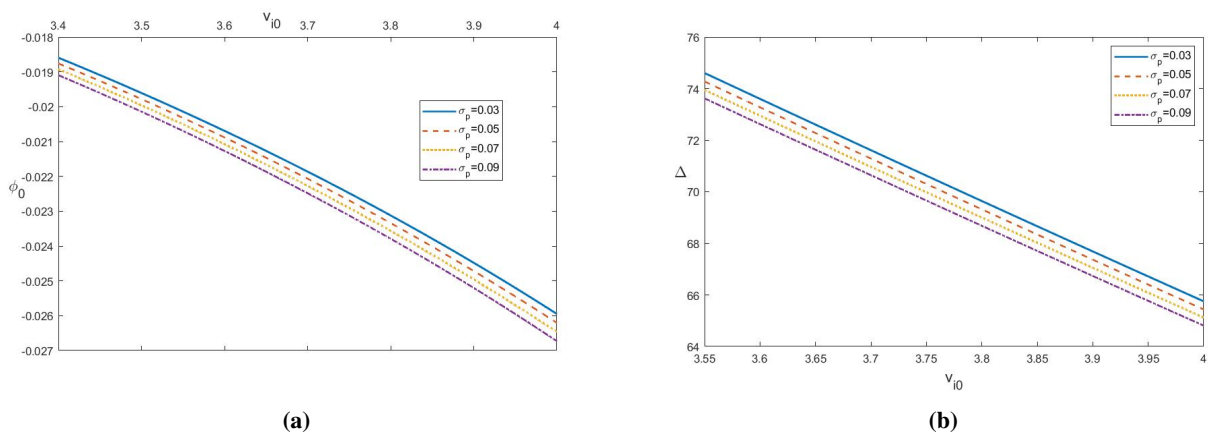


Figure 7. The variation of (a)  $\phi_0$  and (b)  $\Delta$  versus  $v_{i0}$  for different values of  $\sigma_p$ .

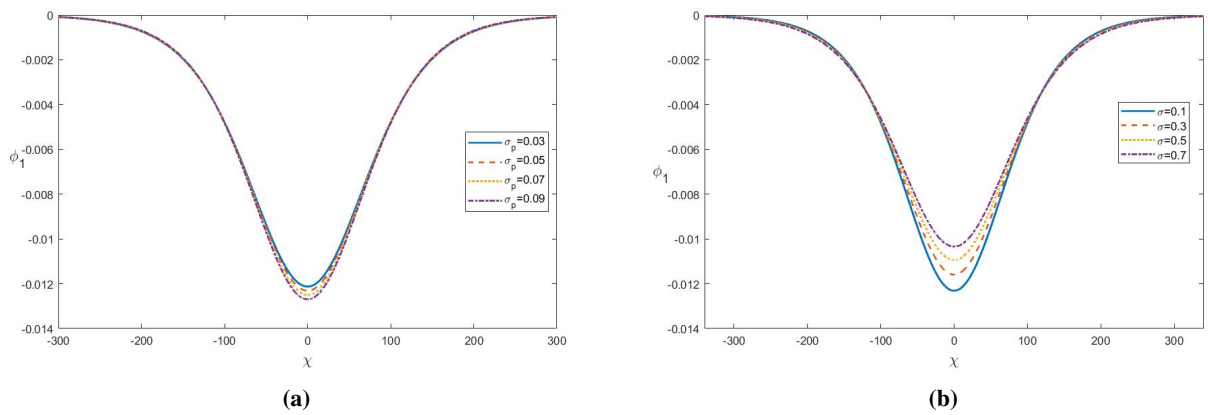


Figure 8. The variation of electric potential ( $\phi_1$ ) versus  $\chi$  for different values of (a)  $\sigma_p$  with  $\alpha = 1.1$  and (b)  $\sigma$  with  $\beta = 0.1$ .

ORCID

Rafia Khanam, <https://orcid.org/0009-0006-8648-0827>; Satyendra Nath Barman, <https://orcid.org/0000-0003-1136-8364>

REFERENCES

[1] S. Abe, and Y. Okamoto, editors, *Nonextensive statistical mechanics and its applications*, (Verlag, Berlin Heidelberg, 2001), pp. 3-98.

- [2] E.I. El-Awady, and W. Moslem, "On a plasma having nonextensive electrons and positrons: Rogue and solitary wave propagation," *Physics of Plasma*, **18**, 082306 (2011). <https://doi.org/10.1063/1.3620411>
- [3] A. Renyi, "On a new axiomatic theory of probability," *Acta Math. Hungaria*, **6**, 285-235 (1955). <https://doi.org/10.1007/bf02024393>
- [4] C. Tsallis, "Possible generalization of boltzmann-gibbs statistics," *Journal of Statistical Physics*, **52**, 479-487 (1988). <https://doi.org/10.1007/BF01016429>
- [5] M. Rahman, and S.N. Barman, "Existence of small amplitude KdV and mKdV solitons in a magnetized dusty plasma with q-nonextensive distributed electrons," *East European Journal of Physics*, (2), 74–89 (2024). <https://doi.org/10.26565/2312-4334-2024-2-06>
- [6] P. Douglas, S. Bergamini, and F. Renzoni, "Tunable Tsallis Distributions in Dissipative Optical Lattices," *Physical Review Letters*, **96**, 110601 (2006). <https://doi.org/10.1103/PhysRevLett.96.110601>
- [7] C. Tsallis, D. Prato, and A.R. Plastino, "Nonextensive Statistical Mechanics : "Some Links with Astronomical Phenomena," *Astrophysics and Space Science*, **290**, 259–274 (2004). <https://doi.org/10.1023/B:ASTR.0000032528.99179.4f>
- [8] H.R. Pakzad, "Effect of q-nonextensive distribution of electrons on electron acoustic solitons," *Astrophysics and Space Science*, **333**, 247–255 (2011). <https://doi.org/10.1007/s10509-010-0570-0>
- [9] L.A. Gougam, and M. Tribeche, "Weak ion-acoustic double layers in a plasma with a q-nonextensive electron velocity distribution," *Astrophysics and Space Science*, **331**, 181–189 (2011). <https://doi.org/10.1007/s10509-010-0447-2>
- [10] A.N. Dev, M.K. Deka, R.K. Kalita, and J. Sarma, "Effect of non-thermal electron and positron on the dust ion acoustic solitary wave in the presence of relativistic thermal magnetized ions," *The European Physical Journal Plus*, **135**, 843 (2020). <https://doi.org/10.1140/epjp/s13360-020-00861-3>
- [11] M. Tribeche, R. Amour, and P.K. Shukla, "Ion acoustic solitary waves in a plasma with nonthermal electrons featuring Tsallis distribution," *Physical Review E*, **85**, 037401 (2012). <https://doi.org/10.1103/PhysRevE.85.037401>
- [12] M. Tribeche, and L. Djebarni, "Electron-acoustic solitary waves in a nonextensive plasma," *Physics of Plasmas*, **17**, 124502 (2010). <https://doi.org/10.1063/1.3522777>
- [13] L. Liyan, and D. Jiulin, "Ion acoustic waves in the plasma with the power-law q-distribution in nonextensive statistics," *Physica A: Statistical Mechanics and its Applications*, **387**(19-20), 4821-4827 (2008). <https://doi.org/10.1016/j.physa.2008.04.016>
- [14] U.K. Samanta, A. Saha, and P. Chatterjee, "Bifurcations of dust ion acoustic travelling waves in a magnetized dusty plasma with a q-nonextensive electron velocity distribution," *Physics of Plasmas*, **20**, 022111 (2013). <https://doi.org/10.1063/1.4791660>
- [15] A.A. Mahmoud, E.M. Abulwafa, A.F. Al-Araby, and A.M. Elhanbaly, "Plasma parameters effects on dust acoustic solitary waves in dusty plasmas of four components," *Advances in Mathematical Physics*, **11**, 7935317 (2018). <https://doi.org/10.1155/2018/7935317>
- [16] F. Araghi, S. Miraboutalebi, and D. Dorrani, "Effect of variable dust size, charge and mass on dust acoustic solitary waves in nonextensive magnetized plasma," *Indian Journal of Physics*, **94**, 547–554 (2020). <https://doi.org/10.1007/s12648-019-01488-6>
- [17] S. Guo, L. Mei, and A. Sun, "Nonlinear ion-acoustic structures in a nonextensive electron–positron–ion–dust plasma: Modulational instability and rogue waves," *Annals of Physics*, **38-55**, 332 (2012). <https://doi.org/10.1016/j.aop.2013.01.016>
- [18] S.N. Paul, C. Das, I. Paul, B. Bandyopadhyay, S. Chattopadhyaya, and S.S. De, "Ion acoustic solitary waves in an electron–ion–positron plasma," *Indian Journal of Physics*, **86**, 545–553 (2012). <https://doi.org/10.1007/s12648-012-0080-8>
- [19] B. Boro, A.N. Dev, B.K. Saikia, and N.C. Adhikary, "Nonlinear Wave Interaction with Positron Beam in a Relativistic Plasma: Evaluation of Hypersonic Dust Ion Acoustic Waves," *Plasma Physics Reports*, **46**, 641–652 (2020). <https://doi.org/10.1134/S1063780X20060021>
- [20] P. Eslami, M. Mottaghizadeh, and H.R. Pakzad, "Nonplanar dust acoustic solitary waves in dusty plasmas with ions and electrons following a q-nonextensive distribution," *Physics of Plasmas*, **18**, 102303 (2011). <https://doi.org/10.1063/1.3642639>
- [21] S. Guo, L. Mei, and A. Sun, "Nonlinear ion-acoustic structures in a nonextensive electron–positron–ion–dust plasma: Modulational instability and rogue waves," *Annals of Physics*, **332**, 38-55 (2012). <https://doi.org/10.1016/j.aop.2013.01.016>
- [22] P. Chatterjee, K. Roy, and U.N. Ghosh, *Waves and Wave Interactions in Plasmas*, (World Scientific Publishing Co Pte Ltd, 2022), pp. 25-28.
- [23] A.W. Strong, and I.V. Moskalenko, "Propagation of Cosmic-Ray Nucleons in the Galaxy," *Astrophysical Journal*, **509**, 212 (1998). <https://doi.org/10.1086/306470>
- [24] Y.N. Nejoh, "Effects of Positron Density and Temperature on Large Amplitude Ion-acoustic Waves in an Electron–Positron–Ion Plasma," *Australian Journal of Physics*, **50**(2), 309-317 (1997). <https://doi.org/10.1071/P96064>
- [25] U.N. Ghosh, A. Saha, N. Pal, and P. Chatterjee, "Dynamic structures of nonlinear ion acoustic waves in a nonextensive electron–positron–ion plasma," *Journal of Theoretical and Applied Physics*, **9**, 321–329 (2015). <https://doi.org/10.1007/s40094-015-0192-6>
- [26] M.G. Hafez, M.R. Talukder, and R. Sakthivel, "Ion acoustic solitary waves in plasmas with nonextensive distributed electrons, positrons and relativistic thermal ions," *Indian Journal of Physics*, **90**, 603–611 (2016). <https://doi.org/10.1007/s12648-015-0782-9>
- [27] A. Danehkar, "Electrostatic solitary waves in an electron-positron pair plasma with suprathermal electrons," *Phys. Plasmas*, **24**, 102905 (2017). <https://doi.org/10.1063/1.5000873>

**УТВОРЕННЯ ІОННО-АКУСТИЧНИХ ОДИНОЧНИХ ХВИЛЬ У ПЛАЗМІ З НЕЕКСТЕНСИВНИМИ ЕЛЕКТРОНАМИ І ПОЗИТРОНАМИ****Рафія Ханам<sup>a</sup>, Сатьєндра Нат Барман<sup>b</sup>**<sup>a</sup> *Департамент математики, Університет Гаухаті, Гувахаті - 781014, Ассам, Індія*<sup>b</sup> *B. Borooah College, Guwahati-781007, Ассам, Індія*

У цій моделі плазми теоретично досліджено іони, електрони та позитрони, коли і електрони, і позитрони підкоряються  $q$ -неекстенсивному розподілу швидкостей. Метод відновного збурення використовується для отримання рівняння Кортевега де Фріза (KdV), що описує базовий набір нормалізованих рівнянь рідини. Чисельно досліджено існування іонно-акустичних одиночних хвиль залежно від неекстенсивного параметра, відношення температур електрона до позитрона, відношення температур іона до електрона та швидкості потоку. Було виявлено, що лише швидкі іонно-акустичні моди можуть викликати співіснування розріджених солітонів малої амплітуди.

**Ключові слова:**  $q$ -неекстенсивний розподіл; редуکتивний метод збурень; рівняння KdV

## GENERALIZED GHOST PILGRIM DARK ENERGY IN BRANS–DICKE THEORY

 Yetchena Prasanthi,  Davuluri Neelima

*Department of Mathematics, GITAM (Deemed to be University), Visakhapatnam-530045, India*

*Corresponding Author e-mail: [neeludavuluri@gmail.com](mailto:neeludavuluri@gmail.com)*

Received August 29, 2024; revised November 12, 2024; in final form November 14, 2024; accepted November 24, 2024

This paper aims to investigate, how the Bianchi Type-V cosmological model can be solved using the generalized ghost pilgrim dark energy postulated by the Brans-Dicke theory of gravitation (Phys. Rev.124, 925 1961). To discover the answers, we rely on the assumptions of (i) the correlation between metric potentials and (ii) the exponential relationship between scale factor and scalar field. The generalized ghost pilgrim dark energy model has been found to be correlated with the polytropic gas dark energy model. A few physical quantities have been used to explain the solutions' physical behavior.

**Keywords:** *Brans-Dicke theory of gravitation; Bianchi Type-V cosmological model; Ghost Pilgrim Dark Energy*

**PACS:** 04.50.Kd; 95.36.x; 95.35.d; 98.80.-k

### 1. INTRODUCTION

The cosmos is expanding more quickly than previously assumed, which is the most remarkable finding in contemporary cosmology. High Red shift Supernova is provided the first indication of this expansionary behavior, which was evidence by a wide range of astronomers. According to Cosmic Microwave Background Radiation (CMBR) and supernovae surveys radiation, dark energy and dark matter are the three primary constituents of the cosmos. Dark matter (DM) is an unidentified form of matter that exhibits the same clustering features as ordinary matter, whereas dark energy (DE) is an unusual form of an unidentified repulsive force.

The Bianchi V model is a natural extension of the homogeneous and isotropic Friedmann-Robertson-Walker (FRW) models that allows for a certain form of anisotropy. This model implies homogeneity but not isotropy, making it a helpful tool for investigating how deviations from perfect isotropy may affect the universe's evolution. Because scalar fields are sensitive to the universe's expansion rate, an anisotropic model such as Bianchi V can show behaviors that differ from those observed in isotropic environments. Bianchi models, notably Bianchi V, enable researchers to evaluate the potential level of anisotropy and its impact on observable values. This model bridges the gap between idealized isotropic models and more realistic cosmological phenomena, allowing researchers to investigate how minor anisotropies and curvature influenced the early universe's history and current condition.

Among the different dynamic models for dark energy, the equation of state (EoS) parameter is seen as the best choice to serve as dark energy. The Quintessence K-essence is popular DE models. Phantom, quantum, tachyon, holographic DE, age graphic DE, two fluids DE, anisotropic DE and so on. The solution came from the phantom dark energy, which is a scalar field with negative kinetic energy. A phantom-like dark energy results in everything crashing as our universe approaches its big-rip ending. The pilgrim dark energy model (PDE) was proposed by Wei [1]. This idea was supported by the idea that the strong repulsive force of DE makes it possible to prevent the development of black holes (BHs). The investigations of Babichev et al. [2] support the same conclusion, namely that BH mass decreases as a result of the phantom accretion event. To create a black hole free phantom universe, several authors have suggested several methods. Sharif and Jawad [3,4] have researched the interacting PDE in universes with both flat and non-flat configurations and various IR cutoffs. Sharif and Rani [5] and Jawad and Debnath [6], as well as Jawad [7], have conducted research on PDE cosmological models within different modified theories of gravitation. The connection between PDE and scalar field models was explored by Jawad and Majeed [8]. Jawad et al. [9] conducted a study on the properties of several newly developed versions of PDE within the DGP braneworld. Feng and Shen [10], Movahed and Sheykhi [11], S.D. Katore, and D. V. Kapse [12], Zubair and Abbas [13], Fayaz and Hossienkhani [14], Honarvaryan and Moradpour [15] have explored the different elements of ghost and generalized ghost dark energy (GGDE) models. The GGDE density is referred to as generalized ghost pilgrim dark energy (GGPDE) in the terms of PDE.

The Brans and Dicke [16] developed a scalar-tensor theory of gravity to integrate Mach's principle into Einstein's theory of gravitation. The Brans and Dicke theory suggest that all types of matter interact equally with a scalar field that has dimensions inversely proportional to the gravitational constant. The Brans-Dicke theory is an important scalar-tensor theory that has been widely used in contemporary cosmology, as highlighted by Banerjee and Pavon [17] and Bertolami and Martins [18]. The extended chaotic inflation (Linde [19]), the potential challenge of a 'graceful exit' (Pimental [20]) and an inflationary universe (Johri and Mathiazhagan [21]), all stem from the Brans-Dicke scalar-tensor theory.

Setare [22] investigated the holographic dark energy in non-flat Brans–Dicke cosmology. Vagenas and Setare [23] have examined the cosmological dynamics of interacting holographic dark energy models. Kiran, Reddy and Rao [24]

have recently conducted research on Brans–Dicke theory of gravitation, specifically focusing on minimally interacting holographic DE models. Regarding the HDE cosmological model, Rao [25] has taken into consideration the Brans–Dicke theory of gravitation. Because they are homogenous and anisotropic, cosmological models of the Bianchi type are crucial for understanding how the universe isochronizes over the course of cosmic history.

The idea behind the construction of cosmological models is the same as ours and Bhardwaj et al. [26]. The process differs slightly when energy momentum tensors are included. Furthermore, the assumptions used to obtain the solutions are different. They compared their results with observational data, but we compared our results using mathematical results. We are inspired by their work, yet our results are not the same.

In this paper, there are various astrophysical reasons to adopt anisotropic models in the current epoch. In general relativity, isotropic solutions (such as the Friedmann–Lemaître–Robertson–Walker metric) are not the sole universe-modeling possibilities. Anisotropic models, like Bianchi cosmologies, provide mathematically sound answers to Einstein's field equations. Studying these solutions broadens our understanding of the types of worlds that are theoretically feasible under general relativity, even if they do not appear to apply to our universe. Analyzing anisotropic models may help us understand how an initially anisotropic state might change into the isotropic cosmos we see today or whether there are still theoretically significant traces of this early anisotropy that are too faint to detect today.

In this paper, we will be exploring the Bianchi type-V GGPDE model within the context of the Brans–Dicke theory of gravitation. Section 2 of the paper will present the metric and field equations for the Bianchi type-V within the Brans - Dicke theory of gravitation. Section 3 is devoted to presenting the solutions obtained from the field equations, along with a discussion of the calculations of different physical parameters. These solutions are the basis for our comprehension of the behavior and dynamics of the GGPDE model within the framework of the Bianchi type-V space-time cosmological model. Section 4 delves into the subject of sound speed. Section 5 discusses the analysis of the  $\omega_G - \omega_G'$ -plane. Section 6 offers conclusions, and Section 7 includes a detailed list of references cited in the paper.

## 2. METRIC AND FIELD EQUATIONS

The line element of the Bianchi type-V space-time cosmological model can be expressed as

$$ds^2 = dt^2 - D_1^2 dx^2 - D_2^2 e^{-2x} dy^2 - D_3^2 e^{-2x} dz^2. \tag{1}$$

Where  $D_1, D_2$  and  $D_3$  are functions of time  $t$  only.

The action for Brans–Dicke theory is given by

$$s = \frac{1}{16\pi} \int \sqrt{-g} \left( \varphi R - \omega \frac{\varphi_{,i} \varphi^{,i}}{\varphi} \right) d^4 x + \frac{1}{16\pi} \int \sqrt{-g} L_m d^4 x. \tag{2}$$

Where  $L_m$  stands for Lagrangian matter field,  $\varphi$  denotes the Brans–Dicke scalar field and  $\omega$  is the Brans–Dicke coupling constant.

The Brans–Dicke field equations can be expressed as follows

$$R_{uv} - \frac{1}{2} R g_{uv} = \frac{-8\pi}{\varphi} T_{uv} - \omega \varphi^{-2} \left( \varphi_{,u} \varphi_{,v} - \frac{1}{2} g_{uv} \varphi_{,i} \varphi^{,i} \right) - \frac{1}{\varphi} (\varphi_{u;v} - g_{uv} \varphi_{,i}^{,i}), \tag{3}$$

and

$$\nabla \varphi = \varphi_{,i}^{,i} = \frac{8\pi T}{3 + 2\omega}. \tag{4}$$

Here  $\omega$  is constant,  $G_{uv} = R_{uv} - \frac{1}{2} R g_{uv}$  is the Einstein tensor,  $R_{uv}$  is Ricci curvature tensor,  $R$  is Ricci scalar and  $T_{uv}$  is the energy momentum tensor of matter,  $\varphi$  is the Brans–Dicke scalar field,  $g_{uv}$  is the metric tensor of space time.

Brans–Dicke field equations can now be expressed as follows

$$G_u^v = \frac{-8\pi}{\varphi} T_u^v - \omega \varphi^{-2} \left( g^{uv} \varphi_{,u} \varphi_{,v} - \frac{1}{2} \delta_u^v \varphi_{,i} \varphi^{,i} \right) - \frac{1}{\varphi} (g^{uv} \varphi_{u;v} - \nabla \varphi). \tag{5}$$

Also, the energy conservation equation in the Brans–Dicke theory is

$$T_{;v}^{uv} = 0. \tag{6}$$

The equation of the energy momentum tensors for matter and dark energy as follows

$$T_{uv} = T_{uv}^m + T_{uv}^\wedge. \tag{7}$$

Where  $T_{uv}^m$  and  $T_{uv}^\wedge$  are represents the energy momentum tensor for dark matter and dark energy respectively and are defined as the energy momentum tensor for dark matter

$$T_{uv}^m = \text{diag} (1, 0, 0, 0) \rho_m = \text{diag} (\rho_m, 0, 0, 0).$$

$$T_{11}^m = T_{22}^m = T_{33}^m = 0 \text{ and } T_{44}^m = \rho_m. \tag{8}$$

The energy momentum tensor for dark energy

$$T_{uv}^\wedge = \text{diag}(\rho_G, P_G, P_G, P_G),$$

$$T_{uv}^\wedge = \text{diag} (1, -\omega_G, -\omega_G, -\omega_G) \rho_G = \text{diag} (\rho_G, -\omega_G \rho_G, -\omega_G \rho_G, -\omega_G \rho_G). \tag{9}$$

Here the  $T_{44}$  component reflects the energy density in the stress-energy tensor. The diagonal spatial components ( $T_{11}, T_{22}, T_{33}$ ) correspond to pressures in each spatial direction ( $P_{xx}, P_{yy}, P_{zz}$ ).

$$T_{11}^\wedge = T_{22}^\wedge = T_{33}^\wedge = -\omega_G \rho_G \text{ and } T_{44}^m = \rho_G, \tag{10}$$

$$T_{uv} = T_{uv}^m + T_{uv}^\wedge = \text{diag} (\rho_m, 0, 0, 0) + \text{diag} (\rho_G, -\omega_G \rho_G, -\omega_G \rho_G, -\omega_G \rho_G),$$

$$T_{uv} = \text{diag} (\rho_G + \rho_m, -\omega_G \rho_G, -\omega_G \rho_G, -\omega_G \rho_G). \tag{11}$$

Where  $\rho_m$  and  $\rho_G$  are the energy densities of dark matter and the dark energy respectively and  $p_G$  is the pressure of the dark energy.  $\rho_m, \rho_G$  and  $p_G$  are dependent only on the variable time t.

Components of energy momentum tensors are

$$T_1^1 = T_2^2 = T_3^3 = -\omega_G \rho_G \text{ and } T_4^4 = \rho_G + \rho_m. \tag{12}$$

Substitute the values of Einstein tensor, metric tensor of Bianchi type-V space-time and energy momentum tensor in Brans-Dicke theory, we obtain the field equations of the model.

The metric's field equations (1) can be represented using equation (12) as shown

$$\frac{\ddot{D}_2}{D_2} + \frac{\ddot{D}_3}{D_3} + \frac{\dot{D}_2 \dot{D}_3}{D_2 D_3} - \frac{1}{D_1^2} + \frac{\omega \dot{\phi}^2}{2 \phi^2} + \frac{\dot{\phi}}{\phi} \left( \frac{\dot{D}_2}{D_2} + \frac{\dot{D}_3}{D_3} \right) + \frac{\ddot{\phi}}{\phi} = \frac{8\pi}{\phi} T_1^1 = -\frac{8\pi}{\phi} \omega_G \rho_G, \tag{13}$$

$$\frac{\ddot{D}_1}{D_1} + \frac{\ddot{D}_3}{D_3} + \frac{\dot{D}_1 \dot{D}_3}{D_1 D_3} - \frac{1}{D_1^2} + \frac{\omega \dot{\phi}^2}{2 \phi^2} + \frac{\dot{\phi}}{\phi} \left( \frac{\dot{D}_1}{D_1} + \frac{\dot{D}_3}{D_3} \right) + \frac{\ddot{\phi}}{\phi} = \frac{8\pi}{\phi} T_2^2 = -\frac{8\pi}{\phi} \omega_G \rho_G, \tag{14}$$

$$\frac{\ddot{D}_1}{D_1} + \frac{\ddot{D}_2}{D_2} + \frac{\dot{D}_1 \dot{D}_2}{D_1 D_2} - \frac{1}{D_1^2} + \frac{\omega \dot{\phi}^2}{2 \phi^2} + \frac{\dot{\phi}}{\phi} \left( \frac{\dot{D}_1}{D_1} + \frac{\dot{D}_2}{D_2} \right) + \frac{\ddot{\phi}}{\phi} = \frac{8\pi}{\phi} T_3^3 = -\frac{8\pi}{\phi} \omega_G \rho_G, \tag{15}$$

$$\frac{\dot{D}_2 \dot{D}_3}{D_2 D_3} + \frac{\dot{D}_1 \dot{D}_3}{D_1 D_3} + \frac{\dot{D}_1 \dot{D}_2}{D_1 D_2} - \frac{3}{D_1^2} + \frac{\omega \dot{\phi}^2}{2 \phi^2} + \frac{\dot{\phi}}{\phi} \left( \frac{\dot{D}_1}{D_1} + \frac{\dot{D}_2}{D_2} + \frac{\dot{D}_3}{D_3} \right) = \frac{8\pi}{\phi} T_4^4 = \frac{8\pi}{\phi} (\rho_G + \rho_m), \tag{16}$$

$$2 \frac{\dot{D}_1}{D_1} = \frac{\dot{D}_2}{D_2} + \frac{\dot{D}_3}{D_3}, \tag{17}$$

$$\ddot{\phi} + \frac{\dot{\phi}}{\phi} \left( \frac{\dot{D}_1}{D_1} + \frac{\dot{D}_2}{D_2} + \frac{\dot{D}_3}{D_3} \right) = \frac{8\pi}{3 + 2\omega} (\rho_m + \rho_G - 3\omega_G \rho_G). \tag{18}$$

Energy conservation equation is

$$\dot{\rho}_m + \rho_m \left( \frac{\dot{D}_1}{D_1} + \frac{\dot{D}_2}{D_2} + \frac{\dot{D}_3}{D_3} \right) + \dot{\rho}_G + \rho_G \left( \frac{\dot{D}_1}{D_1} + \frac{\dot{D}_2}{D_2} + \frac{\dot{D}_3}{D_3} \right) + \omega_G \rho_G \left( \frac{\dot{D}_1}{D_1} + \frac{\dot{D}_2}{D_2} + \frac{\dot{D}_3}{D_3} \right) = 0. \tag{19}$$

Where notation dot ( $\dot{\cdot}$ ) representing ordinary differentiation with respect to time t.

From (13) to (18), the equations 13, 14 and 15 represents rr components and equation 16 represents 00 component of the field equations.

### 3. SOLUTIONS OF THE FIELD EQUATIONS

Now, equations (13)-(18) constitute a system of six distinct equations containing eight unknown variables  $D_1, D_2, D_3, \rho_m, \omega_G, \rho_G$  and  $\varphi, P_G$ .

From equation (14), we have

$$D_1^2 = D_2 D_3. \quad (20)$$

We assume that the metric potentials  $D_2$  and  $D_3$  have a relationship

$$D_2 = D_3^k. \quad (21)$$

Here  $k$  is a constant and  $k \neq 1$ .

A power-law relationship between scalar field  $\phi$  and average scale factor  $a(t)$  of the form (Johri and Sudharsan [27]; Johri and Desikan [28]),

$$\varphi \propto [a(t)]^n.$$

Where  $n$  denotes a power index.

This form of scalar field has been the subject of investigation by numerous writers. We use the following assumption to simplify the system mathematically, taking into account the physical importance of the previous relationship.

$$\varphi = \varphi_0 [a(t)]^n,$$

$$\varphi = [a(t)]^n \text{ where } \varphi_0 = 1. \quad (22)$$

Where  $n$  represents a constant that is greater than zero.

The scalar field and the scale factor are deeply interlinked in Brans-Dicke scalar-tensor theory. Their relationship determines the cosmic expansion rate, affects structure formation, and provides a pathway to test deviations from GR. This interplay makes the connection fundamental to understanding both early-universe and late-time cosmology.

In Bianchi V models, the metric can typically be expressed in terms of distinct directional scale factors, which represent the expansion along each spatial direction. These factors vary independently, leading to different expansion rates in each direction. The effective or average scale factor is then often defined as the geometric mean of these directional components:

$$a(t) = (D_1 D_2 D_3)^{\frac{1}{3}}. \quad (23)$$

This definition provides a single parameter for describing the average expansion rate, even though the expansion is anisotropic.

In the Bianchi Type-V cosmological model, the spatial volume can be described using the scale factors  $D_1, D_2$  and  $D_3$ .

The Volume scale factor  $V$  can be written as

$$V = [a(t)]^3 = D_1 D_2 D_3. \quad (24)$$

Using equations (20), (21), (22), (24) and (14), we get

$$D_3 = \left[ \frac{(3+n)(k+1)}{2} (c_1 t + c_2) \right]^{\frac{2}{[(3+n)(k+1)]}}. \quad (25)$$

Where  $c_1$  and  $c_2$  are the integration constants.

From (21), we have

$$D_2 = D_3^k = \left[ \frac{(3+n)(k+1)}{2} (c_1 t + c_2) \right]^{\frac{2k}{[(3+n)(k+1)]}}. \quad (26)$$

From equations (20), (25) and (26), we have

$$D_1 = \left[ \frac{(3+n)(k+1)}{2} (c_1 t + c_2) \right]^{\frac{(k+1)}{[(3+n)(k+1)]}}. \quad (27)$$

Therefore, the corresponding metric can be expressed as

$$ds^2 = dt^2 - \left[ \frac{(3+n)(k+1)}{2} (c_1 t + c_2) \right]^{\frac{(k+1)}{[(3+n)(k+1)]}} dx^2 - e^{-2x} \left[ \frac{(3+n)(k+1)}{2} (c_1 t + c_2) \right]^{\frac{2k}{[(3+n)(k+1)]}} dy^2 - e^{-2x} \left[ \frac{(3+n)(k+1)}{2} (c_1 t + c_2) \right]^{\frac{2}{[(3+n)(k+1)]}} dz^2 \tag{28}$$

We determine the universe's scale factor using equations (24), (25), (26), and (27) as

$$a(t) = \left[ \frac{(3+n)(k+1)}{2} (c_1 t + c_2) \right]^{\frac{(k+1)}{[(3+n)(k+1)]}} = [c_3 (c_1 t + c_2)]^{\frac{k+1}{2c_3}} \tag{29}$$

Where  $c_3 = \frac{(3+n)(k+1)}{2}$ .

Hence from equations (22) and (29), we have scalar field ( $\phi$ ) as

$$\phi = [c_3 (c_1 t + c_2)]^{\frac{(k+1)n}{2c_3}} \tag{30}$$

From equation (29), we find the Hubble's parameter as

$$H = \frac{\dot{a}(t)}{a(t)} = \frac{c_1 (k+1)}{2c_3 (c_1 t + c_2)} \tag{31}$$

According to Sharif and Nazir [29], as well as Santhi et al. [30], and Rao and Prasanthi [31], the GGPDE is defined as follows

$$\rho_G = (\alpha_1 H + \alpha_2 H^2)^\gamma \tag{32}$$

Where  $\gamma$  is the dimensionless constant.

Therefore, the energy density of GGPDE is derived from equations (31) and (32).

$$\rho_G = \left( \frac{\alpha_1 c_1 (k+1)}{2c_3 (c_1 t + c_2)} + \frac{\alpha_2 c_1^2 (k+1)^2}{4c_3^2 (c_1 t + c_2)^2} \right)^\gamma \tag{33}$$

We can determine the energy density of matter using equations (6), (14), (25), (26), (27), (30), and (32). Then

$$\rho_m = \frac{c_1^2 [c_3 (c_1 t + c_2)]^{\frac{n(k+1)}{2c_3}}}{8\pi c_3^2 (c_1 t + c_2)^2} \left\{ k^2 + 4k + 1 - \frac{3c_1^{-2}}{[c_3 (c_1 t + c_2)]^{\frac{k+1-2c_3}{c_3}}} - \frac{\omega n^2 (k+1)^2}{8} + \frac{3n(k+1)^2}{4} \right\} - \left( \frac{\alpha_1 c_1 (k+1)}{2c_3 (c_1 t + c_2)} + \frac{\alpha_2 c_1^2 (k+1)^2}{4c_3^2 (c_1 t + c_2)^2} \right)^\gamma \tag{34}$$

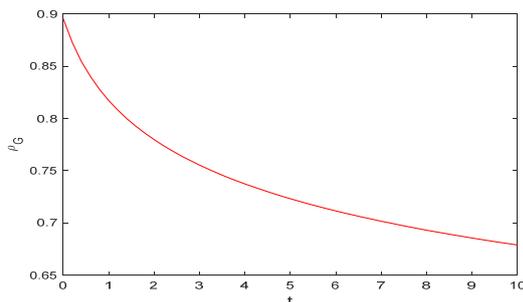


Figure 1. The energy density ( $\rho_G$ ) of GGPDE versus time t

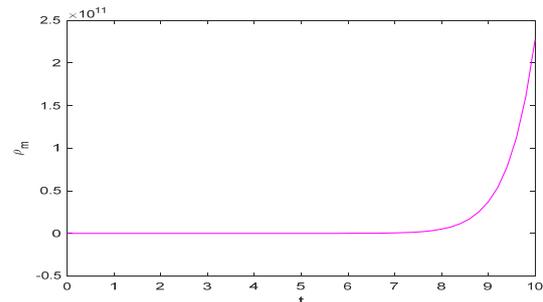


Figure 2. The energy density ( $\rho_m$ ) of matter versus time t

Hence from equations (13) and (34), we have equation of EoS of GGPDE as

$$\omega_G = \left\{ \left( k^2 + k + 1 \right) - c_3 (k + 1) + \frac{\omega n^2 (k + 1)^2}{8} - \frac{c_1^{-2}}{[c_3 (c_1 t + c_2)]^{\frac{k+1-2c_3}{c_3}}} + \frac{n(k+1)^2}{2} + \frac{n^2(k+1)^2 c_1 [n(k+1) - 2c_3]}{4c_3 (c_1 t + c_2)} \right\} \frac{-[c_3 (c_1 t + c_2)]^{\frac{n(k+1)}{2c_3}}}{8\pi \left( \frac{\alpha_1 c_1 (k+1)}{2c_3 (c_1 t + c_2)} + \frac{\alpha_2 c_1^2 (k+1)^2}{4c_3^2 (c_1 t + c_2)^2} \right)^\gamma c_3^2 (c_1 t + c_2)^2} \tag{35}$$

Hence from equations (18), (33) and (34), we find the pressure of GGPDE as

$$p_G = \frac{-[c_3(ct_1 + c_2)]^{\frac{n(k+1)}{2c_3}} c_1^2}{8\pi c_3^2 (c_1t + c_2)^2} \left\{ \begin{aligned} & \left( (k^2 + k + 1) - c_3(k + 1) + \frac{\omega n^2 (k + 1)^2}{8} - \frac{c_1^{-2}}{[c_3 (c_1t + c_2)]^{\frac{k+1-2c_3}{c_3}}} + \frac{n(k+1)^2}{2} \right) \\ & \frac{n^2 (k + 1)^2 c_1 [n(k + 1) - 2c_3]}{4c_3 (c_1t + c_2)} \end{aligned} \right\}. \tag{36}$$

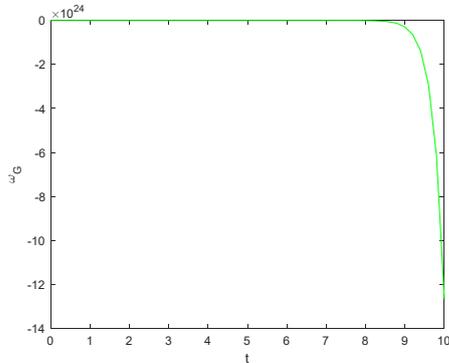


Figure 3. The EoS ( $\omega_G$ ) of GGPDE versus time

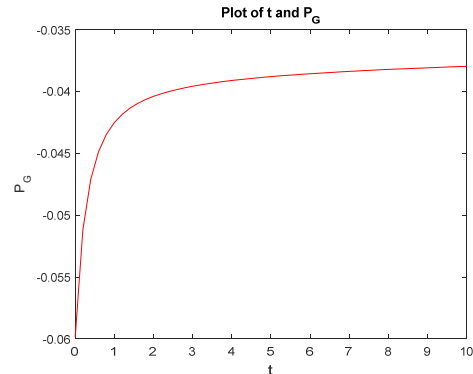


Figure 4. The pressure ( $P_G$ ) of the D.E versus time t

In the cosmological model of Bianchi type-V, the Volume scale factor V can be written as

$$V = [a(t)]^3 = [c_3 (c_1t + c_2)]^{\frac{3(k+1)}{2c_3}}. \tag{37}$$

The Hubble parameter represented by H; the Hubble parameter H is explicated as the speed at which the scale factor a (t) evolves as time t progresses.

The Hubble's parameter can be calculated from equations (25) and (29) as follows

$$H = \frac{\dot{a}(t)}{a(t)} = \frac{c_1 (k + 1)}{2c_3 (c_1t + c_2)} \tag{38}$$

The deceleration parameter, represented by q is another major parameter in cosmology. The value of q decides whether the cosmos is slowing down or speeding up. A positive value of q indicates the cosmos is slowing down while a negative value of q indicates the cosmos is speeding up.

The definition of the Deceleration parameter q is

$$q = \frac{-\ddot{a}(t)}{a(t)H^2}$$

From equations (29) and (38) as follows

$$q = \frac{-\ddot{a}}{aH^2} = -1 + \frac{2c_3}{k + 1} = -1 + c_4 \tag{39}$$

where  $c_4 = \frac{2c_3}{k + 1}$

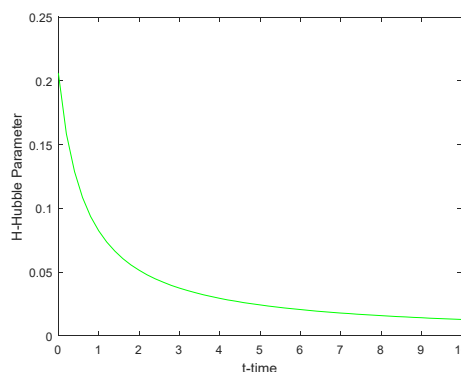


Figure 5. The Hubble's Parameter (H) versus time t

**The statefinder Parameters (r,s):** In order to differentiate between multiple D.E possibilities, Sahni and Varun [32] suggested a new parameters called the statefinder parameter (r,s).The pair consists of the calculation of r using the scale factor a(t) and its derivatives in relation to time (t) up to the third order, as well as combining 'r' with the deceleration parameter 'q' to create 's'.

The statefinder parameters are described as

$$r = \frac{\ddot{a}}{aH^3} = c_3^3 \left[ 1 - \frac{2c_3}{k+1} \right] \left[ 1 - \frac{4c_3}{k+1} \right] \text{ and } s = \frac{r-1}{3\left(q-\frac{1}{2}\right)} = \frac{c_3^3 \left[ 1 - \frac{2c_3}{k+1} \right] \left[ 1 - \frac{4c_3}{k+1} \right] - 1}{3\left(\frac{-3}{2} + \frac{c_3}{k+1}\right)} \quad (40)$$

As the statefinder depends on the scale factor the statefinder parameters are analyzed geometrically. The Statefinder parameters are an essential tool in contemporary cosmology and is used to distinguish different models of dark energy. In this particular scenario, different paths in the {r, s} plane illustrate the time progression of various dark energy models. A popular region can be elucidated using the pair as follows: (r, s)=(1,0) which represents the Einstein-de Sitter limit, which is connected with a matter-dominated universe, (r, s)=(1,1) analogous to the  $\Lambda$ CDM limit, which is often associated with a universe controlled by dark energy with a cosmological constant, while  $s > 0$  and  $r < 1$  shows the parameter space associated with quintessence and phantom DE, the analysis of any deviation of a D.E model from these specific points is carried out in the {r, s} plane. Equation (40) display the diagnostic pairs (r, s) for the suggested model.

**Density Parameter:** Usually, many researchers depict the total density parameter as being close to one i.e.  $\Omega \approx 1$ . Determining the density parameter is essential in establishing if  $\Omega > 1$ ,  $\Omega < 1$ , or exactly  $\Omega = 1$ , since it ultimately dictates the fate of the cosmos. If the value  $\Omega$  is greater than 1, this indicates that the cosmos is closed and will eventually stop expanding, collapsing in the future. If the value of  $\Omega < 1$ , it indicates that the cosmos is open and is expected to keep expanding indefinitely. If the value is  $\Omega = 1$ , it means that the cosmos is flat and has enough matter to slow down its expansion, but it may possibly have enough to cause it to collapse.

The dimensionless density parameter described as

$$\Omega = \Omega_m + \Omega_G \text{ where } \Omega_m = \frac{\rho_m}{3H^2} \text{ and } \Omega_G = \frac{\rho_G}{3H^2}. \quad (41)$$

From equations (34) and (38) we have

$$\Omega_m = \left[ \frac{c_1^2 [c_3 (c_1 t + c_2)]^{\frac{n(k+1)}{2c_3}}}{8\pi c_3^2 (c_1 t + c_2)^2} \left\{ \frac{k^2 + 4k + 1}{2} - \frac{3c_1^{-2}}{[c_3 (c_1 t + c_2)]^{\frac{k+1-2c_3}{c_3}}} - \frac{\omega n^2 (k+1)^2}{8} + \frac{3n(k+1)^2}{4} \right\} - \frac{4c_3^2 (c_1 t + c_2)^2}{3c_1^2 (k+1)^2} \right] \left( \frac{\alpha_1 c_1 (k+1)}{2c_3 (c_1 t + c_2)} + \alpha_2 \frac{c_1^2 (k+1)^2}{4c_3^2 (c_1 t + c_2)^2} \right)^\gamma \quad (42)$$

From equations (33) and (38) we have

$$\Omega_G = \left( \frac{\alpha_1 c_1 (k+1)}{2c_3 (c_1 t + c_2)} + \frac{\alpha_1 c_1^2 (k+1)^2}{4c_3^2 (c_1 t + c_2)^2} \right) \frac{4c_3^2 (c_1 t + c_2)^2}{3c_1^2 (k+1)^2}. \quad (43)$$

From equations (42) and (43), we have density parameter defined as

$$\Omega = \frac{c_1^2 [c_3 (c_1 t + c_2)]^{\frac{n(k+1)}{2c_3}}}{8\pi c_3^2 (c_1 t + c_2)^2} \frac{4c_3^2 (c_1 t + c_2)^2}{3c_1^2 (k+1)^2} \left\{ \frac{k^2 + 4k + 1}{2} - \frac{3c_1^{-2}}{[c_3 (c_1 t + c_2)]^{\frac{k+1-2c_3}{c_3}}} - \frac{\omega n^2 (k+1)^2}{8} + \frac{3n(k+1)^2}{4} \right\}. \quad (44)$$

#### 4. STABILITY ANALYSIS

We use the squared speed of sound to assess the stability of our model. The parameter squared speed of sound, denoted as  $v_s^2$ , it is an essential factor in determining the stableness of the DE model. It is valuable in grasping the stability of dark energy models and is dependent on its sign.

The dark energy model is considered as stable if  $v_s^2 > 0$  and the dark energy model can be classified as unstable  $v_s^2 < 0$ .

The formula for squared speed of the sound is  $v_s^2 = \frac{\dot{p}_G}{\dot{\rho}_G}$ .

From equations (30), (33) we find the squared speed of sound

$$v_s^2 = \frac{\frac{c_1^3}{16\pi} [c_3(c_1t + c_2)]^{\frac{n(k+1)}{2c_3}-3} \left\{ (k^2 + k + 1) - c_3(k + 1) + \frac{\omega n^2(k + 1)^2}{8} - \frac{c_1^{-2}}{[c_3(c_1t + c_2)]^{\frac{k+1-2c_3}{c_3}}} + \frac{n(k + 1)^2}{2} + \frac{n^2(k + 1)^2 c_1 [n(k + 1) - 2c_3]}{4c_3(c_1t + c_2)} \right\} - \frac{(k + 1 - 2c_3)c_1}{8\pi} [c_3(c_1t + c_2)]^{\frac{(k+1)(n-2)-2c_3}{2c_3}} + \frac{n^2(k + 1)^2 c_1^4 c_3 [n(k + 1) - 2c_3]}{8\pi} [c_3(c_1t + c_2)]^{\frac{n(k+1)}{2c_3}-4}}{\frac{-\gamma c_1^2(k + 1)}{2c_3(c_1t + c_2)^2} \left( \frac{\alpha_1 c_1(k + 1)}{2c_3(c_1t + c_2)} + \frac{\alpha_2 c_1^2(k + 1)^2}{4c_3^2(c_1t + c_2)^2} \right)^{\gamma-1} \left[ \alpha_1 + \frac{\alpha_2 c_1(k + 1)}{2c_3(c_1t + c_2)} \right]^\gamma}$$
(45)

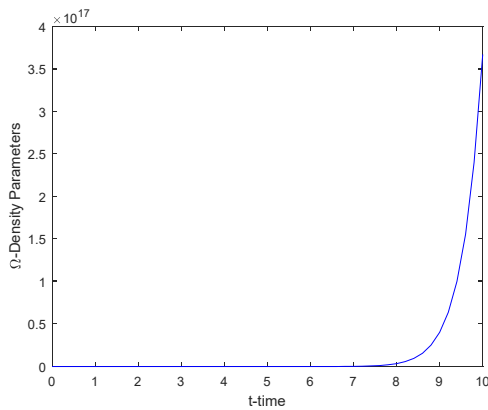


Figure 6. The Density Parameters  $\Omega$  versus time  $t$

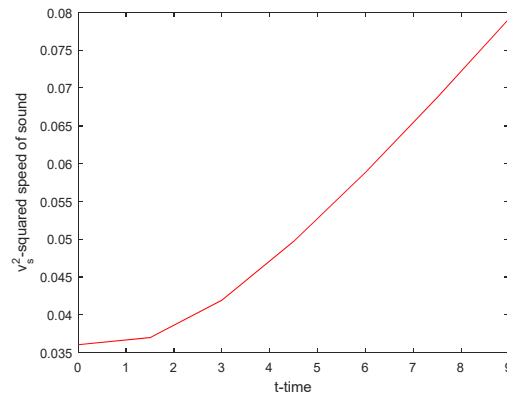


Figure 7. The squared speed of the sound versus time  $t$

### 5. $\omega_G - \omega'_G$ PLANE

Caldwell and Linder [33] implemented a plane analysis of  $\omega_G - \omega'_G$ . The  $\omega_G - \omega'_G$  plane investigation is utilized to analyze the dynamic characteristics of D.E models, where  $\omega'_G$  is the derivative in terms of  $\ln a$ . This method has been used with the quintessence model, resulting in two models of planes. The region's ( $\omega_G < 0, \omega'_G > 0$ ) interior represents the thawed region, whereas the area beneath the region ( $\omega_G < 0, \omega'_G < 0$ ) represents the frozen region. Calculate the derivative of the equation (35) when it comes to  $\ln a$ , we obtain the expression for  $\omega'_G$  as

$$\omega'_G = -\frac{c_1^2 c_3}{4\pi(k + 1)} \left[ \frac{n(k + 1) - 4c_3}{2c_3} \right] [c_3(c_1t + c_2)]^{\frac{n(k+1)-4c_3}{2c_3}} \left[ \frac{\alpha_1 c_1(k + 1)}{2c_3(c_1t + c_2)} + \frac{\alpha_2 c_1^2(k + 1)^2}{4c_3^2(c_1t + c_2)^2} \right]^{-\gamma} \left\{ (k^2 + k + 1) - c_3(k + 1) + \frac{\omega n^2(k + 1)^2}{8} - \frac{c_1^{-2}}{[c_3(c_1t + c_2)]^{\frac{k+1-2c_3}{c_3}}} + \frac{n(k + 1)^2}{2} + \frac{n^2(k + 1)^2 c_1 [n(k + 1) - 2c_3]}{4c_3(c_1t + c_2)} \right\} - \frac{c_1^2 \gamma}{8\pi} \left[ \frac{\alpha_1 c_1(k + 1)}{2c_3(c_1t + c_2)} + \frac{\alpha_2 c_1^2(k + 1)^2}{4c_3^2(c_1t + c_2)^2} \right]^{-\gamma-1} \left[ \frac{\alpha_1 c_1}{(c_1t + c_2)} + \frac{\alpha_2 c_1^2(k + 1)}{c_3(c_1t + c_2)^2} \right] [c_3(c_1t + c_2)]^{\frac{n(k+1)-4c_3}{2c_3}}$$
(46)

$$\left\{ (k^2 + k + 1) - c_3(k + 1) + \frac{\omega n^2(k + 1)^2}{8} - \frac{c_1^{-2}}{[c_3(c_1t + c_2)]^{\frac{k+1-2c_3}{c_3}}} + \frac{n(k + 1)^2}{2} + \frac{n^2(k + 1)^2 c_1 [n(k + 1) - 2c_3]}{4c_3(c_1t + c_2)} \right\} - \frac{c_3(c_1t + c_2)}{4\pi(k + 1)} \left\{ \frac{(k + 1 - 2c_3)c_3}{[c_3(c_1t + c_2)]^{\frac{k+1-c_3}{c_3}}} - \frac{n^2(k + 1)^2 c_1 [n(k + 1) - 2c_3]}{4c_3(c_1t + c_2)^2} \right\} [c_3(c_1t + c_2)]^{\frac{n(k+1)-4c_3}{2c_3}} \left[ \frac{\alpha_1 c_1(k + 1)}{2c_3(c_1t + c_2)} + \frac{\alpha_2 c_1^2(k + 1)^2}{4c_3^2(c_1t + c_2)^2} \right]^{-\gamma}$$

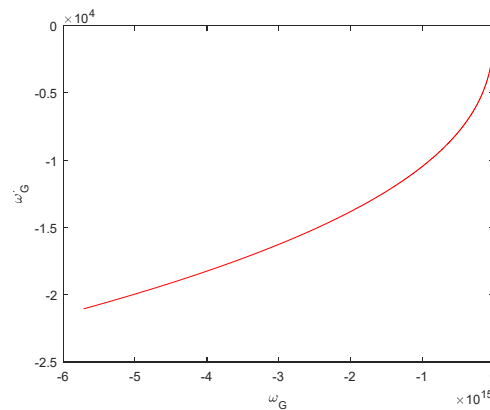


Figure 8. The plot of  $\omega_G - \omega'_G$ .

### 6. CONCLUSION

This paper discusses Bianchi Type-V cosmological model and the generalized ghost version of pilgrim dark energy in the Brans-Dicke scalar-tensor theory of gravitation (1961). The solutions to the field equations were obtained by making an assumption about the variation of Hubble's parameter. This paper delved into various physical aspects of the model. This portion provides a concise overview of the intriguing findings that were seen during the current investigation. We have taken  $n = 1.8, k = 1.5, c_1 = 0.06, c_2 = 0.04$  and  $c_3 = 9.1$  values to plot the graphs.

- In Figure 1, A graph is constructed showing the energy density of GGPDE as a function of time  $t$ . It demonstrates that the energy density of GGPDE stays positive throughout cosmic evolution, and it was also observed that the energy density of GGPDE diminishes as time passes.

- In Figure 2, A graph is created to illustrate how the energy density of matter changes over time. The graph indicates that the energy density starts at zero and then gradually moves towards the phantom region. As time increases, the energy density of matter is observed to also increase.

- In Figure 3, the EoS parameter for GGPDE versus time  $t$  is plotted. The model indicates that it starts in the matter dominated era and transitions into the phantom era.

- In Figure 4, we plotted the pressure of the dark energy against time  $t$ . The graph indicates that as time goes on, the pressure of the dark energy also goes up.

- At time  $t=0$ , the Hubble's parameter  $H$  is constant. In Figure 5, we plotted the Hubble's parameter  $H$  versus time  $t$ . It shows that the Hubble's parameter tends to zero as the time  $t$  tends to infinite per theoretical desire. It is also observed that the time  $t$  increases, the Hubble's parameter  $H$  as decreases.

- In Figure 6, we plotted the density parameter versus time  $t$ . It shows that the result is zero initially and then approaches towards the phantom region. As time increases, the density parameter is seen to increase.

- In Figure 7, the graph shows the square of the speed of sound as a function of time  $t$ . The square of the speed of sound increases with time, indicating positive values. The paths of the squared speed of the sound consistently exhibit positive behavior and stability in the model.

- In Figure 8, We graphed the  $\omega_G - \omega'_G$  plane against time  $t$  and noticed that the trajectories of the  $\omega_G - \omega'_G$  plane vary in the freezing region. It is concluded that the  $\omega_G - \omega'_G$  plane Analysis of the current situation indicates that the accelerated expansion of the cosmos is consistently supported,

- The deceleration parameter  $q$  serves as an indicator of whether the model is expanding or not. A positive indication shows that the cosmos is decelerating, while a negative sign indicates that the universe is accelerating. In this paper is observed that,

For  $0 < c_4 < 1$ , the negative deceleration parameter  $q$  indicates that the cosmos is experiencing acceleration during its evolution within this parameter range.

For  $c_4 = 0$ , the deceleration parameter  $q$  is less than zero, indicating that the universe is undergoing acceleration as it evolves in this condition.

For  $c_4 > 1$ , if the deceleration parameter  $q$  is positive, it means that the cosmos is experiencing deceleration within this parameter range.

For  $c_4 = 1$ , the deceleration parameter  $q=0$  indicating expansion with constant velocity. This means that the universe's expands when velocity remains constant over time under this specific condition.

### Acknowledgement

We are thankful to the respected reviewer for his helpful comments, which have substantially improved the caliber of the study and the presentation of our work.

## ORCID

✉ Yetchena Prasanthi, <https://orcid.org/0009-0001-3784-4819>; ✉ Davuluri Neelima, <https://orcid.org/0000-0003-1625-5596>

## 7. REFERENCES

- [1] H. Wei, “Pilgrim dark energy,” *Classical and Quantum Gravity*, **29**, 175008 (2012). <https://doi.org/10.1088/0264-9381/29/17/175008>
- [2] E. Babichev, V. Dokuchaev, and Yu. Eroshenko, “Black hole mass decreasing due to phantom energy accretion,” *Physical Review Letters*, **93**, 021102 (2004). <https://doi.org/10.1103/PhysRevLett.93.021102>
- [3] M. Sharif, and A. Jawad, “Analysis of pilgrim dark energy models,” *The European Physical Journal C*, **73**, 2382 (2013). <https://doi.org/10.1140/epjc/s10052-013-2382-1>
- [4] M. Sharif, and A. Jawad, “Pilgrim dark energy with apparent and event horizons in non-flat universe,” *The European Physical Journal C*, **73**, 2600 (2013). <https://doi.org/10.1140/epjc/s10052-013-2600-x>
- [5] M. Sharif, and S. Rani, “Pilgrim dark energy in  $f(T)$  gravity,” *Journal of Experimental and Theoretical Physics*, **119**, 75-82 (2014). <http://dx.doi.org/10.1134/S1063776114070152>
- [6] A. Jawad, and S. Chattopadhyay, “Cosmological analysis of models via pilgrim dark energy,” *Astrophysics and Space Science*, **357**, 37 (2015). <https://doi.org/10.1007/s10509-015-2285-8>
- [7] A. Jawad, “Cosmological reconstruction of pilgrim dark energy model in  $f(T, G)$  gravity,” *Astrophysics and Space Science*, **356**, 119–127 (2015). <https://doi.org/10.1007/s10509-014-2191-5>
- [8] A. Jawad, and A. Majeed, “Correspondence of pilgrim dark energy with scalar field models,” *Astrophysics and Space Science*, **356**, 375–381 (2015). <https://doi.org/10.1007/s10509-014-2206-2>
- [9] A. Jawad, I.G. Salako, and A. Sohail, “Ghost dark energy models in specific modified gravity,” *The European Physical Journal Plus*, **131**, 299 (2016). <https://doi.org/10.1140/epjp/i2016-16299-7>
- [10] C.L. Feng, X.L. Li, X.Y. Shen, “Thermodynamic of the ghost dark energy universe,” *modern Physics Letters A*, **27**, 1250182 (2012). <https://doi.org/10.1142/S0217732312501829>
- [11] A. Sheykhi, and M.S. Movahed, “Interacting ghost dark energy in non-flat universe,” *General Relativity and Gravitation*, **44**, 449–465 (2012). <https://doi.org/10.1007/s10714-011-1286-3>
- [12] S.D. Katore, and D.V. Kapse, “Phantom Behaviour of Generalized Ghost Pilgrim Dark Energy Models in Self Creation Theory,” *Bulgarian Journal of Physics*, **49**, 297-313 (2022). <https://doi.org/10.55318/bgjp.2022.49.4.297>
- [13] M. Zubair, G. Abbas, “Reconstructing QCD ghost  $f(R, T)$  models,” *Astrophysics and Space Science*, **357**, 154 (2015). <https://doi.org/10.1007/s10509-015-2387-3>
- [14] V. Fayaz, H. Hossienkhani, P. Pasqua, Z. Zarei, and M. Ganji, “Anisotropic universe and generalized ghost dark energy in Brans–Dicke theory,” *Canadian Journal of Physics*, **94**, 201 (2016). <https://doi.org/10.1139/cjp-2015-0538>
- [15] M. Honarvayan, A. Sheykhi, and H. Moradpour, “Thermodynamical description of the ghost dark energy model,” *International Journal of Modern Physics D*, **24**, 1550048 (2015). <https://doi.org/10.1142/S0218271815500480>
- [16] C.H. Brans, and R.H. Dicke, “Mach’s Principle and a Relativistic Theory of Gravitation,” *Physical Review Letters*, **124**, 925 (1961). <https://doi.org/10.1103/PhysRev.124.925>
- [17] N. Banerjee, and D. Pavon, “Cosmic acceleration without quintessence,” *Phys. Rev. D*, **63**, 043504 (2001). <https://doi.org/10.1103/PhysRevD.63.043504>
- [18] O. Bertolami, and P.J. Martins, “Nonminimal coupling and quintessence,” *Physical Review Letters D*, **61**, 064007 (2000). <https://doi.org/10.1103/PhysRevD.61.064007>
- [19] A. Linde, “Extended chaotic inflation and spatial variations of the gravitational constant,” *Physics Letters B*, **238**, 160-165 (1990). [https://doi.org/10.1016/0370-2693\(90\)91713-L](https://doi.org/10.1016/0370-2693(90)91713-L)
- [20] L.O. Pimental, “New Exact Vacuum Solutions in Brans–Dicke Theory,” *Modern Physics Letters A*, **12**, 1865-1870 (1997). <https://doi.org/10.1142/S0217732397001904>
- [21] C. Mathiazhagan, and V.B. Johri, “An inflationary universe in Brans-Dicke theory: a hopeful sign of theoretical estimation of the gravitational constant,” *Classical and Quantum Gravity*, **1**, L29 (1984). <https://doi.org/10.1088/0264-9381/1/2/005>
- [22] M.R. Setare, “The holographic dark energy in non-flat Brans–Dicke cosmology,” *Physics Letters B*, **644**, 99-103 (2007). <https://doi.org/10.1016/j.physletb.2006.11.033>
- [23] M.R. Setare, and E.C. Vagenas, “The Cosmological Dynamics of Interacting Holographic Dark Energy Model,” *International Journal of Modern Physics D*, **18**, 147-157 (2009). <https://doi.org/10.1142/S0218271809014303>
- [24] M. Kiran, D.R.K. Reddy, and V.U.M. Rao, “Minimally interacting holographic Dark energy model in Brans-Dicke theory,” *Astrophysics and Space Science*, **356**, 407-411 (2015). <https://doi.org/10.1007/s10509-014-2213-3>
- [25] V.U.M. Rao, *et al.*, “FRW Holographic Dark Energy Cosmological Model in Brans-Dicke Theory of Gravitation,” *Prespacetime Journal*, **6**, 10 (2015). <https://prespacetime.com/index.php/pst/article/view/823/805>
- [26] V.K. Bhardwaj, A. Dixit, and A. Pradhan, “Bianchi type-V transitioning model in Brans–Dicke theory with observational constraints,” *International Journal of Geometric Methods in Modern Physics*, **20**(02), 2350022 (2023). <https://doi.org/10.1142/S0219887823500226>
- [27] V.B. Johri, and R. Sudharsan, “BD-FRW Cosmology with Bulk Viscosity,” *Australian J. of Phys.* **42**(2), 215–222 (1989). <https://doi.org/10.1071/PH890215>
- [28] V.B. Johri, and K. Desikan, *Gen. Relat. Gravit.* **26**, 1217–1232 (1994). <https://doi.org/10.1007/BF02106714>
- [29] M. Sharif, and K. Nazir, “Cosmological evolution of generalized ghost pilgrim dark energy in  $f(T)$  gravity,” *Astrophysics and Space Science*, **360**, 57 (2015). <https://doi.org/10.1007/s10509-015-2572-4>
- [30] M.V. Santhi, Y. Aditya, and V.U.M. Rao, “Some Bianchi type generalized ghost pilgrim dark energy models in general relativity,” *Astrophysics and Space Science*, **361**, 142 (2016). <https://doi.org/10.1007/s10509-016-2731-2>
- [31] V.U.M. Rao, and U.Y.D. Prasanthi, “Bianchi type VI0 generalized ghost pilgrim dark energy model in Brans–Dicke theory of gravitation,” *Canadian Journal of Physics*, **94**(10), 1040-1044 (2016). <https://doi.org/10.1139/cjp-2016-0331>
- [32] V. Sahni, T.D. Saini, A.A. Starobinsky, and U. Alam, “Statefinder – a new geometrical diagnostic of dark energy,” *Journal of Experimental and Theoretical Physics Letters*, **77**, 201-206 (2003). <https://doi.org/10.1134/1.1574831>

[33] R.R. Caldwell, and E.V. Linder, “Limits of quintessence,” *Physical review letters*, **95**(14), 141301 (2005).  
<https://doi.org/10.1103/PhysRevLett.95.141301>

#### УЗАГАЛЬНЕНА GHOST PILGRIM ТЕМНА ЕНЕРГІЯ В ТЕОРІЇ БРАНСА–ДІКЕ

**Й. Прасанті, Давулурі Ніліма**

*Факультет математики, GITAM (вважається університетом), Вісакхапатнам-530045, Індія*

Ця стаття має на меті дослідити, як космологічна модель Б'янкі типу V може бути розв'язана за допомогою узагальненої темної енергії привидів-пілігримів, постулованої теорією гравітації Бранса-Дікке (Phys. Rev.124, 925 1961). Щоб знайти відповіді, ми покладаємося на припущення про (i) кореляцію між метричними потенціалами та (ii) експоненціальний зв'язок між масштабним фактором і скалярним полем. Було виявлено, що узагальнена модель темної енергії примарного паломника корелює з моделлю темної енергії політрофічного газу. Кілька фізичних величин було використано для пояснення фізичної поведінки розчинів.

**Ключові слова:** *теорія гравітації Бранса-Дікке; космологічна модель Біанкі типу V; темна енергія Ghost Pilgrim*

## FINITE ELEMENT ANALYSIS OF A DYNAMIC LINEAR CRACK PROBLEM

 Brian E. Usibe<sup>a\*</sup>, Williams E. Azogor<sup>a</sup>,  Prince C. Iwuji<sup>a\*</sup>,  Joseph Amajama<sup>a</sup>, Nkoyo A. Nkang<sup>b</sup>,  
 Oruk O. Egbai<sup>c</sup>,  Alexander I. Ikeuba<sup>d</sup>

<sup>a</sup>Department of Physics, University of Calabar, Nigeria

<sup>b</sup>Department of Science Laboratory Technology, University of Calabar, Nigeria

<sup>c</sup>Department of Environmental Resource Management, University of Calabar, Nigeria

<sup>d</sup>Materials Chemistry Research Group, Department of Pure and Applied Chemistry, University of Calabar, Nigeria

\*Corresponding Author e-mail: [princechigozie42@yahoo.com](mailto:princechigozie42@yahoo.com); [beusibe@unical.edu.ng](mailto:beusibe@unical.edu.ng)

Received July 14, 2024; revised October 20, 2024; in final form October 22, 2024; accepted October 30, 2024

This work investigates the problem of a linear crack in the middle of a uniform elastic medium under normal tension-compression loading. The direct Finite Element numerical procedure is used to solve the fractured media deformation problem, which also includes an examination of the dynamic field variables of the problem. A Finite Element algorithm that satisfies the unilateral Signorini contact constraint is also described for solving the crack faces' contact interaction, as well as how this affects the qualitative and quantitative numerical results while calculating the dynamic fracture parameter.

**Keywords:** Harmonic loading; Linear crack; Fracture parameter; Contact interaction; Elastic medium; Finite Element Analysis

**PACS:** 62.25.Mn

## INTRODUCTION

Engineering materials are prone to cracking and delamination, which compromise the integrity of structures and components. The relationship between the load being applied and the dimension and location of a crack in an element can be determined using Fracture Mechanics solutions, which also help to predict the rate of crack formation and propagation [1, 2, 16]. As a result, it is vital to predict how fractured materials will react under dynamic loadings, as they are prone to failure under extremely small, unexpected loads. This is why it is critical to correctly determine the fracture parameter from the field variables, particularly as it is clear that under harmonic loading, the interior crack expands and contracts during the tension and compression phases, and the opposite crack faces move with respect to each other, significantly altering the stress and strain field near the crack tip [3, 4]. Until recently, the impacts of crack closure on fractured mechanics solutions were overlooked due to their level of complexity. However, it is extremely important to consider this phenomenon as the stresses and displacement jumps in cracked materials are usually higher for dynamic time-dependent conditions than in a static case, causing sudden failures in engineering structures even under small loads [5]. This is because the dynamic loading conditions induce more complex stress fields and crack propagation patterns than the static loading conditions.

The most important fracture parameter, the Dynamic Stress Intensity Factor (DSIF), which measures the intensity of the crack-tip stress field, is affected by the loading frequency, load direction and amplitude, material properties, and the crack dimension (shape and size). Therefore, the analysis of dynamic linear crack problems requires more advanced numerical methods and experimental techniques than the analysis of static linear crack problems [6]. Due to the complexity and non-linearity (even for LEFM conditions) presented by considering the dynamic effect of the problem [7], a numerical technique has been adopted for the solution, rather than using analytical methods that are limited to static solutions and simple crack configurations. As a result, the Finite Element numerical approach was employed in this study for obtaining the stress and displacement fields because it is reliable, convenient, and simple to calculate the appropriate fracture parameter [8-10]. The current method of Finite Element Analysis (FEA), which examines an in-plane linear crack situated in the centre of a homogeneous elastic medium, will provide knowledge of the dynamics of a cracked structural element under harmonic loading, as well as the computational determination of an essential fracture parameter, the dynamic Stress Intensity Factor (DSIF), which estimates an appropriate crack size and level of stress before crack propagation occurs. Finite Element Analysis (FEA) is a powerful numerical technique used to solve complex engineering problems, including analysing dynamic linear crack problems. Here, we refer to a dynamic linear crack problem as the study of how cracks propagate in a material when subjected to dynamic loading conditions. In the case of this study of a dynamic linear crack problem, the material is subjected to harmonic tension-compression incident pulse, causing the crack faces to move relative to each other. The Finite Element (FE) model of this study takes into account the material properties, the nature of applied loads, and the original centroid crack configuration. This information is critical in many science and engineering fields where structural health and integrity are important, including mechanical engineering, structural engineering, materials science, and physics. It aids in understanding failure mechanisms, enhancing material design, and forecasting the lifespan of engineered structures containing delamination and cracks. Because FEA is an approximation, its accuracy is determined by the mesh fineness, input data quality, and appropriate model assumptions. Despite some of

its limitations, the FEA remains the most dependable technique for handling fracture mechanics problems that need dynamics analysis. It is crucial to highlight that under harmonic loading, both sides of the crack come into contact (during the compressive phase), which considerably changes the condition of the solution [11, 21 - 25]. In these works, the effects of crack closure were also examined, and the findings are provided in the following sections.

For the present study, the FE solution for the boundary value problem was implemented in the commercial software ABAQUS/CAE. The isoparametric hexahedral element was adapted for simulating the centroid crack. This choice was influenced by the fact that typical cracks are 3D in nature and the hexahedral elements satisfy the geometry of the fractured medium and the crack shape of the current study. The faces of the hexahedral elements align with the geometry and discontinuities of the discretized linear crack. The use of these hexahedral elements also makes it possible to accurately model the singularity of the crack front. The hexahedral isoparametric finite elements generally offer a solution with acceptable accuracy at a lower cost [18, 20]. It best describes the properties of this model as a three-dimensional continuous (solid) cube with explicit analysis (for dynamic stress and displacements) that allows for the modelling of various geometries and structures [16]. Mesh refinement and analysis of its sensitivity are used to determine the stress singularity. To satisfy the unilateral Signorini conditions, the "Hard contact" mechanical constraint was imposed in the Abaqus explicit solver.

**THE PROBLEM DESCRIPTION**

A harmonic incident wave with a unit amplitude of normal tension-compression load, propagating in a homogeneous elastic material is considered on the linear crack faces. Ideal elastic waves propagate through materials without causing a permanent change in their condition when the load is removed, but the material deforms and their cracked faces come into contact relative to each other, due to harmonic loading, as considered in this work.

This dissipation mechanism causes elastic waves to attenuate and scatter as they travel, and the rate of attenuation is usually proportional to the incident wave's frequency [12, 13].

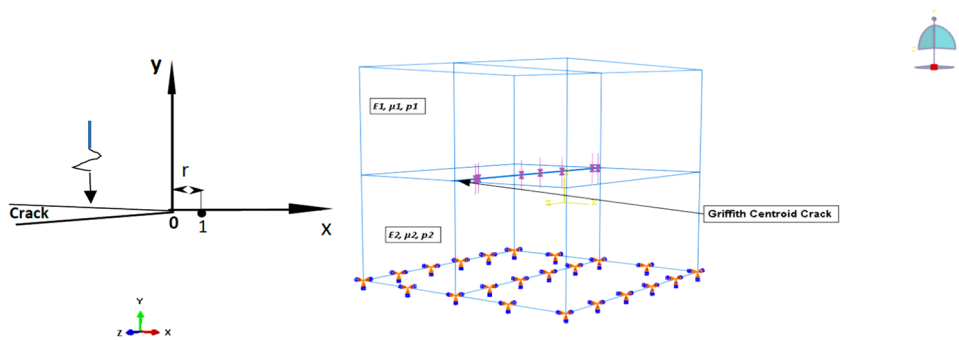


**Figure 1.** (a) - Crack geometry, (b) - FE Model of linear crack under normal tensile-compressive loading

The homogeneous material is composed of two half-spaces with identical material properties. The linear crack is located at the center of the domain. The solid domain ( $\Omega_1 = \Omega_2$ ) with both lower and the upper half-spaces ( $E_1 = E_2, \nu_1 = \nu_2, \rho_1 = \rho_2$ ) has the following properties of steel [The Young's modulus ( $E$ ) = 200 GPa, The Poisson's ratio ( $\nu$ ) = 0.3, density ( $\rho$ ) = 7800 kg/m<sup>3</sup>], and we assume that only small deformations occur according to LEFM. Figure 1 shows the 3D model built with Abaqus/CAE with an initial non-zero crack opening of  $h_0 = 10^{-6}$ mm in a Cartesian coordinate system, such that the path of the incident wave is at right angles to the interface. The incident wave was applied at frequencies and corresponding wavenumbers of  $k_\alpha = 0.1$  and the normal angle of the wave incidence,  $\theta_0 = 0^0$ .

The interface separating the half-spaces,  $\Gamma^*$ , serves as the boundary for the top half-space,  $\Gamma^1$ , while the bottom half-space is represented by  $\Gamma^2$ . In this model case, surfaces 1 and 2 consist of a finite part (crack surface) with a specific dimension and crack size ( $2a$ ), and the bonding interface; all of which satisfies the plane strain condition. The crack surface for materials 1 and 2 is represented by  $\Gamma^{cr}$  such that;

$$\Gamma^{cr} = \Gamma^{1(Cr)} \cup \Gamma^{2(Cr)} \tag{1}$$

The spatial distribution of tractions at the point of bonding,  $\Gamma^* = \Gamma^{1(Cr)} \cap \Gamma^{2(Cr)}$ , meets the continuity criteria for displacements and stresses, so that;

$$U^1(x, t) = -U^2(x, t), P^1(x, t) = -P^2(x, t) \{x \in \Gamma^*, t \in T\} \tag{2}$$

The unknown traction vectors on the crack's surfaces induced by the external loads are:

$$\begin{aligned} p^1(x, t) &= -g^1, \{x \in \Gamma^{1(Cr)}, t \in T\} \\ p^2(x, t) &= g^2, \{x \in \Gamma^{2(Cr)}, t \in T\} \end{aligned} \tag{3}$$

Where  $(x, t)$  is the displacement vector,  $p(x, t)$  is the traction vector, and  $g(x, t)$  is the load caused from the incoming wave [3, 9].

The traction vector,  $(x, t)$ , on each face of the fracture is given by:

$$(x, t) = g(x, t) + q(x, t) \tag{4}$$

The vector  $(x, t)$  represents the contact force at the contact area ( $\Gamma^{cr}$ ).

The “small” initial crack opening introduced in the model problem of this work satisfies the condition of non-zero initial opening. Signorini constraints must be imposed for the normal components of the contact force and the displacement discontinuity vectors [13-15]. The constraints ensure that there is no interpenetration of the opposite crack faces and there are no initial contact forces due to a non-zero initial opening of the crack. The constraints are given by the following inequalities;

$$\Delta u_n(x, t) \geq -h_0(x) ; h_0(x) > 0, \tag{5}$$

$$q_n(x, t) \geq 0,$$

$$\therefore (\Delta u_n(x, t) + h_0(x)) q_n(x, t) = 0. \tag{6}$$

Where  $h_0$  is the initial crack initial opening:

$$h_0 = b\Delta u^{stat, max} a (1 + \cos(\pi\sqrt{x_1^2 + x_2^2}/a)) / 2 \tag{7}$$

The maximum crack opening under static normal loading is represented by  $\Delta u^{stat, max} = 2(1 - \nu)/\mu$ , while  $b$  represents the normalized magnitude of the crack's initial opening [13].

**Dynamic Stress Distribution in Elastic Homogeneous Material**

The magnitude of the applied load is defined with a step time using the Fourier function;

$$f(t) = a_0 + \sum_{n=1}^{\infty} (A_n \cos \omega t + B_n \sin \omega t) \tag{8}$$

The amplitudes  $A_n$  and  $B_n$  of the Fourier functions are depicted by the elements of the tractions and displacements, respectively, as illustrated below:

$$p_{cos}(x) = \frac{\omega}{2\pi} \int_0^T p(x, t) \cos(\omega t) dt, \quad u_{cos}(x) = \frac{\omega}{2\pi} \int_0^T u(x, t) \cos(\omega t) dt \tag{9}$$

$$p_{sin}(x) = \frac{\omega}{2\pi} \int_0^T p(x, t) \sin(\omega t) dt, \quad u_{sin}(x) = \frac{\omega}{2\pi} \int_0^T u(x, t) \sin(\omega t) dt. \tag{10}$$

The potential function defines the incident tension-compression harmonic wave as:

$$\Phi(x, t) = \Phi_0 e^{i(k_\alpha x_n - \omega t)} \tag{11}$$

In Figure 2,  $\Phi_0$  and  $\omega$  represent the amplitude and circular frequency ( $\omega = 2\pi f$ ) of the incident wave, respectively.  $k_\alpha$  is the generalized wave number given by  $k_\alpha = \omega/c_\alpha$  and  $C_\alpha$  are the velocities of incident waves in isotropic elastic media [3,11,13].

$$C_1 = \sqrt{\frac{\lambda + 2\mu}{\rho}} \text{ (Longitudinal wave)}, \quad C_2 = \sqrt{\frac{\mu}{\rho}} \text{ (Transverse wave)}. \tag{12}$$

Where  $\lambda$  and  $\mu$  are lame constants, and  $\rho$  is the density of the material (steel). Figure 2 depicts the unit amplitude of the incident sine wave (equation 10) travelling as a function of time,  $t$ , along the normal  $y$ -direction ( $x_2$  axis), with tensile (crest) and compressive (trough) phases.

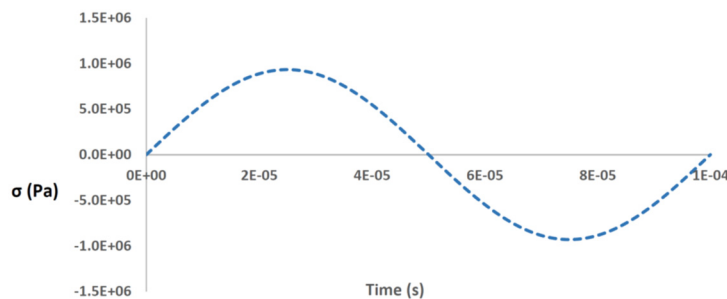


**Figure 2.** Harmonic incident wave pattern

The applied load of 1 MPa is a time-dependent sinusoidal incident wave, and at a given frequency, the generalized wave number ( $k_\alpha$ ) is obtained and the corresponding dynamic field variable is then extracted. Since the two half-spaces are made of the same materials, there is no change in the properties of the wave distribution between them. The incident wave is completely transmitted into lower material and there is no reflection. The initial incident wave propagates through both half-spaces with the magnitude of reflected and transmitted waves equal to zero. Section 5 of this work describes the distribution of the normal components of the dynamic field variables.

### Finite Element Approximation

The appropriate Finite Element approximation for the linear interface crack is based on those obtained in [16] and briefly described in Section 1 of this study. Again, to establish the presence of stress singularities at the crack tip only requires a mesh refinement around that region of interest. This enables the accurate assessment of reliable field variables at the crack tip.

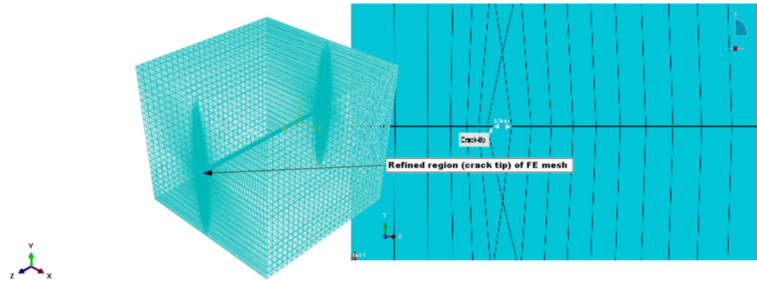


Figure 3. FE mesh discretization for the Griffith crack

In this Finite Element composition, no specific crack tip elements were required. Mesh refinement and sensitivity analysis were adequate to approximate the singularity condition at the crack tip of the FE model. Figure 4 depicts the numerical GUI results of the FE model. When the harmonic load is applied, under compression, the stress level at the contact region of the crack surfaces increases, and the model deforms depending on the load increment, with each successive step until the entire process is completed [16].

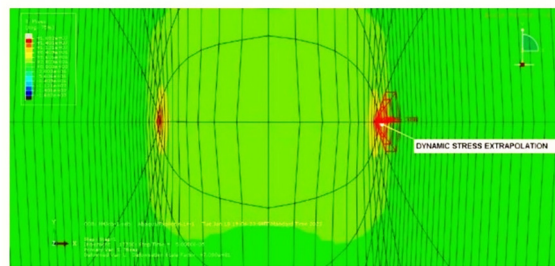


Figure 4. FE model with Stress Extrapolation

### NUMERICAL RESULTS AND DISCUSSIONS

In this study, the numerical distribution of the stress field variables is extracted at the points of integration nearest to the crack tip, whereas displacements are determined at relative nodal points indicating the vicinity of the tip [16-18]. Note that  $r = 0$  is the crack tip with infinite stresses (which is not realistic in real materials). Away from the crack tip, field variables become less valuable for fracture parametric analysis. Therefore, the region under consideration must be as close to the tip as possible ( $0 < r/a \leq 1$ ) [19, 20] to obtain accurate results with desired stability and reduced distortion of the elements around the crack-tip region. To model this “small” distance from the crack tip, the meshing “art” becomes very useful. Another way to avoid infinite stresses is to assume some elastic deformation during loading in order to provide a large area during the contact of crack faces.

The desired stresses are in the y-direction of the tension-compression load, and they are extracted at the Integrating Points in the FE model and then extrapolated to nodal points to represent the crack tip, for evaluation. This also gives a good approximation of stress singularity.

The distribution of the normal component of the harmonic stress waves along the crack plane during the entire period of oscillation ( $0 \leq \omega t \leq 2\pi$ ) for wave number  $k_\alpha = 0.1$  is shown in Figure 5. It shows that the stresses rapidly decrease with distance from the crack front and vice versa.

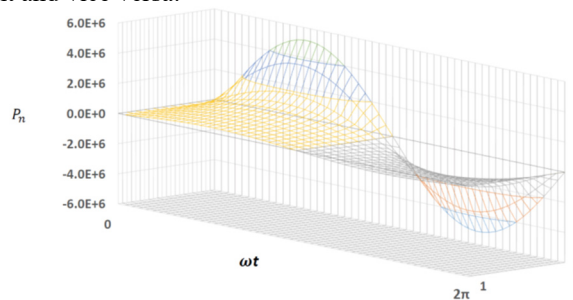
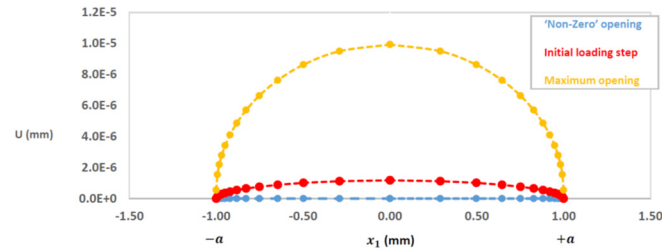
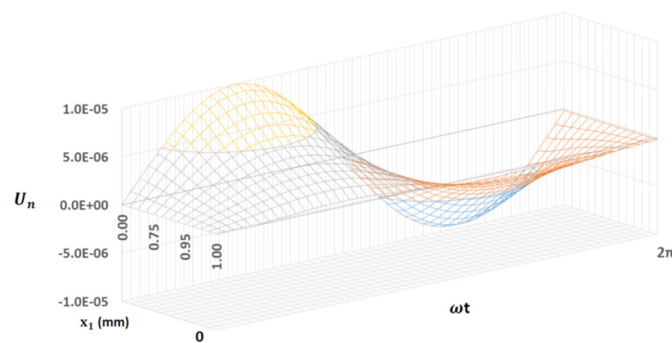


Figure 5. Normal distribution of stresses near the crack front

On the other hand, the magnitudes of normal displacement discontinuities along the diametrical crack surface before and after loading are presented in Figure 6. The normal distribution of displacement of the crack surfaces during the oscillation period ( $0 \leq \omega t \leq 2\pi$ ) for wave number  $k_\alpha = 0.1$  is also presented in Figure 7 for the leading edge of the crack. In the current study, there is symmetry between the leading (+) and trailing (-) crack fronts (see Figure 6), so only one front (the leading) of the specimen is used for the analysis.



**Figure 6.** Magnitude of normal displacements along the diametrical crack face before and after loading (upper half-space)



**Figure 7.** Normal distribution of displacement discontinuity without contacts interaction (upper half-space)

It should be noted that the tangential components of the stresses and displacements are absent or negligible due to the location of the crack in relation to the direction of the loading and the small curvature of the crack faces. Therefore, it was only necessary to evaluate the normal components of the solution.

There are no contact forces during the tensile phase of harmonic loading and crack opening, as shown in Figure 8. However, when unilateral constraints are enforced, the contact forces become present (see section 6 below).

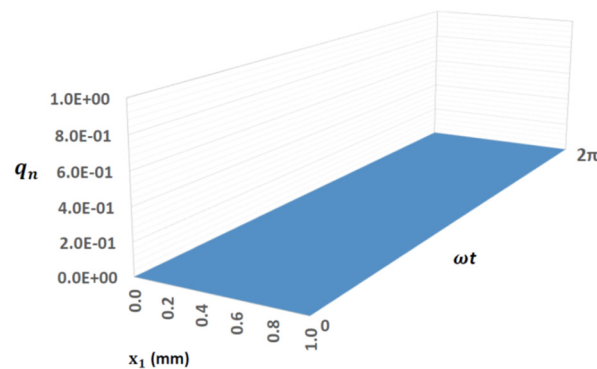


**Figure 8.** Absence of contact forces at the crack surface due to the opening of the crack faces

### Finite Element Algorithm for Contact Interaction

Following the solution of the current problem, the Finite Element contact interaction has been implemented with the algorithm below for the next stage of this study.

1. Apply initial harmonic loads, which completes the description of the physical problem
2. Solve for Fourier coefficients using equations (8) to (10)
3. Obtain the initial stresses and displacements without contact constraints
4. Define interaction pair for the crack (contact surfaces) without friction ( $\mu = 0$ )
5. Apply Kinematic contact conditions to satisfy Signorini constraints of equations (5) and (6)
6. Check for overlapping and penetration of crack surfaces; if yes, then go to 5 and repeat
7. Else, go to 8
8. Obtain the unknown stresses and displacements of interest under contact

9. Obtain unknown contact forces resulting from 5 and as part of 8
10. Repeat the algorithm to get all the appropriate extrapolated variables at the crack tip
11. Extract the numerical results and post-process using an IDE
12. Compute the Dynamic Stress Intensity Factors from 3, 8 and 11 without and with contact interaction

Figure 9 shows the linear crack under contact constraints. When external forces or pressures cause the crack surfaces to interact or remain in contact, it is said to be a linear crack under contact constraints. This situation often occurs in materials where the behavior and transmission of the crack are influenced by friction, crack closure or other boundary conditions.

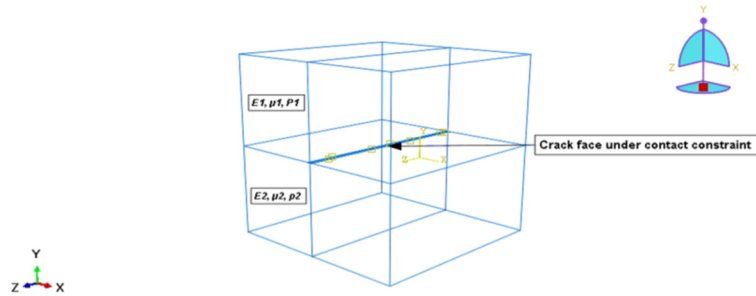


Figure 9. FE Model of Linear crack under contact constraints

In Figure 9, the constraints shown in the middle of the model (with yellow dentations) are the contact interaction properties that are imposed as boundary conditions on the crack faces of the FE model to address the components of the contact forces and load vector on the crack surfaces as indicated in equations (5) through (7). Using isoparametric surface-to-surface contact discretization and a “Hard” Kinematic mechanical constraint method from [19], the Signorini contact conditions are strictly enforced, and the penetration of contact elements is minimized. The numerical results are extracted without and with the effects of the crack closure.

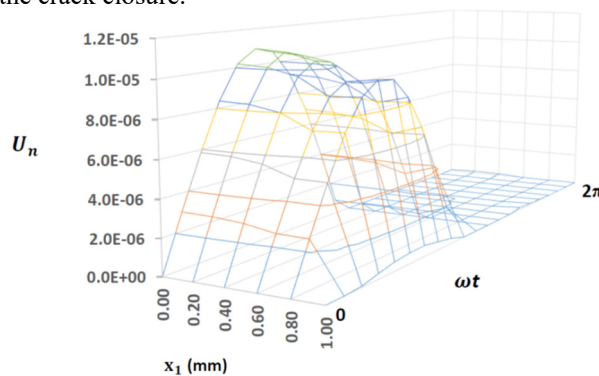


Figure 10. Distribution of normal displacement considering contact interaction

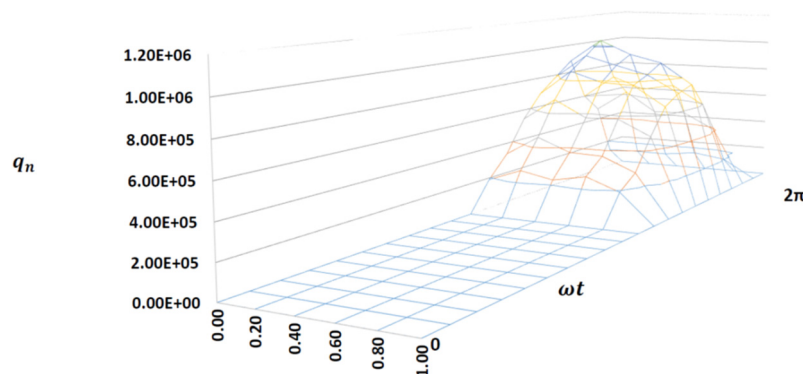


Figure 11. Normal contact forces at the crack surface

Figures 10 and 11 show the normal distribution of displacement and the corresponding contact force at the crack face during the period of oscillation ( $0 \leq \omega t \leq 2\pi$ ) for wavenumber  $k_\alpha = 0.1$  for the upper half-space at the leading edge of the crack. It is shown that the distribution of the normal component of the displacement, even during the tensile phase is significantly altered when the contact interaction of the opposite crack faces is considered (see line 5 of the algorithm). The kinematic contact constraints enforced during the period of oscillation prevent the interpenetration (overclosure) of the crack faces. The displacement discontinuity over the crack surface is observed to be distorted, especially during the

compressive phase where contact takes place. By the elimination of the interpenetration of the contacting (crack) surfaces, there is a corresponding contact force which repels the slave surfaces from the master sections, thereby leading to a substantial decrease in the magnitude of the normal component of the displacement discontinuity (see line 6 of the algorithm). This accounts for the qualitative and quantitative changes in determining the fracture parameter, Stress Intensity Factors (SIF) without and with contact interactions.

Using the asymptotic expression from [21], the Stress Intensity Factors for mode I is determined as the next stage of this study as follows:

$$K_I = \lim_{r \rightarrow 0} \sigma_y \sqrt{2\pi r} \quad (13)$$

Where  $r$  is the distance from the crack front. In this problem, there is symmetry between the leading (+) and trailing (-) crack fronts (see Figure 6), so only one front of the specimen would be used for the determination of the mode I fracture parameter and the values of the Stress Intensity Factors would be normalized by the static value, and the results validated with those from [22, 26].

$$K_I^{stat} = \sigma_y \sqrt{\pi a} \quad (14)$$

From equations (13) and (14), and by the stress extrapolation method shown in Figure 4, the Dynamic Stress Intensity Factor at the crack front can be determined, neglecting, and taking the effects of contact interaction into account.

## CONCLUSIONS

The direct Finite Element Analysis was used to obtain the normal opening mode of dynamic stresses at the crack tip, and the displacements across the diametrical crack face of a homogeneous fractured media. The normal (Mode I) distribution of stresses along the crack plane during the entire period of oscillation ( $0 \leq \omega t \leq 2\pi$ ) for wave number  $k_\alpha = 0.1$  was determined and analyzed. The magnitudes of normal displacements along the diametrical crack face before and after loading were also analyzed for the upper half-space with a distribution of displacement (without and with contact interaction) of the crack faces during the period of oscillation. The dynamic numerical results show that the nature of dynamic loading and the frequency of the incident wave on the cracked elastic media affect the distribution of the stress waves and therefore alter the fracture parameter significantly.

In what follows the solution of the current problem; the implemented Finite Element algorithm satisfies the unilateral Signorini constraints for the contact interaction on the surface of the crack during the period of oscillation and leads to the determination of the dynamic Stress Intensity Factor for varying (higher) wave numbers.

**Funding:** This study received no external funding.

**Conflict of Interest:** There are no conflicts of interest.

## ORCID

© Brian E. Usibe, <https://orcid.org/0000-0003-4388-2480>; © Prince C. Iwuji, <https://orcid.org/0000-0001-5715-9336>  
 © Joseph Amajama, <https://orcid.org/0000-0002-8475-9457>; © Alexander I. Ikeuba, <https://orcid.org/0000-0001-5091-8651>

## REFERENCES

- [1] A.A. Griffith, "The phenomena of rupture and flow in solids," *Philosophical Transactions of the Royal Society of London, Series A*, **221**, 163-198 (1921).
- [2] T.L. Anderson, *Fracture Mechanics. Fundamentals and Applications*, 2nd edition, (CRC Press, Boca Raton, 1995).
- [3] O.V. Menshykov, and I.A. Guz, "Effect of Contact Interaction of the Crack Faces for a Crack under Harmonic Loading," *International Applied Mechanics*, **43**, 809-815 (2007). <https://doi.org/10.1007/s10778-007-0082-y>
- [4] A.N. Guz, and V.V. Zozulya, "Contact interaction between crack edges under a dynamic load," *Int. Appl. Mech.*, **28**, 407-414 (1992). <https://doi.org/10.1007/BF00847122>
- [5] L. Zhang, Z. Zhang, Y. Chen, B. Dai, and B. Wang, "Crack development and damage patterns under combined dynamic-static loading of parallel double fractured rocks based on DIC technique," *Acta Geotech*, **18**, 877-901 (2023). <https://doi.org/10.1007/s11440-022-01595-5>
- [6] S. Abu-Qbeitah, M. Jabareen, and K. Y. Volokh, "Dynamic Versus Quasi-Static Analysis of Crack Propagation in Soft Materials," *ASME. J. Appl. Mech.* **89**, 121008 (2022). <https://doi.org/10.1115/1.4055670>
- [7] P. Wriggers, "Finite Element Algorithms for Contact Problems. Archives of Computational Methods in Engineering," *State-of-the-art reviews*, **2**, 1-49 (1995). <https://doi.org/10.1007/BF02736195>
- [8] M. Schäfer, *Computational Engineering – Introduction to Numerical Methods*, (Springer Berlin Heidelberg, New York, 2006).
- [9] K.H. Huebner, D.L. Dewhirst, D.E. Smith, and J.G. Byron, *The Finite Element for Engineers*, (Wiley-interscience, New York, 2001).
- [10] Q. Han, Y. Wang, Y. Yin, and D. Wang, "Determination of stress intensity factor for mode I fatigue crack based on finite element analysis," *Engineering Fracture Mechanics*, **138**, 118-126 (2015). <https://doi.org/10.1016/j.engfracmech.2015.02.019>
- [11] O.V. Menshykov, M.V. Menshykova, I.A. Guz, and V.A. Mikucka, "Contact Problems for Interface Cracks under Harmonic Loading," *Appl. Math.* **10**, 127-128 (2010). <https://doi.org/10.1002/pamm.201010056>
- [12] S.M. Walley, and J.E. Field, *Elastic Wave Propagation in Materials*, (Cavendish Laboratory, Cambridge, UK, 2016). <https://doi.org/10.1016/B978-0-12-803581-8.02945-3>

- [13] O.V. Menshykov, V.A. Menshykov, and I.A. Guz, "The contact problem for an open penny-shaped crack under normally incident tension-compression wave," *Engineering Fracture Mechanics*, **75**, 1114–1126 (2008). <https://doi.org/10.1016/j.engfracmech.2007.04.017>
- [14] M.V. Menshykova, O.V. Menshykov, and I.A. Guz, "Modelling crack closure for an interface crack under harmonic loading," *Int. J. Fracture*, **165**, 127–134 (2010). <https://doi.org/10.1007/s10704-010-9492-7>
- [15] M.V. Menshykova, O.V. Menshykov, V.A. Mikucka, and I.A. Guz, "Interface cracks with initial opening under harmonic loading," *Composites Science and Technology*, **72**, 1057-1063 (2012). <https://doi.org/10.1016/j.compscitech.2011.10.010>
- [16] B.E. Usibe, and O.V. Menshykov, "Evaluation of Dynamic Stress Intensity Factor of Griffith Crack Using the Finite Element Method," *International Journal of Mechanics and Applications*, **10**, 1-10 (2021). <https://doi.org/10.5923/j.mechanics.20211001.01>
- [17] S.K. Chan, L.S. Tuba, and W.K. Wilson, "On the Finite Element Method in Linear Fracture Mechanics," *Engineering Fracture Mechanics*, **2**, 1-17 (1970). [https://doi.org/10.1016/0013-7944\(70\)90026-3](https://doi.org/10.1016/0013-7944(70)90026-3)
- [18] B. Zafošnik, and G. Fajdiga, "Determining Stress Intensity Factor  $K_I$  with Extrapolation Method," *Technical Gazette*, **23**, 1673-1678 (2016). <http://dx.doi.org/10.17559/TV-20150424160509>
- [19] ABAQUS/CAE User's Manual, Version 6.14-1
- [20] C. Obbink-Huizer, *Modelling a crack using Abaqus: Simuleon FEA*, Accessed 16 December 2022. <https://info.simuleon.com/blog/modelling-a-crack-using-abaqus>
- [21] D. Gross, and T. Seelig, *Fracture Mechanics with an Introduction to Micromechanics*, (Springer Heidelberg Dordrecht, New York, 2011).
- [22] A.N. Guz, and V.V. Zozulya, "Elastodynamic unilateral contact problems with friction for bodies with cracks," *International Applied Mechanics*, **38**, 895–932 (2002). <https://doi.org/10.1023/A:1021266113662>
- [23] O.V. Menshykov, M.V. Menshykova, and I.A. Guz, "3-D elastodynamic contact problem for an interface crack under harmonic loading," *Engineering Fracture Mechanics*, **80**, 52– 59 (2012). <https://doi.org/10.1016/j.engfracmech.2010.12.010>
- [24] O.V. Menshykov, M.V. Menshykova, and I.A. Guz, "Effects of crack closure and friction for linear crack under normal impact," *Eng. Anal. Bound. Elem.* **115**, 1–9 (2020). <https://doi.org/10.1016/j.enganabound.2020.02.013>
- [25] O.V. Menshykov, V.A. Menshykov, and I.A. Guz, "The effect of frequency in the problem of interface crack under harmonic loading," *Int. J. Fract.* **146**, 197-202 (2007). <https://doi.org/10.1007/s10704-007-9157-3>
- [26] V.A. Mikucka, O.V. Menshykov, and M.V. Menshykova, "Elastodynamic Contact Problems for Interface Cracks under Harmonic Loading," *Proceedings in Applied Mathematics and Mechanics*, **11**, 165-166 (2011). <https://doi.org/10.1002/pamm.201110074>

**КІНЦЕВО-ЕЛЕМЕНТНИЙ АНАЛІЗ ПРОБЛЕМИ ДИНАМІКИ ЛІНІЙНОЇ ТРІЩИНИ**  
**Брайан Е. Усібє<sup>a</sup>, Вільямс Е. Азгор<sup>a</sup>, Принц Ч. Івудзі<sup>a</sup>, Джозеф Амаджама<sup>a</sup>, Нкойо А. Нканг<sup>b</sup>,**  
**Орук О. Егбай<sup>c</sup>, Олександр І. Ікеуба<sup>d</sup>**

<sup>a</sup>Департамент фізики, Університет Калабара, Нігерія

<sup>b</sup>Департамент наукових лабораторних технологій, Університет Калабара, Нігерія

<sup>c</sup>Департамент управління екологічними ресурсами, Університет Калабара, Нігерія

<sup>d</sup>Дослідницька група з хімії матеріалів, Департамент чистої та прикладної хімії, Університет Калабара, Нігерія

У роботі досліджено задачу про лінійну тріщину в середині однорідного пружного середовища при нормальному навантаженні розтяг-стискування. Пряма чисельна процедура кінцевих елементів використовується для розв'язання задачі деформації середовища з тріщинами, яка також включає дослідження змінних динамічного поля задачі. Алгоритм кінцевих елементів, який задовольняє одностороннє контактне обмеження Синьоріні, також описано для вирішення контактної взаємодії поверхонь тріщин, а також як це впливає на якісні та кількісні числові результати під час розрахунку динамічного параметра руйнування.

**Ключові слова:** гармонічне навантаження; лінійна тріщина; параметр руйнування; контактна взаємодія; еластичний середній; кінцево-елементний аналіз